Laminated Composites of Continuous Steered Fibres along Curved Paths: Characterisation and Optimisation

by

Ali Jameel Hassan, M.Sc.

Thesis submitted to the University of Nottingham for the degree of Doctor of Philosophy

Supervisors:

Prof. Shuguang Li

Dr. Elena Sitnikova

September 2019

Abstract

The need for lighter structure in the airplane industry has led to wide applications of fibre-reinforced composites due to their higher specific strength and specific stiffness. The directionality of these materials has motivated the researchers to take advantage of this feature. An investigation has been performed in this thesis by using the optimisation process to enhance structural performance or minimize structural weight. It is possible to reduce stresses in the most concentrated regions in the composite structures, such as notches and holes, by steering the fibre paths in a curved manner. In general, steering the fibre can lead to a good-balanced distribution of the local fibre angles in the composite materials. The directional properties in the laminated structures can be designed.

An optimisation framework has been developed and applied to find the optimal design variables for the optimisation design as present in this thesis. A genetic algorithm in a Matlab was used for its robustness to find the global minimum point and an excellent ability to work in a noisy environment of the objective function. In this framework, a technique of the client and server has been employed to facilitate the communications between the Matlab as the optimiser and Abaqus/Standard as stress analysis solver. Efforts have been made to avoid time delay during opening the startup session dialogue box when Abaqus/CAE is called for each iteration of the optimisation.

Optimisation of different orders of variations of the local fibre angles has been investigated concerning their effects on the local stiffness, as the ability to resist buckling load. The first-order variation has approved to be the most significant, especially when the variation was perpendicular to the direction of the applied load. A gap of variable width is present between curved fibre tow paths. It leads to a non-uniform distribution of fibre volume fraction. Therefore, the stiffness and buckling response have been influenced negatively.

A laminated composite cylinder can be designed using steered fibre. Therefore, the influence of steered fibre has been investigated in terms of the structural performance of circular and elliptical cylindrical shells. The local fibre angles vary linearly around the circumference. Optimum local fibre angles have been obtained, that result in a maximum buckling capacity. Steering the fibre around the elliptical

cylindrical shells improves the structural performance by redistributing loads from the flatter areas to the higher curved areas. The influence of the aspect ratio of the elliptical shells on the enhancement of the ability of the structure to resist the buckling load has been studied. The directions of the applied bending moment for both circular and elliptical cylindrical shells have been investigated, to find the applicable range that offers an improvement in buckling load.

The maximum stress criterion and Tsai-Wu criterion have been used to predict the failure load of curved fibre laminates. The gaps of variable width led to reduced strength with an exception for some patterns of curvilinear fibre panels, where no significant difference in failure loads has been found between the laminates of the uniform and non-uniform fibre volume fraction distributions.

A mesoscale modelling of the curvilinear tow with its variable gap width has been established to determine the constitutive relationship of the material. The effective material properties for different configurations of local fibre angles have been predicted using a unit cell model based on translational symmetries. The periodic boundary conditions have been derived. The analysis has been carried out using the Python script, which is considered as a secondary development of Abaqus/CAE. Extensive verifications have been conducted. A good corresponding has been achieved between UC models and rule of mixtures (ROM) for the obtained effective material properties.

Acknowledgements

First of all, I would like to acknowledge my supervisors, Prof. Shuguang Li and Dr. Elena Sitnikova, for their encouragement, expert advice and invaluable guidance at every stage of my PhD research and thesis writing. Honestly, I owe my deepest gratitude to them for the great support.

I gratefully acknowledge the scholarship support provided by the Higher Committee for Education Development in Iraq (HCED).

Many sincere thanks also go to my colleagues of Composite Group, who provided a comfortable research environment. Especially, I would like to thank Peng Zhuo and Mingming Xu for their help in my research.

Finally, I need to express my highest gratitude to my family for their continued support and encouragement. They are the source of motivation behind my long student career from an undergraduate, master to PhD.

Contents

List of Figures

List of tables

Abbreviations and Notations

Abbreviations

2D	Two-dimensional
3D	Three-dimensional
ESL	Equivalent single layer laminate theory
LW	Layer wise laminate theory
CLT	Classical laminate theory
FSDT	First order shear deformation theory
HSDT	Higher-order shear deformation theory
CS	Constant stiffness laminate
VS	Variable stiffness laminate
FEM	Finite element method
RVE	Representative volume element
UC	Unit cell
UD	Unidirectional fibre reinforced composite

Notations

$[A]$	Membrane stiffness of a laminate
$[B]$	Bending-extension coupling stiffness of a laminate
$[D]$	Bending stiffness of a laminate
E	Young's modulus
E_{11}	Longitudinal Young's modulus
E_{22}	Transverse Young's modulus
G	Shear modulus

G_{23}	Transverse shear modulus
K	Shear correction factor
Nx, Ny, Nxy	Membrane forces per unit length at the mid-surface
Mx,My,Mxy	Bending moments per unit length at the mid-surface
S	Tensile strength
S_{Xc}	Compressive strength along *x*-direction
S_{Xt}	Tensile strength along *x*-direction
S_{xy}	Shear strength in *xy*-plane
S_{Yc}	Compressive strength along *y*-direction
S_{Yt}	Tensile strength along *y*-direction
T_i	local angle
L	Length
x, y, z	Coordinates
γ	Shear strain component
ε	Strain component
v	Poisson’s ratio
σ	Stress
ϕ_x, ϕ_y	Rotations of a transverse normal about the *y* and *x*-axes

1 Introduction

1.1 Background

Composite materials are widely used for aviation and aerospace applications because of their high strength and stiffness-to-density ratios. In the aerospace industry, the demands for high performance of aircraft drive need for weight savings. The weight savings in the structure of the aeroplane can contribute dramatically to the reduction of fuel consumption. However, this reduction in weight of structure must not compromise the safety, durability and the performance of the aeroplane. The consequence of weight savings varies with the applications that used the composite materials in their structures where each kilogram of weight saving could offer a monetary value as shown in Figure 1.1 according to the study of Jones (2014).

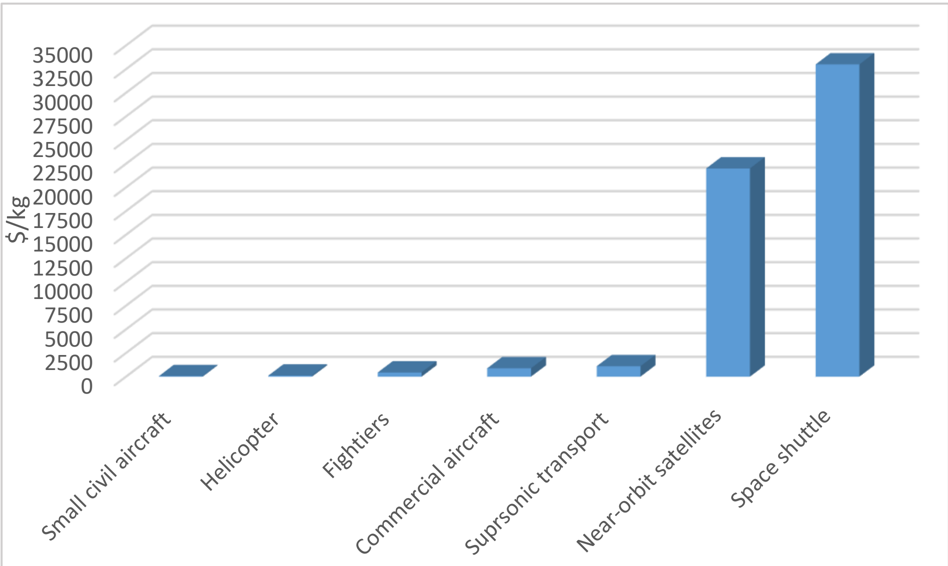

Figure 1.1: Values of weight savings for different applications

From another point of view, the reduction in thickness leads to weight savings in the composite structures. However, this tends to reduce the buckling resistance of the structure. Therefore, the reduction must be balanced against the requirements of the structural stability, but the performance could be increased by steering the fibre inefficient way to tailor the stiffness of the structure and improve the structural stability. Consequently, the designers and engineers must be fully aware of the concerns of the collapse of structures and the means to avoid it by tailoring stiffness.

The aircrafts structures are subjected to a wide range of static and dynamic loads emerging during flight, such as manoeuvres and the turbulent flow of the air, while on the ground, landing and taking off. In the particular case of landing, a significant bending moment to the fuselage is produced. This bending loading case produces compressive stresses in the skin on one side of the fuselage or the wings and tensile stresses on the other side as shown in Figure 1.2. Steering the fibres around the fuselage can redistribute the stresses. It could exploit all opportunities of composites that offer to reduce these stresses. Therefore, steering the fibres could be considered as one of the available solutions to improve the structural design of aircraft structures.

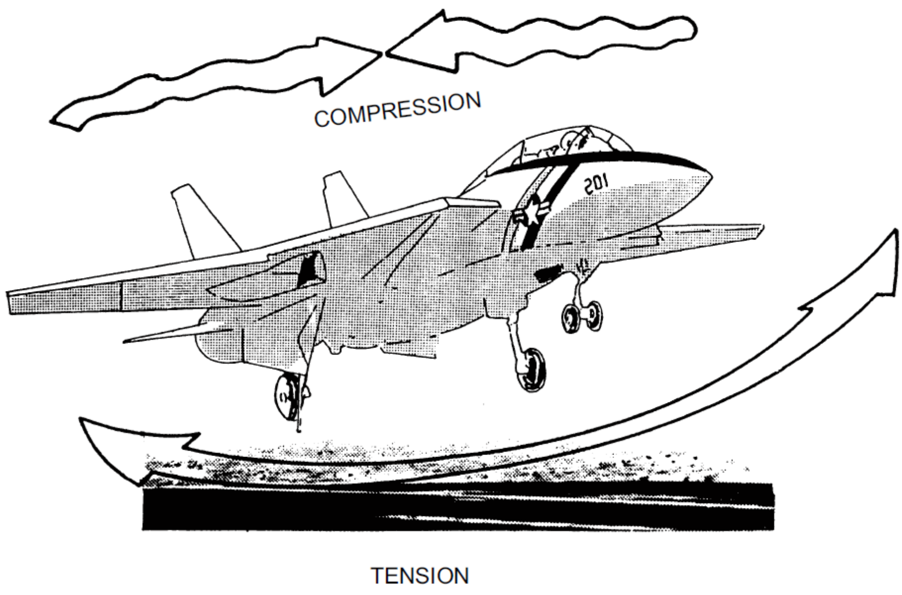

Figure 1.2: Subjected load on the aircraft during landing (Megson, 2007)

Furthermore, in addition to the stiffness weight ratio, an attractive advantage of composite materials is that they can be moulded into more complex shapes than their metallic counterparts. This could reduce the number of parts needed to produce a complex component and reduce the number of fasteners and joints. Taking advantage of this feature of composites, the weaknesses and stress concentrations due to the fasteners and joints could be reduced, avoiding crack initiation in the structure as a result of the use of fasteners. Also, reduce the number of fasteners and joints could lead to reducing time in assembly and hence cost-saving.

One of the methods that could produce a complex layout of fibre reinforcements without using fasteners and joint is steering the fibre in different ways by using automated fibre placement. This technology was developed in the mid-1980s (Evans, 1998) which allows for varying orientation of fibres along the structure by steering the fibre tow resulting in a variable stiffness laminate. This new type of laminate added more flexibility in the design process to achieve better load redistribution, resulting in great potential of improvements in the structural performance.

In order to investigate the inherent tailoring capacity of composite laminates for specific design cases, optimisation methods could be used to achieve that aim. Early work addressing composite optimisation can be traced back to the development of lamination parameters by Tsai et al. in the late 1960s. The employment of the high-performance computers has contributed to increasing applications of numerical optimisation solutions and enhances the performance of optimisation methods. Furthermore, in recent years, the new optimisation methods, such as genetic algorithms (Kramer, 2017) and simulated annealing (Arora, 2015) have been explored, which are considered new developments against the traditional searching methods. Consequently, these methods have contributed to improving the ability to find the optimum design for composite laminates under different constraints.

1.2 Aim and objectives

Steering the tows along the curved paths of identical pattern one beside another inevitably results in forming of gaps or overlaps between the adjacent tows. Shifting the tows apart between the fibre tows can avoid the overlaps and deviation of the local angles between parallel tows but tends to produce a gap of variable width as shown in Figure 1.3, assuming the fibre tow width remains constant. This leads to non-uniformity of fibre volume fraction. Therefore, the aim and objectives of this research are to study and investigate the effects of such gaps of variable width on the performances of the composite.

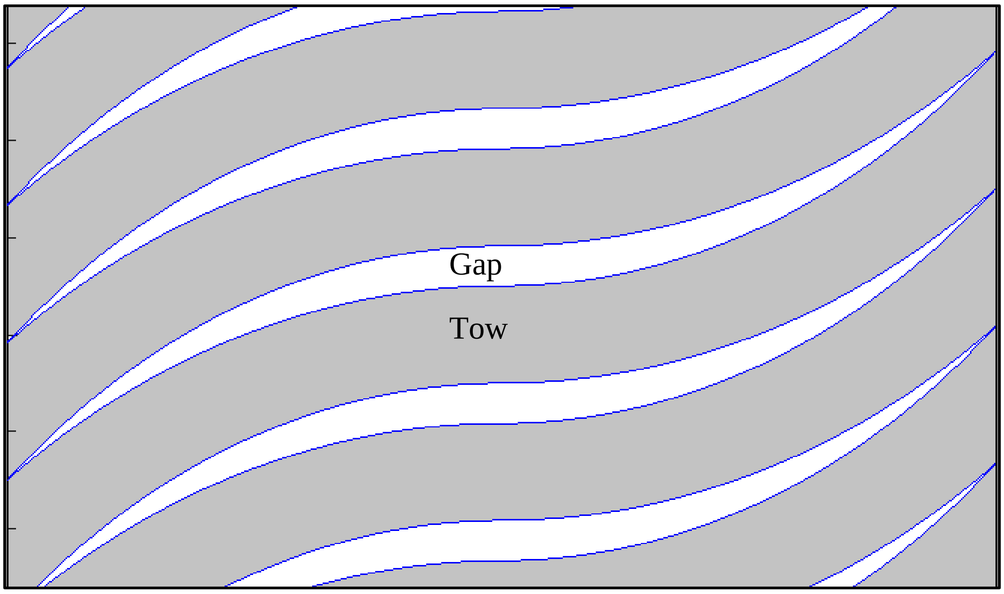

Figure 1.3: Lamina with a variable gap width

The study will endeavour to understand the influence of gaps of variable width and the effect of linear variation of local fibre angles on the buckling responses for different structures, equivalent stiffnesses and strengths. One aspect of the work is to demonstrate the significance of this gap by comparing the behaviours of composites between the uniform and non-uniform fibre volume fraction distributions. Attempts will be made to find the optimum design of a curvilinear fibre path for uniform and non-uniform of fibre volume fraction distributions of several composite structures to achieve maximum buckling load.

According to the geometric considerations of the aeroplanes and their loading conditions, steering the fibre in cylindrical structures can improve their performances by redistributing the load in different parts of the fuselage. Further investigations could help to understand to what extent steering the fibre can improve the structural performance and how much the range of directions of the bending moment to a reference direction could contribute to this improvement. Efforts will be further extended to a non-circular cylindrical shell, such as elliptical cross-sections that used as the fuel tank and a wing of aircraft. For instance, to what extent steering the fibre could improve the stability of this structure and why and how much the range of directions of the axis of bending moment to a reference direction that can affect positively.

Furthermore, one of the objectives of this study is to establish a unit cell model for the curvilinear tow pattern with gaps of variable width that has not been investigated to yet, particularly the influence of the variability of the gap width along the composite structures. This is because the geometry of the gap requires an accurate finite element modelling that is not of easy conception using customary procedures. Therefore, proper mesoscale could be performed to predict the equivalent stiffness for different configurations of local fibre angles.

1.3 Thesis layout

This thesis consists of nine chapters. Apart from the introduction as presented in this chapter, the layout of the remaining chapters is outlined as follows.

Chapter two is devoted to the literature review which covers the main themes relevant to the present research.

In Chapter three, background theoretical accounts have been presented about the micromechanics analysis, laminate theories of both classical laminate theory and first-order shear theory, and finally, the principles of the failure criteria (Maximum strain, Maximum stress, and Tsai-Wu criterion) for the subsequent applications in this thesis.

The optimisation framework is established and presented with its verifications in Chapter four.

Chapter five explores different orders of variations of local fibre angles and different approaches of representing the fibre volume fraction for the curvilinear fibre path. Also, it includes the effect of different directions of variation of local fibre angles on the in-plain stiffness and buckling response for curvilinear fibre laminates.

Chapter six focused on the influence of the curvilinear fibre paths on the buckling response of different cylindrical shells. In this chapter, the optimum fibre paths for different composite structures to sustain maximum buckling load are obtained and compared with the maximum buckling loads of straight fibre structures. Also, the applicable range of directions of bending moment has been studied.

In Chapter seven, the strength evaluations of curved fibre panels according to failure criterion is implemented for uniform and non-uniform approaches of fibre volume fraction. The linearised Tsai-Wu failure criterion is employed.

Chapter eight presented a unit cell model of complicated geometry for the curvilinear fibre architecture incorporating gaps of variable width. It is successfully formulated and applied to predict the effective material properties of the composites represented by the unit cell. In this chapter, the constraint for vertices, edges and faces involved in the unit cell model are derived in detail.

In the last chapter, conclusions of this thesis have been drawn on the major achievements during this research as presented in this thesis, with a list of suggestions for future work.

2 Literature review

2.1 Introduction

Fibre reinforced composites can be defined as a mixture of constituent materials (fibre and matrix) of different properties. The fibres are generally stiff and strong, while the matrix holds fibres and redistribute the load on fibres. The process of transmitted load in composite laminates is achieved optimally by using continuous fibre embedded in a matrix as a magnitude of the maximum value of the interfacial bond between the fibre and matrix phases. This feature could offer significantly improved performance for the structures. Besides, continuous fibres provide many benefits such as high strength, impact resistance, improved surface finish, dimensional stability and low shrinkage (Campbell, 2004). Therefore, most structural composites have continuous fibres with different forms. However, continuous fibres are more expensive to process than short fibres.

Several composite fabrication processes involving continuous fibres will be reviewed first, including filament winding, 3D printing and automated fibre placement, in which fibre paths are curved.

2.1.1 Filament winding

The filament winding process is a fabrication technique of composites, which is used for manufacturing open cylinders or closed-end structures (pressure vessel). The filament winding process appeared in the early of the 1940s, and the first attempt was made to develop the filament winding as manufacturing method (McLaughlan et al., 2011). The filament winding machine was a straightforward design. It is used to perform the simple tasks by using two axes of motion, one rotational and one axial, like the configuration of a lathe, as shown in Figure 2.1.

Since then, the filament winding machine has been further developed and improved, and became more sophisticated in design, by adding the third axis of motion, which was a radial axis (Peters, 2011). By the 70s, high-speed computers allowed for more data processing and this was reflected in more regular motion and greater placement accuracy. A schematic of the filament winding machine guided by a computer is shown in Figure 2.2. In the 1980s and 1990s, the development of the computer technology allowed for further improvement of the filament winding machines by designing a motion card hardware, which became an essential part in every filament winding machine (Peters, 2011). Furthermore, the additional axes of motion of fibre-reinforced, allowing the four, five and six axes of motion as shown in Figure 2.3(Peters, 2011).

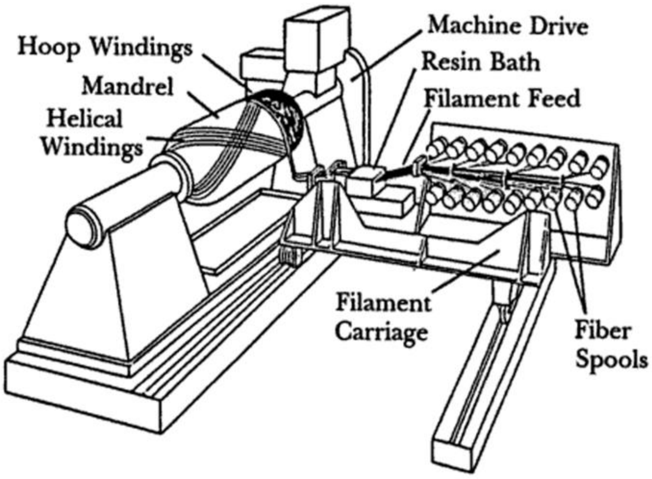

Figure 2.1: A lathe-type filament winding machine (Campbell, 2004)

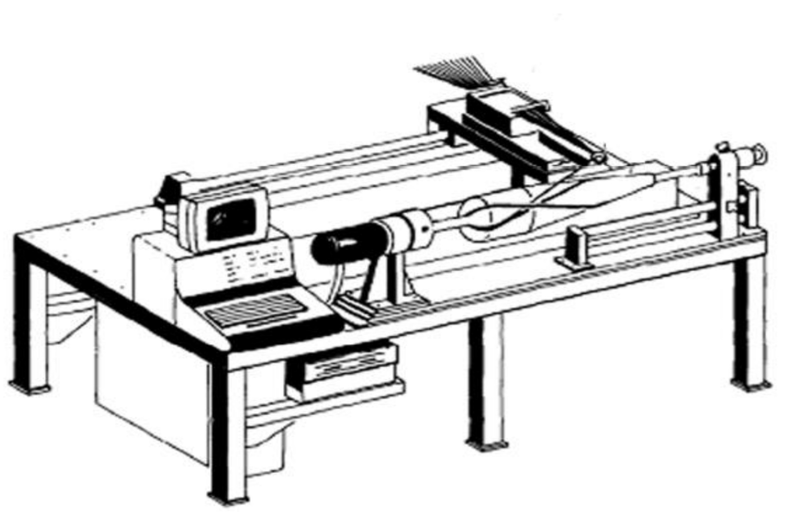

Figure 2.2: Filament winding machine guided by a computer (Campbell, 2004)

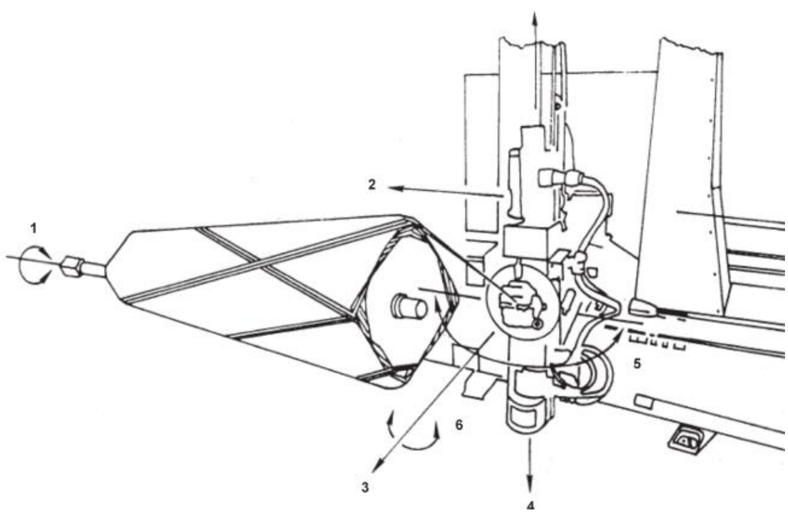

Figure 2.3: A six-axis filament winding machine (Peters, 2013)

2.1.2 3D printing of continuous fibre reinforced polymer composites.

The 3D printing of continuous fibre could be considered as one of the manufacturing processes that steers the fibre in a specific path. It is defined as a method of adding materials to manufactured object as layer by layer in order to create a three-dimensional model. Therefore it is known as additive manufacturing (AM) (Parandoush and Lin, 2017). The 3D printing as a technique in the manufacturing processes of composite material offered an opportunity to produce a load carrying structures such as the lugs and joints (Zhuo et al., 2017). Hence, it offers the fibre continuity, which cannot be achieved by using the conventional methods of cutting such as drilling to produce a hole in a composite structure.

Printing continuous fibre by using fused deposition modelling (FMD) technology is the widest technique. Matsuzaki et al. (2016) developed the new technique to impregnate the continuous fibre with thermoplastic resin in the nozzle. In this printer, the continuous fibre and the thermoplastic resin are supplied separately to the head of the printer, as shown in Figure 2.4. Then they are transformed directly to the small heater to melt the resin filament with continuous fibre. This process offers an adhesion between fibre and matrix in the printer head. Finally, the composite mixture is ejected on the printing bed to produce the printed path according to the wanted path. The path could be supplied through G-code text file to cover whole area pixel by pixel of a layer and then layer by layer to complete 3D model.

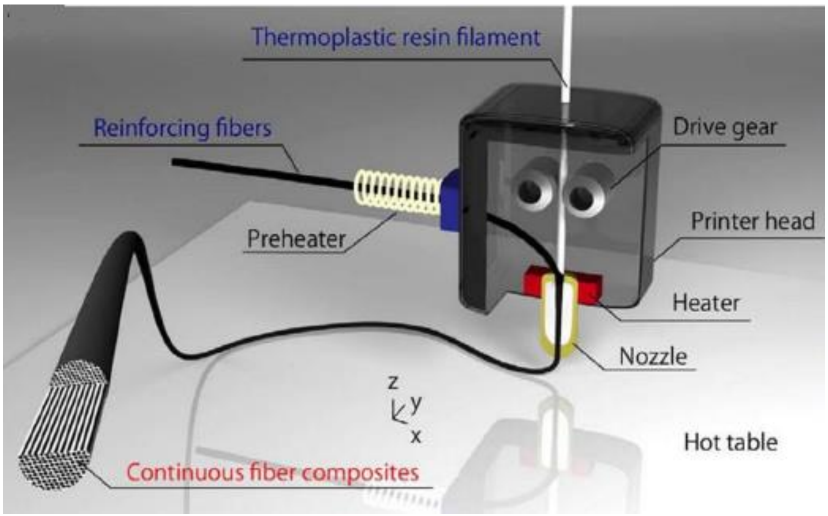

Figure 2.4: Drawing of 3D printer head for continuous fibre composite (Matsuzaki et al., 2016)

In addition, it can use a short form of fibre like fillers of cellular carbon fibre as reinforcement in the extruded matrix (Compton and Lewis, 2014). This type is known as a 3D extrusion printer, where the micro-nozzle of the printer head can align the fillers under the shear force and extensional flow, as illustrated in Figure 2.5. This technique guides the fillers of short fibre in the printing direction to improve the stiffness of the printed composite. It could give a substantial improvement in the stiffness when compared with random orientation of fillers in the printed path. However, it still not comparable with a printed continuous fibre reinforced composite.

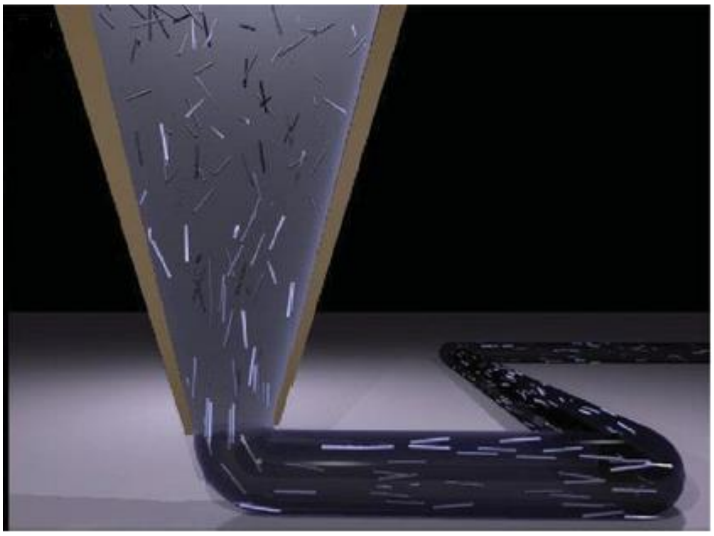

Figure 2.5: Extrusion of the 3D printed path with the progressive alignment of fillers (Compton and Lewis, 2014)

The most limitations in the 3D printing that are considered as dominant challenges are a lack in adhesion between fibre and matrix, void formation, blockage in the nozzle due to filler inclusion and increased curing times (Parandoush and Lin, 2017). Therefore, the mechanical properties for composite materials that are produced by the conventional manufacturing processes such as Prepreg/ Autoclave and RTM are better than that of 3D printing. In addition, the deposition rate can be considered as one of the limitations of 3D printing, which depends on the nozzle size, the material used, required print resolution and complexity of part to be printed.

The fibre volume fraction of the continuous printed composite is affected by the existence of an appropriate space between two adjacent lines of the printed path. This can allow the printed fibre to be uniformly compacted. Besides, using a compaction system such as a roller could increase the compaction pressure to reduce the voids and prevent the deboning between the layers (Zhuo et al., 2017).

2.1.3 Fibre placement machine

In recent years, there has been an increasing trend of using curvilinear fibre paths in composite laminates. This new configuration offers excellent potential for performance improvements over the conventional straight fibre laminates. The manufacturing of laminates with curvilinear fibre paths is carried out by employing the fibre placement technology, which gives the capability of steering individual fibre tows through the surface of a mould or the build-up of previously laid laminae (Lozano et al., 2015).

There are two leading manufacturing technologies for the automated placement that can be classified according to the width of the tow or tape into Automated Tape Laying (ATL), and Automated Fibre Placement (AFP). Each tow or tape consists of a set of unidirectional fibres. With AFP technology, multiple individual fibre tows are placed automatically onto a mandrel. Tows are typically 1/8, 1/4 or 1/2 in. wide, whereas tapes are wider, typically 3, 6 or 12 in. wide. Each band of simultaneously placed tows is called a course (Blom, 2010b).

Fibre placement technique is applicable for different materials, including thermoset and thermoplastic materials, as well as the dry fibres. A fibre placement machine as shown in Figure 2.6, typically consists of a control system, a robotic arm, a materials storage centre and the fibre placement head. In addition to the degrees of freedom due to the robotic arm, an extra degree of freedom is available due to the mandrel rotation, which is allowed for more flexibility of the fibre placement head to access every point on the surface of processing. Also, the individual supply of fibre tows and their small width, material type and the size of compaction roller allow placing the prepreg tows on the complex surface. Tows can also be cut and restarted individually, and that contributes to manufacturing parts similar to their final shape; hence, reducing scrap rates. In addition, the ability of this apparatus to regulate the speed of the tows individually, known as differential tow payout, provides the main potential of AFP, as it enables the lay-up of curvilinear paths within each ply on complex surfaces (Waldhart, 1996). With the fibre placement technique, the stiffness and strength parameters, which depend on the fibre orientation angle, can be altered spatially from point to point as fibre path be in a curved manner as shown in Figure 2.8 to tailor the structure to the designated loads and stresses.

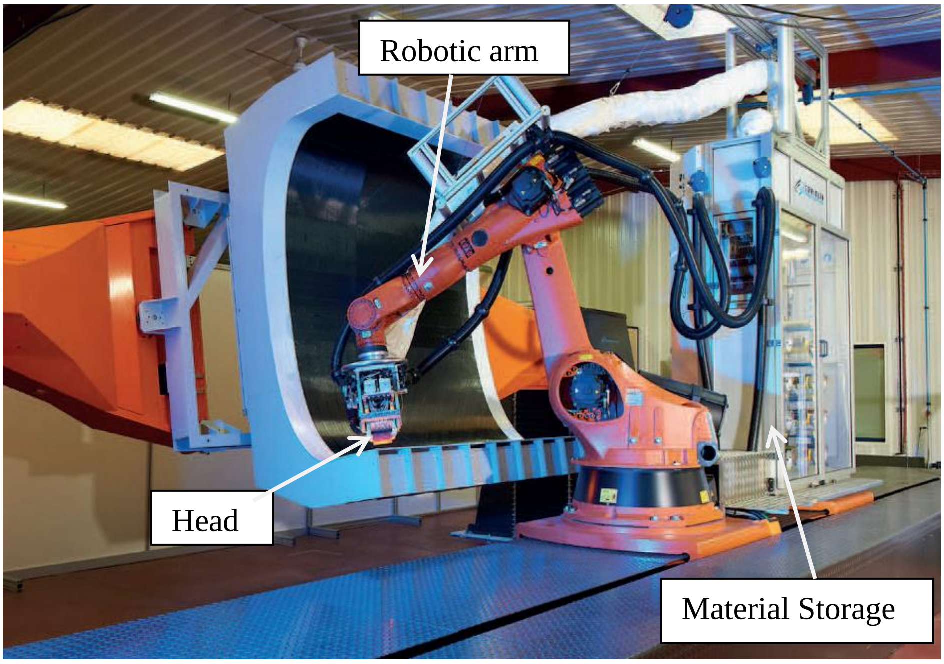

Figure 2.6: Fibre placement machine with typically mean parts (www.coriolis-composites.com)

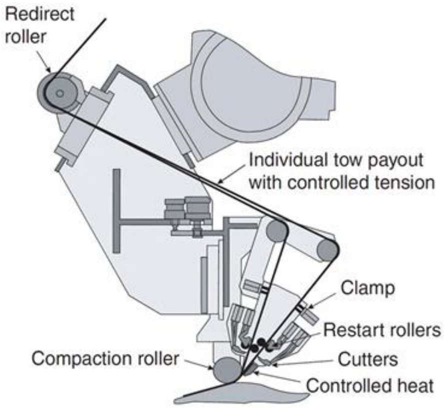

Figure 2.7: Machine head (Evans, 1998)

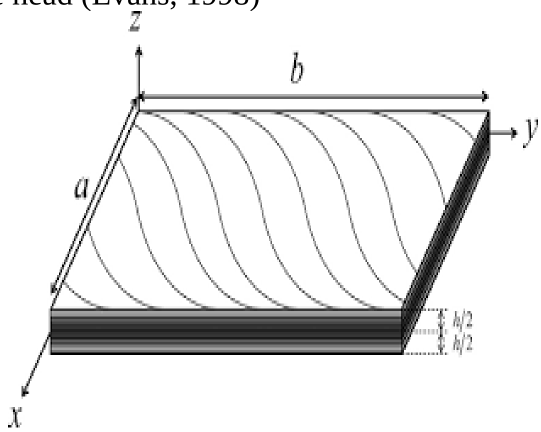

Figure 2.8: Curved fibre path with different orientations

Furthermore, applying the fibre placement technique allows for enhancing the performance of the structure without an increase in weight over traditional laminates. As a result, the varying fibre angle orientation, the stiffness properties will vary across the laminate plane. Hence, this kind of laminate is termed as the variable stiffness laminates (Olmedo and Gurdal, 1993).

2.1.3.1 Applications of fibre placement technology

The increasing interest in composite materials and their applications in aerospace, automotive and other structures puts an increasing demand on the manufacturing automation. The first company which applied the fibre placement technology was Boeing Helicopters in the early 1990s. Boeing developed a process to produce the aft fuselage section by the fibre placement technology. The aft fuselage section was manufactured by dividing it into nine individual panels built using hand lay-up. By using fibre placement in order to produce the aft fuselages, the required amount of fasteners are reduced, the trim and assembly labour is reduced, and the amount of materials scrap are also reduced (IJsselmuiden, 2011b).

Lightweight bicycle components such, as brake boosters, link plates and bicycle frames can be produced applying the fibre placement technology because it allows to arrange the reinforcing fibres in any direction and for any complex shape (Mattheij, Gliesche et al. 1998).

Fibre placement technology has advantages when producing large and complex structures. It allows reducing the costs without compromising efficiency and quality. However, it is still an expensive technology. As such, it is commonly applied in the aerospace industry, where the relatively expensive large parts are produced over a long time. Recently, there has been a decrease in machine costs and an increase in the production rate. Therefore, the fibre placement process applicability is expanding to other industries, such as automotive, maritime and wind energy.

2.1.3.2 Manufacturing limitations of the fibre placement technology

In the manufacturing process of fibre placement, some issues are rising to the surface, which affect the practical applications of variable stiffness laminates. For instance, sometimes the boundaries of neighbouring courses do not match at some locations, i.e. they do not lay parallel to an adjacent one. This generates variable regions between the tows courses. When the one tow laid on the other, so, it is called overlap defects, while in other instances when space is left between the tows, forming a gap, as shown in Figure 2.9(a) (Lopes et al., 2008a). The overlaps could be useful because a thicker region can serve as an integral stiffener, which enhances the load-carrying ability of the structure. One more type of defects is the tow drop, which happens when the fibre placement machine cuts the tow individually to prevent the overlap regions and thickness build-up, as shown in Figure 2.9(b), (Lopes et al., 2008a). In this case, during the laminate curing process, the small fibre-free area could be a region of a resin-rich pocket, where the stress concentration can occur.

Furthermore, a collision of the machine head with the model and fibre bridging of concave surfaces or complex geometries must be one of the limitations which takes through the design considerations (Lozano et al., 2015). Also, the steered fibre route could deviate from the design route, for example, when the dry fibre is used. The fibre angles at the boundaries of the course will deviate from the centre line of a steered course as the result of the fibres being placed parallel to one another as illustrated in Figure 2.9(c). The amount of deviation could be influenced by the fibre path and the course width (IJsselmuiden, 2011b). Therefore, the designer should consider that defining fibre angles according to the angle at the course centreline could result in the differences between the model and the manufactured parts. Deposition rate can be considered as a crucial aspect in manufacturing limitations of fibre placement that describes the amount of materials that can be laid per unit time. It is the usual performance metric for fibre placement (Lozano et al., 2015). The deposition rate could be affected by process speed, the chosen staking sequence, the desired amount of steering, and the shape of the part.

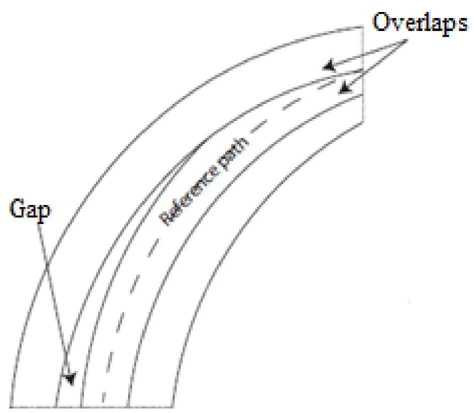

(a)

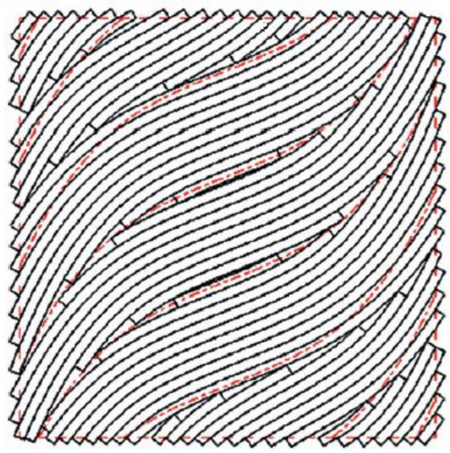

(b)

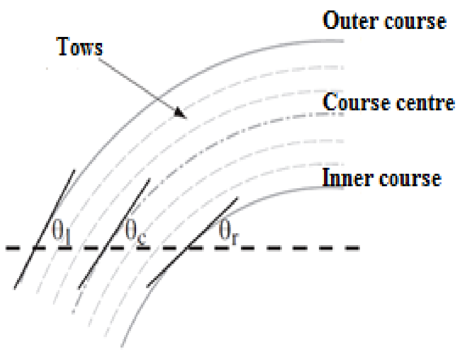

(c)

Figure 2.9: Defects of the AFP machine; (a) gaps and overlap, (b) tow drop, and (c) deviation of fibre angle through the course centre

Furthermore, steering the tow in a curved path could result in the compression of the inside of the fibre tows where the tows bend. The maximum allowable steering curvature of each course depends on the type of fibre used and the course width, as shown in Figure 2.10. The wrinkling of the tows appears inside of tows when the excessive steering is applied to the tows, and this could lead to a reduction of the quality, and the wall thickness of the structure may increase (Lozano et al., 2015). Another limitation is when the boundaries of the tow are not cut in normal directions to lay up, forming the so-called jagged or saw-tooth edge, forming small gaps, overlaps or a combination of both.

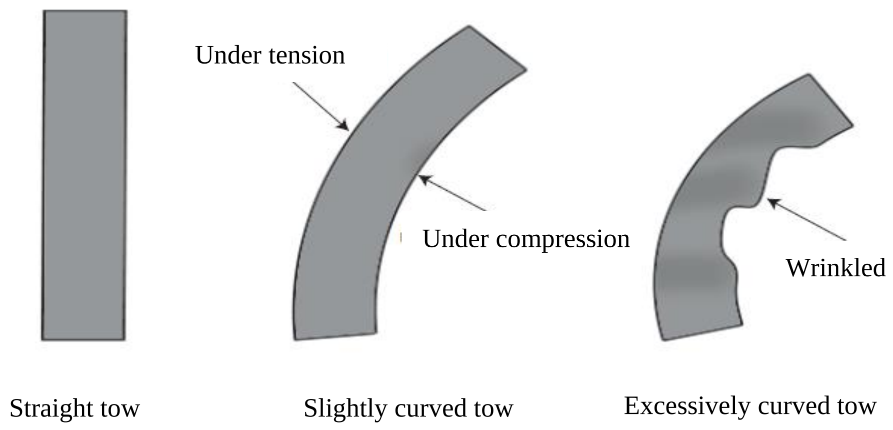

Figure 2.10: Wrinkling due to increasing steering curvature

Furthermore, in the AFP, within a single course, the local fibre angles could vary over its cross-section. A difference between the local angles on both sides of the course centre in relation to that of the centre of the tow can often be observed as illustrated in Figure 2.9(c) This deviation results from the variation of the width in the course. Without such variation in tow width, either a gap or overlap between neighbouring courses will emerge. In order to avoid the overlap, a certain shift between adjacent tows needs to be introduced. However, this produces a gap with variable width along the tow paths. Also, some tows in the course are not continuously placed from side to side of the panel; they are cut to fit the geometry of the structure to be manufactured. This could undermine the load transformation, e.g. in a panel under tensile load. Therefore, placement a continuous tow, as presented in this thesis, could be a subject to these considerations in the AFP.

2.2 Composite laminates

Composite laminates are composed of a number lamina of fibres set in a matrix. Composite laminates have been commonly used in aerospace, civil and mechanical structures because they offer high strength to weight ratio over traditional materials. In addition, an excellent corrosion resistance, thermal insulation, good damping coefficient and long fatigue life are considered as additional factors in favour of using the composite laminates. The mechanical behaviour of composites laminates is strongly dependent on their laminate configurations, i.e. layer fibre orientation, layer thicknesses and the layup sequence. Laminates are efficiently used in structural design because it is relatively easy to tailor their mechanical properties to meet the specific design requirements. Gürdal et al. (1999b) have demonstrated that laminates also have their problems, for instance, the mismatch of materials properties between the laminas may result in shear stress between layers and especially near the edges of the laminate, and this may lead to delamination in the laminates.

2.2.1 Constant stiffness laminates (CS)

In the conventional laminates, which consist of many laminae having a straight fibre path, i.e. the fibre orientation of lamina is constant, as shown in Figure 2.11. Hence, these laminates would have constant stiffness (CS). The [A], [B] and [D] stiffness matrices that depend on fibre angle orientation are constant over the laminate. In general, some elements of the [A], [B] and [D] matrices could vanish depending on the type of laminate. In these laminates, the design variables for CS laminates include ply angles, the ordering of the plies, and number of the plies and material type, which should be considered in order to obtain the preferred design.

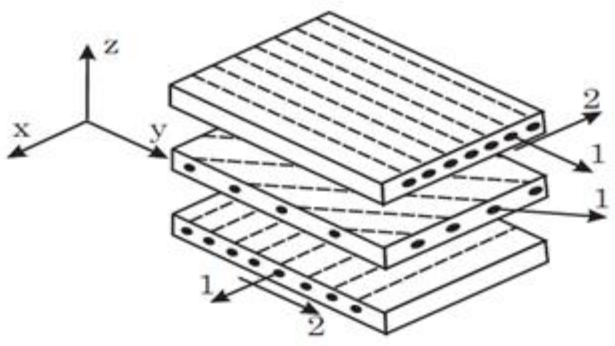

Figure 2.11: Straight fibre laminate

Fibres in the lamina are principal reinforcement responsible for its load-carrying capacity. The fibres are stiffer and stronger than the matrix. Whereas, the matrix could support the fibres and distribute the load among the fibres (Jones, 1998). Therefore, the composite laminate properties (strength and stiffness) are significantly dependent on the fibre orientation of the lamina. The directional nature of the fibres in the composite laminates introduces a directional dependence for composite material properties. Consequently, the laminates are classified as an anisotropic material. Different types of laminates that can be constructed depending on fibre orientation of lamina and stacking sequence such as symmetric, antisymmetric, balanced, quasi-isotropic, cross-ply and angle-ply laminates. Most laminated structures are symmetric laminates, as shown in Figure 2.12, where the material type, thickness and fibre orientation of laminas are symmetric for the middle plane of the laminate.

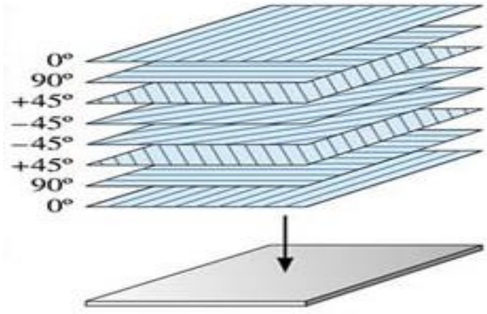

Figure 2.12: Symmetric configuration of the laminates

2.2.2 Variable stiffness laminates (VS)

The variable stiffness laminate is a laminate that having stiffness matrix varies from one location in the laminate to another according to the thickness and fibre angle orientation that dictate the stiffness matrix. Therefore, the variable stiffness laminates could be classified into two groups as follows.

2.2.2.1 Variable stiffness laminates through fibre path variations

The laminates that have a variable fibre path in their laminae lead to local variation in stiffness. The variable stiffness is based on the spatial change of the local angles that could be achieved in the lamina by 3D printer and fibre placement machine. Since the variation of local angles is continuous through the lamina, the variation of stiffness is also continuous. Also, because of the spatial variation of the local angle, the design variables that describe the variable stiffness laminates will be more than that of constant stiffness laminates and the structural design will be more complex. Wu et al. (2012) carried out the buckling analysis and the optimisation of the variable stiffness laminates having a variable angle of tow. They calculated the critical buckling load according to the Rayleigh-Ritz approach. It was found that variable stiffness laminate gives the designer more flexibility in improving the load distribution as compared to the traditional fibre reinforced composite laminates, whereas the elements of the [A], [B] and [D] matrixes are related to the *x*-and *y*-coordinates. Lopes et al. (2008a) revealed that variable stiffness laminates were more efficient as compared to straight fibre laminates in terms of finding the maximum buckling load and first-ply failure load. Gürdal et al. (2008) showed that the spatial variation of fibre orientation, which varied perpendicular to the loading direction in the rectangular composite laminates, improved the buckling load, as a result of redistribution of the loads from the centre of the panel to the simply supported sides of the panel.

The redistribution of the load shown in Figure 2.13 gives a clear picture of the changing stiffness in the laminates, where the relationship between the load and stiffness is directly related. This led to non-uniform in-plane stresses distribution that will have a significant influence on the buckling load of panels. Also, the variable stiffness of layers of curvilinear fibre paths provides more adjustability to the designer for balancing between overall panel stiffness and buckling load for different applications.

Actually, the improvement in the buckling load as a result of variation of local angles could be affected by the ratio of the lamina material properties (E_x/E_y), as well as with aspect ratio of the characteristic dimensions. Also, the in-plane boundary condition along the edges of the panels could be affected.

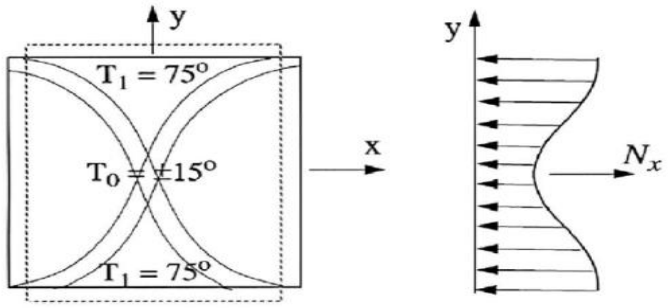

Figure 2.13: Load redistribution of variable stiffness laminates (Gürdal et al., 2008)

Steering the fibre in the variable stiffness laminates could be done in different ways. Olmedo and Gurdal (1993), presented the shifted method, which depends on the one-dimensional of local angles variation. In order to achieve the required variation of local angles along the whole lamina, the centreline of the steered tow should match the curvilinear path reference to cover a course. Then, covering the entire surface of the laminate is accomplished by placing subsequent courses and moving them perpendicularly to the direction of variation. A parallel method was suggested by Waldhart et al. (1996). The main course is placed on the surface, and the neighbouring courses were adjusted parallel to the main course, whereas the entire surface, of the laminate, is covered by steered fibres. The shortage of control over the fibre angle distribution has been considered as a deficiency of this method because the fibre local angles of only the first course could be actively controlled and the others will have a deviation in the local angles of the main one. When larger surface needs to be covered, the maximum curvature in the parallel approach increases with each successively placed path and results in a large deviation in the local angles of the parallel tows, which can be considered the second disadvantage of this method.

2.2.2.2 Variable stiffness laminates through thickness variations.

One way to change the stiffness of a thin laminate is by altering the number of plies per location, which changes the thickness of the laminate, as well as the stiffness characteristics of the shell. According to the classical laminate theory, the stiffness matrix of laminate could be calculated by integrating the wall thickness. Therefore, the effect of thickness variations is completely considered within the [A], [B], and [D] stiffness matrices. The dropped ply construction is shown in Figure 2.14, where the thickness of each ply is t_p, and H is the thickness of the original laminate with no thickness variation (Tatting, 1998). The additional plies are assumed to be symmetric about the mid-surface of the laminate and consist of φ_p and $-\varphi_p$ layers so that the structure remains balanced. The addition to the stiffness terms of the original stiffness laminate can then be calculated for symmetric laminates as follows (Tatting, 1998):

$$A_{ij} = 4t_P . Q_{ij}(\varphi_p)\ ,\ B_{ij} = 0,\ D_{ij} = \frac{1}{12}[(H + 4t_P)^3 - H^3]Q_{ij}(\varphi_p)\quad j \neq 6 \qquad (2.1)$$

$$A_{ij} = 0, \qquad B_{ij} = 0,\quad D_{ij} = \frac{2}{3}[(3Ht_P^2 + 7t_P^3)]Q_{ij}(\varphi_p) \qquad j = 6 \qquad (2.2)$$

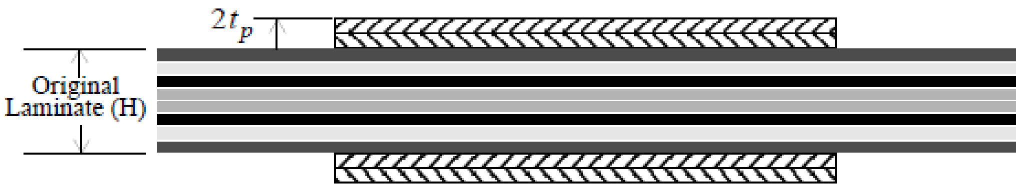

Figure 2.14: Geometry of dropped ply construction (Tatting, 1998)

Therefore, the change in the wall thickness is reflected on the value of the stiffness of laminates that have been changed to the thicker structure. For laminates have a smooth variation in thickness over a region of varying thickness, the method for dropped/added plies also could be applied (Tatting, 1998). Curry et al. (1992)

showed that both the tensile and the compressive strengths reduced significantly because of the discontinuity of the thickness that occurs in the dropped plies. They stated that the reduction in the tensile strength is smaller than the reduction in compressive strength for a given configuration of dropped plies. Paschero and Hyer (2009) have shown that variation of the wall thickness along the circumferential direction of the cylinder could enhance the axial buckling capacity of cylindrical shells with an elliptical cross-section. They applied the stress of the buckling relation of uniform thickness of the circular cylindrical shell to the elliptical cylindrical shell, to design the variable wall thickness of elliptical shells having buckling load of the circular shells.

Adali et al. (1993), used the variable wall thickness as a design variable to maximise the internal pressure and minimise the weight of pressure vessel structures by taking the Tsai-Wu failure criterion as a constraint. They found there is an improvement to increase the internal pressure capacity for variable shell thickness about 20% more than the constant thickness shell at low internal pressure, but this improvement decreases with high pressure applications.

Actually, changing the wall thickness of the composite structures to change the stiffness matrix is an undesirable method. Since if the thickness is increased, the structure weight will be also increased, and that not acceptable with a principle of using composite materials. In addition, using the method adding or trimming plies to vary the stiffness of the laminate could produce the unwanted out-of-plane stress concentrations in tapers that can initiate in-plane matrix cracking and delamination.

2.3 Design of curvilinear fibre path

In a traditional straight fibre laminate, fibre orientation within every layer is represented by a constant angle, while in a variable stiffness layer, the fibre orientation changes on the *xy*-plane as a function of both coordinate directions $\theta=\theta(x, y)$. In order to study the variable stiffness laminates, a model for of curved fibre path is required. Several approaches have been developed to model the curved fibres, and these are outlined in the subsections below.

2.3.1 Functional fibre path definition

The functional fibre path is defined as function describes the path of fibre in term of the x and y coordinates. It has the advantage of ensuring the continuity of the fibre path and implementation of AFP manufacturing constraints in the curvilinear fibre path definition. It can be classified into two parts according to the variation type of the curve path.

2.3.1.1 The linear variation of the local angles

A simple description employed to model the continuous variation of the laminate stiffness properties is based on the linear function of variation in terms of x- or y-directions of a panel for the local fibre angles of the individual layers proposed by study of Gurdal and Olmedo (1993). This definition assumes that the local fibre angles of the reference of fibre path varies linearly from the value T_0 in the centre of the panel to T_1 at a specified distance d. Tatting and Gürdal (2001) have developed the model of Gurdal and Olmedo (1993), where they generalised the fibre path by rotating the axis of fibre orientation by an angle φ from the geometric axis of the panel. The local fibre orientation can be denoted by $\varphi(T_0 \mid T_1)$, and vary linearly along the r direction, rotated from the x-axis by φ from T_0 at the centre to T_1 at the characteristic dimension of the panel as shown Figure 2.15.

The piecewise continuous functions which define the fibre path orientation could be determined in terms of φ, T_0, T_1 and r according to Tatting and Gürdal (2001) as follows.

$$\theta(r) = \varphi + (T_1 - T_0).\frac{r}{d} + T_0\,, -d \le r < 0 \tag{2.3}$$

$$\theta(r) = \varphi + (T_0 - T_1).\frac{r}{d} + T_0\,,\;\; 0 \le r < d \tag{2.4}$$

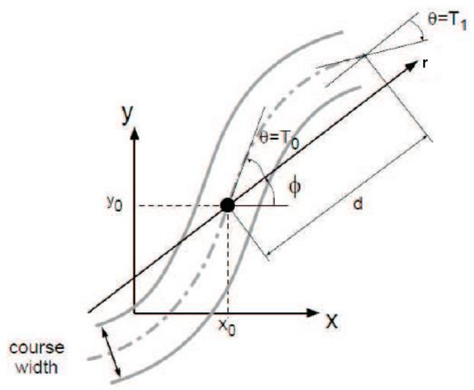

Figure 2.15: Curvilinear fibre path (Tatting and Gürdal, 2001)

2.3.1.2 Circular arc (Constant Curvature Path)

Gürdal et al. (2005) developed a new definition for fibre orientation variation based on circular arcs representation as an alternative of linear variation of the local fibre angles. This approach had the advantage of producing courses of constant curvatures, which more accurately represented the manufacturing constraints of a tow placement machine. Furthermore, Ungwattanapanit and Baier (2012) showed that placing the fibres along the periphery of the circular holes substantially reduced the stress peaks at the cut-out edges when tensile, or to a lesser extent, shear loads were applied. The in-plane shear deformation could be used to generate the circular arc for fibre placement as in the study of the Tam and Gutowski (1990). The shear deformation was applied for incremental parts of fibre that kept the fibre remaining perpendicular to the radius.

2.3.2 Discrete approach

The linear and constant variations, which have been described in the previous sections, are the predefined curves that represent the limited classes of fibre orientation variations in a continuous way. These types of curves result in a small design space where the fibre path could be described using a specific number of parameters. On the contrary, for an expanded design space, the fibre orientation angles can be modelled to provide laminate stiffness variation of a steered fibre laminate by dividing the structure domain into several discrete regions and assigning an independent laminate stiffness to each region as shown in Figure 2.16 (Huang and Haftka, 2005, Hyer and Charette, 1991). The discontinuity of the optimum stacking sequence between discrete regions was considered as one of the disadvantages of assigning independent laminate stiffness properties to different discrete regions of the structure. The independent stiffness properties could be assigned to each element in order to improve the compressive strength of a plate with a hole (Huang and Haftka, 2005). The weakness of this approach was that it was difficult to impose the fibre continuity and ensuring convergence for fibre angle variation between nodes of the adjacent elements. Also, the dependency of the number of design variables to the mesh density was challenging to consider, since the with each integration points there was a certain value of the local fibre angle that is not defined by a specific function. Also, it tended to consume a lot of time and computational efforts as compare with functional fibre path.

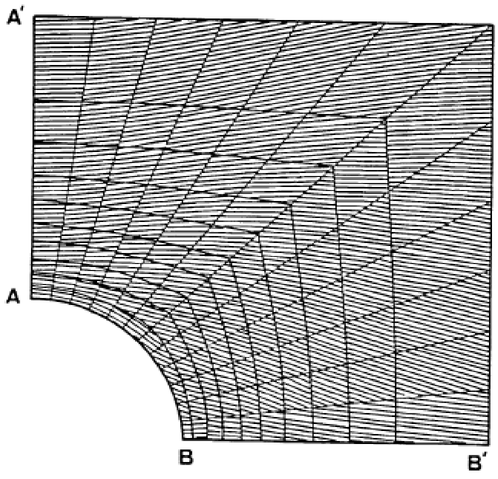

Figure 2.16: Distribution of curvilinear fibres in [+45°,θ $_8$]s laminate (Hyer and Charette, 1991)

2.4 Design types of laminated composite cylindrical shells

Laminated cylindrical shells are one of the widely used in structural components of aircraft and aerospace vehicles (e.g. fuselage and rocket motors), containers (e.g. tanks, reservoirs, pressure vessels), pipes and tubes, submarines, etc., due to high specific stiffness/strength of laminated composites. Therefore, they are considered as the most important motives for the design and manufacture of lightweight and efficient structures.

The stiffness of a laminate is strongly dependent on fibre orientation in its constitutive plies. Consequently, the design types for laminated cylindrical shells can be defined based on the way of placing the fibres in the laminates.

2.4.1 Conventional or straight fibre laminated cylinders

Tailoring the stiffness of straight fibre cylindrical laminates has been developed for many applications, such as aerospace systems to reduce costs and weight, and improve the safety and stability of the structure. Tailoring the stiffness of straight fibre laminated cylinders could be achieved in two ways. The first one is by varying the number of plies, ply angle orientation and the stacking sequence as design variables in order to achieve a specific stiffness. The second way uses lamination parameters in order to design the required stiffness of cylindrical laminates.

Several studies of tailoring the stiffness of the straight fibre laminated cylinders have used the first type. Koide and Luersen (2013) investigated the optimal stacking sequence design of laminated cylindrical composite shells with and without cut-out to maximise the fundamental frequencies. Topal (2009) used a predefined set of ply angles as discrete design variables, to maximise the natural frequencies and buckling loads of laminated composite cylindrical shells. The optimisation problem was formulated as the weighted combinations of the two objective functions of the natural frequencies and buckling loads. Mian et al. (2013) used the fibre orientations in each ply as design variables to achieve the minimum weight for different ply laminate of the composite pressure vessel by using finite element method as a procedure of optimisation. They used different sets of predefined laminates such as cross-ply $[0°/90°]_{s}$, angle-ply $[\pm\theta]_{ns}$, $[90°/\pm\theta]_{ns}$ and $[0°/\pm\theta]_{ns}$. As an outcome of that research, the angle-ply $[\pm 54°]_{ns}$ configuration, was found to provide the minimum weight of pressure vessel, as compared with others.

In other studies, the ply angles were not predefined and were considered as continuous design variables in the optimisation problems. For instance, Silva et al. (2010), considered fibre orientation of each ply angle as a continuous design variable that can vary 0° to 90° to find the optimum orientation that would ensure the minimum weight design of laminated composite tubes under different loading cases. They found under axial force the optimal fibre orientation is at 0°, for torque loading the optimum fibre angle was [+45°,-45°] for internal pressure it was approximately [+54°/-54°], while for the external pressure it was [90°/90°]. Nine design variables, including fibre orientation, thickness, the volume fraction of fibre and material type for each ply, were employed by Azarafza et al. (2009), to determine the optimum design of a circular cylindrical composite shell under compressive axial and transverse transient dynamic loads. The lamination design affect the natural frequencies of the structures, as was shown by Abouhamze and Shakeri (2007), who studied stacking sequence optimisation of laminated cylindrical shells according to the weighted sum of the first natural frequency and buckling load as optimisation of multi-objective functions.

The second type of optimisation involves the lamination parameters being used as design variables, instead of ply orientation angles and the stacking sequence. The lamination parameters are introduced as functions of stacking sequence and ply thickness and orientation. Five material invariants (four of which are independent) and 12 lamination parameters are introduced as parameters that only depend on the stacking sequence, in order to express the [A], [B] and [D] matrices (IJsselmuiden, 2011b). Fukunaga and Sekine (1993) have applied a technique of lamination parameters for tailoring the mechanical properties of laminated composites to meet desired requirements. Diaconu et al. (2002) used a numerical code to obtain the optimum lamination parameters and the equivalent laminate configurations, including the ply angle and thickness, in laminated long cylindrical shells subjected to combined axial compression and torsion, to maximise the buckling load. Todoroki and Ishikawa (2004) have adopted lamination parameters as design variables of approximation design function of the design space instead of the ply angle, to find the optimum stacking sequence, for a response surface of buckling load of cylindrical laminated shells.

This approach of lamination parameters has the advantage of allowing continuous design variables and this result in more flexibility in the implementation of the optimisation function. The other advantage is the design variables are independent of the number of plies in the laminate. However, post-processing is required in order to find local angles distribution from the lamination parameter.

In the conventional laminated cylindrical shell, the design space of the optimisation problem is not too large, could be limited by the orientations, number and staking sequence of the layers that make the composite laminates. Also, this design space could be reduced by considering a combination of predefined ply laminates. Therefore, the search process to find the optimum design for the conventional laminated cylindrical shell is easier and less time-consuming.

2.4.2 Segmented laminated cylindrical shells

Division of a laminated cylindrical shell into equal segments in the longitudinal direction or circumferential direction relying on the loading conditions could provide a good performance. A laminated cylindrical shell in which the laminate stacking sequence varies circumferentially with a certain value of stacking sequence along the segment is called segmented stiffness laminates (Riddick and Hyer, 1997). These segments had one laminate stacking sequence for the crown and keel and another laminate stacking sequence for the two sides depending on the load case variation, as shown in Figure 2.17 and hence, resulted in a variation of the laminate properties at circumferential locations. Hyer and Riddick (1999) obtained a range of predictions related to a response of segmented-stiffness composite cylinders, constructed from pseudo-isotropic laminates and subjected to internal pressure while maintaining no overall axial extension. They concluded that the feature, which distinguished these segmented stiffness cylinders from the conventional single-laminate cylinders, was the circumferential displacement.

The segmented construction could give an interesting response as a result of differences in coefficients of thermal expansion in segmented cylinder shells that could be used in some applications of measurements. Furthermore, a number of segments offered more design freedom when designing laminated cylindrical shell, as well as increase the number of design variables.

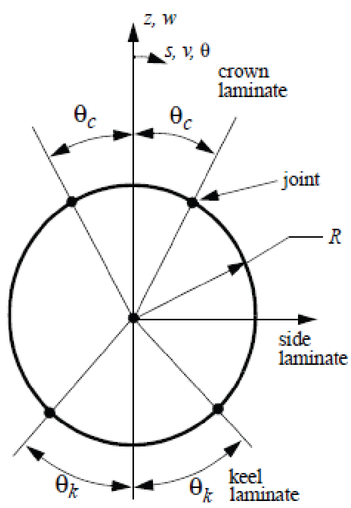

Figure 2.17: Segmented cylinder construction (Riddick and Hyer, 1997)

Abosbaia et al. (2003) have segmented a composite tube into three different materials regions in the axial direction, each one with its material properties as shown in Figure 2.18. They studied the effects of segmentation on the crushing behaviour of woven roving laminated tube experimentally under axial compressive load. They found segmented composite tubes offered a good energy absorbing ability and more stable load-carrying capacity. Segmentation of the tube with the axial segments offered a minimum volume structure that could absorb a given amount of energy in a crushing process.

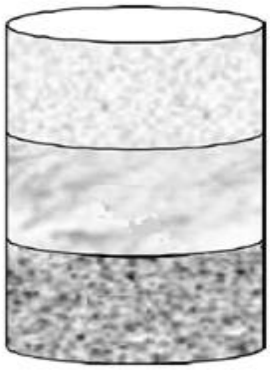

Figure 2.18: Schematic diagram of a segmented composite tube. (Abosbaia et al., 2003)

2.4.3 Steered fibre in laminated circular cylinders shells

The technology of controlled fibre placement allows for the fabrication of advanced composite structures, defined here as those in which the fibre orientation varies continuously in a structure within a particular ply. In order to overcome the dominant bending loading in the fuselage of aircraft Wu (2008) steered the tows along the fuselage length on the crown and keel for high extensional stiffness to resist the bending loads as shown in Figure 2.19. In addition, the shell sides have high shear stiffness which could provide resistance for the relative deflection of the crown and keel. Also, he investigated the effect of using a straight fibre laminate for the crown and keel and concluded that significant improvements in the shell bending stiffness are also possible for this pattern.

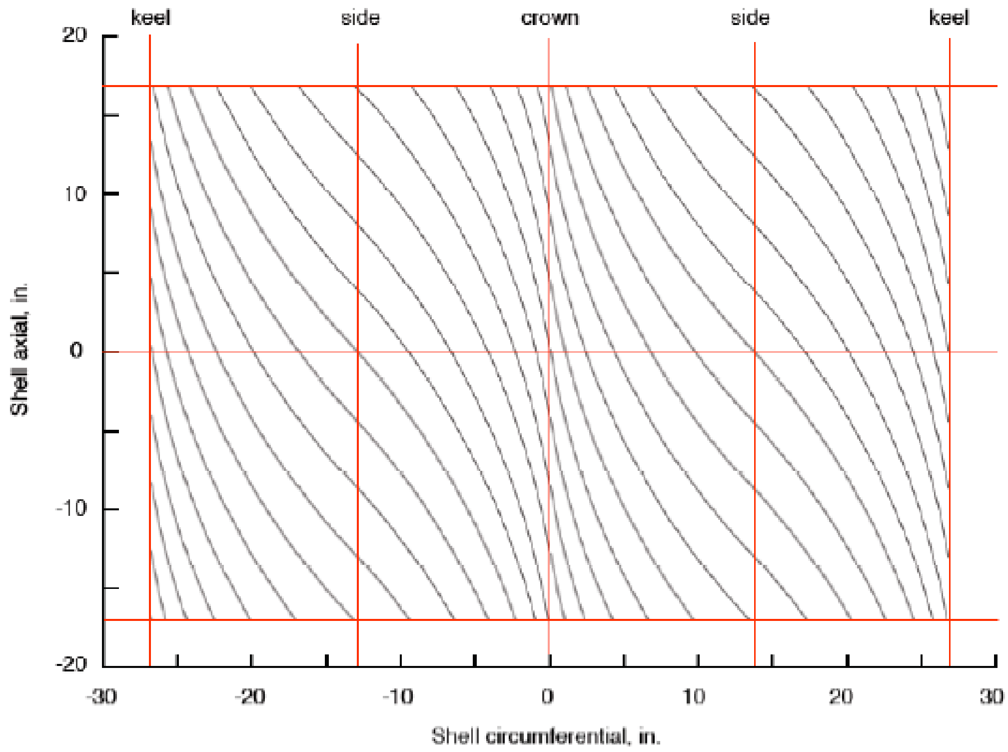

Figure 2.19: Developed view of a cylindrical shell with the steered tow (Wu, 2008)

Blom et al. (2009c) noted that small dimensions of shell required a small turning radius of tows because it could lead to the formation of local wrinkling in tows (called puckering) during lay down, which could be invisible on the completion of the product. On the other hand, a larger turning radius of tows could be used with larger dimension to get the same stiffness variation and reduce the puckering. The structural parameter of cylinders, like radius (R) and aspect ratio (L/R), could affect the structural improvement of the variable stiffness cylinders, as was shown by Rouhi et al. (2014). Also, they found the improvement in the structural performance of the cylinder by keeping a constant fibre steering was ≅25% after increasing the aspect ratio to $L/R \geq 0.3$. Blom et al. (2010b), studied circumferential tailoring of a circular cylinder to carry a maximum buckling load under bending by using a multiple-segment of constant curvature fibre path variation in the circumferential direction and including the Tsai-Wu criterion as a constraint. They concluded that circumferential tailoring produced improvements of up to 17% in increasing the buckling load of a cylinder with respect to quasi-isotropic laminates. In addition, they defined the desired fibre orientation angle φ, with respect to the longitudinal axis, as shown in Figure 2.20. The fibre angle was assumed to vary as a function of the circumferential coordinate θ and to vary in each of the multiple circumferential segments of the cylinder. They chose the path definition of the curvature constraints to be constant in-plane curvature within a segment, and the angle variation was defined as follows (Blom et al., 2010b):

$$\cos\varphi(\theta) = \cos T_i + (\cos T_{i+1} - \cos T_i)\frac{\theta-\theta_i}{\theta_{i-1}-\theta_i} \qquad (2.5)$$

The in-plane curvature k within a segment is:

$$k = \frac{\cos T_i - \cos T_{i+1}}{R(\theta_{i-1}-\theta_i)} \qquad (2.6)$$

where T_i is the fibre angle at the θ_i the location around the circumference and R is the radius of the cylinder.

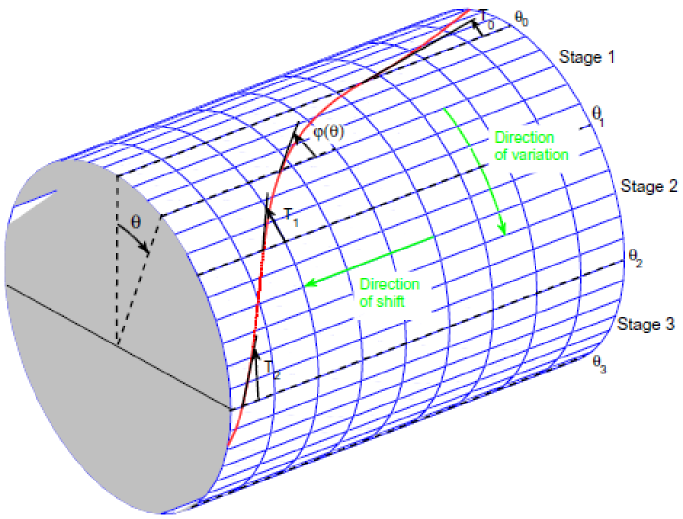

Figure 2.20: Fibre angle and segment definition (Blom et al., 2010b)

Blom et al. (2009b) tested and analysed the conventional lay-up cylinders and varying fibre orientation lay-up cylinders and achieved good agreement between the measured and calculated stiffness values. Furthermore, they stated that as a result of the higher laminate bending stiffness in the circumferential direction, the fundamental frequencies of the conventional shell are higher than those of the variable stiffness shells, which could play an essential role in the formation of waves in a circumferential direction. Blom et al. (2010a) showed that improvements in bending obtained analytically could also be achieved experimentally. They stated that the maximum tensile strains in the variable stiffness cylinder in the preferred orientation were about 35% smaller than in the baseline cylinder, and the maximum compressive strains were about 10% lower than those of the baseline cylinder.

2.4.4 Steered fibre in laminated non-circular cylinder shells

Thin laminated composite shells are usually used in aerospace applications. In structures of these applications, the reduction in the thickness of the skin to gain weight savings must be balanced against the structure stability. For that reason, the buckling response of thin laminated composite shells must be carefully studied. According to the geometric considerations of the structure of the aeroplane, a non-circular cross-section could be used such as an elliptical in the fuel tank and wing of aircraft. The elliptical cross-section has the non-equality of curvature, where there is a larger radius of curvature with a flat portion that is more likely to buckle than that of smaller curvature part, causing a clear reduction in the buckling capacity as compared with circular section (Sun and Hyer, 2008). It could be described alternatively as the lack of structural performance. Therefore, in order to compensate for the lack of structural performance, an efficient way to increase the stiffness of the structure locally on the circumference. For instance, in an isotropic material, improvement of structural performance could be achieved by several means, including changing the wall thickness, using stiffeners, etc. (Paschero and Hyer, 2009). For structures of composite material, the compensation of structural performance could be done by using reinforcement fibres follow a curvilinear path to tailor the stiffness in the required way. Along the curvilinear path, the variation of stiffness is smooth, and the structure called variable stiffness composite (VS). Ghayoor et al. (2017) investigated the influence of using curvilinear fibre paths on the buckling load for the elliptical composite cylindrical shell. They employed a metamodeling approach for the optimisation problem to obtain the optimum fibre path. Indeed, a metamodeling approach could reduce the time of the optimisation process. However, a metamodeling approach could not give the actual results as the objective function since it based on statistical analysis.

To consider the fuselage of an aircraft under multi-loading conditions, Rouhi et al. (2015) used a multi-objective function to investigate the effect of using two opposite directions of load cases on variable stiffness composite cylinders. They used the Pareto frontier as the main decision-making tool with different combinations of weight factors for the loading ceases.

Apparently, the non-circular cross-section of the cylindrical shell could offer a good opportunity for steered fibres in curvilinear paths on the circumference to improve structural performances as introduced in Chapter 6 of this thesis.

2.5 The prediction of failure load of steered fibres laminates

In order to predict the failure load in the composite laminates, it is crucial to understand failure in a composite. The failure of composites is a substantially more complex mechanism than that of the metals. The failure depends on the fundamental properties of composite material and strengths. Analysis of failure in the laminates is based on the two major elements, laminate stress analysis and lamina failure criteria type. The laminate stress analysis deals with the stress distribution in the laminate and the failure in the laminates can be either First Ply Failure (FPF) or the Progressive Ply Failure (PPF). In the First Ply Failure (FPF), the laminate is considered to have failed with the first ply fail. It is numerically straight forward and easy to use. However, this approach predicts a conservative failure load relative to the actual failure load of laminate since when the first ply fails, there are other plies that can carry more load. While in the Progressive Ply Failure (PPF), the predicted failure load is assumed when the last ply fails in the laminate. Therefore, it could be considered as ply by ply failure and modelled as a stiffness reduction for each failed ply in the laminate. It is similar to a continuous cycle of stress analysis until the whole laminate fails.

The second element of the laminates failure analysis is the type of failure criteria, which can predict the failure mode or not. For instance, the Maximum Stress/Strain failure criteria can predict the failure mode as fibre breakage, transverse matrix and shear matrix failure. While, the Tsai-Wu and Hill-Tsai criteria could not predict the failure mode of the lamina (Knops, 2008).

To determine the optimum design for the composite laminates, designers often apply failure criteria in their optimisation problems as constraints or objective functions (Akbulut and Sonmez, 2008, Silva et al., 2010 and Mian et al., 2013).

Some of them used the First Ply Failure (FPF) and other used Progressive Ply Failure (PPF). Akbulut and Sonmez (2008) applied the Tsai-Wu and Maximum stress criteria together in order to improve the safety of the optimised design of composite structures. It helped to avoid false optimum design for some loading cases resulting from use of a single criterion, due to the particular feature of its failure envelope. In a study of Silva et al. (2010) the FPF was used as the criterion to define when the laminate failed, while the maximum stress and the Tsai-Wu criteria were applied to identify the failure in a lamina.

Blom et al. (2009a), used the progressive failure analysis and LaRC failure criteria to study the influence of tow drops in the steered fibre laminates on the strength of the structure. They revealed that the damage onset at tow-drop areas, mostly in the regions where local fibres are orientated at large angles concerning the axis of the applied load. They found for the wider tows the tow-drop areas were larger and could decrease the strength of design. Ijsselmuiden (2011a) used the lamination parameters approach that has a continuous nature and reduced number of the design variables, in the Tsai-Wu failure criterion. They derived the failure envelope equation in term of strains to obtain a safe region of strain space. This equation is considered as the objective function required to find the optimum values of the lamination parameters. They established the laminate strength was more sensitive to the layup than laminate stiffness. In the work of the Falcó et al. (2014), numerical procedures were developed for a three-dimensional structural simulation to predict the failure load. They used the first-ply failure analysis, and they found the fibre tensile failure stress was directly affected by the local fibre angle relative to the axis of the applied load.

The strength of the steered fibre laminates could be calculated according to failure criteria that depend on the stress analysis of the unidirectional laminates. Whereas each local point in a steered fibre laminate could be described as a unidirectional laminate with a certain layup. Therefore, the elastic properties and strengths of the UD lamina could be used to represent the steered fibre laminate. Based on the variation of the local angles in the steered fibres that could vary over a wide range, the UD lamina failure criteria must be evaluated in order to predict the failure load for that range of local angles.

2.6 Homogenisation of composite materials

The combination of composite produces a new material has a significantly different effective property that cannot be achieved with either of the constituents acting alone. According to this definition, the effective properties are strongly affected by the internal micro/mesostructures of the composite. Hence, representing the material properties of constituent materials at the micro-level as a single monolithic equivalent effectively, i.e. the composite, at the meso or macro-level is usually considered as a process of homogenisation.

In order to calculate the effective properties of the composite, generally, there are three types of approaches: (a) analytical methods (b) semi-empirical methods (c) finite element methods(numerical).

In analytical methods, the effective properties of the unidirectional composites could be estimated by using the rule of mixtures (Voigt, 1889 and Reuss, 1929) as a simple approximation. The rule of mixtures is based on assumptions of perfect bonding between fibre and matrix, fibre uniformly distrusted in the matrix, and both fibre and matrix are behaving linearly elastically. The longitudinal stiffness is calculated based on equal longitudinal strains in fibre and matrix, while the transverse stiffness is obtained based on equal stresses in fibre and matrix in the transverse direction. The longitudinal Young's modulus is predicted more accurately compared with the experimental data than transverse Young's modulus because the assumed stress state in the former is closer to the reality than that in the latter.

Many studies and researches have used sophisticated assumptions to predict the effective elastic properties, for instance, the cylindrical assemblage model by Hashin and Rosen (1964) and the periodic microstructure model (PMM) analysed using the Fourier series (Luciano and Barbero, 1994).

In the semi-empirical methods, the effective material properties are predicted by using some experimental data along with a certain analytical formulation. A better prediction for the transverse stiffness can be obtained with the semi-empirical as revealed in the study of Halpin and Tsai (1969).

Analytical and semi-imperial methods have been successfully used for composites of relatively simple microstructures. Attempts made for 3D textile composites had to resort to a lot of assumptions, given the challenges faced. Shokrieh and Mazloomi (2012) introduced a new analytical model of the 3D four-directional braided composites. They divided a volume of three-dimensional braided composite into three different types interior, surface and corner. Each one of them possess unique mechanical properties and was treated as a unidirectional composite. The stiffness of the original cell was calculated by using a volume averaging method for the three cells. Mukhopadhyay and Adhikari (2016) developed an analytical approach to calculate the equivalent elastic properties of irregular honeycombs cells. They used a representative volume element (RVE) approach to generate a closed-form formula.

Analytical and semi-imperial methods can be considered computationally efficient and less tedious than the expensive finite element modelling and simulation. However, it can be seen that these methods are based on various assumptions of either uniform stress distribution or uniform strain distribution. In addition, these methods disregard some of the geometric complications of the structure within the composite. Consequently, the predictions of effective stiffness of composites from them could have inaccurate. Also, they are difficult to implement in an automated manner.

In the meso-FE modelling of the composite, the effective material properties can be predicted based on the micromechanics of composite. Thus, the properties of the constituents and architecture of composite in the representative volume element (RVE) must be known. In the micro or mesoscale, if the micro/mesostructure appears to be periodic, a unit cell (UC) can be introduced which is always an RVE (Li and Sitnikova, 2018b). Therefore, the terminology of RVE can be replaced by the unit cell when the condition of the periodicity is satisfied.

Implementing the FE model of the unit cell needs to follow the steps as shown in Figure 2.21 and described in detail in Chapter 8 of this thesis. The geometry characterisation of the composite unit cell is considered as the key to identifying mechanical behaviour correctly. Actually, most of the challenges faced by the researchers are related to the complicated geometry of the unit cell and appropriate boundary conditions for the unit cell. To impose the boundary conditions correctly, identical meshes on the opposites faces of the unit cell are essential.

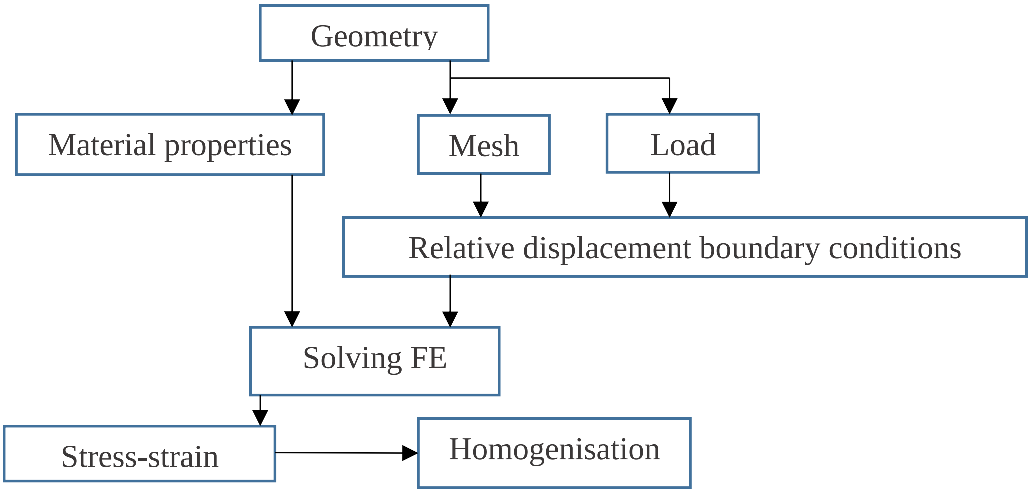

Figure 2.21: Chart of FE modelling of unit cells

A simple geometry of the unit cell for UD composite having unidirectional fibre reinforcement is implemented for two typical packing system of square and hexagonal arrays ones in the study of Li (2000). He stated that the hexagonal packing system has large fibre volume fraction and more sophisticated than that from a square packing. A two-dimensional UC analysis is used in that work. However, using 3D analysis, it could give a clear picture of the nine constants that are required to describe the orthotropic material. Liu et al. (2019) introduced a complicated geometry of woven composite for the pressure pipes. The geometry of the UC is of a pie shape and consists of a hoop weft yarns, axial warp yarns and radial binders, as shown in Figure 2.22. They illustrated that using the woven composite for pressure pipe could overcome the delamination and weakness of interlaminar bonding of filament-wound pressure pipes. This way of using woven composite in the pressure pipes could not offer a better solution as filament winding process to control the hoop and longitudinal stresses to obtain a maximum design pressure without bursting. However, it offers a good chance to investigate a more complicated UC for woven composites. A more complicated yarn architecture was presented in the study of Guo-dong et al. (2009), where the 3D four-directional braided composites were analysed. In this study, the squeezing effect of the braided yarns against each other was modelled by varying the yarn cross-section along the path of the yarn.

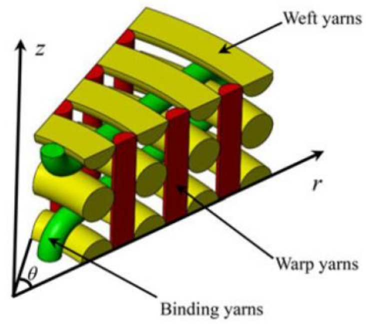

Figure 2.22: Pie shape of the woven unit cell (Liu et al., 2019)

Different yarn architectures and geometries of the composite unit cells in the mesoscale lead to different values of the effective material properties. The conditions of the identical tessellations are considered as the key requirement in the modelling of the unit cells to satisfy the relative displacement boundary conditions (Li et al., 2015, Li, 2008, Li and Wongsto, 2004). Identical tessellations on corresponding faces of the unit cell cannot be achieved automatically usually. This could be accomplished by using appropriate facilities in the pre-processing tools available in commercial FE codes by copying the tessellation from one face to another of the unit cell. The complexity of the geometry and size of the unit cell could be reduced by taking advantage of additional rotational and/or reflectional symmetries as present in the mesostructure. A good example of this kind was shown through the application to the plain weave textile composite in the study of Li et al.

(2011b). Indeed, this did not just reduce the size and the complexity of the geometry of the unit cell; it also reduced the computational time and efforts.

In the present study, the curvilinear paths of tows that are generated based on their linear variation of local fibre orientation along the path with its variable gap being considered as a single unit cell in the mesoscale structure as present in Chapter 8 in order to predict the effective material properties of the composite panel. This approach could be a new attempt that has been used to facilitate a model of the unit cell. This argument is based on the multiscale nature of the composite.

2.7 Summary

This chapter briefly reviews the literature related to the different aspects of composites of curvilinear fibre paths. The aspects that included in this chapter are mostly associated with the composite fabrication processes in which continuous fibres are steered when placed on different surfaces, such as a filament winding, 3D printing and automated fibre placement. The manufacturing limitations and applications of the fibre placement technology have been included. According to the composite fabrication processes above the stiffness of composite laminates could be in a spatially variable form as included and compared with constant stiffness laminates in this review. Also, the ways of designing the curvilinear paths such as a linear variation of the local orientations of fibre paths, constant curvature paths and discrete approach have been reviewed.

Furthermore, the effect of the implementing the curvilinear paths of fibre for different kinds of structures such as flat panels, circular cross-section cylinders, and elliptical cross-section cylinders on the mechanical performances, has also been included. The prediction of the failure load and damage model for this kind of laminates has been reviewed. Finally, attention has been paid to homogenisation and predicting the effective material properties by using the unit cell models and the use of unit cell models for complicated composite architecture.

In this review of the relevant literature it is indicated that most researchers assumed the curvilinear paths of steered fibres in a uniform distribution and a constant fibre volume fraction. No gaps have been recognised between fibre tows. Other researchers included the effect the gaps and overlaps according to the procedure of cut and restart as in the automated fibre placement. However, this approach results in the fibre could not transmit the applied load perfectly as compared with continuous steered fibres. It can produce the deformation of matrix around trimmed fibres, and reduction in the strength of the composites. Therefore, implementing the continuous steered fibre in the presence of the realistic gaps in this thesis would help to obtain improved predictions of the stiffness and strength of composites structures.

3 Background theories

3.1 Micromechanics analysis

The mechanics of materials deal with deformation, strains and stresses of an elastic body subjected to mechanical and/or thermal loads. In the microscopic scale, the concept of micromechanics is used based on the representative volume element (RVE). The analysis of micromechanics deals with the collection of both constituents of composite materials, fibre and matrix. Therefore, understanding the interaction between the constituents and effective properties as functions of the fibre volume fraction could help the designer to select the appropriate type of fibre and matrix to be used in the composite materials in order to achieve the required stiffness, strength and thermal expansion coefficients. The micromechanics formulations underpin the elastic and thermal properties of a lamina. It will serve as the basis for the mechanical analysis at a macroscopic scale where the predicted effective material properties are obtained from homogenisation.

In order to predict the material properties of the unidirectional lamina, basic assumptions and simplifications must be made as follows.

1- Fibres are distributed uniformly in the matrix in a statistic sense to help the definition of an RVE.
2- Perfect bonding is present between the two phases of composite, fibre and matrix.
3- The two phases of the composite behave linearly elastically.

The unidirectional lamina could be described as transversely isotropic material with an axis of symmetry in the fibre direction. The plane that perpendicular to fibres is a plane of reflectional symmetry. The effective material properties of the composite lamina can be classified as follows.

3.1.1 Longitudinal Young's modulus (E_1)

It is a feature that describes the elasticity of lamina in the fibre direction. It could be calculated from their constituent marital proprieties by using the rule of mixtures (ROM) (Voigt, 1889). The formula of this rule is derived based on the assumption that the deformations of fibre and matrix in the fibre direction are equal. In other words, the constituent materials have the same strains in the longitudinal direction in which the material is stressed as shown in Figure 3.1.

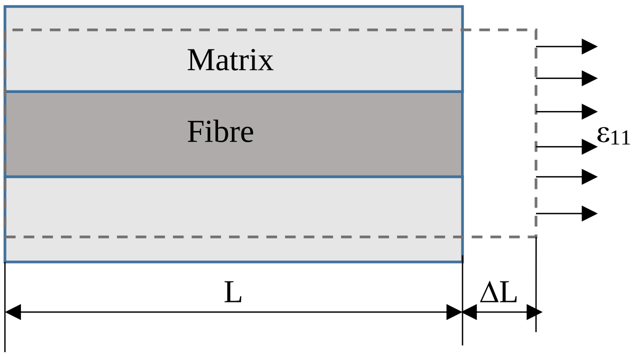

Figure 3.1: RVE under longitudinal uniform strain

According to the definition of strain the longitudinal strain of composite in the direction of fibres can be written as follows.

$$\varepsilon_{11} = \frac{\Delta L}{L} \tag{3.1}$$

where ΔL and L are the elongation and the original length.

The applied load in the direction of fibres equal to on the resultant of stresses over the fibre and matrix, hence it can be described as follows:

$$P = \sigma_{11} A = \sigma_f A_f + \sigma_m A_m \tag{3.2}$$

where $\sigma_{11}, \sigma_f,$ and σ_m are the equivalent stress on the RVE cross-section A, the stress of fibre on fibre cross-section A_f and stress of matrix act on matrix cross-section A_m, respectively.

Then, stresses σ_f and σ_m, in Equation (3.2) can be given in term of longitudinal strain which has been assumed to uniform in the longitudinal direction in all phases, i.e.

$$\sigma_{11} = \varepsilon_{11}(E_f V_f + E_m V_m) \tag{3.3}$$

where the E_f, E_m, V_f and V_m are Young's moduli and volume fractions of fibre and matrix, respectively. Finally, the longitudinal Young's modulus can be written as follows.

$$E_1 = E_f V_f + E_m V_m \tag{3.4}$$

3.1.2 Transverse Young's modulus (E_2)

In order to calculate the transverse Young's modulus of the lamina, the transverse load have to be applied with the assumption of the stresses on the fibre and matrix are the same as shown in Figure 3.2. Therefore, the total deformation of the REV in the transverse direction is equal to the sum of the deformation of fibre and matrix in the same direction, as a result of the perfect bonding.

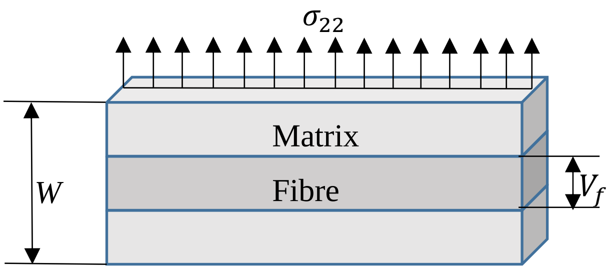

Figure 3.2: RVE under transverse uniform stress

The total elongation in the transverse direction can be written as follows.

$$\Delta W = \varepsilon_{22} W = \varepsilon_f V_f W + \varepsilon_m V_m W \tag{3.5}$$

where ε_{22}, ε_f and ε_m are the strains of composite, fibre and matrix, respectively, in the transverse direction.

According to the assumption, the transverse stress of composite is equal to those in fibre and matrix.

$$\sigma_{22} = \varepsilon_{22} E_2 = E_f \varepsilon_f = E_m \varepsilon_m \tag{3.6}$$

Then the transverse strain could be written as follows.

$$\varepsilon_{22} = \frac{\sigma_{22}}{E_f} V_f + \frac{\sigma_{22}}{E_m} V_m \tag{3.7}$$

Hence, Equation (3.7) can be re-written in term of the transverse modulus as follows.

$$\frac{1}{E_2} = \frac{V_f}{E_f} + \frac{V_m}{E_m} \tag{3.8}$$

Finally, the transverse modulus, according to Equation (3.8) that known as the inverse rule of mixtures (IROM) Reuss, 1929, can be written as follows.

$$E_2 = \frac{E_f E_m}{E_f V_m + E_m V_f} \tag{3.9}$$

3.1.3 In-plane shear modulus (G_{12})

The in-plane shear modulus of the composite lamina is derived by assuming the shear stresses of composite, fibre and matrix are equal, i.e. $\tau_c = \tau_f = \tau_m$. Pure shear stress τ_{12} is applied to an assembly and it produces shear deformation of the composite δ_c that equal to the sum of deformations in the fibre δ_f and in matrixδ_m.

$$\delta_c = \delta_f + \delta_m \tag{3.10}$$

From the definition of shear strain, Equation (3.10) leads to:

$$\delta_c = \gamma_c W = \gamma_f V_f W + \gamma_m V_m W \tag{3.11}$$

where γ_c, γ_f and γ_m are the shear strains of the composite, the fibre and the matrix, respectively.

Then, according to Hooke's law, Equation (3.11) is given as follows.

$$\frac{\tau_c}{G_{12}} = \frac{\tau_f V_f}{G_f} + \frac{\tau_m V_m}{G_m} \tag{3.12}$$

where G_f and G_m are the shear modulus of fibre and matrix, respectively.

Finally, according to the assumption of the equality of shear stress of the composite, fibre and matrix, the in-plane shear modulus of composite will be as follows.

$$\frac{1}{G_{12}} = \frac{V_f}{G_f} + \frac{V_m}{G_m} \tag{3.13}$$

3.1.4 Major Poisson's ratio (v_{12})

The Poisson's ratio is defined as minus the quotient of the normal strain in the transverse direction to the normal strain in the fibre direction when the composite is loaded uniaxially in the fibre direction. Since the transverse deformation of composite equal to the amount of the transverse deformation of matrix δ_m^T and that of the fibre δ_f^T.

$$\delta_c^T = \delta_f^T + \delta_m^T \tag{3.14}$$

According to the strain definition, Equation (3.14) becomes as follows.

$$\varepsilon_c^T = \varepsilon_f^T V_f + \varepsilon_m^T V_m \tag{3.15}$$

where $\varepsilon_c^T, \varepsilon_f^T$ and ε_m^T are the transverse strains of the composite, the fibre and the matrix, respectively.

Then by substituting these strains in term of the Poisson's ratio, the Equation (3.15) would be as follows.

$$\nu_{12}\varepsilon_c^L = \nu_f \varepsilon_f^L V_f + \nu_m \varepsilon_m^L V_m \tag{3.16}$$

where $\varepsilon_c^L, \varepsilon_f^L$ and ε_m^L are the longitudinal strains of the composite, the fibre and the matrix, respectively.

Finally, according to the equality of the strains in the composite, the fibre and the matrix, the major Poisson's ratio of a composite is derived as follows.

$$\nu_{12} = \nu_f V_f + \nu_m V_m \tag{3.17}$$

where ν_f and ν_m are the Poisson's ratio of the fibre and the matrix, respectively.

The above derivations of effective elastic properties of composites from those of their constituents are all based on the so-called rules of mixtures, one way or another. They are meant to offer a first approximation as a rough estimate to facilitate the early stage of design, although some of them, e.g., the effective longitudinal modulus, could be rather accurate. Serious evaluations should come from more realistic models and validated by experiments.

3.2 Laminate theories

To analyse the composite laminates, there are three categories of the structural theories that could be used. These categories are Equivalent Single Layer (ESL) approaches, Layer Wise (LW) methods and 3D Elasticity theories. In the equivalent single layer approaches, the laminate is considered as two-dimensional (2D) equivalently monolithic layer with effective properties. In the LW methods, each layer is dealt with as a monolithic material and joined together with surrounding layers over perfectly bonded interfaces. While the displacement field within the entire domain must satisfy basic continuity requirements, the distribution of the in-plane stress over the thickness can appear in a zig-zag manner. In the 3D Elasticity theories, 3D anisotropic elasticity is employed to derive displacement or stress field before the constitutive equations can be characterised.

This chapter will deal with ESL approaches by using appropriate assumptions of stress and deformation state along with shell thickness. The ESL approaches are classified according to the distribution of displacements over the thickness of the laminate into the classical laminate theory (CLT), first-order shear deformable theory (FSDT) and the higher-order shear deformable theory (HSDT) (Reddy and Liu., 1985)

3.2.1 Classical laminate theory (CLT)

It is the simplest form of ESL theory, based on the definition of the displacement field across the thickness of the laminate. It is formulated based on the assumption that the straight line normal to the mid-plane before deformation remain normal and straight to that plane after deformation (Reddy, 2004). As a result, the influence of the transverse shear strains has been neglected to reduce the problem of the deformation of laminated structures into a 2D idealisation. It was first introduced by Kirchhoff in the nineteenth century. The benefit of this theory is the simplification of structural plates or shell as 3D entities into their 2D equivalence. Also, it reduces the total number of degrees of freedom and governing equations, thus saving time and reduce the computational efforts. Furthermore, it gives reasonable results for symmetric and balanced laminate under loading conditions of pure tension or pure bending. This theory is related to neglected effect of the transverse shear deformation. This effect increases for the thick laminates of composites and especially for laminates having a low ratio of longitudinal to the transverse shear stiffness. The displacement field in the shell could be described as Kirchhoff-Love hypothesis as follows.

$$u(x,y,z) = u_0(x,y) - z\frac{\partial w_0}{\partial x}$$

$$v(x,y,z) = v_0(x,y) - z\frac{\partial w_0}{\partial y} \qquad (3.18)$$

$$w(x,y,z) = w_0(x,y)$$

where u_0, v_0 and w_0 are the displacements in *x*-, *y*- and *z*-direction respectively on the reference plane, while $\frac{\partial w_0}{\partial x}$ and $\frac{\partial w_0}{\partial y}$ are the rotation of normal towards the *y*- and *x*-axis, respectively.

The strains associated with the displacement field can be determined as follows.

$$\begin{Bmatrix} \varepsilon_{xx} \\ \varepsilon_{yy} \\ \gamma_{xy} \end{Bmatrix} = \begin{Bmatrix} \frac{\partial u}{\partial x} \\ \frac{\partial v}{\partial y} \\ (\frac{\partial v}{\partial x} + \frac{\partial u}{\partial y}) \end{Bmatrix} = \begin{Bmatrix} \frac{\partial u_0}{\partial x} \\ \frac{\partial v_0}{\partial y} \\ \frac{\partial u_0}{\partial y} + \frac{\partial v_0}{\partial x} \end{Bmatrix} - z \begin{Bmatrix} \frac{\partial^2 w_0}{\partial x^2} \\ \frac{\partial^2 w_0}{\partial y^2} \\ \frac{\partial^2 w_0}{\partial x \partial y} \end{Bmatrix} \qquad (3.19)$$

According to Kirchhoff's hypothesis, all transverse shear strains ε_{zx} and ε_{zy} and the transverse normal strain ε_{zz} are equal to zero. The normal stress σ_{zz} does not appear in the virtual work expression and, as a result, it is neglected.

The linear constitutive relation of any orthotropic lamina in the local coordinates of a lamina could be described as follows.

$$\begin{Bmatrix} \sigma_{11} \\ \sigma_{22} \\ \tau_{12} \end{Bmatrix}^k = \begin{bmatrix} Q_{11} & Q_{12} & 0 \\ Q_{21} & Q_{22} & 0 \\ 0 & 0 & Q_{66} \end{bmatrix}^k \begin{Bmatrix} \varepsilon_{11} \\ \varepsilon_{22} \\ \gamma_{12} \end{Bmatrix}^k \tag{3.20}$$

where Q_{ij} is the plane stress stiffness matrices of the k^{th} lamina in its material coordinate system and defined as follows in terms of material properties of a lamina.

$$Q_{11} = E_1/\Delta \ , \ Q_{12} = Q_{21} = v_{12}\, E_2/\Delta \ , \quad Q_{22} = E_2/\Delta$$

$$Q_{66} = G_{12}, \quad \Delta = 1 - v_{12}^2\, E_2/E_1 \tag{3.21}$$

where E_1, E_1, G_{12} and v_{12} are the longitudinal, transverse and shear moduli and poison ratio of that lamina, respectively.

Since of the laminate is made by stacking several laminae with different material properties and orientation with respect to the laminate coordinates, the constitutive equations of each lamina should be transformed to the laminate coordinate system to present the stress-strain relations of that lamina in the laminate coordinate system as follows.

$$\begin{Bmatrix} \sigma_{xx} \\ \sigma_{yy} \\ \sigma_{xy} \end{Bmatrix}^k = \begin{bmatrix} \bar{Q}_{11} & \bar{Q}_{12} & \bar{Q}_{16} \\ \bar{Q}_{12} & \bar{Q}_{22} & \bar{Q}_{26} \\ \bar{Q}_{16} & \bar{Q}_{26} & \bar{Q}_{66} \end{bmatrix}^k \begin{Bmatrix} \varepsilon_{xx} \\ \varepsilon_{yy} \\ \gamma_{xy} \end{Bmatrix}^k \tag{3.22}$$

where $\bar{Q}_{ij}$s are the transformed stiffness matrices of the k^{th} lamina as shown in Figure 3.3, and defined as follows.

$$\bar{Q}_{11} = Q_{11}\cos^4\theta + 2(Q_{12} + 2Q_{66})\sin^2\theta\cos^2\theta + Q_{22}\sin^4\theta$$

$$\bar{Q}_{12} = (Q_{11} + Q_{22} - 4Q_{11})\sin^2\theta\cos^2\theta + Q_{12}(\sin^4\theta + \cos^4\theta)$$

$$\bar{Q}_{22} = Q_{11}\sin^4\theta + 2(Q_{12} + 2Q_{66})\sin^2\theta\cos^2\theta + Q_{22}\cos^4\theta \quad (3.23)$$

$$\bar{Q}_{16} = (Q_{11} - Q_{22} - 2Q_{66})\sin\theta\cos^3\theta + (Q_{12} - Q_{22} + 2Q_{66})\sin^3\theta\cos\theta$$

$$\bar{Q}_{26} = (Q_{11} - Q_{22} - 2Q_{66})\sin^3\theta\cos\theta + (Q_{12} - Q_{22} + 2Q_{66})\sin\theta\cos^3\theta$$

$$\bar{Q}_{66} = (Q_{11} + Q_{22} - 2Q_{12} - 2Q_{66})\sin^2\theta\cos^2\theta + Q_{66}(\sin^4\theta + \cos^4\theta)$$

By substituting Equation (3.19) in (3.22)

$$\begin{Bmatrix}\sigma_{xx}\\\sigma_{yy}\\\sigma_{xy}\end{Bmatrix}^k = \begin{bmatrix}\bar{Q}_{11} & \bar{Q}_{12} & \bar{Q}_{16}\\ \bar{Q}_{12} & \bar{Q}_{22} & \bar{Q}_{26}\\ \bar{Q}_{16} & \bar{Q}_{26} & \bar{Q}_{66}\end{bmatrix}^k \left(\begin{Bmatrix}\varepsilon_{xx}{}^0\\\varepsilon_{yy}{}^0\\\gamma_{xy}{}^0\end{Bmatrix} + z\begin{Bmatrix}\kappa_x\\\kappa_y\\\kappa_{xy}\end{Bmatrix}\right)^k \quad (3.24)$$

where $\varepsilon_{xx}{}^0$, $\varepsilon_{yy}{}^0$, $\gamma_{xy}{}^0$, κ_x, κ_y and κ_{xy} are the membrane strains and curvatures of k^{th} lamina in the *xy*-plane, respectively.

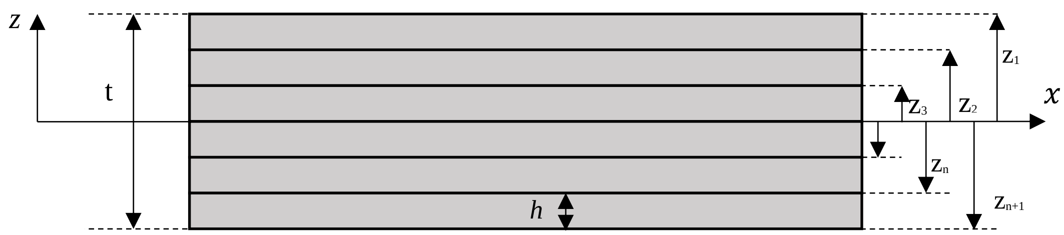

Figure 3.3: Geometry of a laminate with *n* layers

Equation (3.24) states that stresses could vary linearly with the thickness. In addition, it describes the discontinuous stresses through the thickness of the laminate, unlike the strains that give a smooth distribution through the thickness in the laminate. In order to eliminate coordinate *z* from the problem so that the problem for the laminate can be expressed in terms of only two variables *x* and *y*. The stress resultants and moments resultant are obtained as follows.

$$\begin{Bmatrix} N_x \\ N_y \\ N_{xy} \end{Bmatrix} = \sum_{k=1}^{n} \int_{z_{k-1}}^{z_k} \begin{Bmatrix} \sigma_{xx} \\ \sigma_{yy} \\ \sigma_{xy} \end{Bmatrix} dz \tag{3.25}$$

$$\begin{Bmatrix} M_x \\ M_y \\ M_{xy} \end{Bmatrix} = \sum_{k=1}^{n} \int_{z_{k-1}}^{z_k} \begin{Bmatrix} \sigma_{xx} \\ \sigma_{yy} \\ \sigma_{xy} \end{Bmatrix} z\, dz \tag{3.26}$$

By substituting the stresses of each layer from Equation (3.24) in Equations (3.25) and (3.26) the constitutive equation for the laminate is obtained as follows.

$$\begin{Bmatrix} N_x \\ N_y \\ N_{xy} \\ M_x \\ M_x \\ M_{xy} \end{Bmatrix} = \begin{bmatrix} A_{11} & A_{12} & A_{16} & B_{11} & B_{12} & B_{16} \\ A_{12} & A_{22} & A_{26} & B_{12} & B_{22} & B_{26} \\ A_{11} & A_{11} & A_{66} & B_{16} & B_{26} & B_{66} \\ B_{11} & B_{12} & B_{16} & D_{11} & D_{12} & D_{16} \\ B_{12} & B_{22} & B_{16} & D_{12} & D_{22} & D_{26} \\ B_{16} & B_{16} & B_{66} & D_{16} & D_{26} & D_{66} \end{bmatrix} \begin{Bmatrix} {\varepsilon_{xx}}^0 \\ {\varepsilon_{yy}}^0 \\ {\gamma_{xy}}^0 \\ \kappa_x \\ \kappa_y \\ \kappa_{xy} \end{Bmatrix} \tag{3.27}$$

where:

$$A_{ij} = \sum_{k=1}^{n} \overline{\mathrm{Q}}_{\mathrm{ij}}^{\mathrm{k}} \left(z_k - z_{k-1}\right) \tag{3.28}$$

$$B_{ij} = \frac{1}{2} \sum_{k=1}^{n} \overline{\mathrm{Q}}_{\mathrm{ij}}^{\mathrm{k}} \left(z_k^2 - z_{k-1}^2\right) \tag{3.29}$$

$$D_{ij} = \frac{1}{3} \sum_{k=1}^{n} \overline{\mathrm{Q}}_{\mathrm{ij}}^{\mathrm{k}} \left(z_k^3 - z_{k-1}^3\right) \tag{3.30}$$

The coefficients A_{ij}, B_{ij} and D_{ij} are functions of the material properties, laminar thickness, stacking sequence and orientation of the lamina. Matrix $[A_{ij}]$ represents the in-plane stiffness matrix that relates membrane strains to in-plane stress resultants. Matrix $[B_{ij}]$ is called bending extension coupling matrix which relates the membrane stresses to the curvatures and the moments to the membrane strains of a laminate. $[D_{ij}]$ is the flexural or bending stiffness matrix, which relates the curvatures of the preference surface to the moments of a laminate. These coefficients are constant for a given laminate. However, they can be defined as a function of *x*- or *y*-coordinates or both for laminates of curved fibre paths (variable stiffness laminates).

3.2.2 First-order shear deformation theory (FSDT)

In this theory the Love-Kirchhoff hypothesis is relaxed. It assumes the transverse straight lines will remain straight after deformation but they are not normal to the reference plane after deformation (Reissner, 1945). Also, it requires that the displacement component *w* be independent of coordinate *z* in the thickness direction. Similar to the classical laminate theory, with the help of the above assumption, the displacement field of the first-order shear deformable theory would be as follows.

$$\begin{aligned} u(x,y,z) &= u_0(x,y) + z\phi_x(x,y) \\ v(x,y,z) &= v_0(x,y) + z\phi_y(x,y) \\ w(x,y,z) &= w_0(x,y) \end{aligned} \tag{3.31}$$

where u_0, v_0, w_0 are the displacement components of an arbitrary point on plane *z*=0, while the ϕ_x and ϕ_y are the rotations of a transverse normal towards *y*-and *x*-axis, respectively, and they are defined as follows.

$$\phi_x = \frac{\partial u}{\partial z}\,, \phi_y = \frac{\partial v}{\partial z} \tag{3.32}$$

The strains associated with the displacement field and rotations can be determined as follows.

$$\begin{Bmatrix} \varepsilon_{xx} \\ \varepsilon_{yy} \\ \gamma_{yz} \\ \gamma_{xz} \\ \gamma_{xy} \end{Bmatrix} = \begin{Bmatrix} \frac{\partial u_0}{\partial x} \\ \frac{\partial v_0}{\partial y} \\ \frac{\partial w_0}{\partial y} + \phi_y \\ \frac{\partial w_0}{\partial x} + \phi_x \\ \frac{\partial v_0}{\partial x} + \frac{\partial u_0}{\partial y} \end{Bmatrix} + z \begin{Bmatrix} \frac{\partial \phi_x}{\partial x} \\ \frac{\partial \phi_y}{\partial y} \\ 0 \\ 0 \\ \frac{\partial \phi_y}{\partial x} + \frac{\partial \phi_x}{\partial y} \end{Bmatrix} \tag{3.33}$$

Then, following the same procedure as in the CLT, the constitutive relationship of the laminate in FSDT can be derived giving extra terms related to the transverse shear stresses in the material coordinates as follows.

$$\begin{Bmatrix} \sigma_{44} \\ \sigma_{55} \end{Bmatrix}^k = \begin{bmatrix} Q_{44} & 0 \\ 0 & Q_{55} \end{bmatrix}^k \begin{Bmatrix} \gamma_{44} \\ \gamma_{55} \end{Bmatrix}^k \tag{3.34}$$

where Q_{44} and Q_{55} are the intralaminar stiffness matrix and defined as follows.

$$Q_{44} = G_{23}\ ,\ Q_{55} = G_{13} \tag{3.35}$$

Then the transverse shear stresses in the laminate coordinates would be as follows.

$$\begin{Bmatrix} \sigma_{yz} \\ \sigma_{xz} \end{Bmatrix}^k = \begin{bmatrix} \bar{Q}_{44} & \bar{Q}_{45} \\ \bar{Q}_{45} & \bar{Q}_{55} \end{bmatrix}^k \begin{Bmatrix} \gamma_{yz} \\ \gamma_{xz} \end{Bmatrix}^k \tag{3.36}$$

where $\bar{Q}_{44}$, $\bar{Q}_{45}$ and $\bar{Q}_{55}$ are the transformed intralaminar stiffness matrix and defined as follows.

$$\bar{Q}_{44} = Q_{44}\cos^2\theta + Q_{55}\sin^2\theta \tag{3.37}$$

$$\bar{Q}_{45} = (Q_{55} - Q_{44})\sin\theta\cos\theta \tag{3.38}$$

$$\bar{Q}_{55} = Q_{44}\sin^2\theta + Q_{55}\cos^2\theta \tag{3.39}$$

Finally, the laminate constitutive equations will be the same as CLT with extra terms related to the transverse shear resultant as follows.

$$\begin{Bmatrix} N \\ M \end{Bmatrix} = \begin{bmatrix} A & B \\ B & D \end{bmatrix} \begin{Bmatrix} \varepsilon^\circ \\ K \end{Bmatrix} \tag{3.40}$$

$$\begin{Bmatrix} V_y \\ V_x \end{Bmatrix} = K \begin{bmatrix} H_{44} & H_{45} \\ H_{45} & H_{55} \end{bmatrix} \begin{Bmatrix} {\gamma_{yz}}^0 \\ {\gamma_{xz}}^0 \end{Bmatrix} \tag{3.41}$$

where K is the shear correction factor and H_{ij} are the transverse shear stiffness given as follows.

$$H_{ij} = \sum_{k=1}^{n} \bar{\mathrm{Q}}_{\mathrm{ij}}^{\mathrm{k}}\,(z_k - z_{k-1}) \qquad ,\ i,\ j = 4, 5 \tag{3.42}$$

According to the assumptions of FSDT that provide for a more realistic situation as compared with CLT, the shear stresses are not continuous across the boundaries of the two adjacent layers. This theory is more accurate as the deformation allows the plane of the cross-section of the laminate to rotate relative to the reference plane. The accuracy of results in the FSDT depends on the shear correction factor to determine the accurate value of transverse shear stiffness. It accounts for the disparity in the assumed distributions in transverse stresses and strains across the thickness of the laminate. The purpose of this theory is to include the effect of the transverse shear deformation in the calculation of FEM that is relevant to the finding of the next chapters.

3.3 Failure criteria

The objective of the failure criterion is to specify an envelope that defines the strength of the UD lamina under combined stresses. The failure of the composites is usually in a substantially more complex mechanism than that of the metals. The difficulties of defining, verifying and validating failure criteria for the composites are partially related to the definition of failure in composites. Two types of the failure criteria which are employed to predict the failure in the UD composites can be identified according to their association with individual failure modes. The first type of criteria is failure mode-based failure criteria, such as the maximum stress/strain and Hashin criteria (Hashin, 1980) distinguish the mechanisms of failure between different modes. The second type, such as Tsai-Hill and Tsai-Wu failure criteria defines the failure as a single function of the strengths of material independent of the failure modes.

3.3.1 The maximum strain criterion

The maximum strain criterion can distinguish between the failure modes. It is a straight forward criterion expressed in terms of strains rather than stresses (Li and Sitnikova, 2018a). To avoid a failure of the material, the strains must violate the following inequalities (Tsai, 1984).

$\varepsilon_{11} > \varepsilon_{1t}$; if $\varepsilon_{11} > 0$ or abs (ε_{11}) > ε_{1c} ; if $\varepsilon_{11} < 0$

$\varepsilon_{22} > \varepsilon_{2t}$; if $\varepsilon_{22} > 0$ or abs (ε_{22}) >ε_{2c} ; if $\varepsilon_{22} < 0$ (3.43)

abs (γ_{23}) >γ_{23_u} ; abs (γ_{13}) > γ_{13_u}; abs (γ_{12}) > γ_{12_u}

where $\varepsilon_{11,}\varepsilon_{22}, \gamma_{12}, \gamma_{23}$ and γ_{13} are strains components in the material's principal directions, while $\varepsilon_{1t}, \varepsilon_{1c}, \varepsilon_{2t}, \varepsilon_{1c}, \gamma_{12\_u}, \gamma_{13\_u}$ and γ_{23_u} are ultimate strains components for tension and comparison and shear load corresponding directions. Furthermore, the ultimate strains must be determined experimentally in their corresponding uniaxial and pure shear stress states. It delivers a slightly skewed failure envelope in the plane of the two direct stresses as results of the effect of Poisson ratio.

3.3.2 The maximum stress criterion

This criterion predicts the failure of a lamina when at least one of the stresses in the material coordinates ($\sigma_{11}, \sigma_{22}, \sigma_{12}, \tau_{12}, \tau_{23}, \tau_{13}$) exceeds its corresponding strength value. The failure envelope is represented as a rectangular shape in the plane of any two stresses since the stress strength ratio is a constant for a failure mode. The criterion states that failure occurs if any one of the following inequalities is true (Tsai, 1984).

$\sigma_{11} > X_t$ if $\sigma_{11} > 0$ or abs $(\sigma_{11}) > X_c$ if $\sigma_{11} < 0$

$\sigma_{22} > Y_t$ if $\sigma_{22} > 0$ or abs $(\sigma_{22}) > Y_t$ if $\sigma_{22} < 0$ (3.44)

abs $(\tau_{23}) > \tau_{23\,ult}$; abs$(\tau_{13}) > \tau_{13\,ult}$; abs $(\tau_{12}) > \tau_{12\,ult}$

where X_t, X_c, Y_t,and Y_c are tensile and compressive strengths of material along and transverse to the fibre direction respectively, while $\tau_{12\,ult}$, $\tau_{23\,ult}$ and $\tau_{13\,ult}$ are the shear strengths in the material's principal planes.

This criterion could predict three separate failure mode fibre breakage, transverse matrix fracture, and shear matrix cracking with a certain angle of fibre orientation called the critical angle. This angle depends on the material type of lamina. The criterion has a weakness in considering the interactions between the stresses components.

3.3.3 Tsai-Wu Failure Criterion

One of the most commonly applied failure criteria for composite materials is the Tsai-Wu criterion (Tsai and Wu, 1971). In tensor notation, it is expressed for anisotropic materials where full interactions between stresses are present as follows.

$$F_i\sigma_i + F_{ij}\,\sigma_i\sigma_j + F_{ijk}\sigma_i\sigma_j\sigma_k \geq 1 \tag{3.45}$$

where F_i, F_{ij} and F_{ijk} are associated with the lamina strengths in the principal material directions. The F_{ijk} the term is usually neglected, due to a large number of material constants required. Therefore, the criterion for the orthotropic materials is given as follows.

$$F_i\sigma_i + F_{ij}\,\sigma_i\sigma_j \geq 1 \tag{3.46}$$

For in-plain stress problem and transverse isotropy, Equation (3.46) is reduced to

$$F_1\sigma_1 + F_2\sigma_2 + F_{11}\sigma_1^2 + F_{22}\sigma_2^2 + F_{66}\tau_{12}^2 + 2F_{12}\sigma_1\sigma_2 \geq 1 \tag{3.47}$$

where:

$$F_1 = \left(\frac{1}{X_t} - \frac{1}{X_c}\right), \qquad F_2 = \left(\frac{1}{Y_t} - \frac{1}{Y_c}\right) \ , \ F_{11} = \frac{1}{X_t\, X_c}$$

$$F_{22} = \frac{1}{Y_t\, Y_c}, \ F_{66} = \left(\frac{1}{\tau_{12\,u}}\right)^2 \text{ and } \ F_{12} = -\frac{1}{2}\sqrt{F_{11}\, F_{22}} \qquad (3.48)$$

where X_t, X_c, Y_t and Y_c are tensile and compressive strengths of material along and transverse to the fibre direction respectively, while $\tau_{12\,u}$ is the shear strength in the plane of a lamina.

The Tsai-Wu failure criterion is considered to be a quadratic polynomial equation of all stress components and tensorial coefficients (Li et al., 2017). Therefore, the failure envelope is smooth and curved as compared with the envelope of the maximum stress/strain criterion. The Tsai-Wu criterion does not specify the mode of failure for lamina. The mode of failure could be determined resorting to other means, e.g. the maximum stress criterion. In addition, it takes into consideration the effect of the difference between compression and tension strengths. It requires a biaxial test to experimentally determine the interaction term F_{12}, in general. The interaction term between the normal stresses defines the inclination of the ellipse in the $\sigma_1 - \sigma_2$ plane. Therefore, this interaction term could be considered as a factor to identify the shape of failure envelope.

4 Optimisation framework

4.1 Introduction

The optimisation is widely applied in engineering and science to achieve optimum outcomes. The process of optimisation includes searching for the optimum solution within a domain of possible solutions. Optimum design can be described as a process whereby a selected group of design variables varies automatically according to an algorithm in order to obtain the desired outputs (Antoniou and Lu, 2007). Hence, the desired output would usually show an optimised objective, such as performance or cost. As part of the present project, a procedure has been developed to facilitate optimisation of composite components with steered fibre paths.

In general, optimisation is concerned with achieving the optimum outcome for a given function while satisfying certain constraints (Thompson, 2012). Each optimisation problem consists of the following elements in its formulation:

1- Objective function: a measure of effectiveness or efficiency of the design problem. There can be more than one objective function the problem associated with, which is generally called (multi-objective optimisation).

2- Design variables: the parameters that are altered during the optimisation process. They can take continuous or discrete values (Daniels, 1978). Performing optimisation with discrete values is usually more complicated than solving the problem with the continuous design variables.

3- Constraints: the limits that constrain the range of the design variables. The constraints which define the upper or the lower limits on quantities are called inequality constraints, while the others are called equality constraints (Daniels, 1978).

The standard formulation of the optimisation problem is:

$$\begin{aligned} &\text{Minimise } f(\boldsymbol{X}) \\ &g_j(\boldsymbol{X}) \geq 0 \ , \ j=1,\ldots,n_g \\ &h_k(\boldsymbol{X}) = 0, \ \ k=1,\ldots,n_k \end{aligned} \tag{4.1}$$

where $\boldsymbol{X}$ is a vector of design variables with components X_i, $i=1,\ldots,n$, $h_k(\boldsymbol{X})$ are the equality constraints and $g_j(\boldsymbol{X})$ are the inequality constraints.

Depending on the objective function and constraints, the optimisation problem can be classified as linear or nonlinear. In a linear optimisation problem, both the objective function and constraints involve linear functions of the design variables, while in a nonlinear optimisation problem either the objective function or some of the constraints are nonlinear.

4.2 Development of the optimisation framework

The developed framework draws optimisation functionalities from Matlab, which offers different optimisation algorithms, while the stress analysis is conducted in Abaqus/Standard (2017), which is driven by a Python script. The framework introduces a Client/server technique, which is an organic relationship between two programs. The first program (the client) requests a service or resource from the second program (the server), as shown in Figure 4.1. Programs within the same computer can use the client/server model. It also applies to different computers through an appropriate network, although it is more sophisticated when the client creates a connection to the server over a local area network (LAN) or wide-area network (WAN), such as the internet. The framework runs from a Matlab script file (Client file), which then communicates with the server file (Python file), thus providing interaction between Abaqus/CAE and Matlab. The other benefit of using client and server files is to prevent opening the start session dialogue box when Abaqus/Standard is called for each optimisation iteration. Since during the analysis, Abaqus must be called a large number of times, this technique helps to reduce the duration of the analysis. The client file runs a built-in genetic algorithm GA solver (MATLAB2017a).

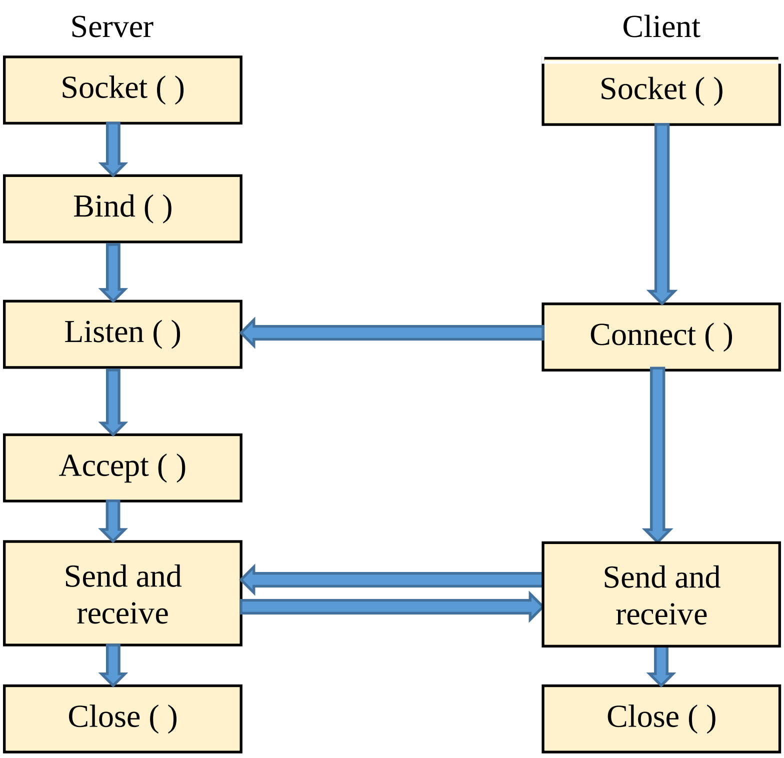

Figure 4.1: Flow chart events of client and server

The optimisation framework, as shown in the flowchart that introduced in Figure 4.2 integrates the high fidelity finite element (FE) analyses of steered fibre laminate model and the GA solver in Matlab. After a round of GA analysis, a set of design variables is fed into the Python script that generates an FE model and the model then runs with the Abaqus solver. Python script sends the outcomes of the stress analysis back to the client, including the coordinates of integration points of elements, the local material properties and orientations. Such information is usually generated by the UMAT and ORIENT user subroutines. The flowchart of this procedure is shown in Figure 4.3. The acquisition of the required data from the stress analysis requires post-processing which can be carried out using Python scripts.

The initial parameters of GA solver are set up, including the population size, maximum number of generations, elite number and the fitness function. A fitness function is a Matlab script that collects the design variables selected by the GA, sends them to a data file in user subroutine, opens a connection between the client and the server, and then runs the Python scripts. It also returns the desired results from Abaqus/Standard back to the client. All the required data are extracted from the resulting Output Data Base (ODB) file through the post-processing, also conducted using the Python scripts, which plays an important part in the main client Python scripts. In addition, GA solver finds optimum outcomes by selecting the better individual that have lower fitness value in each generation as elite passed to a new generation. Hence the procedure of choosing the better individuals will continue and halts when one of the termination conditions is satisfied. The termination condition is either the number of generations reaches the specified maximum number, or there is no difference between the subsequent individual generations.

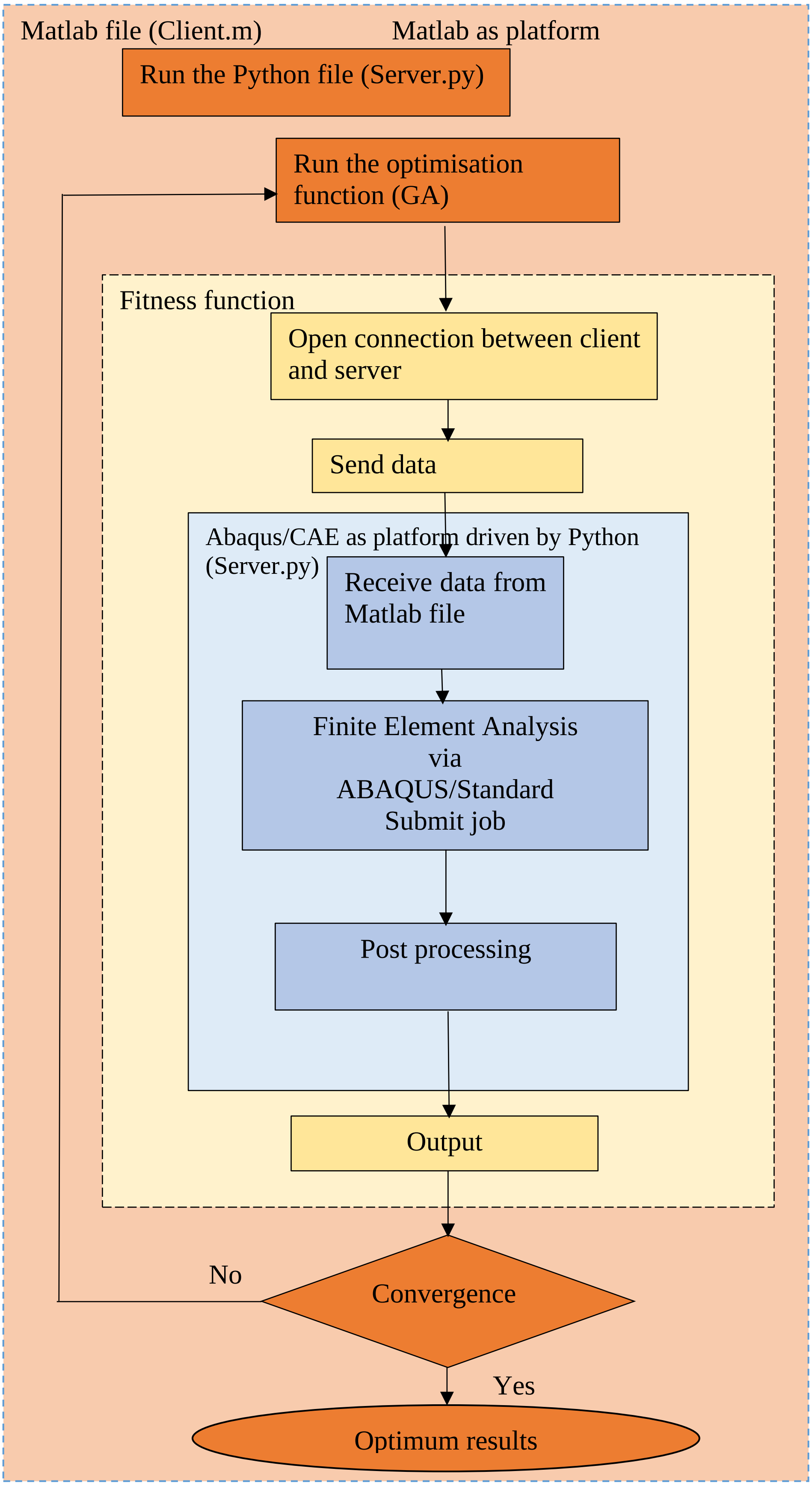

Figure 4.2: Flow chart of the optimisation framework

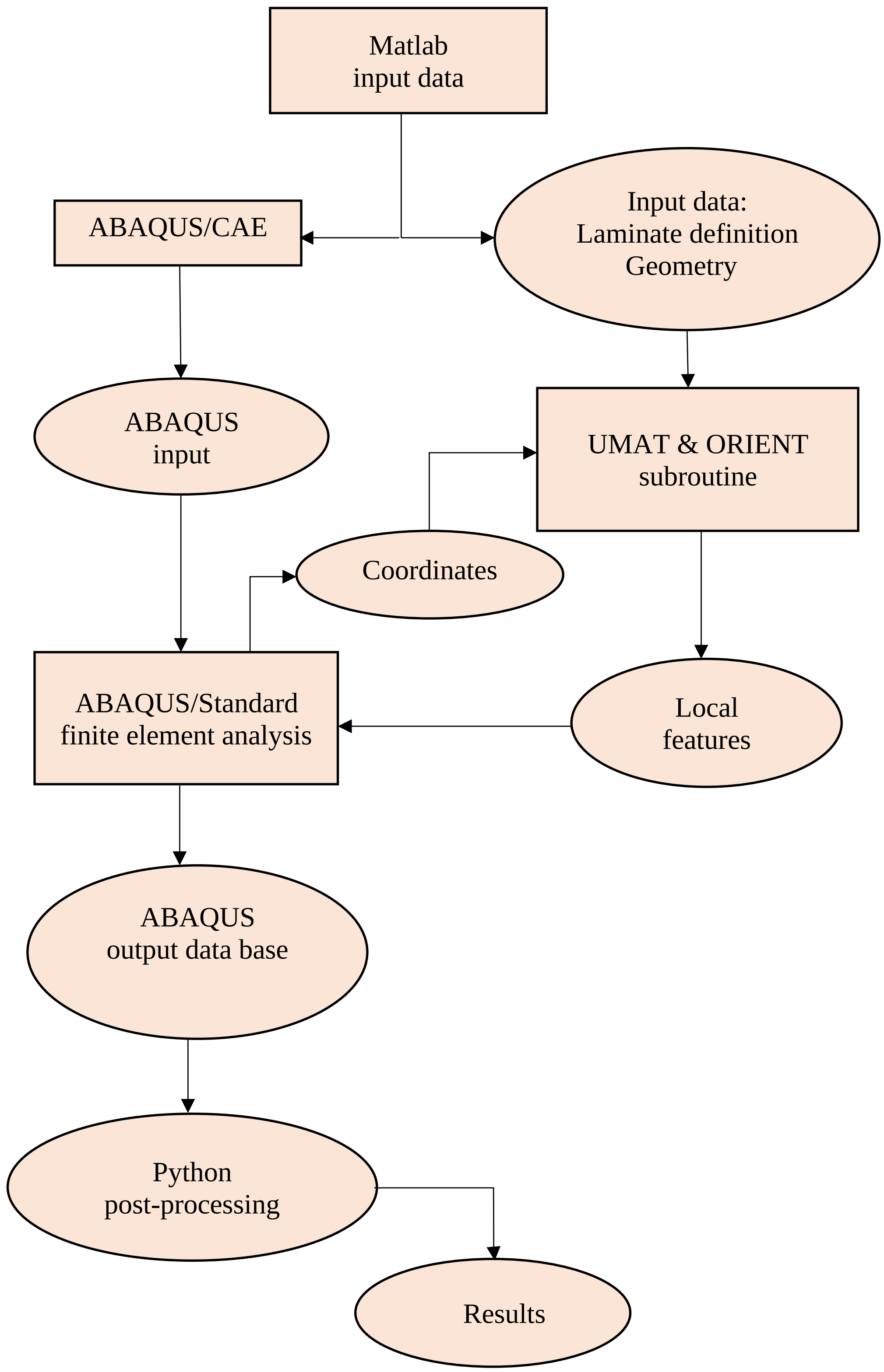

Figure 4.3. Analysis scheme (fitness function)

The objective function which the user desires to minimise or maximise is defined as a fitness function, as indicated in Figure 4.3. It could be considered as a link between the real system and the GA.

The process of submitting FE jobs inside the optimisation framework is serial processing. In addition, it could be used as a parallel algorithm to submit the jobs simultaneously, because the GA produce many individuals of design variable in each generation. However, this method is considered impractical because of the constraints on the number of Abaqus licences available. The framework submits the Python script of the FE model that is modified directly by Matlab, for each iteration of optimisation.

The computational time of the optimisation framework depends on three areas that use computational resources. They are identified as modelling, analysing and optimisation. Therefore, the complexity of each one of them could increase the computational efforts, hence the computational time.

Apparently, the type of analysis to obtain the outcome of the problem at each iteration of optimisation is more significant for the computational cost. For instance, analysing of buckling response is more time consuming than that of finding a static analysis. Furthermore, predicting the maximum failure load of laminates according to the progressive failure process is more complicated and computationally expensive than that used first ply analysis of failure.

Model complexity is associated with a way that used to implement the model to achieve a more accurate solution. For instance, modelling one-quarter of a plate by using the symmetries reduces the computational time significantly, while the accuracy of solution remains the same as modelling the whole plate. In addition, for a case of the discrete representation of the fibre angle that the design variables rely on the number of elements in the model. Hence, this will increase the complexity of the optimisation problem. Therefore, fibre path representation has been employed, in which the number of elements does not affect the number of design variables.

The optimisation objective function complexity contributes to increasing the computational time in terms of the number of design variables and their types, such as discrete or continuous. The relationship between design variables, either linear or nonlinear, makes a significant difference.

4.3 Optimisation function (Genetic algorithm)

The genetic algorithm, which is employed for optimisation in the present project, is a stochastic algorithm and search method to model some natural phenomena such as genetic inheritance and Darwinian strife for survival (Kramer, 2017). Also, it could be defined as mimic natural selection processes to enable the robust version of the individuals to pass to the next generation and weak ones to diminish. The algorithm begins with creating an initial population that represents a range of possible solutions in the domain of design space to the optimisation problem. The population consist of the set of individuals with encoded genes. Through the optimisation process, the principle of survival of the fittest individual identifies the next generation of individuals. The size of the population is considered as an important factor that affects the computing time consumption during the optimisation process. If the population size is too large, the computational time will be increased, while if the population size is small, the GA will converge quickly with a high probability of unreliable results. The new generation is created according to the three operators, which are selection operator (Elite), crossover and mutation. The selection operator could be defined as a selection models nature's survival mechanism of the fittest. It selects the fittest individuals and allows them to pass to the next generation. The mutation can be defined as an operator used to preserve the diversity of the population from one generation to the next generation. Therefore, it could change the solution for the best. In addition, it allows the genetic algorithm to achieve the global minimum point by preventing the individuals in the generation from being too similar to each other and reduce the chance of obtaining the local minimum points. The crossover is considered the most significant phase in the GA. Since it recombines the portions of good parent solution (chromosomes) and produces a child of next generation. Therefore, the new generation consists of the children of the elite, crossover and mutation. The GA could be employed with linear and nonlinear constraints as well as other optimisation functions

A GA has been used in the framework because it is especially appropriate when the search space of design variables is huge, and the number of design variables is high (Michalewicz, 2013).

4.3.1 Case study.

This case illustrates an example to show how the genetic algorithms can be employed to find the global minimum point in a problem involving multiple local minimum points in the Rastrigin's function as given in Equation (4.2).

$$f(x,y) = 20 + x^2 + y^2 - 10 * (\cos 2\pi x + \cos 2\pi\, y) \qquad (4.2)$$

The Rastrigin's function is a function that used as a test for the optimisation algorithms because it has many local minimum points and only one global minimum points. However, the locations of the minimum points are uniformly distributed as shown in the surface plot in Figure 4.4. It is difficult to find the global minimum point by using standard methods of optimisation.

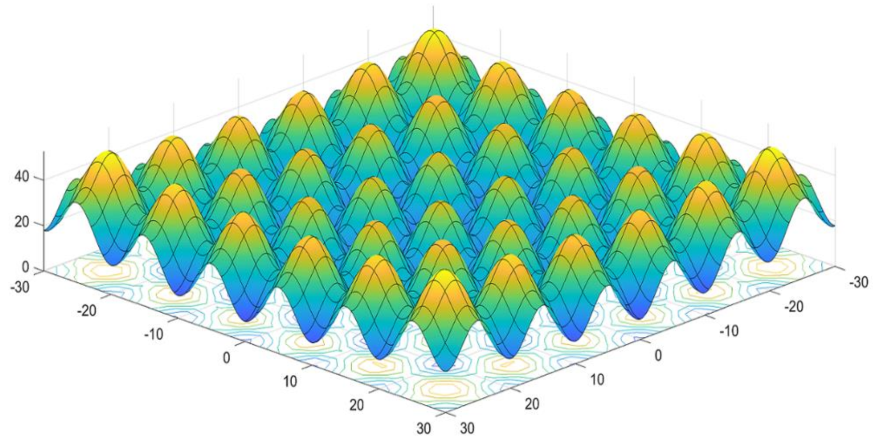

Figure 4.4: Surface plot of Rastrigin's function

Based on the number of design variables and population size, the GA starts by creating an initial population as red points randomly distributed within the domain of interest, as shown in Figure 4.5(a). After a number of iterations in the optimisation process, the number of generation increases and the individuals in the latest generation of the population become very close as a group of red points approach the global minimum point at (0,0) as shown in Figure 4.5(b). Therefore, the GA halted, as the convergence criterion is achieved.

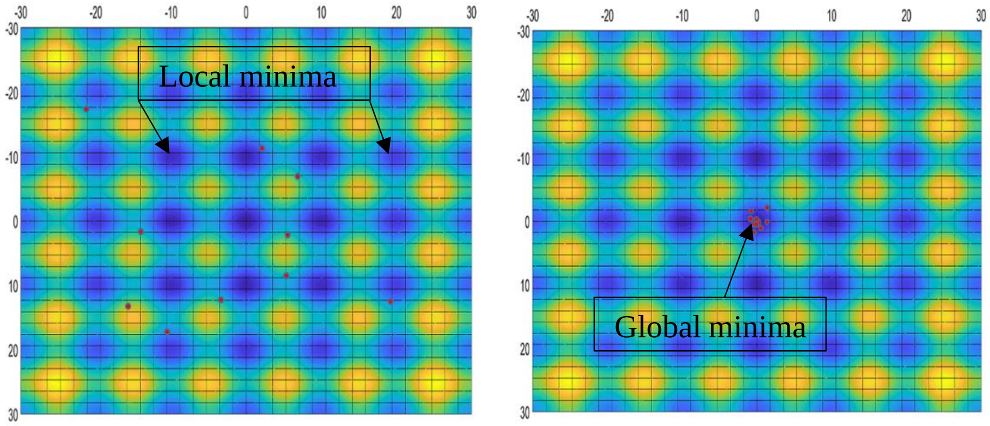

(a) (b)

Figure 4.5: Contour plot of the Rastrigin's function presents the populations; (a) initial population, and (b) last population

Table 4.1 shows the effect of the population size on the fitness value. It worth noting that with increasing the population size, the fitness value becomes more stable and approaches to the value of the global minimum. Practically, specifying the population size depends on the many parameters such as problem size, searching space, number of design variables and number of the objective functions (MATLAB2017a).

Table 4.1: Fitness value of the Rastrigin's function for different population size

Population size	CPU time(s)	Fitness function	Error %	Design variables	No. generation	Fun count
1	0.425	3.0653	306.53	1.121 -0.584	51	52
2	0.169	0.2227	22.27	0.016 -0.335	100	202
3	0.095	9.40E-10	9.4E-08	-8.524E-06 -2.003E-05	80	243
4	0.416	6.59E-08	6.6E-06	1.652E-04 7.701E-05	100	404
5	0.159	5.98E-09	6E-07	5.271E-05 -1.547E-05	97	490
6	0.077	3.54E-09	3.5E-07	-2.739E-05 -3.216E-05	60	366
7	0.075	1.89E-09	1.9E-07	1.914E-05 2.429E-05	76	539
8	0.087	6.75E-09	6.7E-07	5.789E-05 7.206E-06	86	696
9	0.085	6.37E-09	6.4E-07	2.863E-05 4.892E-05	71	648
10	0.078	1.38E-10	1.4E-08	8.340E-06 -3.528E-07	70	710
100	0.921	3.041E-12	3E-10	-4.681E-07 1.146E-07	69	7000
150	1.254	5.126E-11	5.1E-09	5.166E-07 5.057E-06	62	9450
200	1.524	5.452E-11	5.5E-09	1.512E-06 5.021E-06	65	13200

4.4 Verification of the optimisation framework

To verify the developed optimisation procedure, an optimisation case was considered, where composite laminates were optimized by minimising their thickness to have the smallest weight while sustaining a given load without failure.

Two approaches have been used to conduct the optimisation, and then the outcomes of both analyses were compared. The first approach (referred to as Approach I hereafter) was to use the Matlab code, which conducts laminate analysis analytical as defined by Classical Laminate Theory (CLT) and uses (*fmincon*) function (MATLAB2017a) as an optimisation problem solver. The flow chart of the code is shown in Figure 4.6. The second approach (referred to Approach II) was to use the developed optimisation framework to solve the same problem.

The optimisation problem and the inequality constraints have been represented mathematically as follows.

Minimise the thickness $$n = \sum_{i=1}^{k} m_i \tag{4.3}$$

Constraints $$F(\{\sigma^i\}) - 1 \leq 0 \tag{4.4}$$

$$\frac{m_i}{n} \geq \frac{1}{10} \qquad (i=1, 2, 3\ldots k) \tag{4.5}$$

$$\theta_i - \theta_{i+1} \geq 30^\circ \tag{4.6}$$

$$m^L \leq m \leq m^U \tag{4.7}$$

$$\theta^L \leq \theta \leq \theta^U \tag{4.8}$$

where k is the total number of ply angles, m is a number of plies with certain ply angle θ between the upper and lower values.

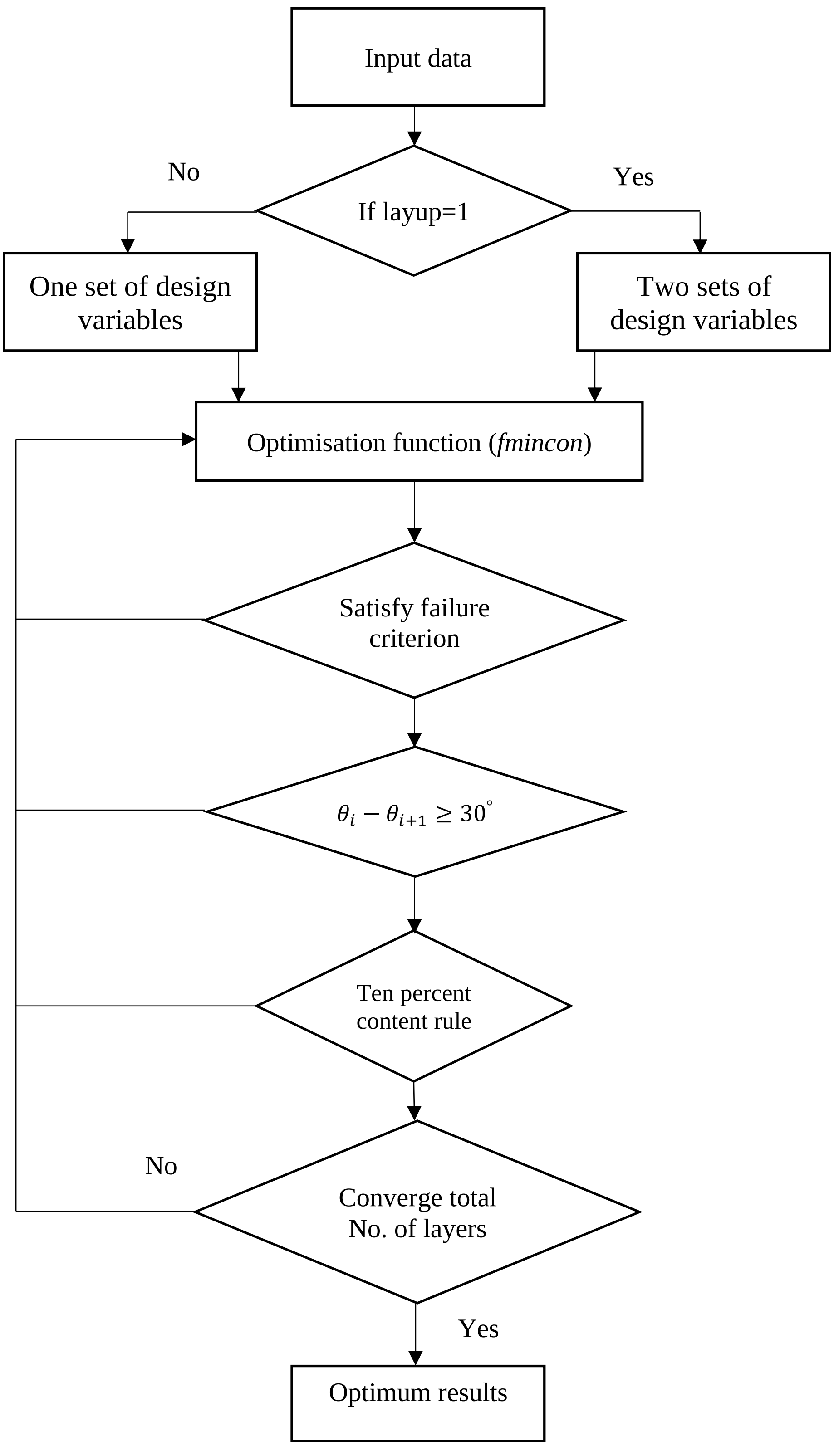

Figure 4.6: Flow chart of Matlab laminate optimisation code

The flat laminates that have been used in the optimisation problem for the two approaches are subjected under combined in-plane loading of the follows: N_x =3 kN/mm, N_y =2 kN/mm, N_{xy}=1 kN/mm, and the number of ply angles are k=4, 6 and 8. The material properties of unidirectional carbon fibre/epoxy composites (IM7/8552) are given in Table 4.2.

Table 4.2: Material properties (Kaddour et al., 2013)

Property	Value
E_{11}	165 GPa
E_{22}=E_{33}	9 GPa
G_{12}=G_{13}	5.6 GPa
G_{23}	2.8 GPa
v_{12}= v_{13}	0.34
Ply thickness(t)	0.125mm
v_{23}	0.5
X_t	2560MPa
X_c	1590MPa
Y_t	73MPa
Y_c	185MPa
S_{12}	90MPa

As can be seen in Table 4.3, the results obtained from the two approaches were found to be in a good agreement. The analyses were conducted for two options for the design variables. The first option, referred to as layup not equal one, was to allow variation of the number of plies that corresponds to each ply angle while keeping the angle orientations of each ply angle fixed.

Table 4.3: Verification results

Approach No.	Layup	No. of ply angle	Ply orientation, °	No. of plies per ply angle	Total No. of plies
1	0	4	-45°, 0°, 0°, -45°	24, 92, 92, 24	232
2	0	4	-45°, 0°, 0°, -45°	33, 83, 83, 33	232
1	1	4	-90°, 0°, 0°, -90°	20, 30, 30, 20	100
2	1	4	-90°, 0°, 0°, -90°	21, 28, 28, 21	98
1	0	6	-30°, 0°, 30°, 30°, 0°, -30°	14, 12, 28, 28, 12,14	108
2	0	6	-30°, 0°, 30°, 30°, 0°, -30°	17, 11, 24, 24, 11, 17	104
1	1	6	-60°, -30°, 30°, 30°, -30°, -60°	8, 6, 16,16,6, 8	60
2	1	6	-60°, 0°, 30°, 30°, 0°, -60°	7, 6, 14, 14, 6, 7	54
1	0	8	-22.5°, 0°, 22.5°, 45° 45°, 22.5°, 0°, -22.5°	8, 8, 8,14, 14, 8, 8, 8	76
2	0	8	-22.5°, 0°, 22.5°, 45° 45°, 22.5°, 0°, -22.5°	9, 7, 7, 12, 12,7, 7, 9	70
1	1	8	-45°, -15°, 15°, 45°, 45°, 15°, -15°, -45°	6, 6, 6, 10, 10, 6, 6, 6	56
2	1	8	-45°, -15°, 15°, 45°, 45°, 15°, -15°, -45°	5, 5, 5, 9, 9, 5, 5, 5	48

The second option, referred to as layup (1), was to allow variation of both angle orientation and a number of plies for each ply angle. Consequently, in the second option, the number of design variables doubles, therefore it has a larger search space and naturally leads to better designs.

It is worth noting that in most cases, Approach 2 gave a smaller number of plies. This is reasonable, since the genetic algorithm, which is used in this approach, determines the global minimum point, while (*fmincon*) solver, as used in Approach 1, can converge at a local minimum.

Based on verification outcomes as presented above, it can be concluded the developed optimisation framework is valid to use in problems that couple FE software with Matlab.

4.5 Summary

A framework has been developed for the optimisation process that used two different pieces of software, Matlab as an optimiser and Abaqus/Standard package as stress analyser. The client and server technique have been used to connect between these two software packages and to avoid time delay during opening the start session dialogue box when Abaqus/CAE is called. A framework has been verified with a simple optimisation case of composite laminates that were optimised by minimising their thicknesses to have the smallest number of plies and the lightest weight, without causing a failure under given combined loading. A comparison between the (*fmincon*) optimisation function and the genetic algorithm has been performed. It has been demonstrated that the GA has a good ability to capture the global minimum point, while (*fmincon*) function can dwell at a local minimum point. In addition, GA can be used to run the FE calculation in the fitness function as a parallel scheme. The consumed time of the optimisation framework and computational effort is more substantial than that of Matlab optimisation code (Approach 1) since the computational effort of Abaqus (Approach 2) is large.

5 Optimisation of steered fibre paths on the flat panels

5.1 Introduction

In terms of the design of composite materials, the most significant advantage is that the designers can tailor the stiffness and strength properties for the needs of a specific application by changing the orientation of the single lamina and the stacking sequence in the laminates (Gürdal et al., 1999a). In addition, the percentage of the layers having certain orientations with respect to the reference direction could be used to design and predict the in-plane stiffness properties of a laminate as in the ten percent rule (Hart-Smith, 1992). On the other hand, the bending properties of laminate are influenced by the location of the layers through the thickness of the laminate, as well as the percentage of certain layers inside the laminate. Therefore, the rearrangement of the stacking sequence through the thickness in the laminate could be considered as a method to design composite laminate.

In recent years, there has been an increasing tendency toward the development of the so-called unconventional laminates, where the fibre paths in the individual laminae are curved. In practice, this is realised by placing the tows of fibre in the curved style, with straight paths of fibre being a special case of curved ones. Steering the fibre that way could be done by varying the orientation of continuous fibre locally from point to point in the single lamina to produce the curved fibre path. This format of fibre placement can result in more beneficial stress distributions, and it can increase the size of design space as compared with a straight fibre format. The improvement in the mechanical performance of curved fibre laminates, in particular, in response to the applied buckling load will be explored and demonstrated in this chapter via the range of carefully designed numerical studies. In this chapter, the analyses will be conducted on square panels, which is the most basic type of laminated structure, to establish the methodology and reveal the effects of fibre variation on mechanical performance. The study will be continued in the next chapter addressing the structures of larger practical significance, such as cylindrical shells.

5.2 Different order of variations of local angles

Varying the local angle of the fibre within the composite panel results in a change of the stiffness of the panel spatially. The influence of fibre variation on the stiffness of the panel can be rationalised by assessing the improvements in the buckling response as compared with that of the panels with straight fibre.

The variation of local fibre angle along *x*-direction can be described by the polynomial equation as follows.

$$\theta(x) = \sum_{i=0}^{n} A_i x^i \tag{5.1}$$

where *n* is the degree of the polynomial equation and A_i are the coefficients of the polynomial equation.

According to the Equation (5.1), the variation of the local angles can be classified by polynomial degree *n* as follows.

5.2.1 No variation (constant local angles)

With this type of variation of local angles, *n*=0 in Equation (5.1), which becomes.

$$\theta(x) = A_0 \tag{5.2}$$

Based on the Equation (5.2), the local angles do not change along the path of fibre, hence the coefficient A_0 is the value of constant fibre angle, which will be denoted as T_0 for consistency with notations that will be introduced in the sections to follow. This type of variation defines a conventional straight fibre lamina. Such laminae can be stacked as shown in Figure 5.1(a) to produce a laminate where plies with fibre angle T_0 are alternated with those having fibre angle T_0. The stiffness of such laminate is constant in the plane of the laminate; hence these laminates are sometimes referred to as constant stiffness (CS) laminates. The design variables for CS laminates include stacking sequence with certain fibre angles, number of the plies and material type which should be considered to find the desired design.

5.2.2 Linear variation of local angles (first-order)

For a linear variation of local angles, n=1 in Equation (5.1), which can then be written as follows.

$$\theta(x) = A_0 + A_1 x \tag{5.3}$$

where the A_0 and A_1 are the coefficients of the polynomial equation that can be determined using the pre-defined values of the local angles T_0 at the centre of panel and T_1 at the edge of the panel as shown in Figure 5.1(b). Therefore, Equation (5.3) can be rewritten as follows.

$$\theta(x) = T_0 + \frac{(T_1 - T_0)2x}{L} \qquad , 0 \leq x \leq \frac{L}{2} \tag{5.4}$$

where L is the length of the panel.

With varying paths of fibre in lamina with linear local angle variation, the stiffness of the laminates based on such lamina, as shown in Figure 5.1(b), will vary continuously and hence the laminates are referred to as variable stiffness laminates. The same terminology applies to laminates with higher-order local angle variations as will be addressed in the next two subsections. In terms of manufacture, the continuous curved fibre path in the lamina can be produced by automated fibre placement (AFP) of pre-impregnated tows, embroidery machine for dry fibres and 3D printing technique.

5.2.3 The nonlinear variation of local angles

The nonlinear variation of local angles is defined by polynomial given by Equation (5.1) when n>1. In this work, two cases of nonlinear variation are considered, namely, quadratic and cubic.

5.2.3.1 Quadratic variation of local angles (second-order)

The quadratic variation of local angles (second-order variation) is defined as follows.

$$\theta(x) = A_0 + A_1 x + A_2 x^2 \tag{5.5}$$

where A_0, A_1 and A_2 are the coefficients of the polynomial equation that can be determined using the pre-defined values of the local angles T_0, T_1 and T_2 at the centre, quarter and edge of a panel, respectively, as shown in Figure 5.1(c).

Hence the Equation (5.5) can be rewritten as follows.

$$\theta(x) = T_0 + \frac{2x}{L}(4T_1 - 3T_0 - T_2) + \frac{8x^2}{L^2}(T_2 + T_0 - 2T_1)\ ,\ 0 \leq x \leq \frac{L}{2} \tag{5.6}$$

5.2.3.2 Cubic variation of local angle (third-order)

The third order of the polynomial equation can be expressed as follows.

$$\theta(x) = A_0 + A_1 x + A_2 x^2 + A_3 x^3 \tag{5.7}$$

where A_0, A_1, A_2 and A_3 are the coefficients of the polynomial equation that can be calculated using the pre-determined values of the local angles T_0, T_1, T_2 and T_3 in the middle, at one third of half-length of the panel, two thirds of half-length of the panel and the edge of the panel, respectively, as shown in the Figure 5.1(d).

Hence the Equation (5.7) can be re-written as follows

$$\theta(x) = T_0 + \frac{x}{L}(18T_1 - 11T_0 - 9T_2 + 2T_3) + \frac{18x^2}{L^2}(4T_2 - 5T_1 + 2T_0 - T_3) + \frac{36x^3}{L^3}(3T_1 - 3T_2 - T_0 + T_3)\ , \qquad 0 \le x \le \frac{L}{2} \tag{5.8}$$

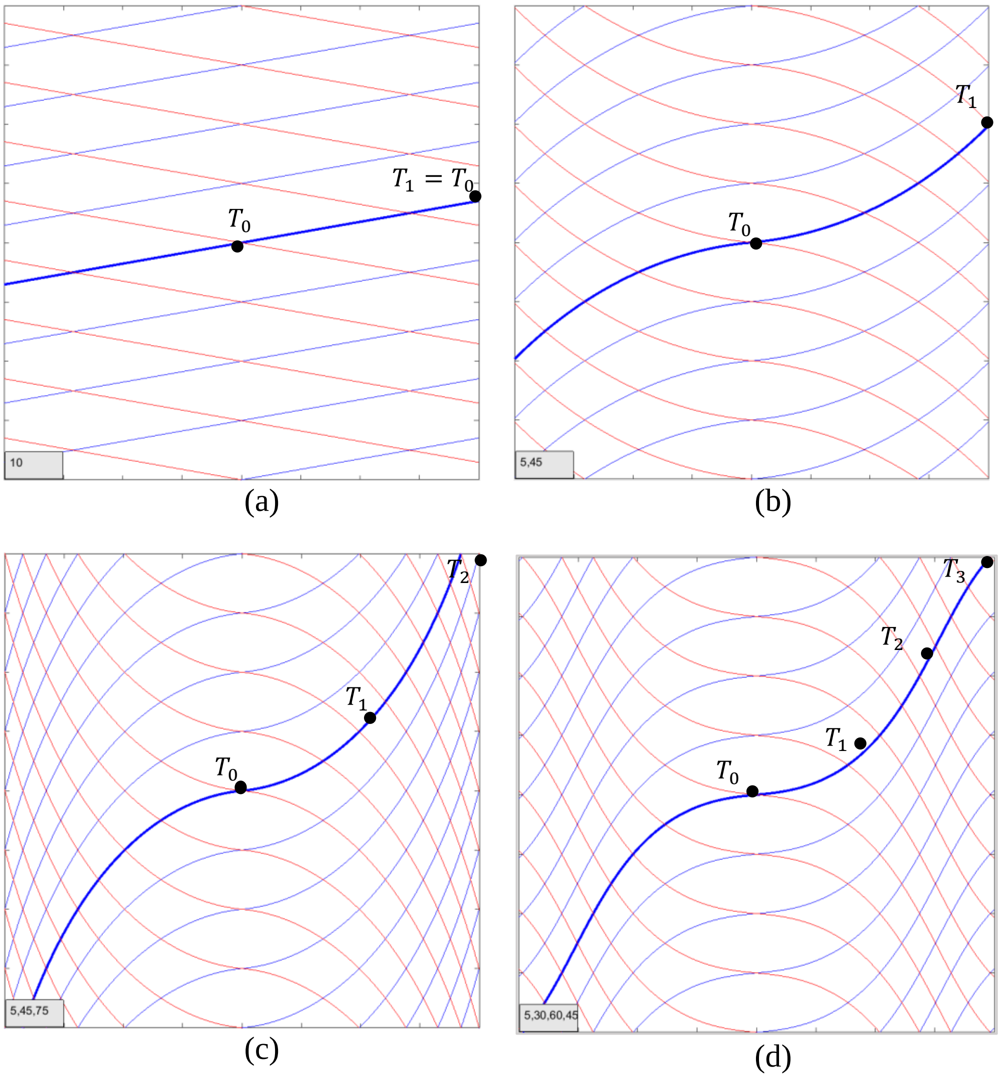

Figure 5.1: Fibre path according to different variations of local angles; (a) straight fibre (zero-order), (b) first-order variation of local angles, (c) second-order variation of local angles, and (d) third-order variation of local angles

5.3 Definition of uniform fibre volume fraction distribution in curvilinear fibre lamina

The placement and steering of the continuous tows having a linear variation of their local angles, one beside another, can produce the gaps and overlaps of the tows. The latter one can be prevented by shifting the centre line of the tow at a specific distance. Consequently, covering the entire surface of the structure with the tows in such a way prevents the thickness build-up (Gurdal and Olmedo, 1993). On the other hand, shifting of the tows will generate a gap of variable width between the two adjacent tows. Using the capability of automated fibre placement machine (AFP) to cut and restart a placement of the tow, the gap area could be filled locally with segments of tows, which is a technique employed when producing the course of tows (Wu et al., 2009). The size of the gap to be filled depends on the tow width and the variations of local angles. It should be noted that, for some configurations of the local angles, the maximum gap width can be smaller than the tow width.

After filling the gaps, small areas not covered by the fibre tows can still be present; these typically occur near the cut end of the tows. However, they can be considered to be negligibly small as compared to the entire area of the panel. Therefore, the panel can be considered to have a uniform fibre volume fraction distribution over it. The main drawback of this approach of fibre placement is the segmentation of tows that affects the ability of the panel to sustain the applied tensile load. Excessive deformation of the matrix can occur near the cut ends of the tows, which leads to the reduction in the strength of the composite. Therefore, in order to achieve the best performance in terms of load bearing, the tow should be continuous along the panel especially when the tensile load is applied.

5.4 Definition of non-uniform fibre volume fraction distribution in curvilinear lamina

The overlapping of tows leads to the thickness build-up. This produces local areas having higher fibre volume fraction and high stiffness. However, some fibre tows, such as carbon ones, are brittle, and can easily fail in areas where the tows overlap. Therefore, the overlapping of tows should be avoided to keep a constant thickness of the laminated structure.

In order to avoid such thickness build-up, tows can be shifted perpendicularly to the direction of variation of the local angles. Consequently, they would come into contact only at the edges of the panel, as shown in Figure 5.2. This leads to non-uniformity of fibre volume fraction and material properties distributions over the laminate. In particular, local reduction the stiffness and strength may occur. Alternatively, the effect of gaps on the fibre volume fraction variation can be neglected, and the uniform distribution of volume fraction can be assumed. In this chapter, both of these approaches have been applied in the analyses to identify their impacts on predicted structural behaviour.

Based on the curvilinear path of tows on the flat plates (Gürdal et al., 2008), The variation of the gap width can be derived analytically. In the *xy*-plane, locally, the local angle is defined as follows.

$$\frac{dy}{dx} = \tan\big(\theta(x)\big) \tag{5.9}$$

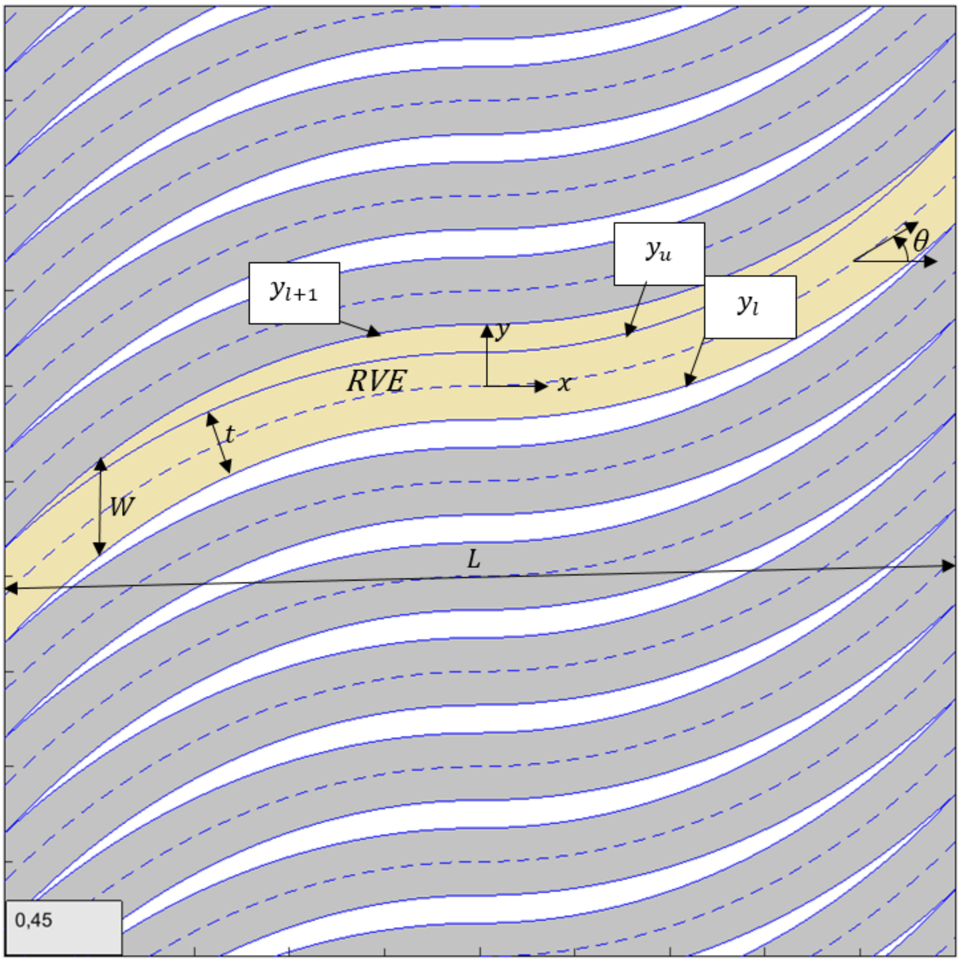

Figure 5.2: Schematic drawing for curvilinear lamina with a representative volume element being highlighted in yellow

The path definition can be written as an explicit function of *x*-coordinate by integrating both sides of Equation (5.9) as follows.

$$y = \int_0^{\frac{L}{2}} \tan\big(\theta(x)\big)\, dx \tag{5.10}$$

by substituting Equation (5.4) of linear variation into Equation (5.10) yield the expression of the curved path as.

$$y = -\frac{\ln\left|\cos\left(\frac{2x\,(T_1 - T_0)}{L} + T_0\right)\right|}{(T_1 - T_0)\frac{2}{L}} + \frac{\ln|\cos(T_0)|}{(T_1 - T_0)\frac{2}{L}} \tag{5.11}$$

where T_0 and T_1 are local angles at the centre and at the edge of the panel, respectively, and L is the length of the panel.

Referring to the geometry of the single tow as shown in Figure 5.2, the upper boundary of tow, y_u, will be as follows.

$$y_u = y + \frac{t}{2*\cos\left(\frac{2x\,(T_1-T_0)}{L}+T_0\right)} \tag{5.12}$$

where *t* is the width of tow.

Similarly, the lower boundary of a single tow y_l is defined as

$$y_l = y - \frac{t}{2*\cos\left(\frac{2x\,(T_1-T_0)}{L}+T_0\right)} \tag{5.13}$$

Then lower boundary of upper tow y_{l+1} is defined as follows.

$$y_{l+1} = y - \frac{t}{2*\cos\left(\frac{2x\,(T_1-T_0)}{L}+T_0\right)} + W \tag{5.14}$$

where W is the vertical distance of the representative volume element (RVE) tow and gap, as marked by yellow in Figure 5.2 and defined as follows.

$$W = t/\cos(T_1) \tag{5.15}$$

The gap width is defined as the difference between the lower boundary of upper tow, given by Equation (5.14) and the upper boundary of the reference tow Equation (5.12), resulting in the expression as follows.

$$y_{l+1} - y_u = W - \frac{t}{\cos\left(\frac{2x\,(T_1-T_0)}{L}+T_0\right)} \tag{5.16}$$

In order to determine the variation of fibre volume fraction over the panel, the percentage of the vertical distance of tow to the vertical distance of the representative volume element (RVE) is defined as follows.

$$Var(x) = \frac{y_u - y_l}{y_{l+1} - y_l} \tag{5.17}$$

Finally, by substituting Equations (5.12), (5.13) and (5.14) into (5.17) the variation of fibre volume fraction becomes as follows.

$$Var(x) = \frac{\cos\,(T_1)}{\cos\,((2x(T_1-T_0)/L)+T_0)} \tag{5.18}$$

Making use of this relation, the local variation of fibre volume fraction in the *x*-direction can be determined as follows.

$$V_{local} = \frac{\cos(T_1)}{\cos((2x(T_1 - T_0)/L) + T_0)} * V_{tow} \tag{5.19}$$

where V_{tow} is the fibre volume fraction within the tow.

5.5 Optimisation formulation

In order to investigate the influence of different variations of the local angles on the distribution of variable stiffness over the panel, according to their configurations of local angles. The buckling response of laminates has been simulated. In order to determine the maximum buckling load for the variable stiffness laminates of different configurations, the optimisation formulation for that problem has been set up as follows.

$$maximise \quad buckle(\boldsymbol{X}) \tag{5.20}$$

where the $buckle$ is the objective function that calculates the buckling load and $\boldsymbol{X}$ is the vector of design variables that represents the local angles.

Variation of the local angles corresponds to a variation of stiffness along the structure that could be captured by obtaining the buckling response. The optimisation function is used to find the optimum design that delivers the maximum buckling load based on the results of finite element simulation. The computational time of simulation is considered to be one of the most influential factors when establishing the optimisation procedure. A large number of coefficients in the higher-order variations of local angles could increase the computational cost of the optimisation. Therefore, a comparison of the outcomes of the different orders of local angles variation could avoid higher computational effort and longer time, by neglecting the order that has an inefficient improvement in the buckling load. The detailed description of the optimisation process and its framework has been given in Chapter 4.

Table 5.1: Material properties of the constituent fibre and matrix (Kaddour et al., 2013)

Property	Glass fibre	IM7	8552 epoxy
Longitudinal modules E_{11} (GPa)	74	276	4.08
Transverse modules E_{22} (GPa)	74	19	-
Transverse modules E_{33} (GPa)	74	19	-
In-plane shear modules G_{12} (GPa)	30.8	27	1.478
Transverse shear modules G_{23} (GPa)	30.8	7	-
Major Poisson's ratio v_{12}	0.2	0.2	0.38
Fibre volume fraction of tow	60%		

5.6 Finite element model

The major objective of the finite element method is to find an estimated solution for complex engineering problems which are difficult to solve analytically. In the present study, a commercial FE code Abaqus/Standard (2017) has been employed to model the buckling response of square laminated panels based on lamina with different tow paths as outlined in Sections 5.2 - 5.4.

The variation of the local angles that produces variable stiffness and changing gap width is given by Equations (5.1) - (5.4) according to their order of variation. They were implemented into an FE model through the ORIENT user-defined subroutine. This subroutine is a user-written FORTRAN code that defines the direction cosines with respect to the global coordinates at each integration point. In addition, due to the gap width being variable, the material properties of the panel also change from point to point. To account for this in the model, the material properties have been calculated locally according to the rule of mixtures (Reuss, 1929) and (Voigt, 1889) as mention in Chapter 3. The non-uniform distribution of the local fibre volume fraction of linear variation of local angles as defined by Equation (5.19) was implemented through the UMAT subroutine, which is employed to define the mechanical constitutive behaviour of the material at each integration point. The constitutive material model used in the present study relates the stresses and strains under the assumption of the plane stress state.

The FE model of the panel has been meshed with a general-purpose shell elements S4, which are appropriate for modelling both the thick and the thin shells. This element has six degrees of freedom and defines the transverse shear deformation according to the Mindlin-Reissner theory. The S4 elements are applicable to modelling the thin shells having very small transverse shear deformation. The formulation of the element implies that the transverse shear stress distribution should be constant through the thickness, whilst in reality, it is parabolic. To account for that, the shear correction factor is required and defined by matching the transverse shear energy with the shear energy in the three-dimensional structure due to the pure bending (Vlachoutsis, 1992). The shear correction ensures that the transverse shear stress is equal to zero at the outer surfaces of the layer to satisfy the boundary conditions. In the cases analysed in this work, as the thickness of layers was small, the transverse shear stiffness was small. Therefore, the effect of shear correction factor on the transverse shear stiffness could be negligible.

In order to solve any problem of solid mechanics, the boundary conditions need to be specified. In the finite element model of the panel under the buckling load, the panels were simply supported, which was modelled by constraining the displacement in the z-direction at all edges as shown in Figure 5.3. The compression load was defined by applying uniform displacement on two opposite edges of the panel. In order to predict the equivalent in-plane stiffness, different loading cases were modelled, where the uniaxial tensile load was also applied on the two opposite edges.

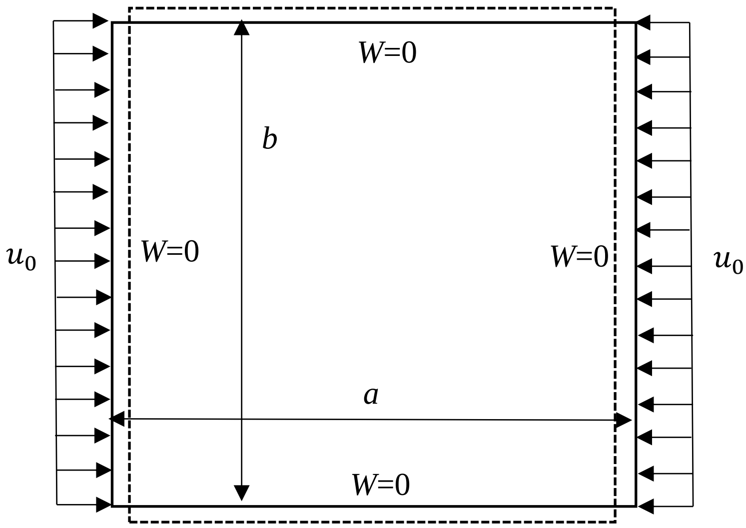

Figure 5.3: Boundary conditions of the panel

Under the applied uniform displacement, the panels produce sectional forces that resist the buckling load. The distribution of the sectional forces over the panels can be uniform, as in case of constant stiffness laminates, or non-uniform for variable stiffness laminates. In the latter case, the average sectional forces were calculated by integrating the variable sectional force with respect to the length as follows.

$$N_x^{av} = \frac{1}{b}\int_0^b N_x(a,y)dy \tag{5.21}$$

$$N_y^{av} = \frac{1}{a}\int_0^a N_y(x,b)dx \tag{5.22}$$

$$N_{xy}^{av} = \frac{1}{a}\int_0^a N_{xy}(x,b)dx \tag{5.23}$$

Therefore, the in-plane overall stiffness of the variable stiffness laminates can be derived as follows.

$$E_{eq\_x} = \frac{a\,N_x^{av}}{2u_0 h} \tag{5.24}$$

$$E_{eq\_y} = \frac{b\,N_y^{av}}{2u_0 h} \tag{5.25}$$

$$G_{eq\_xy} = \frac{b\,N_{xy}^{av}}{2u_0 h} \tag{5.26}$$

where a, b, h and u_0 are the width, length, thickness of the panel and the applied displacement, respectively, as shown in Figure 5.3.

In the model, the panel was comprised of twelve symmetric layers and was defined in term of local angles as $[\pm\langle T_0|\, T_1\rangle]3s$ lay-up, and its constitutive material properties are listed in Table 5.1. In buckling analysis, the material properties of glass fibre and 8552 epoxy have been used. While in the case of predicting the in-plane equivalent stiffness the material properties of IM7 fibre and 8552 epoxy have been used. The thickness of each layer was 0.4mm, resulting in the total thickness of the laminate being 4.8mm, and the side length of the panel was 100mm. However, the laminate is very thin, the in-plane strengths larger than buckling failures have been considered. Thus, the concerns of the in-plane failure of material were avoided.

5.7 Results and discussions

5.7.1 The effect of different orders of variations of the local angles

Different orders of variations of local angles are investigated by determining the optimum fibre path for each order that can offer the maximum buckling capacity as an indication of the local stiffness. The column chart, as shown in Figure 5.4 illustrates the improvement in buckling load as a result of different orders of variation of the local angles in the *x*-direction. These columns are normalized with respect to a maximum buckling load of the straight fibre laminate with T_0 =T_1 =45°, represented by the red column, which was chosen to be a benchmark case. As can be seen from Figure 5.4, with the first, second and third-order local angle variations, the curved fibre laminates show improvement in maximum buckling load by 4%, 6.3% and 6.4%, respectively, as compared with the benchmark case. This indicates that both the second and third-order variations offer just over 2% improvement in maximum buckling load as compared with the linear angle variation. The configuration of the fibre path as obtained by the optimisation is shown in Figure 5.5(a) and it corresponds to parameter values T_0 =74° and T_1 =39°. The distribution of the variable stiffness of the panel having this configuration of fibre paths can be assessed by considering the compressive stress resultant N_x, as shown in Figure 5.5(b). It is worth noting that the shape of deformed panels is concave in a centre of the panel because the Poisson's ratio is smaller in the centre than at the edge of panel. This concave is an indication of the high stiffness portion that provides more resistance to bear the buckling load.

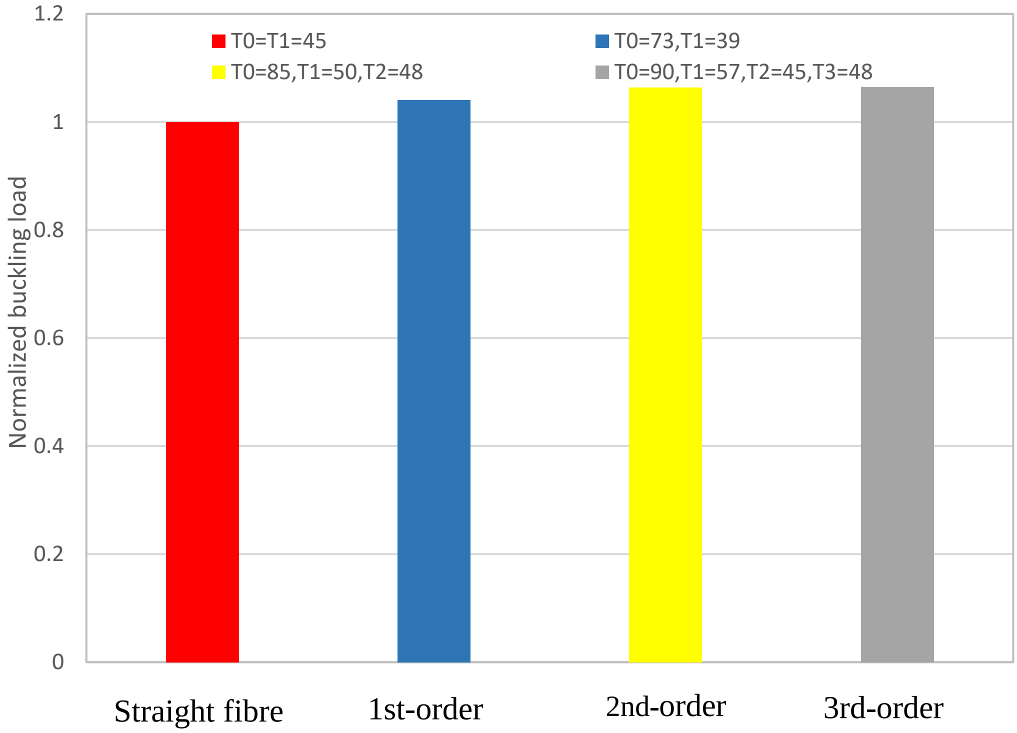

Figure 5.4: Improvement in buckling load due to different order variations in the *x*-direction with respect to the straight fibre

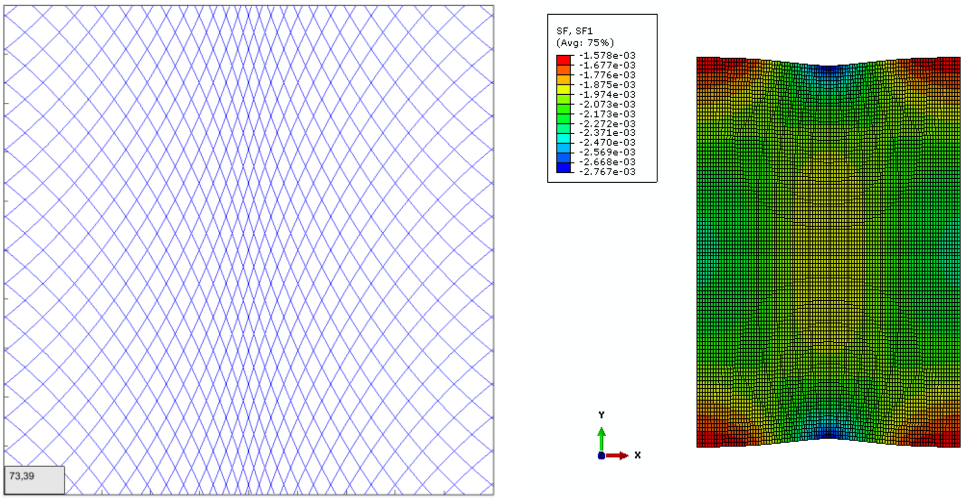

(a) (b)

Figure 5.5: Optimum panel of first-order variation of local angle in *x*-direction; (a) fibre path with T_0=73° and T_1=39°, and (b) Axial compressive stress resultant N_x

The improvement in the maximum buckling load delivered by laminates with different orders of variation of the local angles in the *y*-direction is shown in Figure 5.6. It can be seen the curvilinear laminates with first, second and third-order of local angle variation deliver the same gain in maximum buckling load of 40% as compared to straight fibre laminates. Given that curvilinear laminates with the second and third-order of local angle variations do not offer a substantial improvement in a maximum buckling load, if any, as compared with laminates with linear variation of local angle, and the fact that the former two cases are substantially more computationally costly, further analyses will be conducted on curvilinear laminates with linear variation of local angle, unless otherwise specified. The optimum pattern fibre path with the linear variation of local angle in the *y*-direction is presented in Figure 5.7(a), and it corresponds to T_0 =90° and T_1 =15°. With this arrangement of fibre tows, the local axial stiffness in the centre of the panel along the direction of the applied load is high, whilst the axial stiffness is low at the edges of the panel, where the fibre tend to align with the direction of the load applied. Having higher stiffness in the centre of the panel improves the buckling capacity, where the panel is expected to buckle in the centre. This explanation for the enhanced buckling performance is supported by the predicted axial stress resultant contours shown in Figure 5.7(b), where the axial compression force resultant at the edges of the panel is lower than that of the centre of the panel.

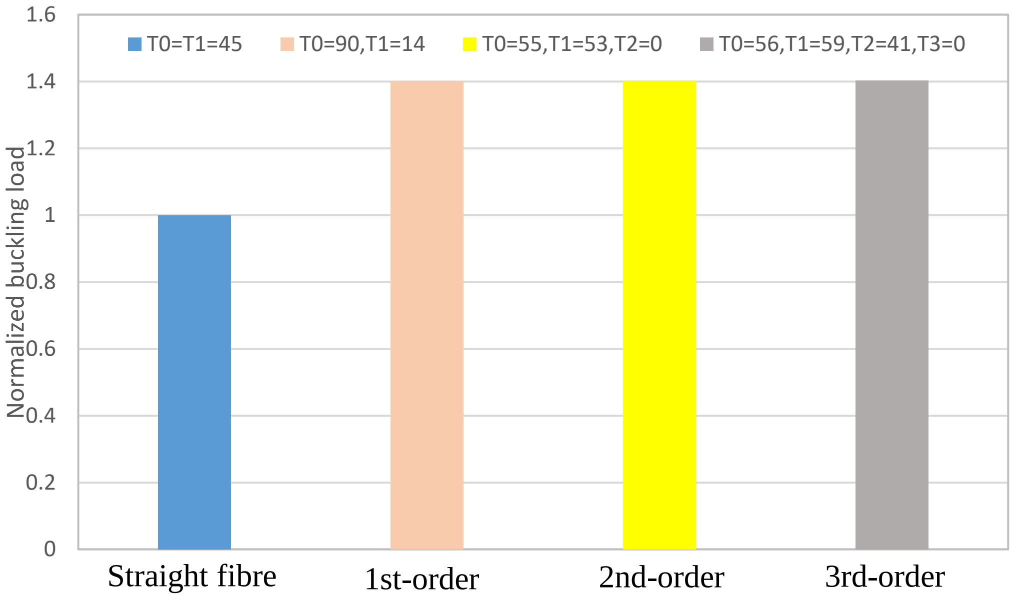

Figure 5.6: Improvement in buckling load due to different orders of local angles variations in *y*-direction

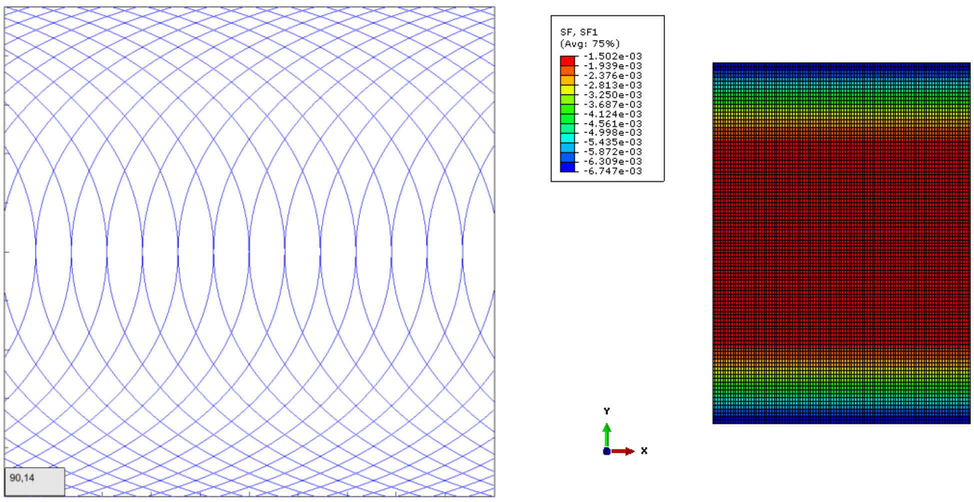

(a) (b)

Figure 5.7: Optimum panel of first-order variation of local angle in *y*-direction; (a) fibre path with T_0=90° and T_1=14°, and (b) axial compressive stress resultant N_x

In order to reveal how much gain or reduction in the buckling load can be obtained with different configurations of a linear variation of local angles in the *x*-direction, a family of the curves has been presented as shown in Figure 5.8. Each curve corresponds to a panel with a fixed value of parameter T_0 and represents a buckling load plotted against the parameter T_1 that was varied continuously from 0° to 90°. All curves were normalised with respect to the maximum buckling load of straight fibre laminate with $T_0 = T_1$ =45°, marked by the black point in Figure 5.8. Each curve of this family intersects with that corresponding to straight fibre laminate at points where $T_0 = T_1$. Moreover, it can be seen, the maximum improvement that could be achieved in the buckling load of the curvilinear fibre with respect to straight fibre is 4% for the configuration of local angles T_0 =70° and T_1 =40°. It is worth noting, for a certain value of the buckling load in Figure 5.8 there are only two possibilities of the orientation of the straight fibre laminates to match this value. While for variable stiffness laminates there are many possibilities of configurations to match the same value of the buckling load. Therefore, that could be considered as one of the most advantages of the curvilinear format of fibre path for offering more flexibility in design.

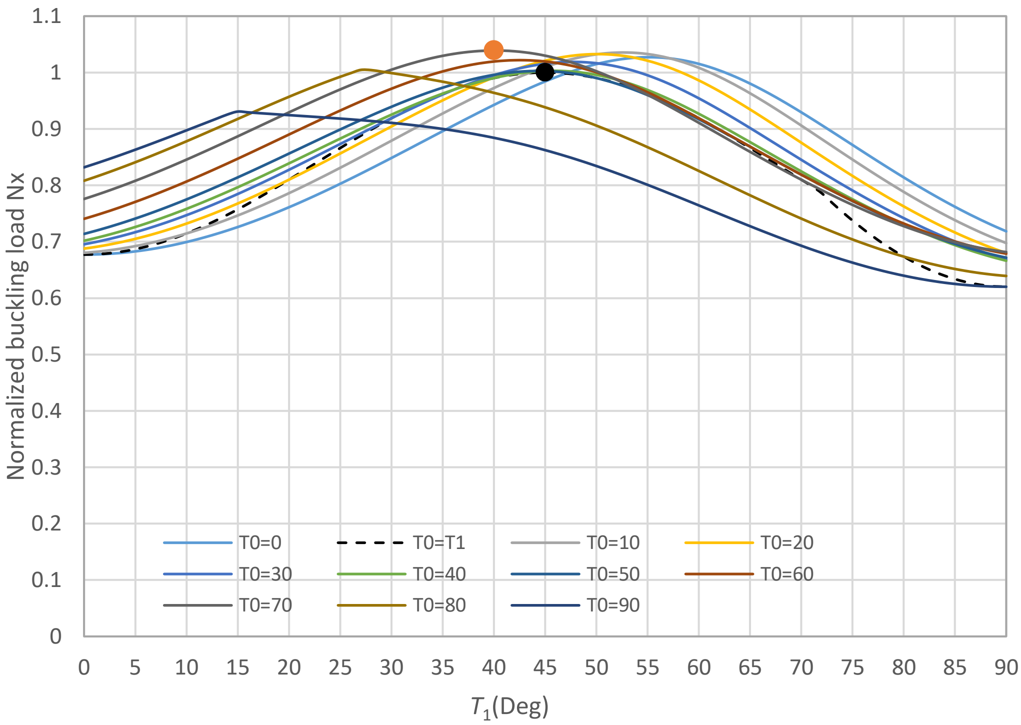

Figure 5.8: Normalized buckling load for different configurations of curved fibre panels having a linear variation of local angle *x*-direction

Similar plot has been produced for curvilinear laminates with the variation of local angles in the *y*-direction as shown in Figure 5.9. Same as before, all the curves have been normalized for the maximum value of buckling load obtained for straight fibre laminate with $T_0 = T_1$ =45°, as marked by the black point. The family of the curves that represent the steered fibre panels, having the various values of T_0 (from 0° to 90° with increments of 10°). It was observed that each curve of this family intersects with a straight fibre curve (dashed curve) at points T_0=T_1, same as in the previous case. However, the peak value of the maximum buckling load was obtained for a curvilinear laminate panel with T_0 =90° and T_1 =10°, as illustrated in the orange point, which indicates the improvement in the buckling load of around 40% compared to straight fibre laminate. In addition, the number of curvilinear laminate panels capable of delivering a buckling load larger than the maximum buckling load of straight fibre laminate is greater than that in the previous case. This is due to the fact that the direction of variation of the local stiffness is perpendicular to the direction of the applied load. As a result, the upper and lower edges of the panel to remain straight and this increases the axial stress resultant in the direction of the applied load, thus increasing the buckling capacity.

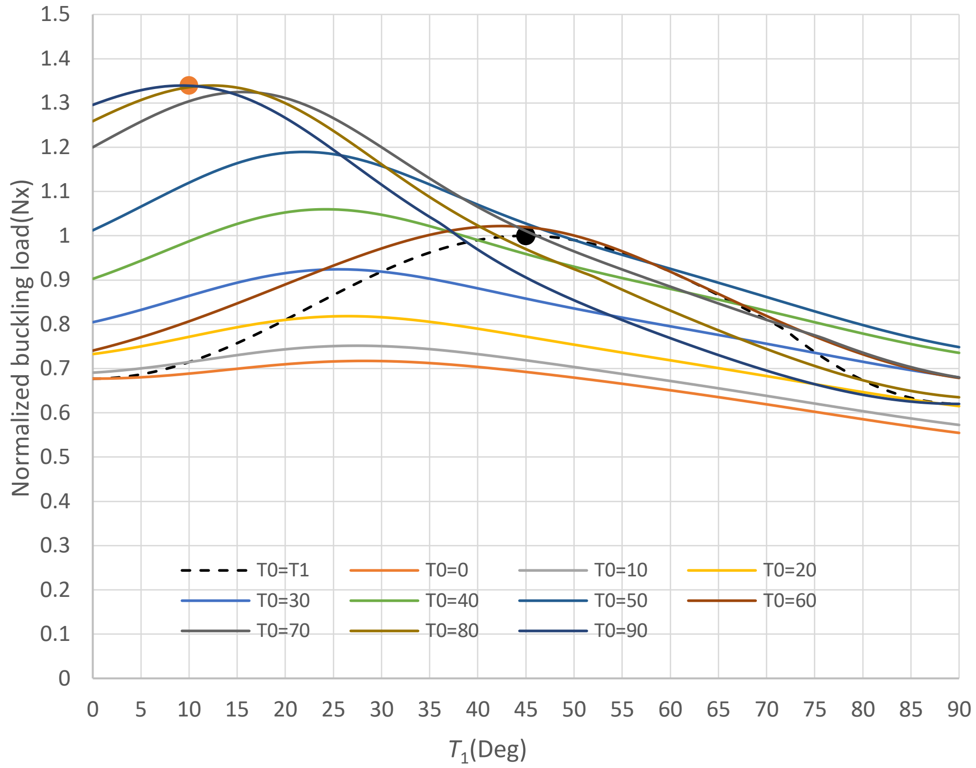

Figure 5.9: Normalized buckling load for different configurations of curved fibre panels having a linear variation of local angle in *y*-direction

5.7.2 Buckling response at uniform and non-uniform fibre volume fraction distributions.

In order to explore the influence of gap of varying width on buckling load predictions, a comparison of results obtained for panels with the uniform and the non-uniform fibre volume fraction distributions was carried out. Specifically, a comparison of buckling load for laminates with local angle variation in the *x*-direction is shown in Figure 5.10(a) and (b), for T_0 =0° and T_0 =30°, respectively. It can be seen that panels with both the uniform and non-uniform fibre volume fraction distributions, where T_0 and T_1 are the same, or nearly the same, have identical or marginally different buckling load. In such cases, the gap between the adjacent tows is very narrow; hence, essentially volume fraction could be considered uniform in both types of panels. As the difference between T_0 and T_1

increases, the gap becomes wider and its effect on the buckling response of the panel becomes significant. The general outlines of the curves obtained for the two approaches are similar. However, the buckling loads of in laminates with non-uniform fibre volume fraction distribution tends to be lower than those in the laminates with the uniform volume fraction distribution. This is due to the fact that the distribution of local stiffness remains the same for both types of fibre volume fraction distribution, but the fibre volume fraction at non-uniform distribution is generally lower because of the presence of the gap.

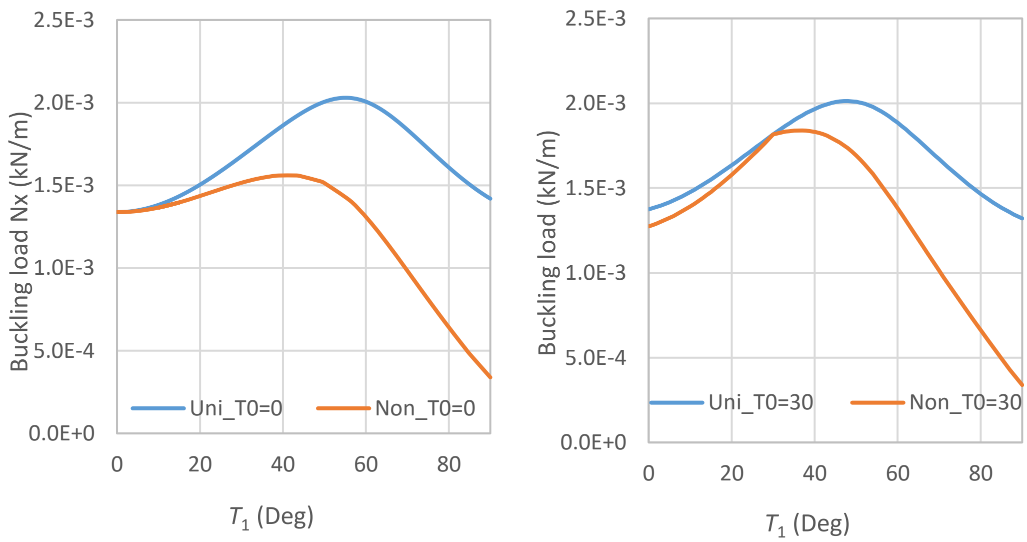

(a) (b)

Figure 5.10: A comparison of buckling load in panels with uniform and non-uniform fibre volume fraction distributions for $\theta = \theta(x)$; (a) laminates having T_0=0°, and (b) laminates having T_0=30°

Figure 5.11(a) and (b) show a comparison of buckling loads for curvilinear laminates with the uniform and non-uniform fibre volume fraction distribution with local angle variation in *y*-direction for T_0 =0° and T_0 =30°, respectively. The general behaviour observed in this case is essentially similar to the previous one, and the same explanations for the behaviours observed apply in this case.

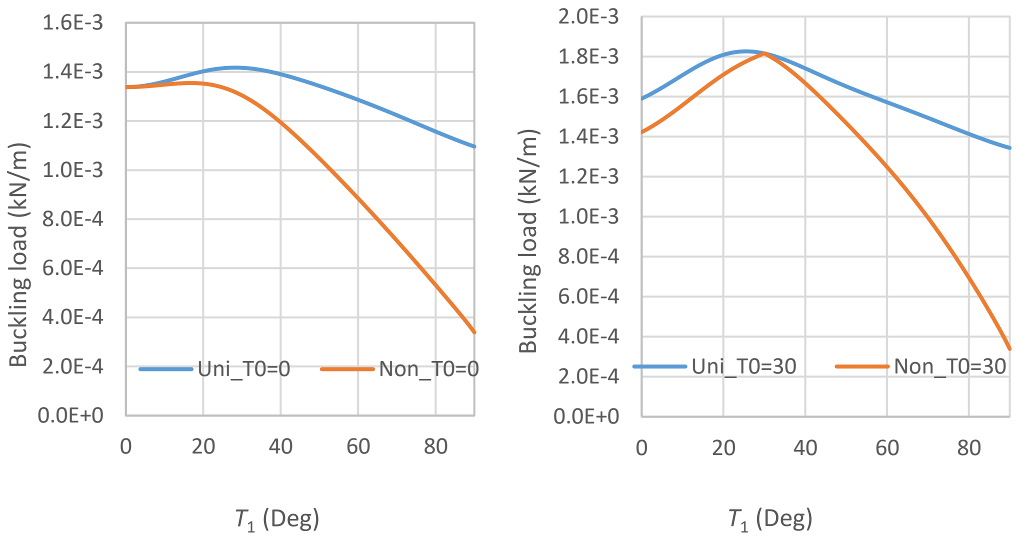

(a) (b)

Figure 5.11: A comparison between the uniform and non-uniform fibre volume fraction distribution for $\theta = \theta(y)$; (a) laminates having T_0=0°, and (b) laminates having T_0=30°

5.7.3 The equivalent stiffness of the variable stiffness laminates for uniform and non-uniform fibre volume fraction distributions.

Figure 5.12 and 5.13 illustrate the overall stiffness of curved fibre panels having local angles variation x- and y-directions, respectively. The results are presented as a family of the curves, each curve corresponding to a fixed value of T_0 (from 0° to 90° with increments of 10°). The dashed curve that represents the equivalent stiffness of the conventional laminates was calculated theoretically based on the CLT as in Chapter 3. Each curve of this family intersects with that calculated for a straight fibre panel at points where $T_0 = T_1$. This is considered as validation of the finite element model with theoretical analysis of the CLT. In both cases of uniform and non-uniform fibre volume fraction distributions, the area where overall stiffness of curved fibre panels is greater than that of straight fibre panels is shaded in grey. As can be seen, in all such cases $T_0 < T_1$. In Figure 5.12, the results in the area shaded in grey were obtained for the panels in which tows orientation at the centre along the vertical direction of the panel tended to align with the loading direction, with one of the examples of such tow arrangements being shown in Figure 5.14(b). Because of that, such panels had high stiffness in this area and hence under the uniaxial tension applied at the longitudinal edges they had a higher resistance to deformation in the centre and lower at the edges of panels as shown in the contour plot of sectional force in Figure 5.14(a). On the other hand, in panels for which $T_0 > T_1$, the local stiffness in the centre was smaller than the other areas as shown in contour plot in Figure 5.14(e), for which tow arrangement was as shown in Figure 5.14(f). Therefore, there is more shrinking in the centre of the panel.

In Figure 5.13, the grey area is larger than that in Figure 5.12, due to the fact that the local angle variation in *y*-direction tends to deliver higher overall stiffness under uniaxial tension. The mechanism of the panel resisting the deformation, in this case, can be assessed considering the stress resultant distribution in Figure 5.15. In this case, the direction of the applied load is perpendicular on the direction of angle variation. In other words, local angles of fibre remain constant along *x*-direction, and the local stiffness is distributed in the horizontal stripes that act as single spring stiffness; therefore, the equivalent stiffness can be considered as a parallel combination of the stiffnesses of springs in *y*-direction.

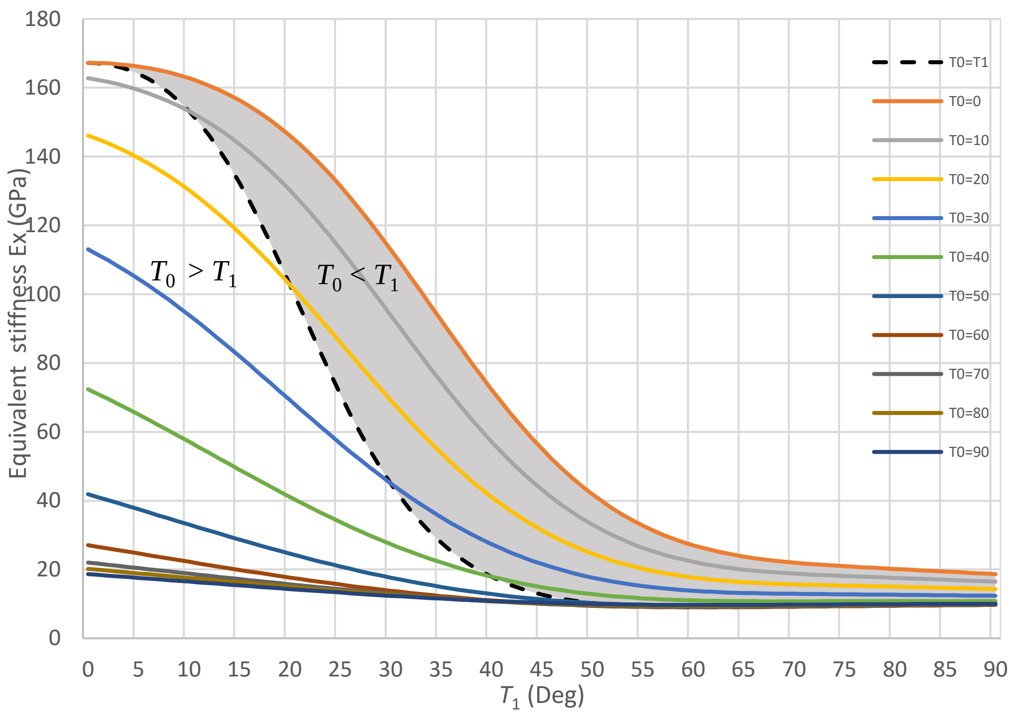

Figure 5.12: Equivalent stiffness of curved fibre panels with uniform fibre volume fraction distribution having $\theta = \theta(x)$ under the uniaxial tension

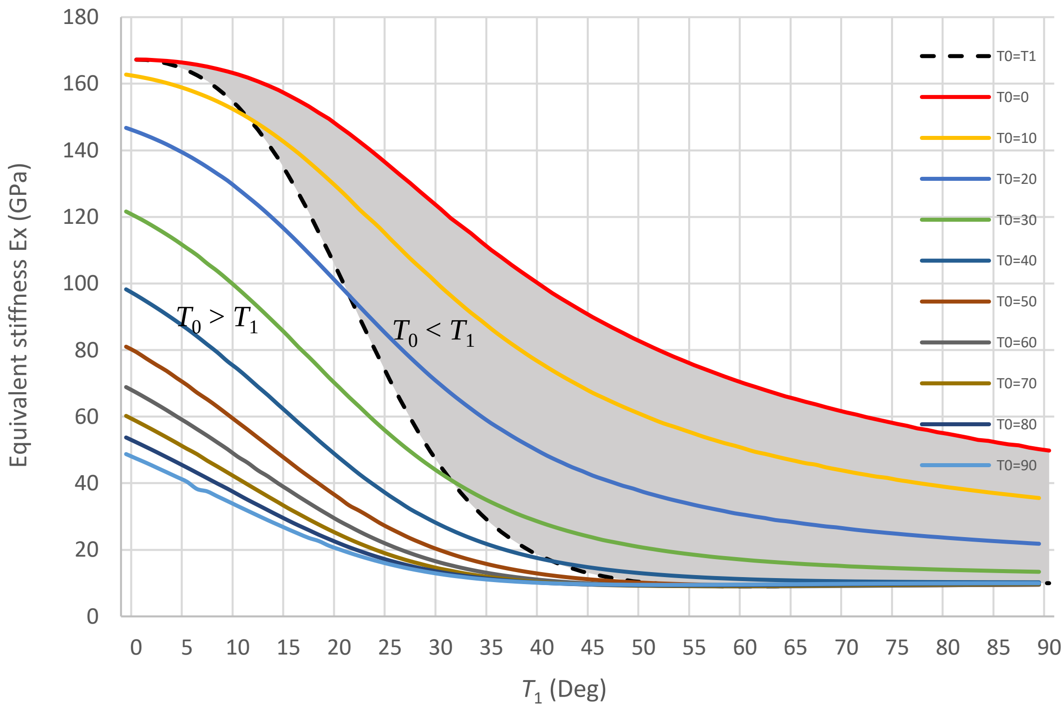

Figure 5.13: Equivalent stiffness of uniform fibre volume fraction distribution for curved fibre panels having $\theta = \theta(y)$ under the uniaxial tension

Through this exercise, it has been established that in terms of overall stiffness, curvilinear laminates can outperform the straight fibre ones when $T_0 < T_1$. Furthermore, such improved performance can be delivered with different tow configurations, which gives extra flexibility in the design process. In addition, Figure 5.12 and 5.13 that show the curves of the overall stiffnesses of curved fibre panels compared with straight fibre panels, can be employed to predict the overall stiffness of any mixed laminate following a similar procedure as in the ten percent rule.

The sign of variation of local angles plays a significant part as far as the stiffness of the panel is concerned. When the variation of local angles changes from positive to negative, the distribution of local stiffness changes accordingly. This effect is presented in Figure 5.14 and Figure 5.15 for the variation in *x*- and *y*-direction, respectively. The effect of positive variation of the local angles panel is demonstrated through in the contour plot of the sectional force and the fibre path as shown in Figure 5.14(a) and (b), respectively. This variation produces a large local stiffness in the middle of the panel as an indication of the bulge out. Figure 5.14(c) and (d) show axial stress resultant and fibre path of a straight fibre panel with T_0= T_1=45°, respectively. The variation of the local angle is zero; therefore, the axial stress resultant is constant along the panel as a result of constant stiffness. The negative variation of local angle is illustrated by the sectional force and the fibre path as shown in Figure 5.14(e) and (f), respectively. This variation represents the local angles T_0=45° and T_1=0°. The smaller value of the local stiffness in the vertical central area, where shrinking of the panel is observed, corresponds to the larger value of the local angles.

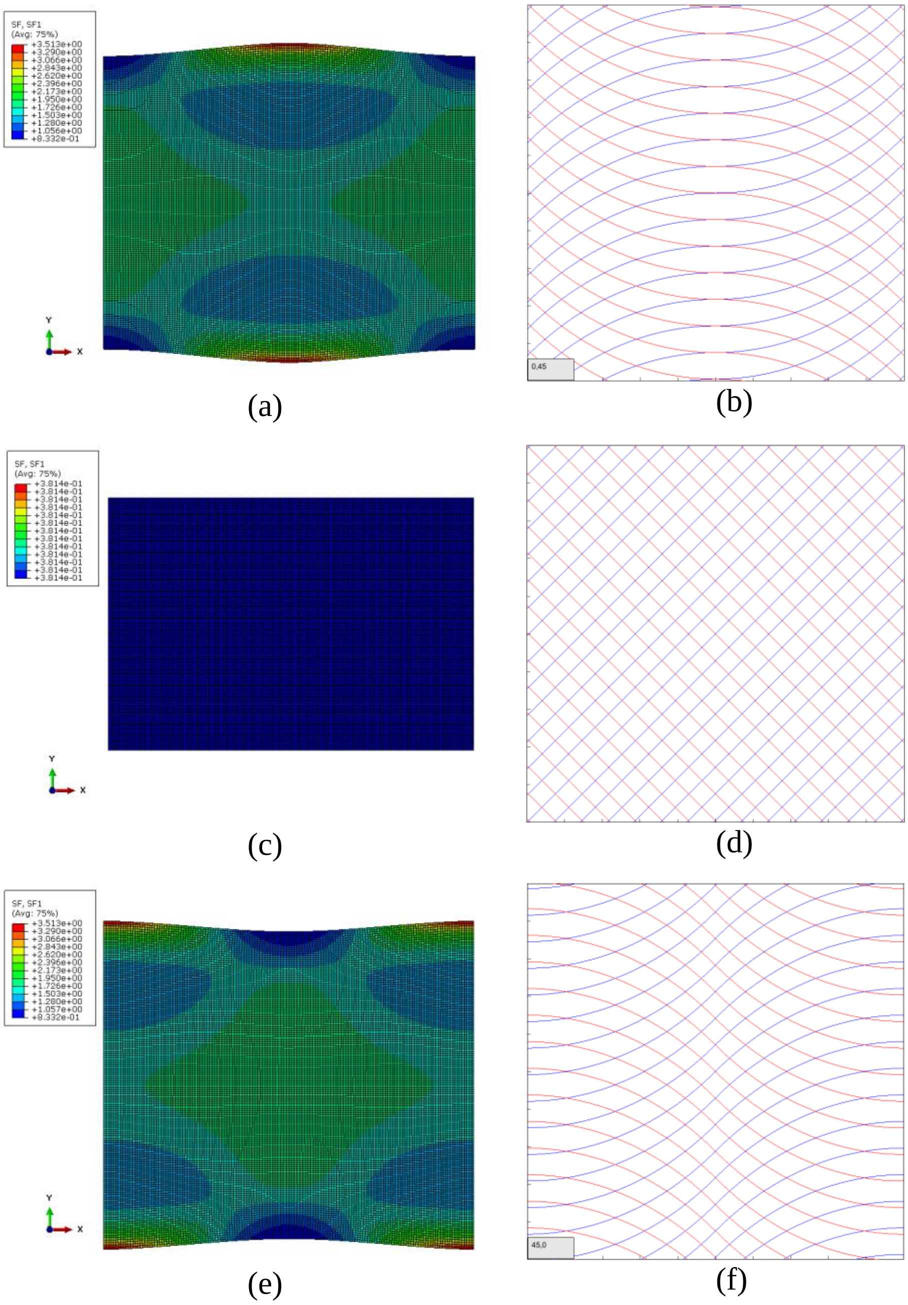

Figure 5.14:Contour plot of a sectional force and fibre path for different variations of local angles in *x*-direction ; (a) sectional force at T_0=0° and T_1=45°, (b) fibre path at T_0=0° and T_1=45°, (c) sectional force at T_0=45° and T_1=45°, (d) fibre path at T_0=45° and T1=45° (e) sectional force at T_0=45° and T_1=0° and (f) fibre path at T_0=45° and T_1=0°

In Figure 5.15 similar plots are shown for the variation of the local angles in the *y*-direction. The effects of positive variation of local angles when T_0=0° and T_1=45° on the sectional force can be seen Figure 5.15(a), where its contour plot is shown with fibre path, in this case, being shown in Figure 5.15(b). Based on the contour plot of the sectional force that resists the extension, the higher local stiffness is in the horizontal central area. Figure 5.15(c) and (d) show the uniform distribution of the sectional force and fibre path for this case, respectively. Finally, the negative variation of local angles was indicated in the sectional force and the fibre path as shown in Figure 5.15(e) and (f), respectively. One can see the smaller value of the local stiffness is at the centre, corresponding to the larger local angle T_0=45°.

The influence of local angles variation on the equivalent in-plane shear stiffness in the curvilinear fibre panels can be assessed by comparing the equivalent shear stiffness of curvilinear laminates with that in straight fibre laminates. To produce pure shear, panels were loaded by applying uniform shear displacement in opposite directions at the opposite edges of panel. The equivalent shear stiffness was calculated according to the Equation (5.26) and presented for different configuration of the local angles as shown in Figure 5.16, which was produced following the same procedure as was employed for equivalent stiffness E_x earlier on.

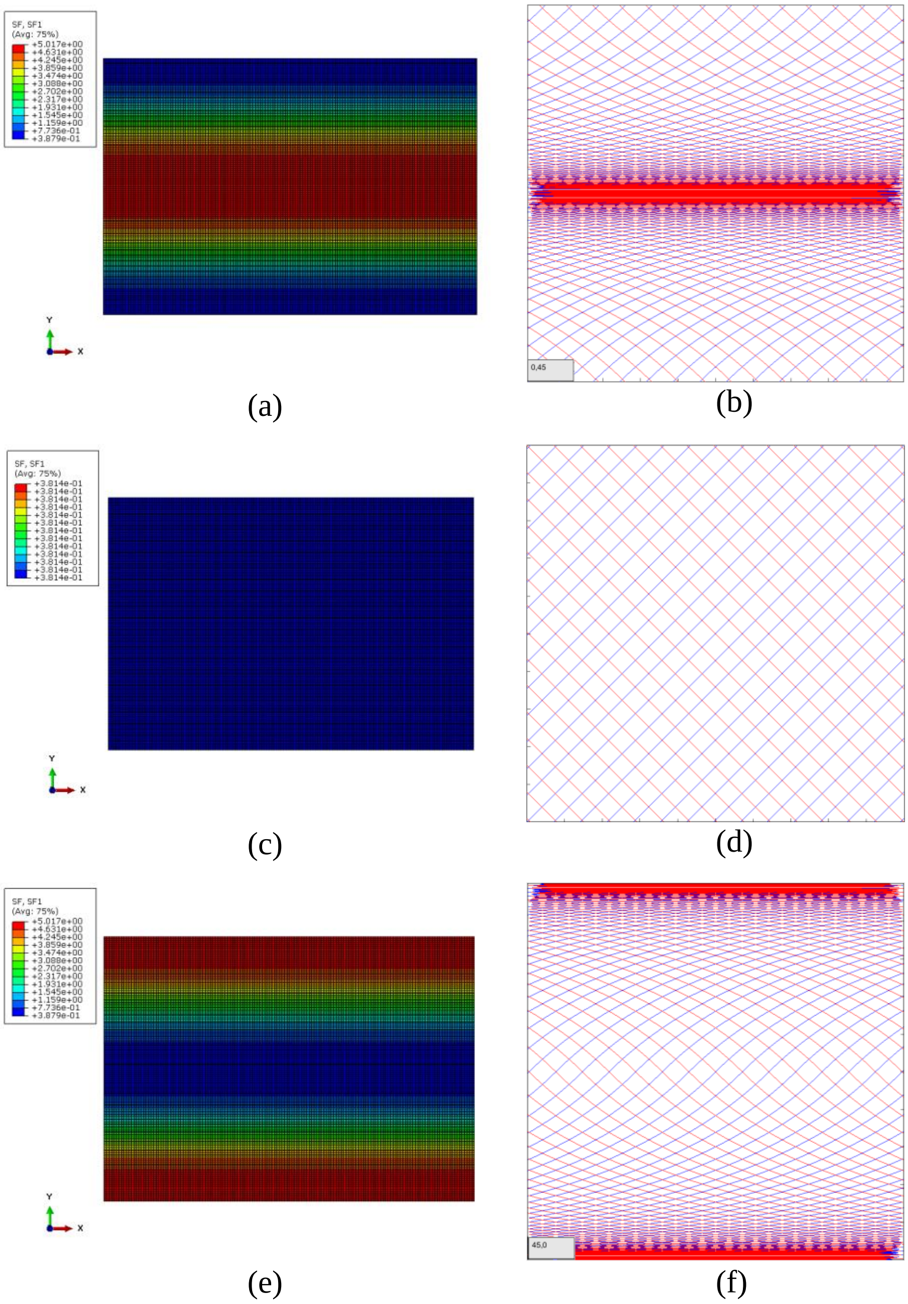

Figure 5.15: Contour plot of a sectional force and fibre path for different variations of local angles in y-direction ; (a) sectional force at T_0=0° and T_1=45°, (b) fibre path at T_0=0° and T_1=45°, (c) sectional force at T_0=45° and T_1=45°, (d) fibre path at T_0=45° and T_1=45° (e) sectional force at T_0=45° and T_1=0° and (f) fibre path at T_0=45° and T_1=0°

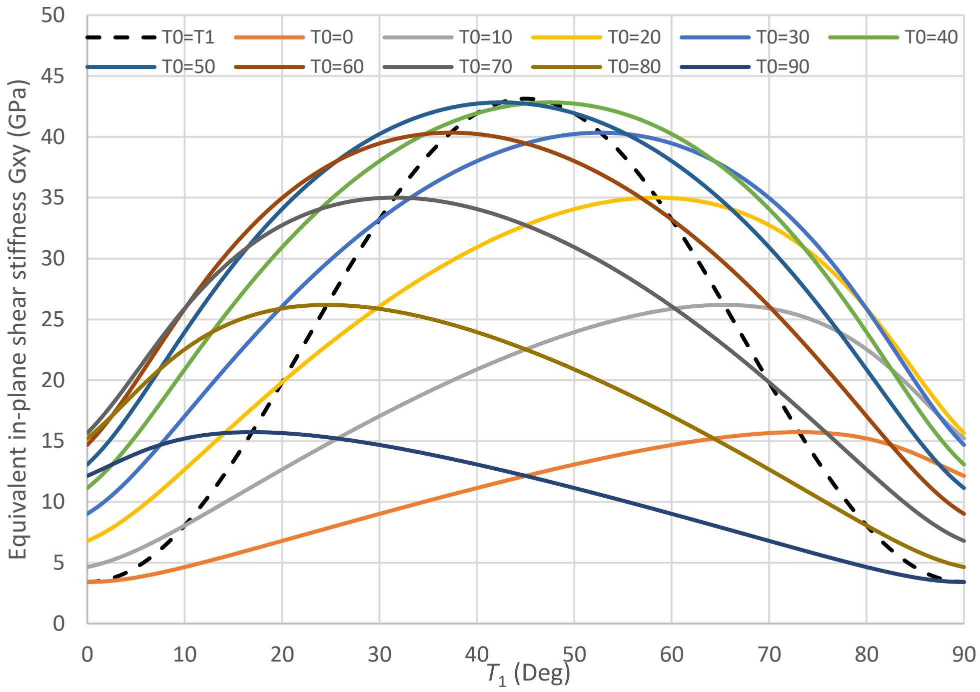

Figure 5.16: Equivalent shear stiffness of uniform fibre volume fraction distributions for curved fibre panels having $\theta = \theta(x)$

The dashed curve in Figure 5.16 corresponds to equivalent in-plane shear stiffness of the straight fibre panels and its maximum value was achieved at $T_0 = T_1 = 45°$, since the pure shear is equivalent to the equal bi-axial tensile and compressive stress state and the maximum tension is expected at 45°. In the broadest sense, this figure can describe the in-plane shear stiffness for all configurations of the local angles. These numerical results reveal that there are many configurations of the tows with which curved fibre panel produce the same value of stiffness as the straight fibre panel, hence their use can increase the flexibility of the design process.

The effect of variability of the gap and the fibre volume fraction as calculated according to the Equation (5.18), on the material properties, was assessed via a comparative study, in which material properties were obtained for a layer of composite with the uniform and non-uniform fibre volume fraction distribution. The arrangement of tows of constant thickness in a single layer with T_0 =0 and T_1 =45° is shown in Figure 5.17(a). As can be seen, the tows do not overlap and because their thickness is constant, a gap is present between the adjacent tows. The arrangement of the tows corresponding to uniform fibre volume fraction distribution is shown in Figure 5.17(b). Figure 5.17(c) illustrates the variability of the gap along the width of layer based on the Equation (5.18) as represented by parabolic function in terms of width of the layer. Since in the layer with a uniform fibre volume fraction there are no gaps between the tows, its variability along the layer is represented by the constant line as shown Figure 5.17(d). The contours of fibre volume fraction distribution in the two cases are shown in Figure 5.17(e) and (f), respectively.

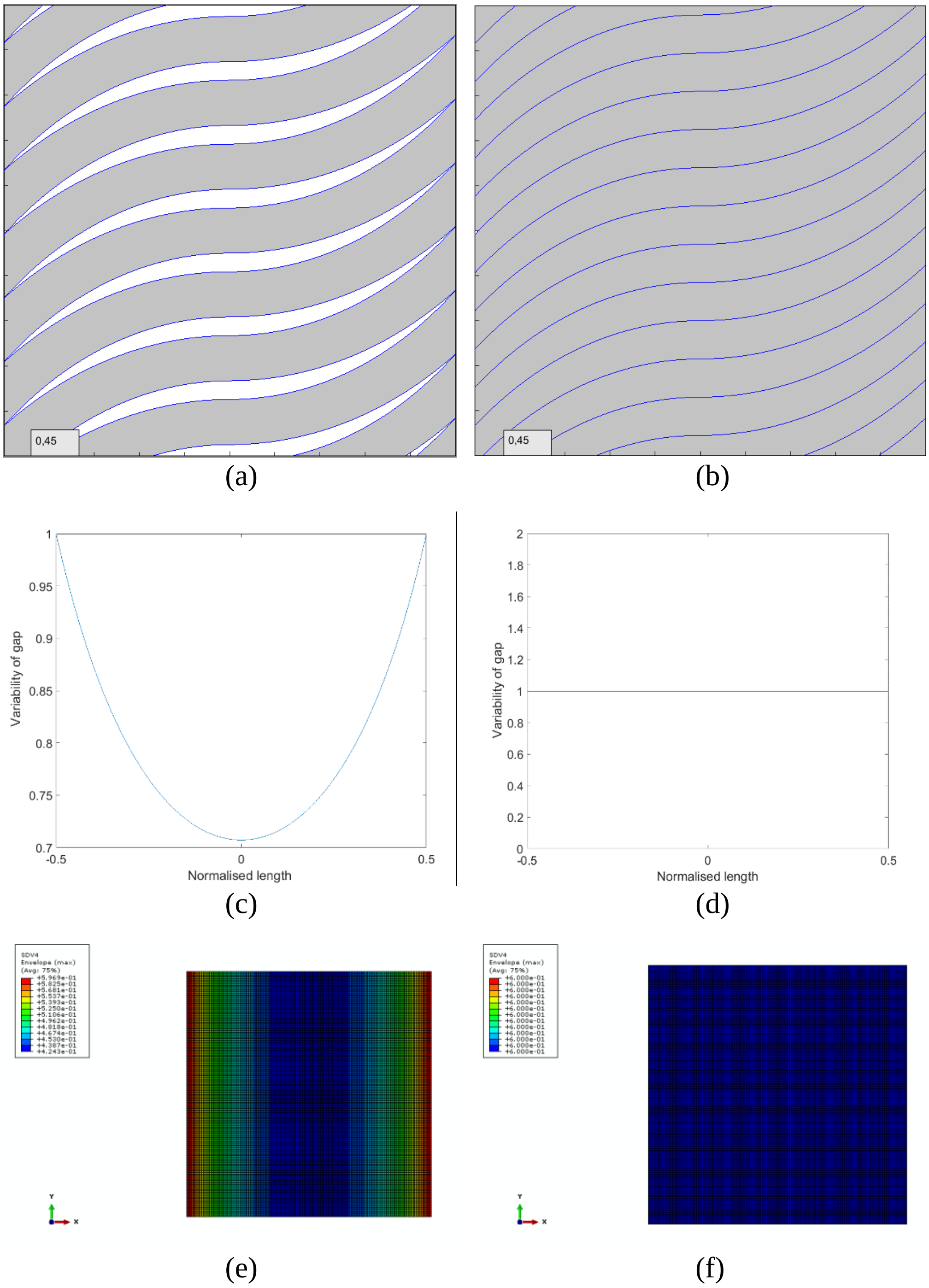

Figure 5.17: A comparison between non-uniform and uniform fibre volume fraction distribution for a lamina has T_0 =0°, T_1=45; (a) analytical pattern of non-uniform distribution, (b) a pattern of uniform distribution, (c) variability of gap of non-uniform distribution, (d) variability of gap of uniform distribution, (e) contour plot of fibre volume fraction of non-uniform distribution, (f) contour plot of fibre volume fraction of uniform distribution

The variability of a gap results in non-uniform fibre volume fraction distributions, which has an effect on the material properties, the distribution of which along the panel also becomes non-uniform. Specifically, contours of the longitudinal, transverse and in-plane shear moduli over the layer with non-uniform fibre volume fraction distribution are shown Figure 5.18(a), (c) and (e), respectively. It can be seen that all material properties vary accordingly along the width of the layer. In contrast to, the layer with uniform fibre volume fraction distribution has a constant longitudinal, transverse and in-plane shear moduli along the layer, as shown in Figure 5.18(b), (d) and (f), respectively.

To clarify how the direction of the variation of the local angles affects the equivalent stiffness, a comparison has been made for panels having a variation in the *x*- and *y*-direction with values of T_0=0° and T_0=20° as presented in Figure 5.19(a) and (b), respectively. The results shown suggest that when the difference of T_0 and T_1 is small or zero, the equivalent stiffness of the curvilinear laminates panel having a variation in the *x*- and *y*-direction are similar and approach to the overall stiffness of the straight fibre panels. When T_0 and T_1 are sufficiently different, the equivalent stiffnesses of variation in the *x*- and *y*-direction tend to diverge, and the value of stiffness of the variation in the *y*-direction is higher than that of the *x*-direction.

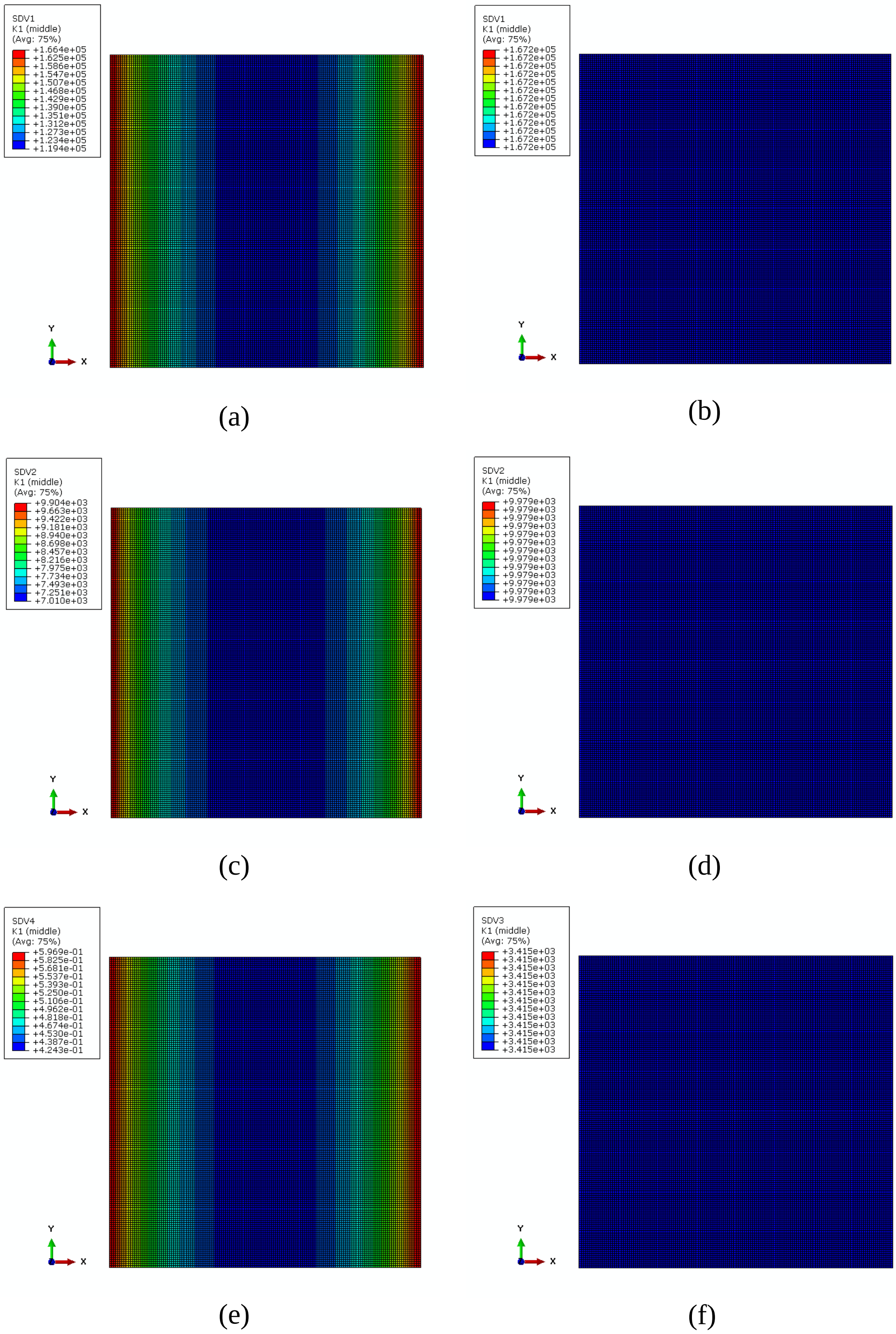

Figure 5.18: Distribution of local material properties according to the non-uniform and uniform fibre volume fraction distribution for T_0=0° and T_1=45°; (a) distribution of E_{11} of non-uniform distribution, (b) E_{11} of uniform distribution, (c) E_{22} of non-uniform distribution, (d) E_{22} of uniform distribution, (e) G_{12} of non-uniform distribution, and (f) G_{12} of uniform distribution

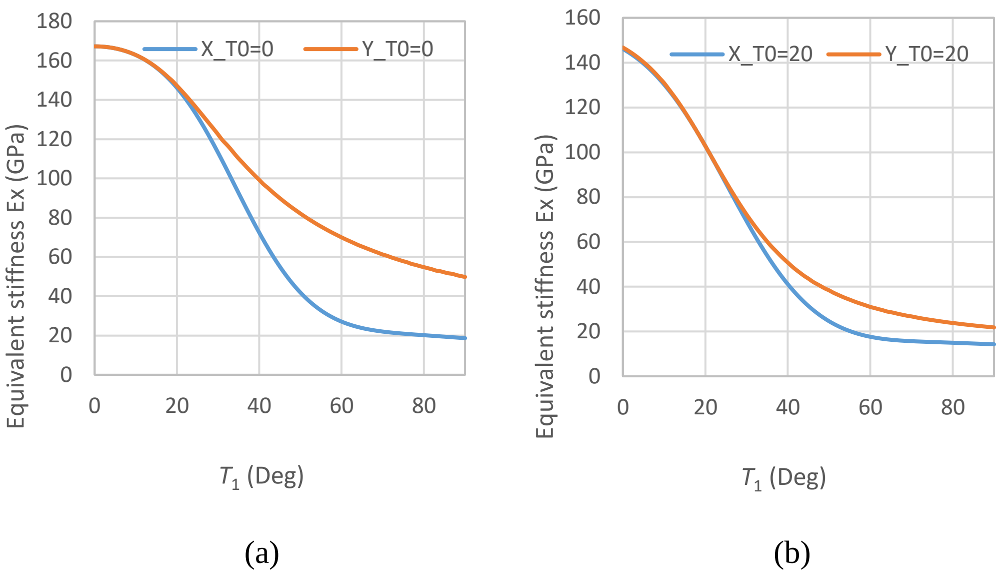

Figure 5.19: A comparison of equivalent stiffness of panels having the variation of local angles in *x*- and *y*-direction for different configurations; (a) laminates having T_0=0°, and (b) laminates having T_0=20°

Figure 5.20(a) and (b) show the effect of uniform and non-uniform fibre volume fraction distributions on the equivalent stiffness for T_0 =0° and T_0 =20°, respectively. It is easy to see that as the difference between T_0 and T_1 increases, so does the difference between the equivalent stiffnesses in panels with uniform and non-uniform fibre volume fraction distributions.

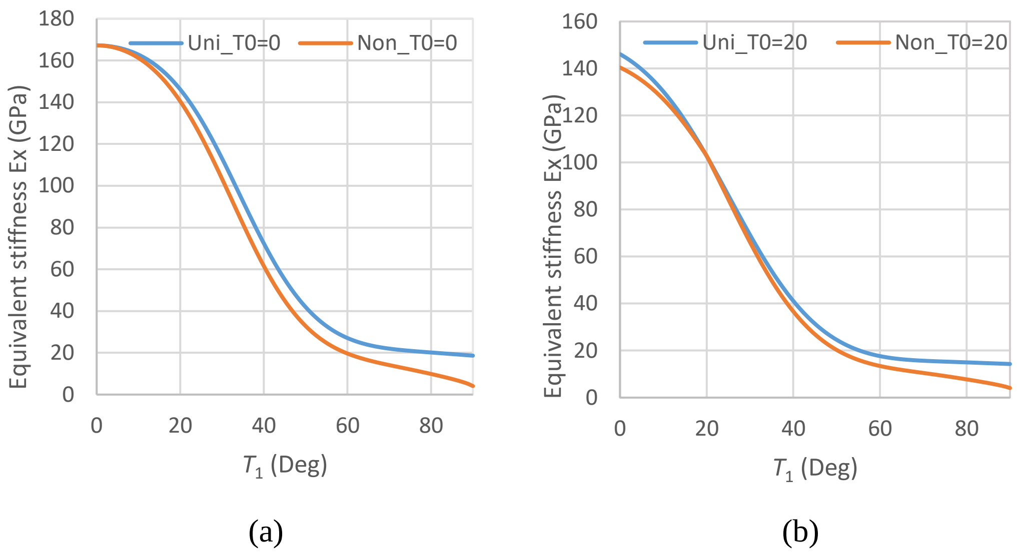

Figure 5.20: A comparison of equivalent stiffness between the uniform and non-uniform for different configurations; (a) laminates having T_0=0°and θ= $\theta(x)$ (b) laminates having T_0=20° and θ= $\theta(x)$.

In Figure 5.21 and Figure 5.22, the equivalent stiffnesses in the direction of the applied load are plotted for curved fibre panels with non-uniform fibre volume fraction distribution having the linear local angles variation in the *x*- and *y*-directions, respectively. The same conclusions regarding the performance of curved fibre panels compared to straight fibre ones apply here as were made when discussing the stiffness of laminates with uniform fibre volume fractions distribution in Figure 5.12 and 5.13. However, the values of the equivalent stiffness are smaller in this case.

For the curve corresponding to panels having T_0= 90°, one can notice an abrupt change in stiffness when T_0= T_1=90°. The explanation for this is as follows. For these types of panels, the overall stiffness is equal to the stiffness value of matrix and changes directly to the stiffness value of the straight fibre panel at T_0= T_1=90°. The reason for this is that with these configurations of local angles, gaps between the tows are along the vertical axis of the panel, which disappear rapidly when the local angles become T_0= T_1=90°. It worth noting that in this case, the size of gap does not have any influence on the stiffness value.

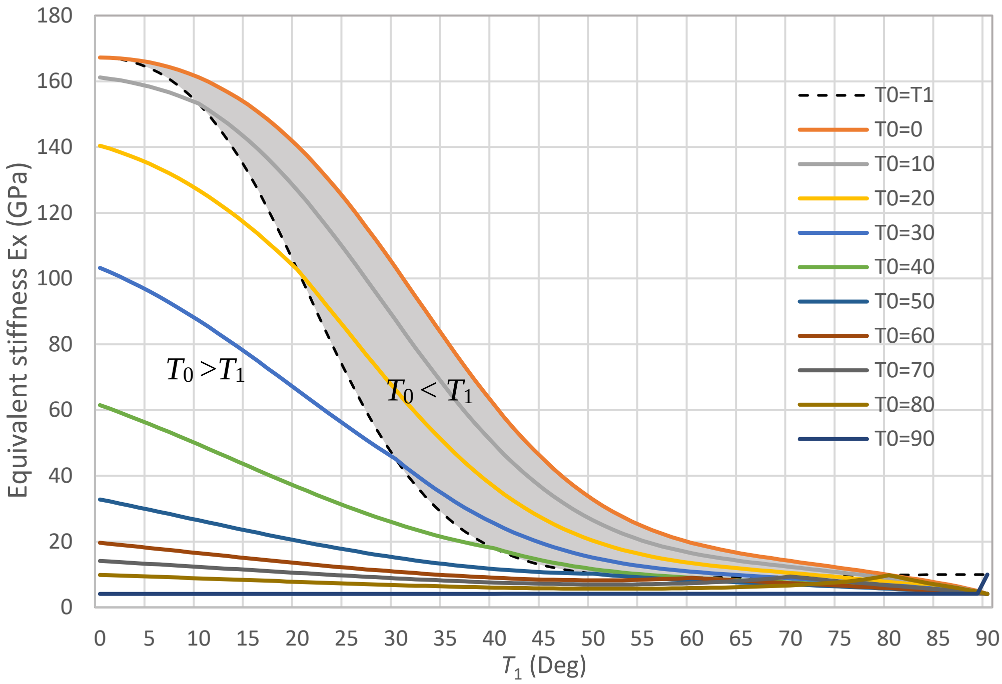

Figure 5.21: Equivalent stiffness of curved fibre panels with non-uniform fibre volume fraction distribution with local angle variation in *x*-direction under the uniaxial tension

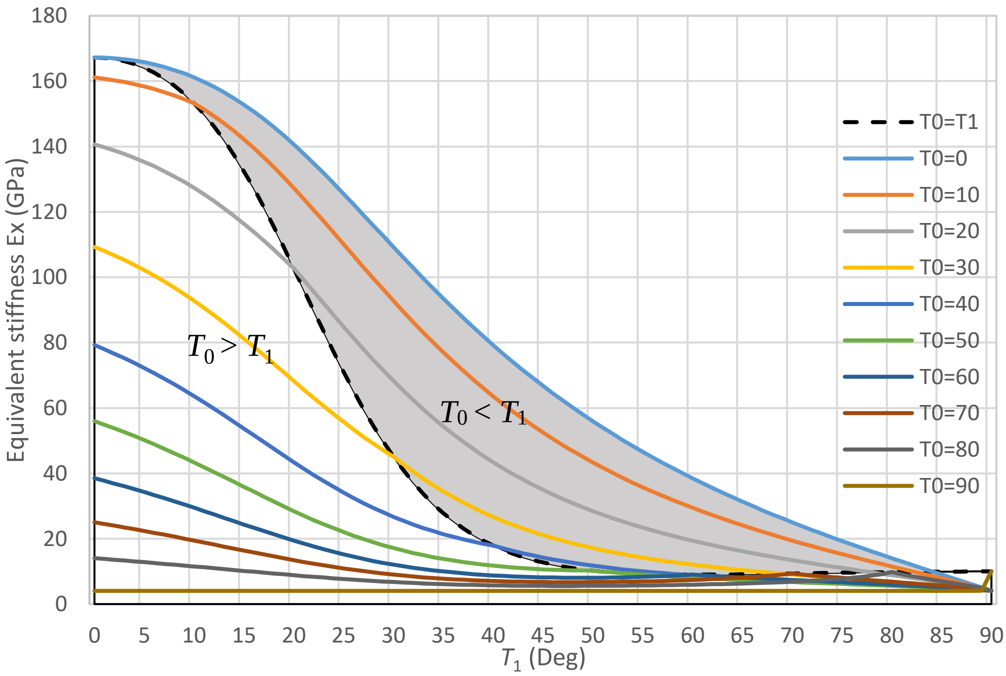

Figure 5.22: Equivalent stiffness non-uniform fibre volume fraction distribution for curved fibre panels having θ= $\theta(y)$ under the uniaxial load

5.7.4 Determining experimentally the distribution of local volume fraction and in-plane stiffness of 3D printed panel.

In addition to the automated fibre placement (AFP), a 3D printing capability of continuous fibre can be employed to steer the fibres. This technique was employed to manufacture a 3D printed carbon reinforced nylon layer as shown in Figure 5.23(a). It was fabricated by using an open-sourced Velleman K8400 RepRap 3D printer, which was customised at the University of Nottingham by Zhuo et al. (2017), who modified the printer so it could print a continuous composite tow rather than plastic. The modification was required for the continuous fibre to allow free movement for filament without clogging inside the nozzle. The new nozzle was designed to be flat instead of conical shape to flatten the printed filament.

The printed fibre as shown in Figure 5.23(a) was steered along a continuous path as shown in Figure 5.23(b) which was defined via a G-code representing a list of commands prescribing the continuous movement of the printer head of the 3D printer. G-code is created by a simple algorithm of Matlab, considering the tow width, the variation of the local angles and the dimension of the panel.

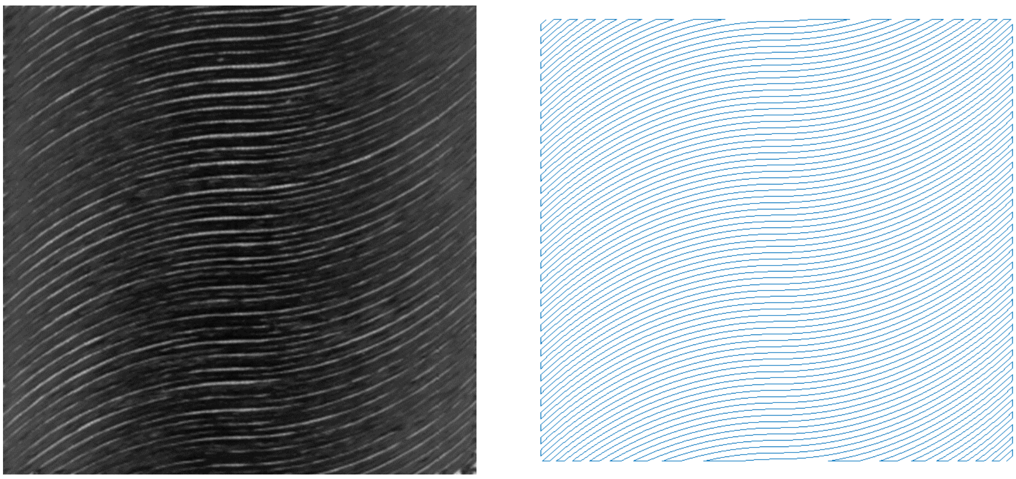

(a) (b)

Figure 5.23: 3D printed; (a) carbon fibre layer and (b) continuous path

In order to characterise the geometry of the variable gap of the 3D printed carbon fibre layer, the image processing was used. A photograph of the 3D printed layer with curvilinear tows was taken with image resolution being around 25 pixel per mm. The raw image was processed employing image processing tool in Matlab to calculate the changing in the gap width along the layer. Once the image was accessed in the image processing, it was converted into a binary image of black and white, with black and white pixels corresponding to the tows and the gap, respectively. The number of pixels of each type was calculated using Matlab code prepared specifically for the purpose. The variability of the gap was calculated as a function of *x*-coordinate according to its definition given by Equation (5.18).

The measured curve of the variability of the gap is shown in Figure 5.24. As can be seen, it is reasonably noisy, but it shows a certain trend that can be revealed by fitting it by a smooth and nonlinear function as presented by the red curve shown in Figure 5.24 of Equation (5.27). This equation of the gap width variation was implemented as a UMAT subroutine that was employed to define the distribution of the local material properties along the layer as shown in the Figure 5.25, based on the individual properties of fibre and matrix as specified in Table 5.1. With local material properties defined, the FE stress analysis can be conducted to determine the equivalent in-plane stiffness of the layer.

$$V(x) = a_1 \sin(b_1\, x + c_1) + a_2 \sin(b_2\, x + c_2) + a_3 \sin(b_3\, x + c_3) + a_4 \sin(b_4\, x + c_4) + a_5 \sin(b_5\, x + c_5) + a_6 \sin(b_6\, x + c_6) + a_7 \sin(b_7\, x + c_7) + a_8 \sin(b_8\, x + c_8) \tag{5.27}$$

where the coefficients *a*, *b* and *c* are, respectively, as follow.

a_1 = 2.771; b_1 = 0.3571; c_1 = 0.221

a_2 = -0.2742; b_2 = 2.367; c_2 = -0.2147

$a_3 = 0.2864$; $b_3 = 4.241$; $c_3 = 0.9891$

$a_4 = 0.8669$; $b_4 = 7.486$; $c_4 = 3.487$

$a_5 = 0.3835$; $b_5 = 6.078$; $c_5 = -1.543$

$a_6 = 1.148$; $b_6 = 9.713$; $c_6 = 0.6747$

$a_7 = -0.6468$; $b_7 = 12.46$; $c_7 = 0.8829$

$a_8 = -0.1641$; $b_8 = 15.19$; $c_8 = -2.111$

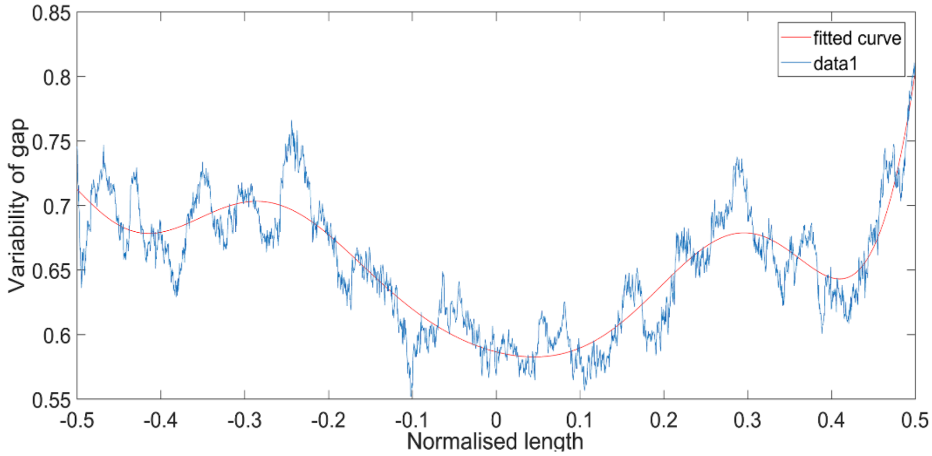

Figure 5.24: Measured and fitted gap variation in a 3D printed layer

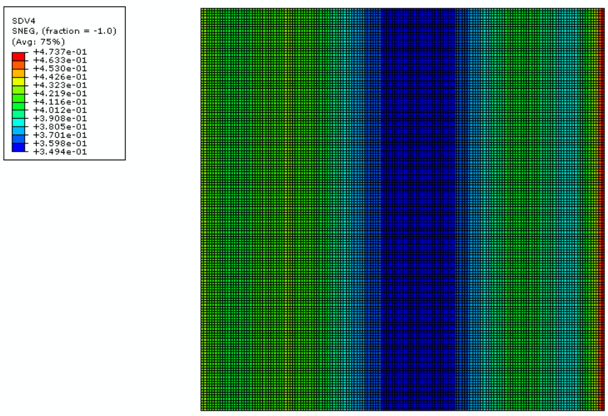

Figure 5.25: Distribution of Young's modulus in the fibre direction E_{11}

The data reported in the previous sections were obtained assuming idealised gap width variation with its typical example shown in Figure 5.17(c) and uniform fibre volume fraction distribution as shown in Figure 5.17(d). Comparing Figure 5.17(c) and Figure 5.24, it is clear that the gap width variations are different in the idealised case and in an actual 3D printed layer. In order to assess how this difference affects the mechanical performance of the layer, the in-plane stiffnesses have been calculated for the layers with uniform and non-uniform fibre volume fraction distribution and for the layer having a gap width variation as have been measured from a 3D printed layer. The comparison of stiffnesses is presented in the form of column chart in Figure 5.26. It can be seen the in-plane stiffnesses of the 3D printed layer is smaller than that of the layers the uniform and nonuniform fibre volume fraction distributions. This difference between the in-plane stiffnesses of 3D printed layer (actual gap) and non-uniform distribution (analytical gap), is 15.9% for the E_x and 13.7% for the E_y these percentage could be considered acceptable. It was related to the fitting function that used to approximate the real distribution of the variability of a gap. In addition, it can be because the 3D printed path does not match the actual one that supplied by the G-code as manufactured issues. Also, the more accurate results could be obtained by using a high resolution camera to increase the number of pixels per mm. This difference of the in-plane stiffness is due to the melted filament of carbon reinforced nylon expand more in the middle of layer than that at the edge layer where the printed filament was restricted with next filament. Another issue affects the results, the cross-section of the printed filament is not rectangular as assumed in the analytical geometry of the tow.

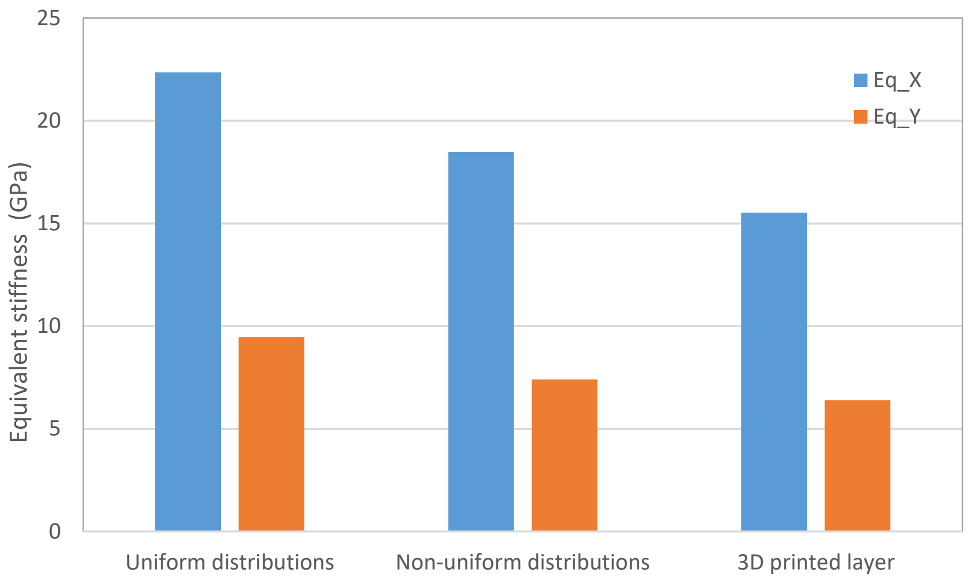

Figure 5.26: A comparison of the in-plane stiffness for different fibre volume fraction distributions

5.8 Summary

The objective of this chapter was to explore the influence the curved arrangement of the tows has on the mechanical response of square panels. The optimisation of panels with three different orders of variations of local angles have been conducted in order determining the optimum fibre path that could carry the maximum buckling load for each order of variation. The optimisation results revealed that all three orders of variation lead to an increase in the maximum buckling load compared to panels with straight tows. However, the improvement of buckling load obtained the higher-order variations (second and third-order) is only marginally larger than that obtained with a linear variation. Given the large computational costs associated with using higher-order variations, on balance, use of linear order variation was considered to be the most advantageous.

For a linear variation of local angles, the panels that could hold the maximum buckling load have a variation direction perpendicular to the direction of the applied load, and this variation has an apparent effect on the buckling load and the overall stiffness of laminates. Hence, steering the fibre according to that variation provides an improvement in structural performance due to the re-distribution of the applied loads along the laminates. Also, steering the fibre offers extra flexibility in the design process by allowing the designer to choose between different combinations of local angles of T_0 and T_1.

The gain value of the buckling load for the curvilinear fibre laminates is influenced by the distribution of local stiffness. Consequently, it is influenced by the aspect ratio of the overall stiffnesses, E_x/E_y. The overall stiffness of panels that have the variation of local angles in the direction of the applied load could be represented as a serial combination of the stiffness of springs, whilst for panels that have variation in the direction perpendicular to the applied load could be represented by a parallel combination of the stiffness of springs. The calculations of the overall stiffness of different configurations could provide a reasonable approximation to predict the overall stiffness of any mixed laminate as approach followed in a ten-percent rule.

One more aspect of employing curved fibre that was explored is the non-uniformity of fibre volume fraction distribution due to the presence of gap of variable width between the adjacent tows. Consequently, this results in non-uniform distribution of the material properties over the panels. It has been shown that this reduces the overall stiffness is detrimental to the ability of the structure to resist the buckling load, compared to the analysis where a uniform fibre volume fraction was assumed. However, the gap between the adjacent tows is a genuine feature in curved fibre laminates, as has been demonstrated by producing a layer with curved fibres employing 3D printing rig. Therefore, it must be accounted for in the analyses of curved fibre laminates when considering their practical applications.

6 Optimisation of steered fibre on the cylindrical shells

6.1 Introduction

One of the advantages of employing the fibre reinforced composites in engineering design is that their stiffness can be tailored, through which more efficient designs can be achieved. The use of composites can improve the structural performance in terms of stiffness and save the weight of the structure. Steering the fibre is employed to produce composite part of a cylindrical shape, which may represent the fuselage of aircraft, appropriate placement of the fibres can improve the resistance to bending, which is a typical loading mode. In addition to cylindrical parts with a circular cross-section, some structures, such as fuel tanks and wings, can be idealised as cylinders with elliptical cross-sections.

In this chapter, circular and elliptical cylinder shell models with the curved fibre reinforcements are analysed to predict the maximum buckling load under constant bending moment as an application of the variable stiffness laminates. Due to a spatial change of the local angles from point to point in the circumferential direction of cylindrical shells, an enhancement for the structural performance in terms of the resistance of flexural load that varies along the circular cross-sectional area can be achieved through appropriate design. For the elliptical cross-sections, there is a larger radius of curvature with a flat portion that could be expected to buckle more than that of the small curvature part, causing an apparent reduction in the buckling capacity as compared with circular section.

6.2 Steered fibre orientation on cylindrical shells

The path of steered fibre in the cylindrical coordinate system of cylindrical shells, schematically shown in Figure 6.1. The position of any point, *P*, on this path can be expressed in terms of the distance, *R*, from a reference axis, which was chosen to be an *x*-axis, the angle θ, and the axial coordinate *x*. The intersection of the tangent to the fibre paths on the shell surface with the axial directions is defined by the fibre local angle φ. Referring to Figure 6.1, the fibre local angle, φ, can be expressed at any θ and *x* as follows .

$$R\frac{d\theta}{dx} = \tan\varphi \tag{6.1}$$

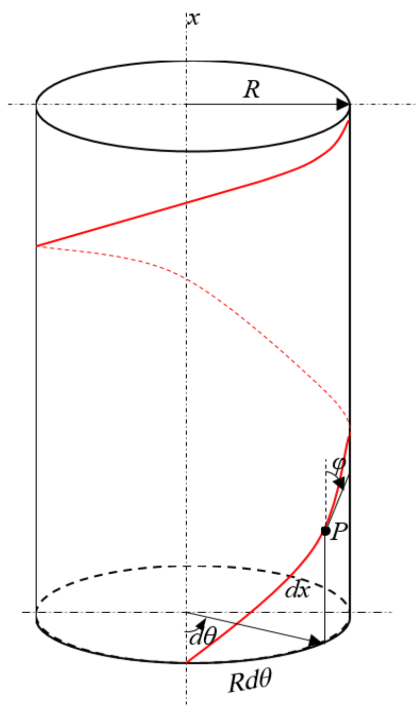

Figure 6.1: Schematic representation of the cylindrical coordinate system for prescribing steered fibre path

Similar to the definition of local fibre orientation as was addressed in the previous chapter for composite panels, the fibre local angles in cylindrical shells can have different degrees of nonlinearity. In this chapter, only the linear variation of local angles is considered. In cylindrical coordinates, the directions of variation of local fibre angle variation can be classified into the axial and the circumferential directions of cylinder.

6.2.1 Axial linear variation of fibre local angles cylindrical shell surface

The linear local fibre angle variation along the length of the shell can be employed to describe multiple segments of local angle variation along the length of the cylindrical shell, in order to expand the design space. Every segment can be considered as a separate cylinder with its own local angles. At the boundary between every two segments, in order to satisfy the continuity and ensure the manufacturability, the local angles can be defined to be identical according to (Blom, 2010a)

$$\varphi(x) = T_i + (\, T_{i+1} - T_i)\, \frac{x - x_i}{x_{i+1} - x_i} \tag{6.2}$$

where *i* is the number of a segment along the length of the cylinder, T_i is the local fibre angle at x_i location along the axial direction.

The circumferential coordinate of the fibre path in terms of the *x*-coordinate can be obtained by substituting Equation (6.2) in (6.1) to be as follows(Blom, 2010a).

$$\theta(x) = \frac{-L}{R\,N(T_{i+1} - T_i)} \ln |\cos \varphi(x)| + \frac{L}{R\,N(T_{i+1} - T_i)} \ln (\cos T_i) \tag{6.3}$$

where *L* and *N* are the length of the cylindrical and the total number of segments, respectively.

6.2.2 Circumferential linear variation of local fibre angles

The linear variation of fibre local angle φ in the circumferential direction is defined as a function of the circumferential coordinate θ (Blom, 2010a) as follows.

$$\varphi(\theta) = T_i + (T_{i+1} - T_i)\,\frac{\theta-\theta_i}{\theta_{i+1}-\theta_i} \tag{6.4}$$

where i is the number of the shell segments along the circumference, T_i is the local fibre angle within the respective segment at the θ_i location along the circumference. For instance, a cylindrical shell, as shown in, Figure 6.2 has been partitioned into six segments on the left part and the same partitioning was applied to the right part of the shell, to increase the flexibility of design process of fibre path.

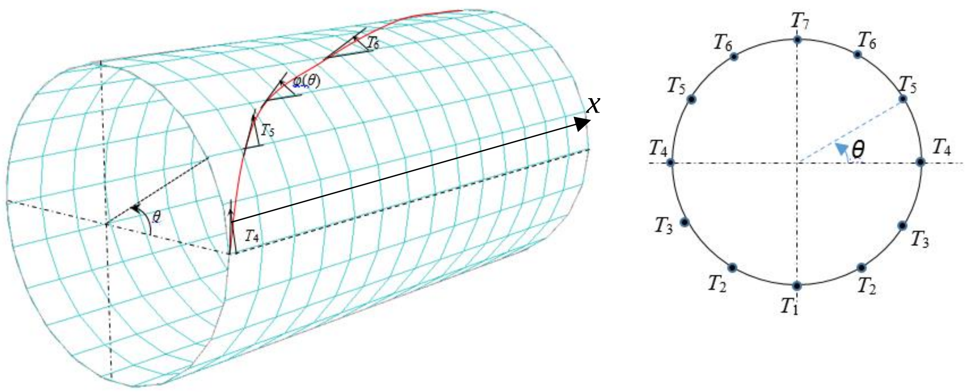

Figure 6.2: Segments division and fibre path definition.

By substituting Equation (6.4) into Equation (6.1), the axial coordinate of the tow at any point on the circumference will be as follows (Blom, 2010a).

$$x(\theta) = R\,\frac{\theta_{i+1}-\theta_i}{(T_{i+1}-T_i)}\,[\ln\sin\varphi(\theta) - \ln\sin T_i] \tag{6.5}$$

The circumferential distance of the tow centre line on the surface of the shell at any θ is as follows.

$$C = R\theta \tag{6.6}$$

Based on the trigonometric relations, the dimension W of the steered tow in the axial direction at any point on the circumference, as shown in Figure 6.3, is given by

$$W(\theta) = \frac{b}{\sin\ \varphi(\theta)} \tag{6.7}$$

where the b is the tow width.

The upper edge of the tow x_u is defined as follows.

$$x_u = x(\theta) + W/2 \tag{6.8}$$

whilst the lower edge x_l is given as follows.

$$x_l = x - W/2 \tag{6.9}$$

Then the lower edge of the adjacent fibre tow with the coordinate of the centre line x_{l+1} is given as follows.

$$x_{l+1} = x - \frac{W}{2} + V_R \tag{6.10}$$

where V_R is the vertical distance of the representative volume element (RVE) of the tow and the gap as shown in Figure 6.3. It is defined as follows.

$$V_R = \frac{b}{\sin\,(T_{max})} \tag{6.11}$$

where the T_{max} is the maximum value of the local angles, T_{i}. Using this value allows to avoid overlapping of the tows.

The percentage of the vertical distance of tow to the vertical distance of the RVE at any point is defined as follows.

$$Pre\_vol(\theta) = \frac{W}{V_R} \tag{6.12}$$

Finally, the local fibre volume fraction in RVE is obtained as follows.

$$V_{local}(\theta) = Pre\_vol * V_{tow} \tag{6.13}$$

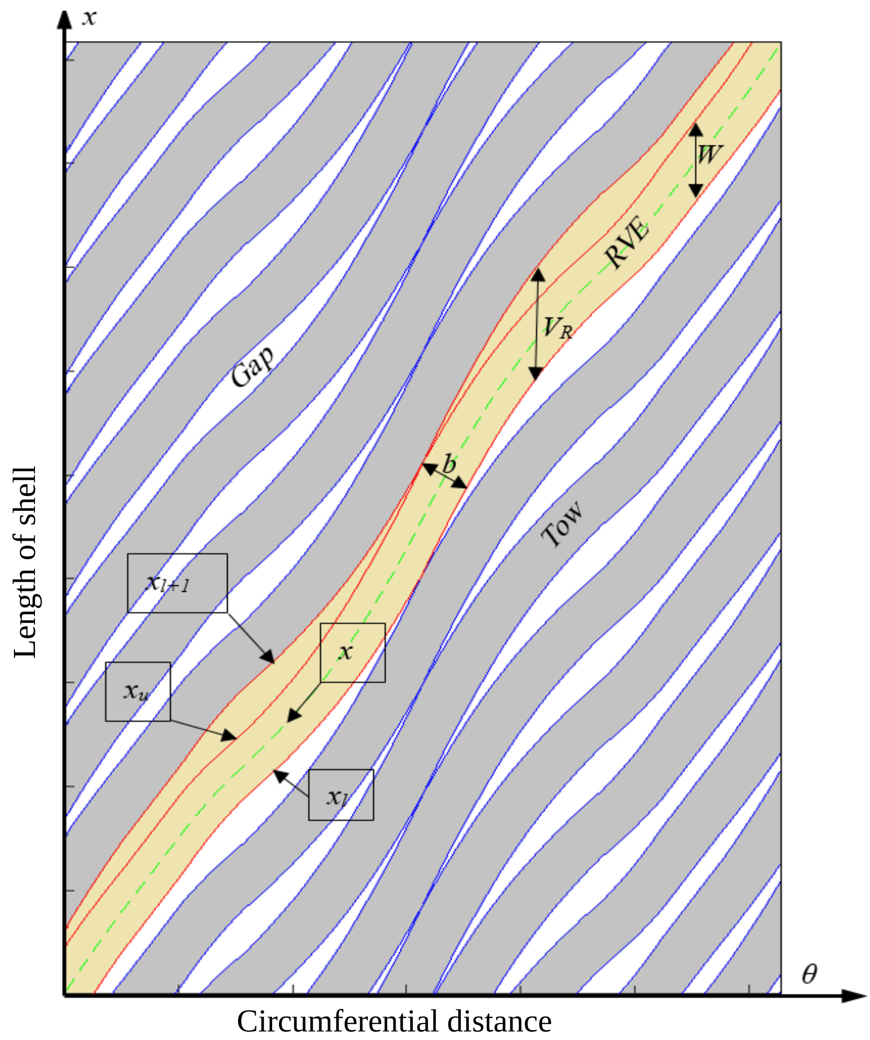

Figure 6.3: Characteristic dimensions of the curved tow and its gap on the unfolded circular cylindrical shell

6.3 Formulation of the optimisation problem

Cylindrical shells with circular and elliptical cross-sections have been optimised to determine the optimum fibre paths with which the curvilinear laminate can sustain the maximum buckling load under a pure bending moment. The local fibre angle in each lamina was a function of the circumferential coordinate θ. This can help to improve the structural performance as a result of bending moment results in loads to vary around the circumference of the cylinder.

The purpose of this design study is to find the optimum vector of the values of local angles describing a fibre path on a cylindrical shell surface to increase its ability to sustain maximum buckling load. The optimisation framework as was employed in the present study was described in Chapter 4.

The circumference of the cylindrical shell has been divided into 12 segments to offer more flexibility in the design of the curved path, as shown in Figure 6.2. Further partitioning of the circumference will make the problem more computationally expensive. It can be considered as a balance between the computational efforts and design flexibility. Therefore, 14 design variables are required to define each layer in the laminated structure. However, the local angle at the common point between two segments is the same in order to achieve the continuity, and orientation of segments of the laminated structure was assumed symmetric as shown in Figure 6.2. This reduced the number of required design variables to 7. These variables are presented as a vector of the local angles $T_{i,}$. The value of these variables identifies the fibre path according to Equation (6.5) of the linear variation for each segment.

Five different layups of 16 layers were considered for circular and elliptical laminated cylindrical shells, defined as $[\theta/-\theta/\theta/-\theta/-\theta/\theta/-\theta/\theta]_s$, $[0°/\theta/90°/-\theta/-\theta/90°/\theta/0°]_s$, $[0°/\varphi/90°/-\varphi/-\varphi/90°/\ \varphi/0°]_s$, $[-\varphi/45°/\ \varphi/-45°/-45°/\ \varphi/\ 45°/-\varphi]_s$, and $[\varphi/-\varphi/\ \varphi/-\varphi/-\varphi/\ \varphi/\ -\varphi/\ \varphi]_s$. The first two layups represented a straight fibre laminate of constant stiffness (CS), while the remaining three corresponded to curved fibre laminates of variable stiffness (VS).

Another issue to be addressed when analysing laminated circular cylindrical shells, is the variable gap width, which can have a significant effect on the buckling performance, as has been shown in Section 5.7.2 of Chapter 5. Therefore, the optimisation process was repeated for the same layup as defined above, but with non-uniform fibre volume fraction distributions in the laminae. The effect of non-uniform fibre volume fraction distributions for the elliptical cylindrical shells was not studied, since the radius of the elliptical shell is a function of circumferential coordinates.

The mathematical optimisation problems of maximising the critical bending moment (M_{cr}), with a constraint of applied buckling load being lower than that could cause material failure (M_f), was defined as:

$$\begin{aligned} &\text{Maximise} && \textit{buckling load} \ (M_{cr}) \\ &\text{Subjected to} && 90° \geq T_i \geq 0° \quad \text{for } i = 0, 1\ldots\ldots, 7 \\ & && M_f > M_{cr} \end{aligned} \tag{6.14}$$

6.4 The finite element model

In order to determine the buckling load of cylindrical shells having a curved fibre format, the finite element package Abaqus/Standard (2017) was used. The local angles of each point in the shell were calculated according to Equations (6.2) and (6.4). They were implemented as the user-defined ORIENT subroutine, which allows to define material orientation at each integration point of the shell element. With material orientation defined via ORIENT subroutine, the stress state can be output for each layer individually, based on which the failure index per each layer can be calculated. In this respect, it is different from UGENS subroutine that was employed in the study of Blom et al. (2010b), which passes the stiffness (ABD matrix) of laminate shell section for each integration point in Abaqus, and hence does not give any indication about the features of each layer.

To account for the non-uniform fibre volume fraction distribution, the effect of variability of the gap was defined by introducing the ratio of the tow area to the total area of the gap and tow combined, using which the local fibre volume fraction as given by Equation (6.13). The UMAT subroutine was used to implement the constitutive model based on the local mechanical properties varying with the local fibre volume fraction. The rule of mixtures was used to calculate the local mechanical properties of composite from the constituent properties as defined in Table 6.1.

In the FE model, a laminated cylindrical shell with 16 layers and dimensions of the length and diameter of 500mm, were used. The bending moment was applied at the reference point, which was connected to the nodes at the one edge of the shell through the multipoint constraint (MPC), as available in Abaqus, as shown in Figure 6.4. Therefore, edges remain circular during deformations to enable following the elementary beam theory, and it was free to move along the axial direction of the cylinder. Another end of the cylinder was simply supported. The model was meshed with S8R5 shell elements having 8 nodes, 4 integration points and five degrees of freedom in each node.

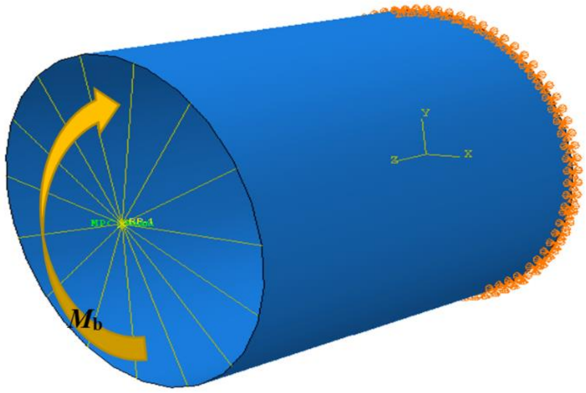

Figure 6.4: Loading conditions and the multipoint constraints for a cylindrical shell

For the elliptical cylindrical shells, the horizontal axis *a* and vertical axes *b* were defined to ensure that the perimeter of the elliptical cross-section is identical to that of a circular cylindrical shell. Two types of the elliptical cylindrical shell were analysed as shown in Figure 6.5. In the first one, the horizontal axis *a* =300mm was larger than the vertical one *b* =194.33mm, whilst in the second, the horizontal axis *a*=194.33mm was smaller than the vertical one *b*=300mm. Each elliptical cylindrical shell was divided into twelve segments, as shown in Figure 6.5, the same as the circular cylindrical shell.

(b)

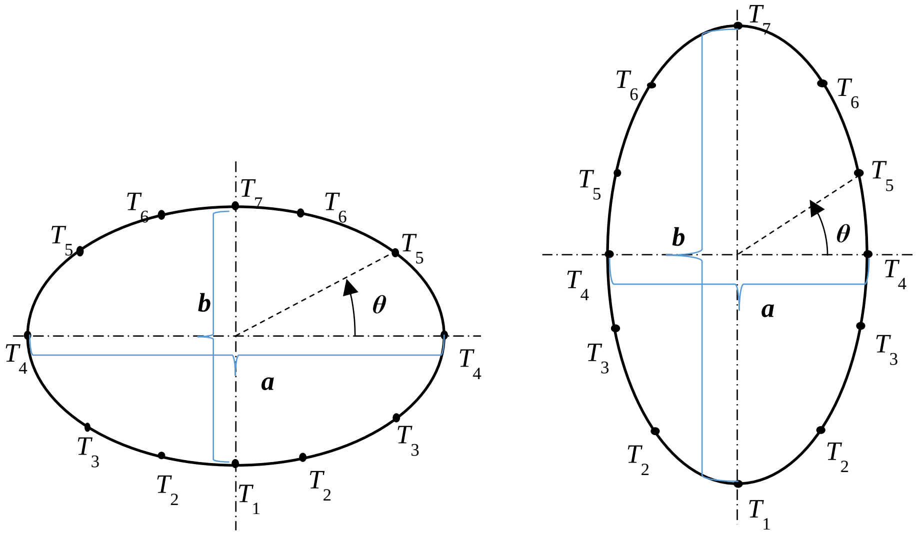

(a)

Figure 6.5: Two types of the elliptical cross-sections with the segmentation of the local angles; (a) *a*>*b*, and (b) *a*<*b*

Table 6.1: Material properties of the constituents (Kaddour et al., 2013)

Property	Glass fibre	8552 epoxy
Longitudinal modules E_{11} (GPa)	74	4.08
Transverse modules E_{22} (GPa)	74	-
Transverse modules E_{33} (GPa)	74	-
In-plane shear modules G_{12} (GPa)	30.8	1.478
Transverse shear modules G_{23} (GPa)	30.8	-
Major Poisson's ratio v_{12}	0.2	0.38
Fibre volume fraction of tow	60%	
Thickness of layer (mm)	0.125	

6.5 Results and discussion

6.5.1 The buckling response of circular cylindrical shells

Before analysing the structural performance, a mesh sensitivity study was conducted to identify the appropriate mesh size of the structure. In the finite element analysis, the mesh convergence can be considered as a verification. As it can be seen in Figure 6.6, where the buckling load is plotted against the number of elements, the curved fibre model requires more number of elements for the mesh to be converged as compared with the straight fibre model.

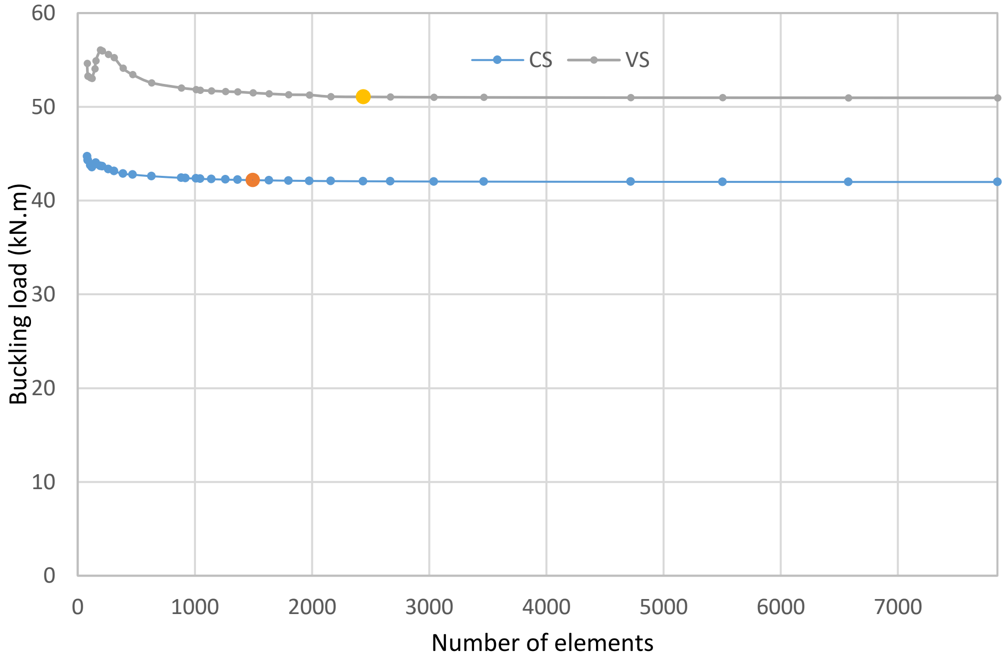

Figure 6.6: Mesh convergence of the buckling load for the variable stiffness and constant stiffness laminate

The optimisation results of the optimum fibre path which only included the failure load M_f of material as a constraint are presented in Table 6.2 and 6.3 for the uniform and non-uniform fibre volume fraction distributions, respectively. In both cases, same five layups were considered, as defined in Section 6.3, which included both the CS laminates (C0 and C1) as well as VS laminates (C2, C3 and C4). The optimum tow path corresponding to case C0 with θ =72° is shown in Figure 6.7. The optimum fibre path for case C1 with θ =45° is shown in Figure 6.8, which indicates that the optimised laminate is essentially quasi-isotropic (QI). Both cases C0 and C1 are considered as benchmarks to which VS laminate cases will be compared.

The optimum results obtained through FE modelling for cases C0 and C1 were compared with a theoretical estimation of buckling load that is also given in Table 6.2. The latter was obtained using the expression for critical buckling load derived by Fuchs et al. (1997), who studied laminated cylindrical shells under buckling load. The analytical expression for buckling load was as follows (Fuchs et al., 1997)

$$M_{cr} = 2\pi R\sqrt{E_\theta H D_{11}} \tag{6.15}$$

where D_{11} is the axial bending stiffness of the laminate, E_θ is the laminate's effective circumferential stiffness, H is the laminate thickness, and R is the radius of the cylinder.

As can be seen from data in Table 6.2, a good agreement was obtained for cases C0 and C1 between the theoretical estimation of buckling load and the finite element results.

For cases, C2, C3 and C4 in Table 6.2, the optimum fibre paths on the surface of the cylindrical shell are given in terms of the coefficients T_i. The optimum fibre path of C2, C3 and C4 on the unfolded cylindrical shell are presented in Figure 6.9, 6.10 and 6.11, respectively. It can be seen that at the keel region of the cylinder the fibre paths are in the axial direction to sustain more tensile load, whilst in the crown region that resisting the compressive load, the local fibre angles are 45° or more. In

Figure 6.12 the linear variation of the local angles along the circumference of a cylindrical shell have been presented for all five cases.

The optimum results of the non-uniform fibre volume fraction distributions are shown in Table 6.3. The maximum buckling loads for the C2, C3 and C4 are smaller than those for their respective counterparts in Table 6.2. It is a result of the stiffness reduction due to the presence of variable gap as predicted in Section 5.7.3 of Chapter 5. Specifically, because of the non-uniform distribution of fibre volume fraction, the material properties vary locally from point to point. Therefore, the stiffness is reduced locally as compared with uniform fibre volume fraction distributions.

Table 6.2: Optimisation results of the circular cylindrical shells having a uniform fibre volume fraction distributions

Cases	Stacking sequence for the laminated circular cylindrical shell	Buckling load (kN.m)	
		FEM	Theoretical estimation
C0	$[\theta/\text{-}\theta/\ \theta/\text{-}\theta/\text{-}\theta/\ \theta/\text{-}\theta/\ \theta]_s$, θ=72°	34.5023	31.633
C1	$[0°/\theta/90°/\text{-}\theta/\text{-}\theta/90°/\theta/0°]_s$, θ=45°	42.0107	40.856
C2	$[0°/\varphi/90°/\text{-}\varphi/\text{-}\varphi/90°/\ \varphi/0°]_s$ T_1=1°, T_2=1°, T_3=65°, T_4=1°, T_5=23°, T_6=49°, T_7=53°	50.9622	-
C3	$[\text{-}\varphi/45°/\ \varphi/\text{-}45°/\text{-}45°/\ \varphi/\ 45°/\text{-}\varphi]_s$ T_1=1°, T_2=0°, T_3=50°, T_4=0°, T_5=18°, T_6=90°, T_7=90°	47.0915	-
C4	$[\varphi/\text{-}\varphi/\varphi/\text{-}\varphi/\text{-}\varphi/\ \varphi/\ \text{-}\varphi/\ \varphi]_s$ T_1=1°, T_2=19°, T_3=63°, T_4=24°, T_5=45°, T_6=67°, T_7=74°	49.0192	-

Table 6.3: Optimisation results of the circular cylindrical shells having a non-uniform fibre volume fraction distributions

Cases	Stacking sequence for the laminated circular cylindrical shell	Buckling load (kN.m)
C0	$[\theta/\text{-}\theta/\ \theta/\text{-}\theta/\text{-}\theta/\ \theta/\text{-}\theta/\ \theta]_s$, θ=72°	34.5023
C1	$[0°/\theta/90°/\text{-}\theta/\text{-}\theta/90°/\theta/0°]_s$, θ=45°	42.0107
C2	$[0°/\varphi/90°/\text{-}\varphi/\text{-}\varphi/90°/\ \varphi/0°]_s$, T_1=48°, T_2=50°, T_3=80, T_4=53°, T_5=48°, T_6=48°, T_7=49°	41.7326
C3	$[\text{-}\varphi/45°/\ \varphi/\text{-}45°/\text{-}45°/\ \varphi/\ 45°/\text{-}\varphi]_s$ T_1=29, T_2=54, T_3=63, T_4=58, T_5=45, T_6=60, T_7=77	35.653
C4	$[\varphi/\text{-}\varphi/\ \varphi/\text{-}\varphi/\text{-}\varphi/\ \varphi/\ \text{-}\varphi/\ \varphi]_s$ T_1=36, T_2=51, T_3=49, T_4=39, T_5=52, T_6=61, T_7=68	37.865

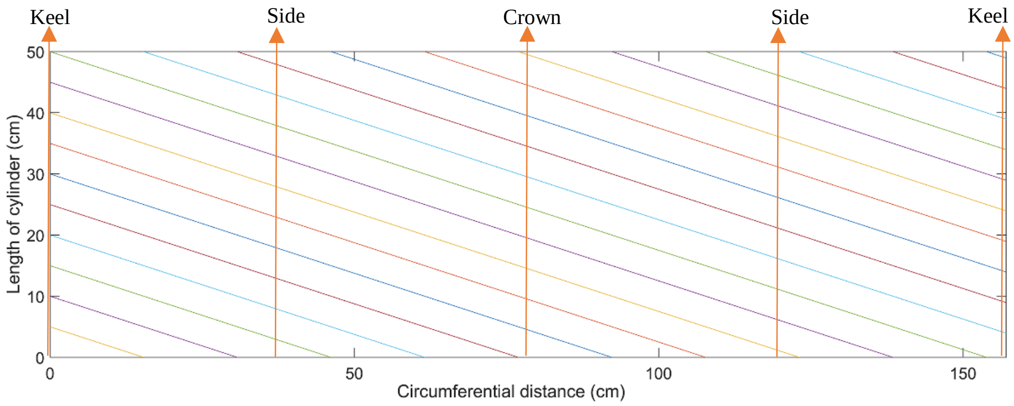

Figure 6.7: Optimum fibre path of case C0 of a single layer

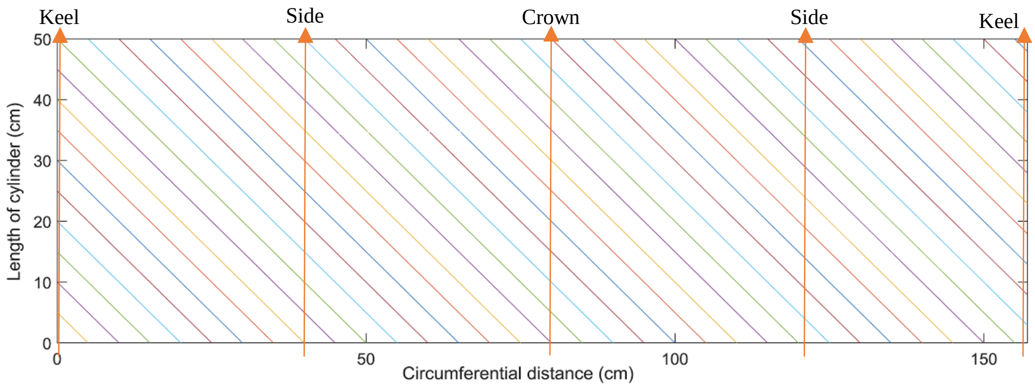

Figure 6.8: Optimum fibre path of case C1 of a single layer

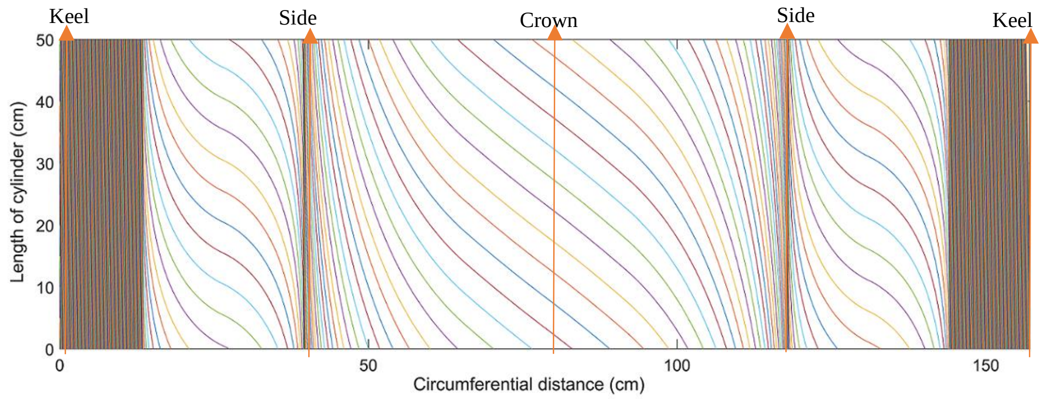

Figure 6.9: Optimum fibre path of case C2 of a single layer

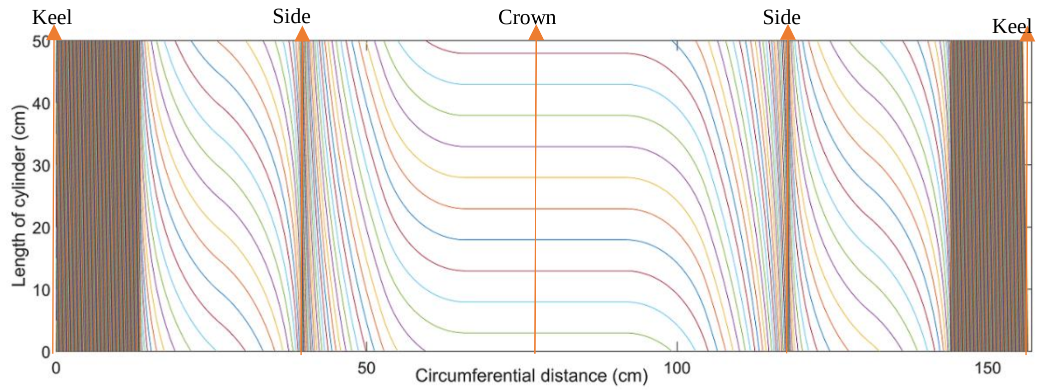

Figure 6.10: Optimum fibre path of case C3 of a single layer

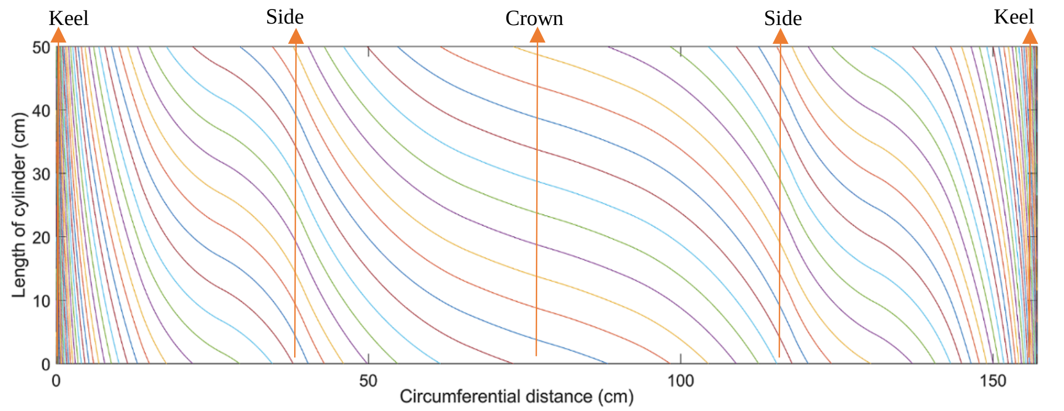

Figure 6.11: Optimum fibre path of case C4 of a single layer

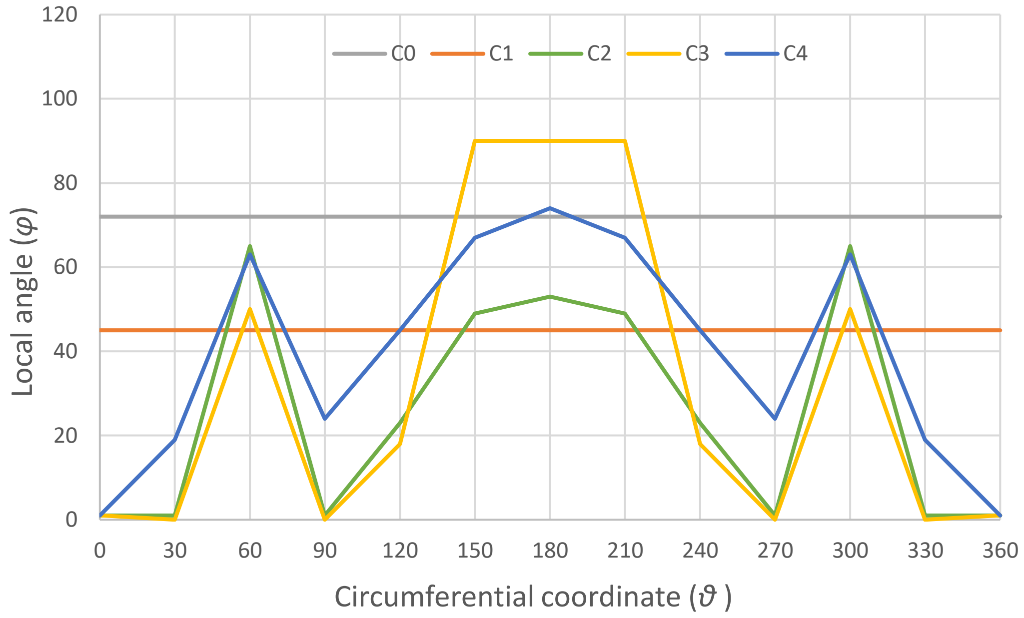

Figure 6.12: Variation of the local angles in circumferential coordinate

The variation of axial strain ε_z along the circumference of laminated cylindrical shells having uniform fibre volume fraction distributions in all five cases considered is shown in

Figure 6.13. It can be seen that the strain variations of all five cases resemble a sine wave. The highest tensile strain was predicted at the keel of the cylinder, while the highest compressive strain (absolute value) is at the crown. It is worth noting that circumferential distance along which the strain is compressive is larger for VS laminated cylinders than that for the CS laminated cylinder.

The variation of sectional force in the axial direction N_x as shown in Figure 6.14 is associated with both the local stiffness and the axial strain variation along the circumference of the cylinder. As can be seen, for VS laminates, the tensile load is higher than that for the CS laminates as a result of the higher local stiffness in this region. Because of the variation of the local angles that produce variable stiffness, the variation of the axial force along the circumferential distance in the

VS laminates as shown in Figure 6.14 deviated from a sine wave shape predicted for the CS laminates. One can see there was an expansion in the area that resists a compressive axial force for the VS laminates. It could be considered as an indication of the stiffness variation of the laminated cylindrical shell.

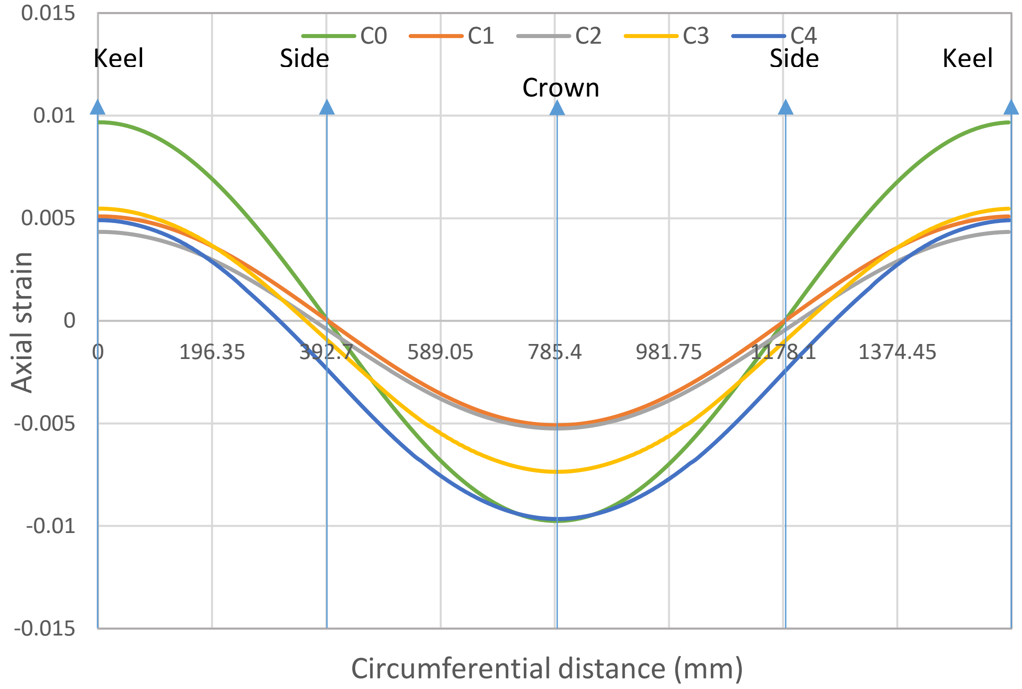

Figure 6.13: Axial strain of different cases of circular cylindrical laminated shells

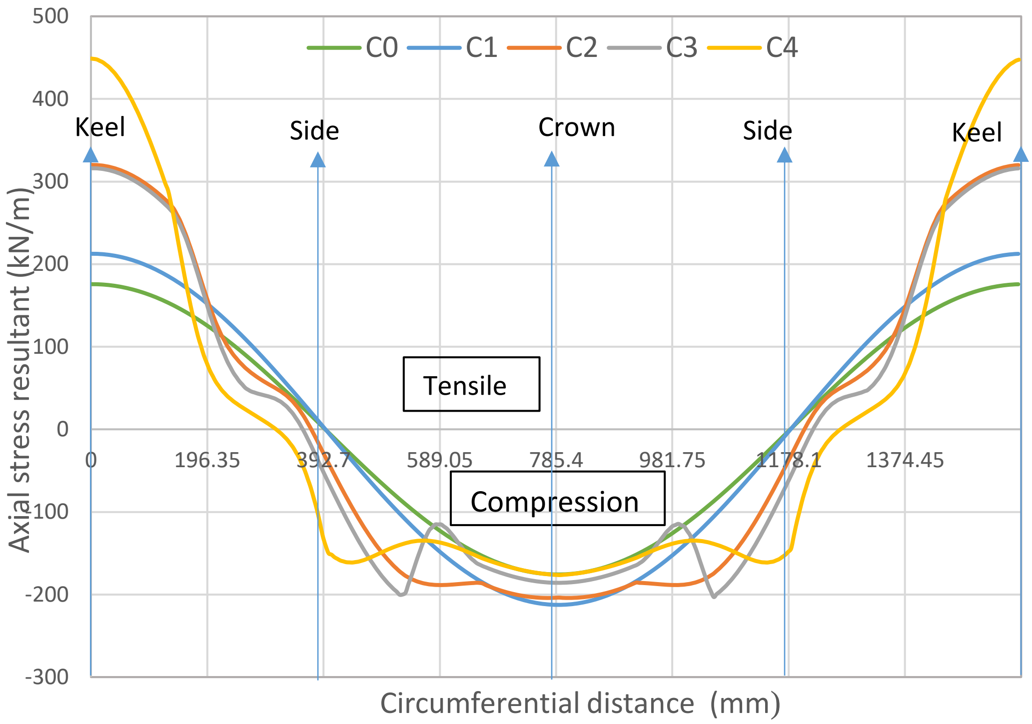

Figure 6.14: Axial stress resultant of different cases of circular cylindrical laminated shells

As shown in Figure 6.15(a) and (b), the most apparent difference between the first buckling modes of case C1 (CS) and case C2 (VS) is an area on the cylindrical shells that undergoes buckling. It can be seen such surface area in the former case is smaller than that in the latter case. Therefore, the value of the buckling load of the laminated cylindrical shells is affected by the size of that surface area that resists buckling load.

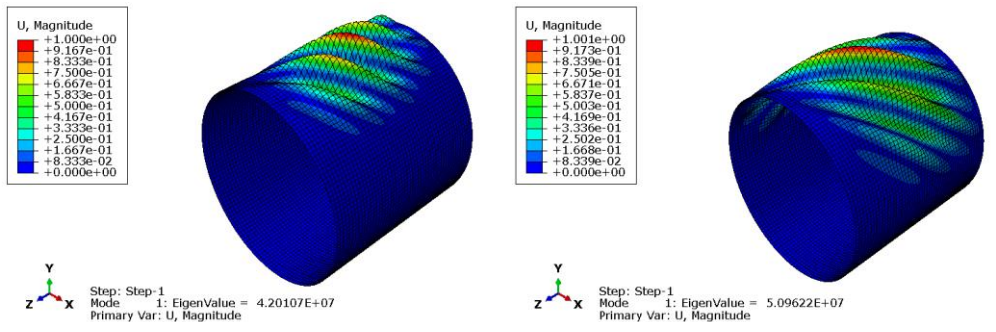

(a) (b)

Figure 6.15: Buckling mode of laminated cylindrical shells; (a) case C1 (CS), and (b) case C2 (VS)

6.5.2 Buckling performance of circular cylindrical shells in terms of the directions of the applied bending moment

For all cases mentioned above, the bending moment was applied to the cylindrical shells in one specific direction, which could be determined based on the right-hand rule. However, the effect of different directions bending moment could give a clear picture of the improvements or losses in the buckling capacity in VS cylinders having steered fibres in a circumferential direction. In other words, the fibre path that offers an improvement of buckling load when load is applied in a certain direction can be detrimental to buckling performance when the direction of the load is reversed. In particular, such loading scenarios are encountered in aerospace structures such as fuselage and wing, during the landing and take-off.

The effects of applying load in different directions are assessed based on the results shown in Figure 6.16 and 6.17. The variations of buckling loads with polar coordinates that represent the direction of the applied bending moment are presented. In Figure 6.16, buckling load in CS circular cylindrical shell (case C1) is compared with that in VS circular cylindrical shell (case C2). One can see that in the former case the buckling load was constant in all directions of loading, whilst in the latter case, there was a gain in the buckling load for specific directions, whilst overall, the reduction in buckling load is apparent as compared with case C1. In this case, same as in all the cases to follow, the buckling load in polar plot varies from a maximum to minimum value symmetrically since the local fibre angles are symmetrically arranged with respect to the vertical axis as shown in Figure 6.2.

Figure 6.17 shows a comparison between cases C0 and C4 cases with fibre orientation as specified in Table 6.2. Same as before, the buckling load for the entire range of directions in polar coordinates is constant for CS shell (case C0), whilst for case C4 that was of the same layup as C0 but with curved fibre laminates. It can be seen that for the cases C2 and C4 shown in Figure 6.16 and 6.17, respectively, the maximum value of buckling load was achieved when the axis of rotation of bending moment was at 180°.

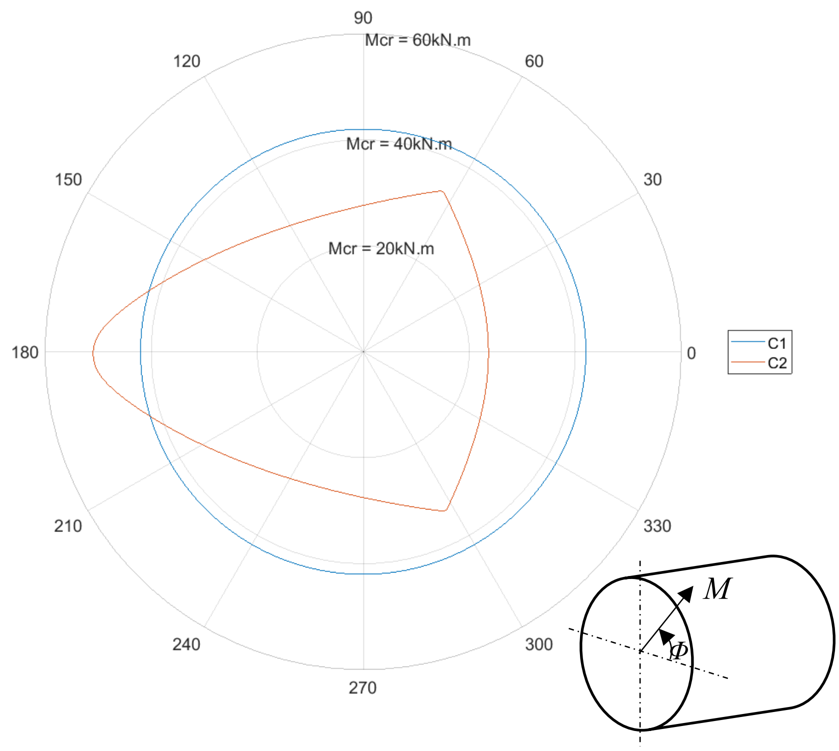

Figure 6.16: Buckling load of laminated circular cylindrical shells against the direction of the applied moment for case C1 and C2

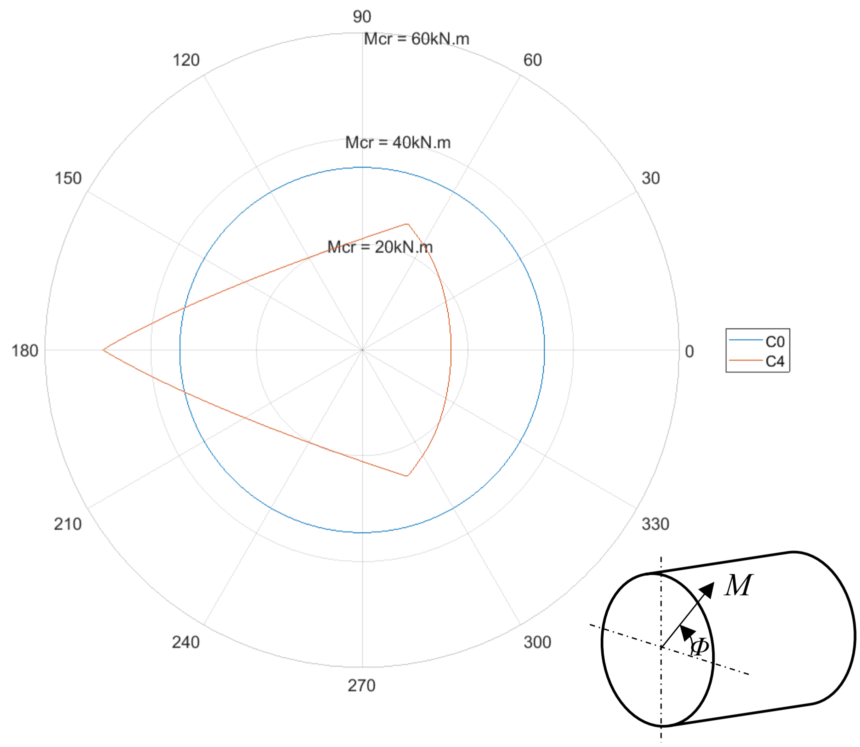

Figure 6.17: Buckling load of laminated circular cylindrical shells against the direction of the applied moment for case C0 and C4

6.5.3 Effect of geometric parameters of the cylindrical shell on buckling performance

The effect of the geometric parameters, namely, the length and the radius of the cylindrical shells have been investigated for all five cases specified in Table 6.2. It can be seen in Figure 6.18(a) that the increase in the length of shells generally led to reduction of the buckling load for all the cases considered. As can be seen, there were no specific qualitative differences between the curves obtained for CS and VS shells, because the variation of stiffness was along the circumferential coordinate and it was not affected by the change in length of the cylinder. In Figure 6.18(b) the buckling load was found to increase linearly with the radius in all cases. Therefore, the expanding circumference of the circular cylinder does not influence on the variation of the local angles; hence, a variation of stiffness does not change with increasing the radius of the cylinder.

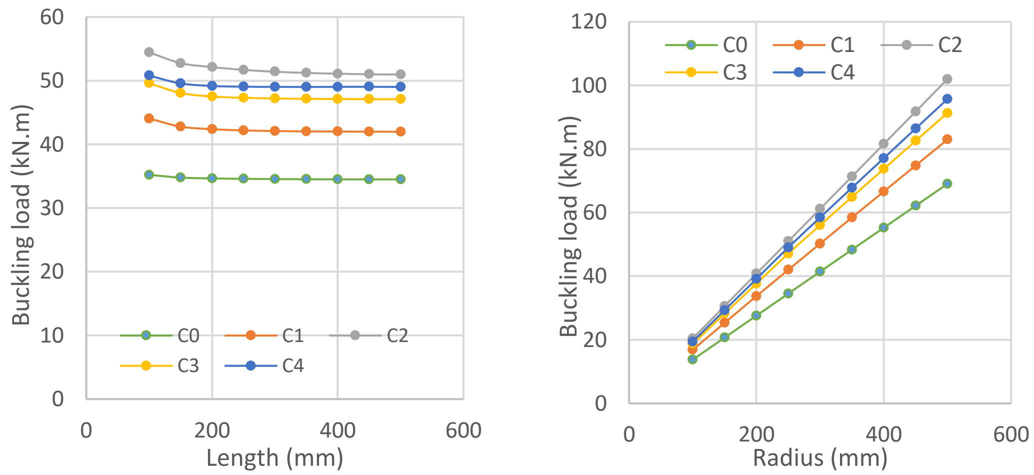

(a) (b)

Figure 6.18: Buckling load of laminated circular cylindrical shells against geometric parameters; (a) length, and (b) radius

6.5.4 The buckling response of the elliptical cylindrical shells

As has been stated in Section 6.4, the elliptical cylindrical shells have a different structural performance compared to circular cylindrical shells due to different curvatures in their elliptical cross-sections. To explore the differences in structural performance, optimisation of cylindrical shells of elliptical cross-sections was conducted for the same types of lay-up as were defined in Section 6.3. The optimisation cases were denoted using the same notations as employed previously for circular cylindrical shells, where cases C0 and C1 were the CS laminates, and cases C2, C3 and C4 were the VS laminates. These cases of the elliptical cylindrical shells were considered just the uniform distributions of the fibre volume fraction.

The optimisation results for the elliptical cylindrical shell with horizontal axis larger than the vertical axis, i.e. $a>b$, are given in Table 6.4. One can see that there was an improvement in buckling load for the VS laminates as compared to CS laminates. The optimisation results for elliptical cylindrical shells having $a<b$ were summarised in Table 6.5. It can be seen that the buckling loads for all such cases are larger than those for their counterparts $a>b$. Also, the buckling loads of the CS cylinders were generally smaller than those of VS cylinders. This is attributed to the inefficient definition of the fibre path in case C0 and C1, where the local angles are kept constant for the whole structure. In the cases, C2, C3 and C4, the fibre is steered on the surface of the elliptical cylindrical shell to produce a continuous change of stiffness. Consequently, it improves structural performance by increasing the ability to resist buckling load.

The axial strain distribution for the five cases with $a>b$ was produced as shown in Figure 6.19, where it was plotted as a function of the circumferential length. It can be seen in the strain distribution curves varied in sinusoidal form as in of circular case. It gives an induction for the local stiffness in a circumferential direction.

Table 6.4: Optimisation results for different cases of elliptical cylindrical shells having $a>b$

Cases	Stacking sequence of a laminated elliptical cylindrical shell	Buckling load (kN.m)
C0	$[\theta/-\theta/\ \theta/-\theta/-\theta/\ \theta/-\theta/\ \theta]_s$, $\theta=72^\circ$	16.3373
C1	$[0°/\theta/90°/-\theta/-\theta/90°/\theta/0°]_s$, $\theta=53^\circ$	20.2843
C2	$[0°/\varphi/90°/-\varphi/-\varphi/90°/\ \varphi/0°]_s$ $T_1=1°$, $T_2=0°$, $T_3=2°$, $T_4=0°$, $T_5=13°$, $T_6=54°$, $T_7=54°$	27.0
C3	$[-\varphi°/45°/\ \varphi°/-45°/-45°/\ \varphi°/\ 45°/-\varphi°]_s$ $T_1=0°$, $T_2=0°$, $T_3=0°$, $T_4=0°$, $T_5=0°$, $T_6=67°$, $T_7=90°$	25.7759
C4	$[\varphi°/-\varphi°/\ \varphi°/-\varphi°/-\varphi°/\ \varphi°/\ -\varphi°/\ \varphi°]_s$ $T_1=3°$, $T_2=0°$, $T_3=53°$, $T_4=1°$, $T_5=32°$, $T_6=72°$, $T_7=73°$	30.7963

Table 6.5: Optimisation results for different cases of elliptical cylindrical shells having $a<b$

Cases	Stacking sequence of a laminated elliptical cylindrical shell	Buckling load (kN.m)
C0	$[\theta/-\theta/\ \theta/-\theta/-\theta/\ \theta/-\theta/\ \theta]s$, $\theta=72^\circ$	47.8082
C1	$[0°/\theta/90°/-\theta/-\theta/90°/\theta/0°]_s$, $\theta=53^\circ$	59.0242
C2	$[0°/\varphi/90°/-\varphi/-\varphi/90°/\ \varphi/0°]_s$ $T_1=0°$, $T_2=5°$, $T_3=90°$, $T_4=1°$, $T_5=50°$, $T_6=53°$, $T_7=28°$	68.9439
C3	$[-\varphi/45°/\ \varphi/-45°/-45°/\ \varphi/\ 45°/-\varphi]_s$ $T_1=1°$, $T_2=7°$, $T_3=71°$, $T_4=3°$, $T_5=21°$, $T_6=36°$, $T_7=0°$	60.1338
C4	$[\varphi°/-\varphi°/\ \varphi°/-\varphi°/-\varphi°/\ \varphi°/\ -\varphi°/\ \varphi°]_s$ $T_1=0°$, $T_2=2°$, $T_3=9°$, $T_4=40°$, $T_5=73°$, $T_6=72°$, $T_7=37°$	57.9523

The variation of axial stress resultant that causes buckling load for all cases with *a*>*b* is presented in Figure 6.20. As can be seen, the circumferential distance along which the axial stress resultant is compressive is larger than the distance where the axial stress resultant was tensile for VS laminates, whilst for the CS laminates the two distances were equal. This indicates that properly designed VS shell can be more efficient in resisting buckling deformation since the part of the shells sustaining the compressive load is larger than that in conventional CS shells.

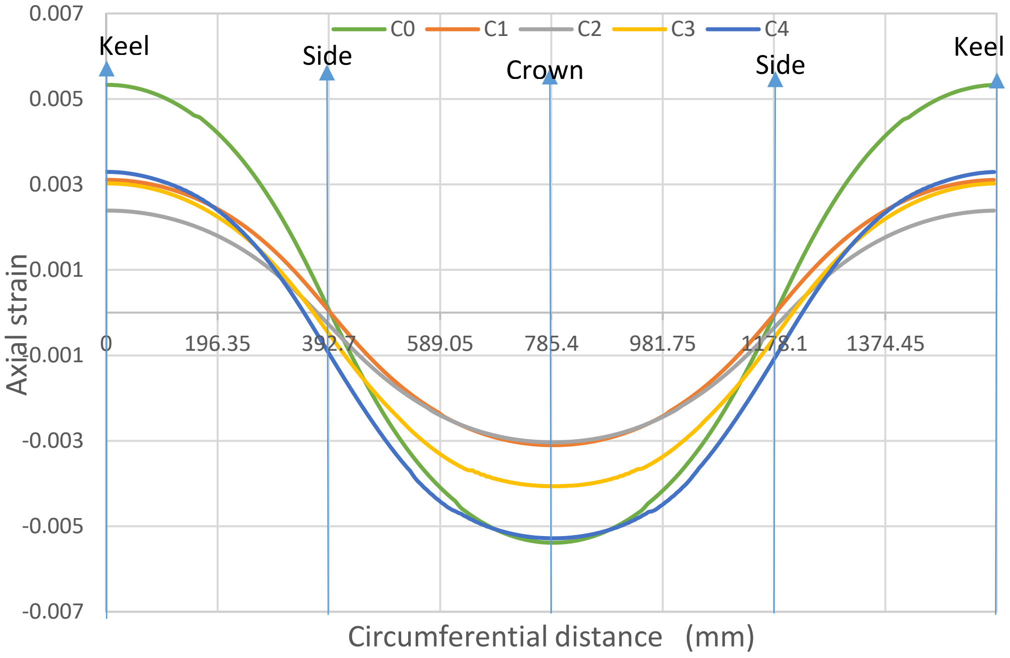

Figure 6.19: Axial strain of different layups of laminated elliptical shells having *a*>*b*

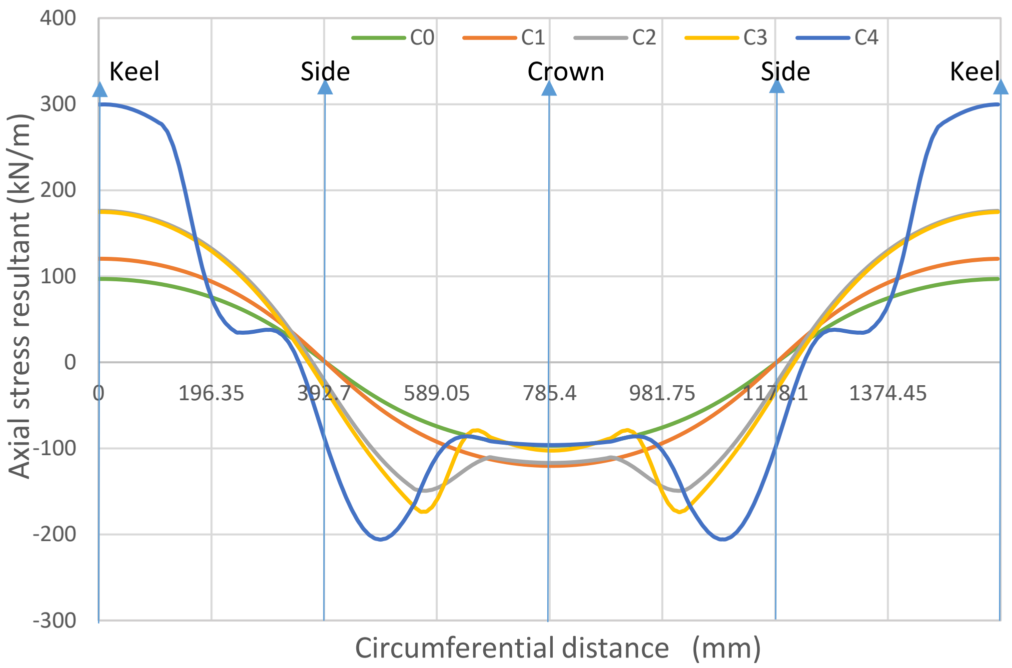

Figure 6.20: Axial stress resultant of different layups of laminated elliptical shells having *a*>*b*

In the case *a*<*b*, the axial strain and axial stress resultant variations were obtained as shown in Figure 6.21 and 6.22, respectively. It can be seen that the axial strain has a sine wave profile along the circumference of the cylindrical shell. The value of the strains in all five cases considered is larger in their respective counterparts with *a*>*b* that are shown in Figure 6.19. Since the direction of the applied bending moment is around the horizontal axis, and the curved parts of the elliptical cylindrical shell with *a*<*b*, which are more structurally stable, can sustain larger buckling load. Consequently, the maxima of the axial stress resultants in Figure 6.22 are significantly larger than whose for cases with *a*>*b* in Figure 6.20. The similarity between the two cases was that the axial load remained compressive over larger circumferential distance than it stayed tensile.

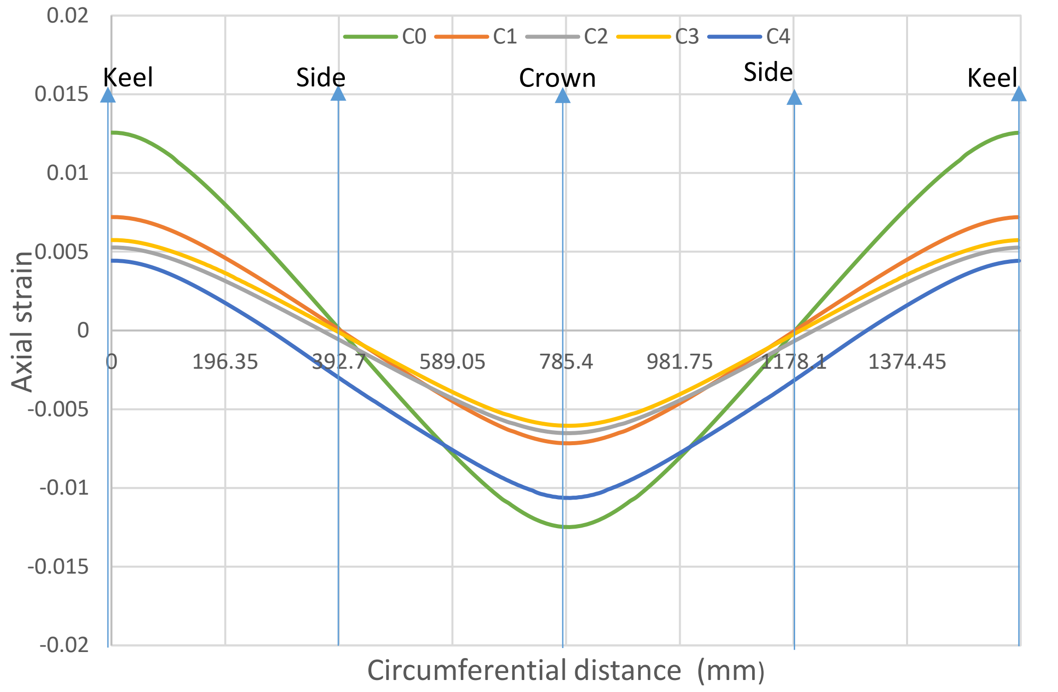

Figure 6.21: Axial strain of different layups of laminated elliptical shells having *a<b*

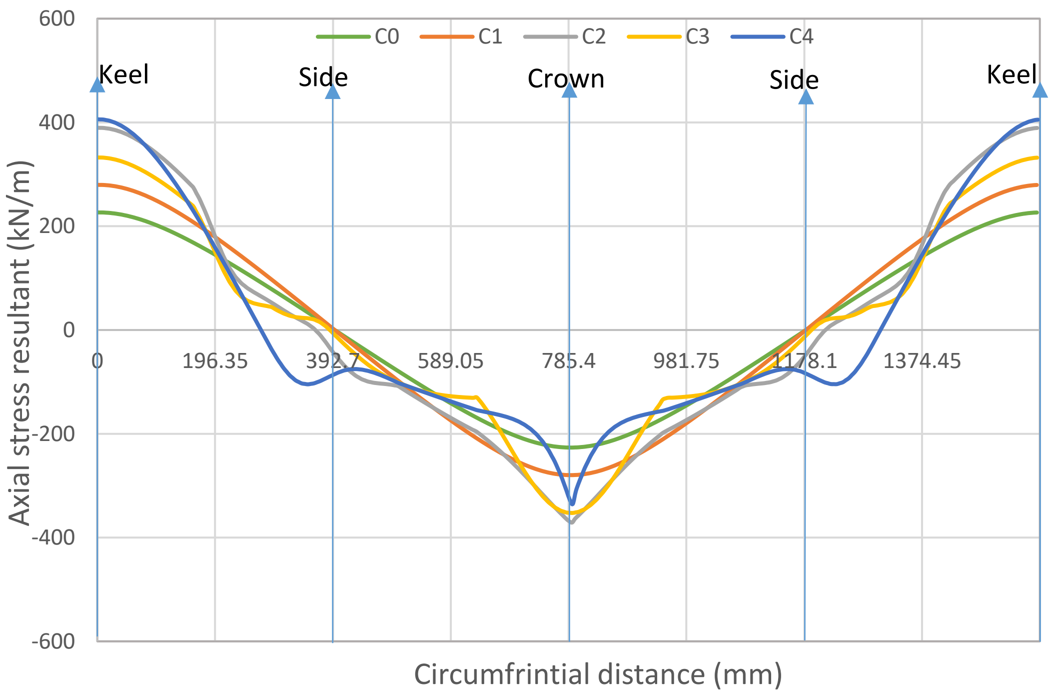

Figure 6.22: Axial stress resultant of different layups of laminated elliptical shells having *a<b*

6.5.5 Buckling performance of elliptical shells in terms of the directions of the applied bending moment

The direction of the axis of applied bending moment on the edges of the CS and VS laminated cylinders can have a significant effect on buckling response. To explore this effect, a range of parametric studies have been carried out where the direction of the axis of the bending moment was varied from 0° to 360°.

Figure 6.23 shows the variation of buckling load with respect to the directions of bending moment for the elliptical shell with $a<b$ for cases C0 (blue curve) and C4 (red curve). Both of curves are symmetric with respect to the horizontal axis and the maximum values of buckling load are achieved 0° and 180° directions. The range of directions where the value of buckling load for VS laminate (case C4) was higher than that for CS laminate, was relatively small, from 173° to 187°, with the maximum being at 180°. A similar scenario was observed comparing cases C1 and C2 in Figure 6.24. However, the buckling loads in these two cases in were larger than those in respective cases C0 and C4 as shown in Figure 6.23.

Similar polar graphs with buckling load being plotted against different directions of bending moment for shells of elliptical cross-sections with $a>b$ are shown in Figure 6.25 and 6.26. In Figure 6.25, showing the results for cases C0 and C4, the largest improvement of buckling load as compared with CS laminate (case C0) was predicted when direction was 180°, whilst the range of directions where buckling load in VS laminate is higher than in CS laminate is from 103° to 253°. Figure 6.26 shows a comparison of buckling load variations for cases C0 and C4. In this case, improvement in buckling load for VS cylinder (case C4) in comparison with CS cylinder (case C0) was between 120° and 240°. The magnitudes of buckling load in all directions were larger than in respective cases in Figure 6.25 as a result of different sequences of layups. Overall, for the elliptical cylindrical shells with *a*>*b*, the ranges of the directions of the applied bending moment that offer a gain in buckling load are wider than those for elliptical cylindrical shells with *a*<*b*. This offers a good assessment for the applicable range of directions of the axis of bending moment, which must be taken as a consideration in design process.

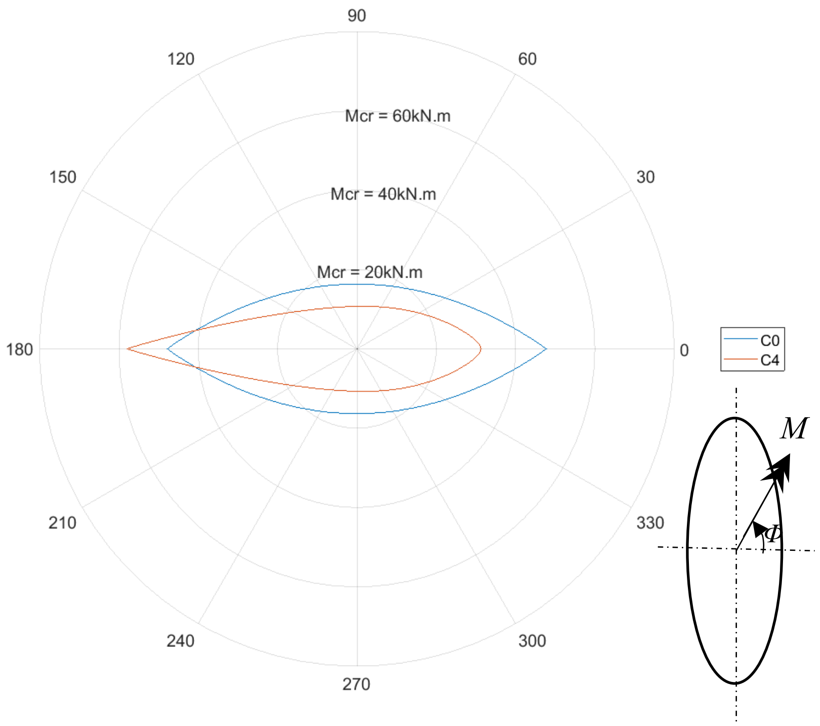

Figure 6.23: Buckling load of elliptical shells with *a*<*b* plotted against the directions of the applied bending moment for cases C0 and C4

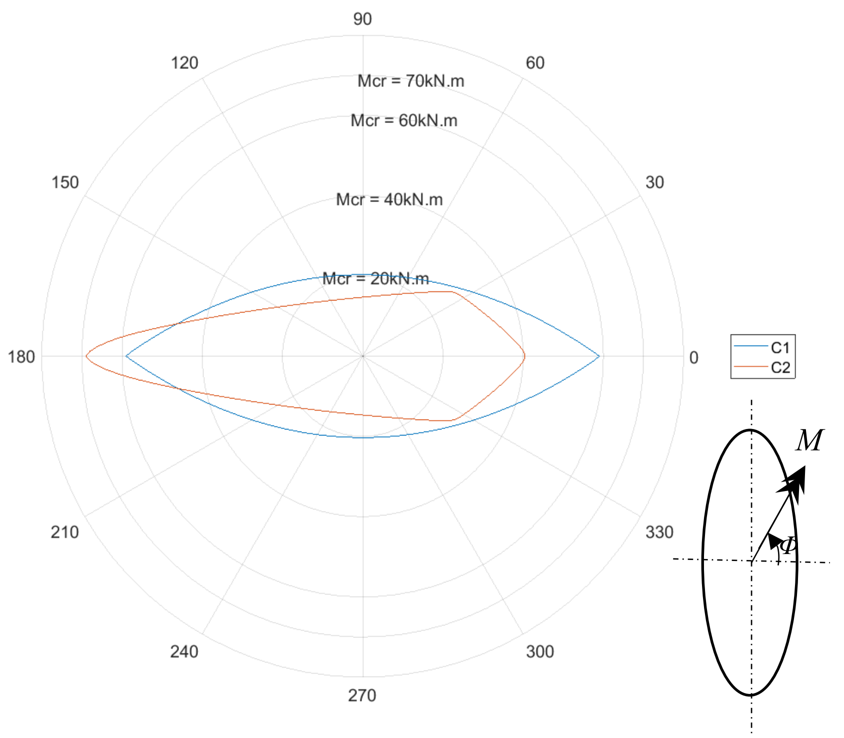

Figure 6.24: Buckling load of elliptical shells with *a*<*b* plotted against the directions of the applied bending moment for cases C1 and C2

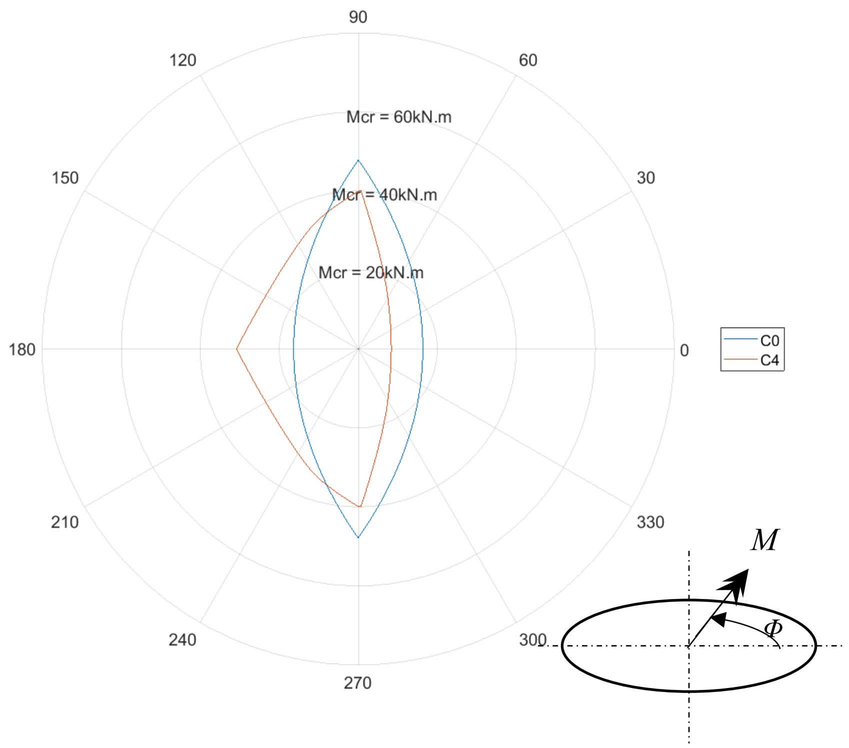

Figure 6.25: Buckling load of elliptical shells with *a*>*b* plotted against the directions of the applied bending moment for cases C0 and C4

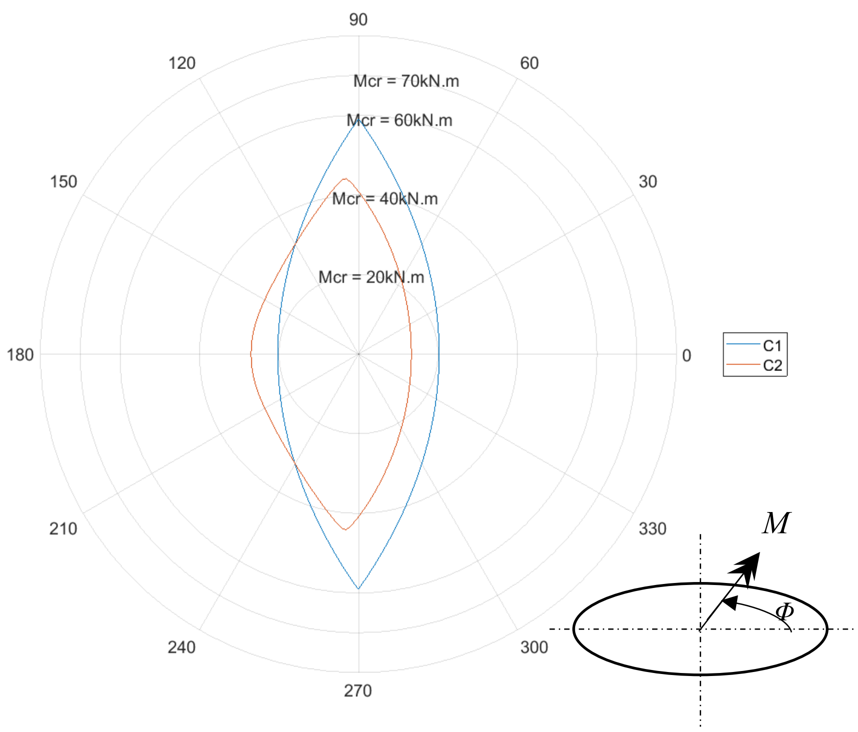

Figure 6.26: Buckling load of elliptical shells with $a>b$ plotted against the directions of the applied bending moment for cases C1 and C2

6.5.6 Effect of geometric parameters of the elliptical cylindrical shell.

The effect of cross-sectional aspect ratio (b/a) on buckling performance of the elliptical cylindrical shell has been investigated, with the results being shown in Figure 6.27. The circumference of the cross-section was kept constant to ensure that the same amount of material was used for shell types considered in resisting the buckling load. It can be seen in Figure 6.27 that the buckling load increases as the aspect ratio b/a approaches unity, that is, the cross-section approaches a circular shape; hence, the curved parts of the elliptical cross-section become wider to approach the circular shape. Hence, the buckling capacity is reduced. It is worth noting, that for some VS cylindrical shells, the variation of the buckling load with aspect ratio b/a is non-monotonic, where it starts to decrease after a certain aspect ratio following the initial increase. This is since the influence of the variation of local angles is more efficient on the flatter portions than that on the curved portions. It is worth noting whilst the difference between buckling loads for different cases is pronounced at large aspect ratios, at small aspect ratios the buckling load is very small and approximately same for all five case. This is to be expected since at small aspect ratio elliptical cross-section can essentially be viewed as two flat plates connected at their ends.

The results demonstrating the effects of the shell length on buckling loads in CS and VS elliptical cylindrical shells are shown Figure 6.28(a) and (b) for shells with *a*>*b* and *a*<*b*, respectively. It can be seen that the buckling load tends to decrease for both CS and VS elliptical cylinders, approaching the asymptotic values as the length increases.

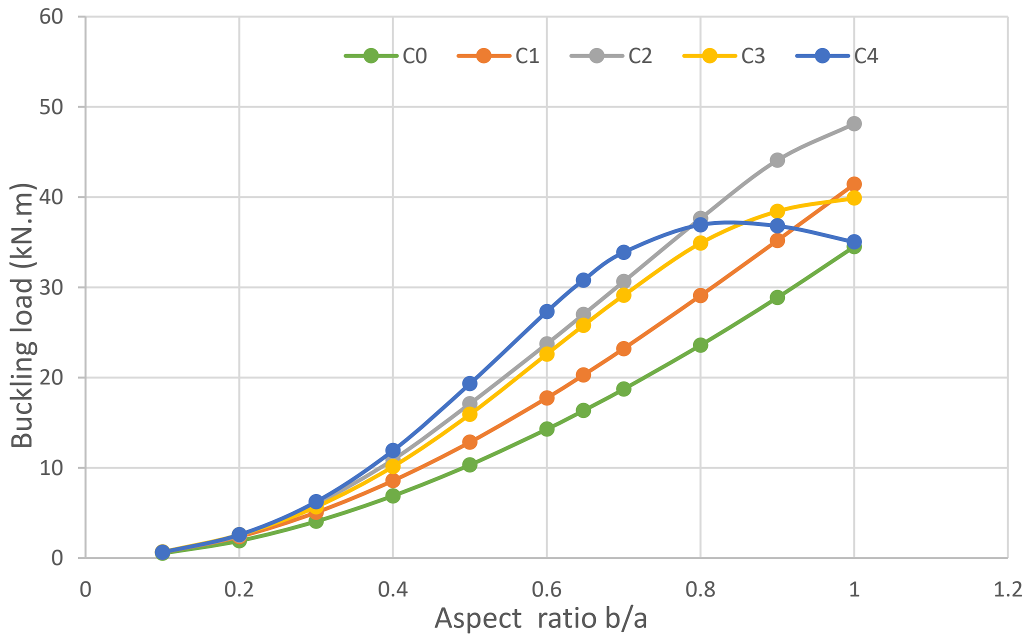

Figure 6.27: Buckling load as the function of the aspect ratio of elliptical laminated cylindrical shells

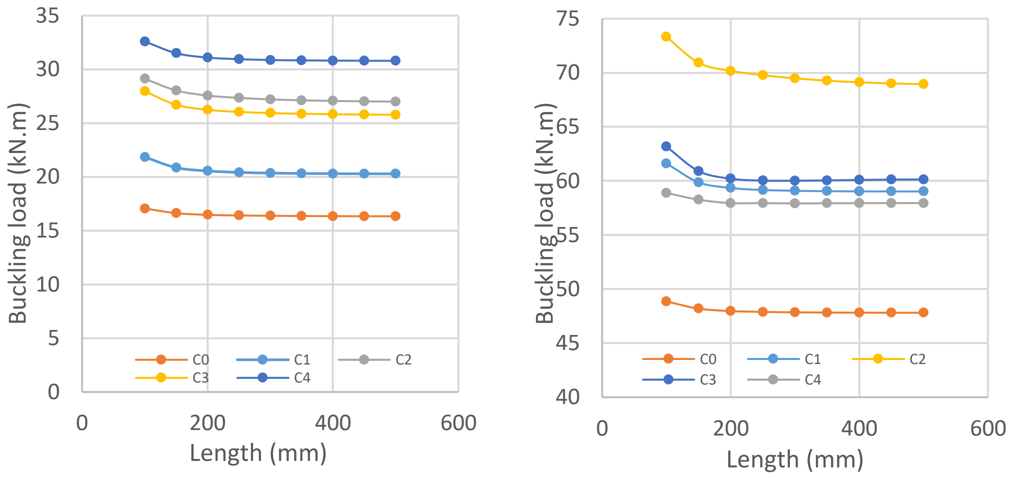

(a) (b)

Figure 6.28: Buckling load against different lengths of the laminated elliptical cylindrical shells having cross-section; (a) *a*>*b* and (b) *a*<*b*

6.6 Summary

Steering the fibre on cylindrical part allows for varying its stiffness, which can help to redistribute the loads, thus improving its structural performance. It was shown that the ability of the VS circular cylindrical shells to sustain buckling load under bending moment can be improved as compared with CS shells. The improvement becomes more apparent in shells with larger number of layers with curvilinear steered fibres.

The presence of the variable gap between the adjacent tows results in a non-uniform distribution of fibre volume fraction and hence the variation of local material properties over the cylindrical shell. Overall, the values of the local material properties are smaller than those obtained assuming uniform fibre volume fraction distributions. Local reduction of stiffness in circumferential direction reduces the ability of laminated cylindrical shells to sustain buckling load.

The numerical study was carried out where the direction of bending moment was varied. It revealed that in general, the buckling load in a cylindrical shell based on VS laminates was lower than that in the CS shells. However, ranges of directions of the applied bending moment were identified for VS shells offer a substantial gain in the buckling load. The prediction obtained also suggest that the range of directions of the applied bending moment at which VS elliptical cylindrical shells outperform CS elliptical cylindrical shells in terms of buckling load was wider for elliptical cylindrical shell with the dimensions of cross-section such that $a>b$ than for shells where $a<b$. Therefore, when designing VS shells, one must be aware of such ranges where superior performance can be offered by VS shells.

In the elliptical laminated cylindrical shells steering the fibre along the circumference allows the axial stresses resultant force to redistribute in the way that the compressive load is partially moved from the area of a larger radius of curvature, which is less structurally stable, to the area of a smaller radius of curvature. Therefore, steering the fibre can help to compensate for the reduction in structural performance occurring in structures of certain geometries.

This indicates that properly designed VS shell can be more efficient in resisting buckling deformation, since the part of the shells sustaining the compressive load is larger than that in conventional CS shells.

It has been shown that in properly designed VS shells the compressive load is distributed over the larger area than in CS cylindrical shells, making them more efficient in resisting the buckling deformations. In overall, steering the fibre showed a good-balanced distribution of the local angles in the composite materials. Hence, the directional feature in the material properties in the laminated structures was fully utilized.

7 Strength evaluations of steered fibre laminates

7.1 Introduction

The application in the aerospace structures of high-performance composite laminates that have a curvilinear path of tows was made possible by automated fibre placement machines for large components and 3D printing for small components. However, these structures still consist of many laminae having a conventional quasi-isotropic layer. The curvilinear tow pattern produced by the tow placement process and based on the linear variation of local angle could yield overlaps or gaps in the lamina. This affects the fibre volume fraction of the laminates locally. The definition of a curved path could be considered as a set of small segments of straight tows. Every such segment of a curved tow could be considered as a unidirectional tow with specific local fibre orientation. The strength of each segment could be determined in terms of the stress state or strain state according to the failure criterion employed.

The stresses and strains of layers in the laminate depend on the laminate loading conditions, local angle orientation and material properties. The stress or strain usually reach critical values in one layer before any other layers. Hence, the failure estimation in the present study is based on the failure in such a layer. However, the remaining layers could still carry more load after failure in one ply in a stable manner, which is often described as progressive failure. The first-ply failure is mainly caused by the in-plane components of the stress tensor in the ply. Delamination between the plies usually does not occur in the laminate before the onset of intralaminar failure and it will not be dealt with in this chapter. Khani et al.

(2011) investigated the maximum strength that could be reached by the variable stiffness laminates using lamination parameters as a continuous design variable. They used a method which incorporated the Tsai-Wu failure criterion with the lamination parameters domain by using a traditional failure envelope. The failure index of Tsai-Wu criterion of unidirectional fibre composites is used in Honda et al. (2013) as the objective function in the optimisation approach of curvilinear fibres, which were defined by a continuous polynomial function to impose continuity in the fibre direction. They dealt with each local point of fibre direction in the curved path as a single point of UD laminate and did not take in consideration of the effect of the gap width variation on the strength value. Lopes et al. (2008b) studied the compressive failure prior to buckling since the variable stiffness laminates can substantially improve the ability to carry more load before buckling. It was found that the first ply failure occurs in the outer 45° plies for compressive loads because of the local strengths of those plies were smaller than it others. Blom et al. (2009a) investigated the effects of the tow–drop produced by cutting the individual tow in the course of many tows to prevent their overlapping. They concluded the failure due to the compressive load took place in the tow-drop area, which had resin-rich pocket, and in the area with sharp turns in the fibre paths.

As reviewed above, calculations of failure load due to the compression were carried out, and some works involved tensile loads. However, the effect of the variable gap width on the strength parameters of the composite has not been considered.

7.2 Ultimate strengths of unidirectional lamina

It is well established from a variety of studies (Kaddour et al., 2013), (Sapozhnikov and Cheremnykh, 2013) and (Torres et al., 2017) that the composite architecture has a great effect on the damage and failure modes of laminates consisting of brittle fibres embedded in a ductile matrix. A curvilinear lamina could be considered as being comprised of multiple small unidirectional elements, with each element being as single point in a lamina. Therefore, the approach used to calculate the mechanical properties from the individual properties of UD laminate could be used for that small part.

Prediction of the strength properties of the unidirectional lamina is more complicated than the calculation of stiffness because the strengths are more sensitive to the fibre-matrix interfaces, geometric non-homogeneities, manufacturing process. For instance, the lack of bonding between the fibre and matrix could result in premature failure in composites when a transverse load is applied. To some extent, it could increase the longitudinal strength of composites. Therefore, in order to determine the ultimate strengths, some assumptions have to be made.

7.2.1 Longitudinal tensile strength (X_t)

It is assumed that the composite consists of continuous fibres and matrix and they are considered to be perfectly bonded, isotropic and linearly elastic up to failure. The failure of composite takes place when the strain in fibre direction reaches the failure strain value of the brittle fibres, which are considered to be the first constituent to fail. Depending on the amount of the fibres in the composite and its minimum value (threshold), there are two possible scenarios to calculate the strength as shown in Figure 7.1 (Kaw, 2005). Variables appearing in Figure 7.1 will be defined with the implications of Figure 7.1 fully elaborated. The two possible scenarios of failure classified as follows.

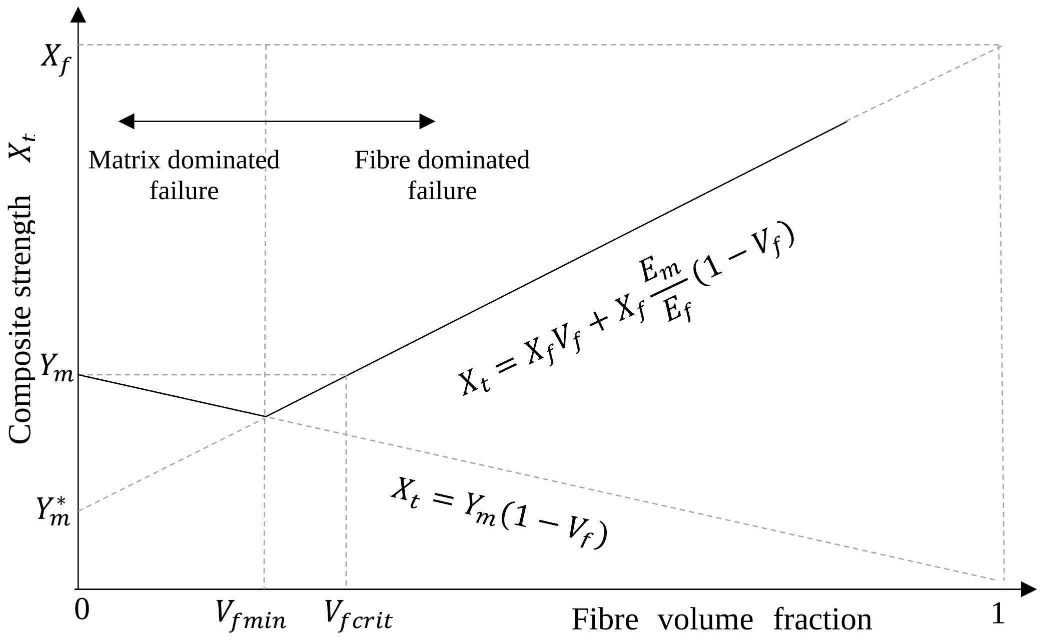

Figure 7.1: The variation tensile composite strength in fibre direction against fibre volume fraction

7.2.1.1 Strength calculations at 0<V_f <V_{fmin}

In this case, there is a minimal amount of fibres in the composite, and hence the stresses in the unidirectional lamina can go high enough to tear the fibres. After the fracture of fibres, they can no longer carry any load, and the fibres will be considered as holes in the cylindrical form embedded in the matrix. Therefore, the effect of these holes on the composite lamina increases the stresses at any given strain. This effect will be more realistic when the failure strain of the matrix is higher than that of the fibre, which is usually true. Therefore, this amount of fibres reduces the strength of lamina instead of improving it; hence, the failure in lamina becomes dominated by matrix in this scenario. The longitudinal tensile strength of the composite is obtained as follows (Kaw, 2005).

$$X_t = Y_m\left(1 - V_f\right) \tag{7.1}$$

where X_t, Y_m and V_f are the composite tensile strength in the longitudinal direction, the strength of matrix and fibre volume fraction, respectively.

The minimum fibre volume fraction that known as a threshold is defined as follows.

$$V_{min} = \frac{Y_m - \sigma'_m}{X_f - \sigma'_m + Y_m} \tag{7.2}$$

where σ'_m is the stress carried by matrix at the fibre failure strain as shown in Figure 7.2.

7.2.1.2 Strength calculations at V_{fmin} < V_f < 1

In this scenario, the fibre volume fraction is greater than the value of the minimum volume fraction. The maximum value of the fibre volume fraction is a function of fibre packing geometry. For instance, the square packing of the fibres of circular cross-sections leads to maximum theoretically achievable fibre volume fraction of $\pi/4 \cong 78.54\%$, while the maximum achievable fibre value fraction for hexagonal packing is $\pi/2\sqrt{3} \cong 90.69\%$ (Li, 2000). The whole composite lamina is assumed to fail when the brittle fibres fail. This scenario is called fibre failure dominated. The longitudinal composite strength is defined as follows (Kaw, 2005).

$$X_t = X_f V_f + \sigma'_m\left(1 - V_f\right) \tag{7.3}$$

$$\sigma'_m = X_f \frac{E_m}{E_f} \tag{7.4}$$

where X_f, E_m and E_f are the tensile strength of fibre, Young's moduli of matrix and of fibre, respectively.

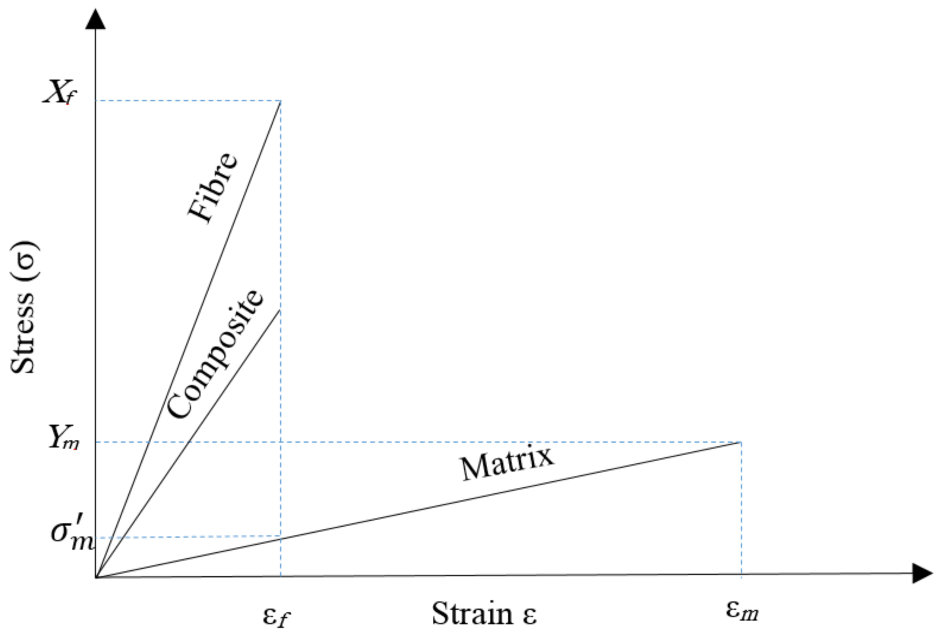

Figure 7.2: Schematic illustrates the stress-strain curve for unidirectional composite and its components

In order to determine which scenario could be applied to each configuration of the curvilinear laminate, the minimum value of local fibre volume fraction needs to be calculated. The local fibre volume fraction changes spatially according to the variation of gap width as a result of linear variation of local orientation along the *x*-axis and can be obtained from Equation (5.19) in Chapter 5 as follows.

$$V_{local} = \frac{\cos(T_1)}{\cos((2x(T_1 - T_0)/L) + T_0)} * V_{tow} \tag{7.5}$$

where V_{local}, T_0, T_1 , L and V_{tow} are the local fibre volume fraction, the local angle at the centre of the panel, the local angle at the edge of the panel, length of the panel and fibre volume fraction of the tow, respectively.

The minimum value of the local fibre volume fraction can be obtained as follows:

$$V_{min} = Min[V_{local}] \tag{7.6}$$

7.2.2 Longitudinal compressive strength (X_c)

The compressive strength of a composite of parallel fibres embedded in the homogeneous matrix is strongly affected by many considerations, such as premature modes of failure, micro-flaws, dislocation mobility of fibre. Compressive load in the fibre direction could produce different types of failure modes.

7.2.2.1 Fracture of matrix and/or fibre-matrix bond due to tensile strains in a matrix

This mode of failure is based on an assumption that the failure of composite in the transverse direction occurs because of the transverse tensile strains that are produced as a result of the longitudinal compressive load (Kaw, 2005). This assumption has to be criticised, since the transverse tensile strain that is considered as uniaxial strain causing the failure of composite, is not equivalent for the uniaxial stress state as elaborated in the study of Li and Sitnikova (2018a). The applied compressive load in the direction of fibres produces the longitudinal compressive strain. However, according to the major Poison's ratio of composite, the transverse strain that causes the fracture of matrix and/or fibre-matrix bond is the transverse tensile strain of composite and is defined as follows:

$$\varepsilon_2 = v_{12}\frac{\sigma_1}{E_1} \tag{7.7}$$

where the v_{12}, σ_1 and E_1 are the major Poison's ratio, compressive stress in the fibre direction and Young's modulus of the composites in the fibre direction, respectively.

According to the maximum strain failure criterion, the composite is considered to have failed in the transverse direction if its transverse strain greater than the ultimate tensile strain $\varepsilon_{2\,ult}^{T}$.

Hence, the longitudinal compressive strength will be as follows:

$$X_c = \frac{E_1\ \varepsilon_{2\,ult}^{T}}{v_{12}} \tag{7.8}$$

The value of the ultimate tensile strain $\varepsilon_{2\,ult}^{T}$ can be derived according to the mechanics of material by assuming a perfect fibre and matrix bonding, uniform spacing of fibres, fibre and matrix following Hooke's law in absence of residual stresses.

By the definition of strain, the extensions can be defined as follows:

$$\delta_c^T = S\varepsilon_c^T \tag{7.9}$$

$$\delta_f^T = d\varepsilon_f^T \tag{7.10}$$

$$\delta_m^T = (S-d)\varepsilon_m^T \tag{7.11}$$

where *d* and *S* are the diameter of the fibre and the distance between centres of neighbouring fibres, respectively, as shown in Figure 7.3 and the $\delta_f^T, \delta_m^T\ and\ \delta_c^T$ are the transverse extensions of fibre, matrix and composite, respectively.

The total transverse extension of a composite is defined as follows.

$$\delta_c^T = \delta_f^T + \delta_m^T \tag{7.12}$$

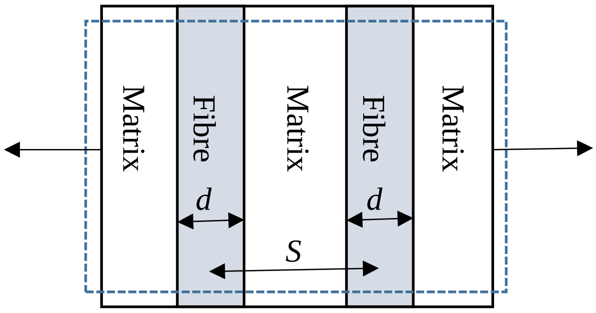

Figure 7.3: Representative volume element shows the transverse tensile load

Hence, the transverse strain of composite will be as follows:

$$\varepsilon_c^T = \frac{d}{S}\varepsilon_f^T + (1 - \frac{d}{S})\,\varepsilon_m^T \tag{7.13}$$

where ε_c^T, ε_f^T and ε_m^T transverse strains of composite, fibre and matrix, respectively.

By assuming equal transverse stresses in the fibre and matrix, the strain of fibre will be as follows.

$$\varepsilon_f^T = \frac{E_m}{E_f}\varepsilon_m^T \tag{7.14}$$

Hence, the transverse strain of composite will become

$$\varepsilon_c^T = \left[\frac{d}{S}\frac{E_m}{E_f} + (1 - \frac{d}{S})\right]\varepsilon_m^T \tag{7.15}$$

According to the assumption that the transverse failure of composites takes place as a result of the failure of a matrix, the transverse failure strain of composite is as follows.

$$\varepsilon_{c\_ult}^T = \left[\frac{d}{S}\frac{E_m}{E_f} + (1 - \frac{d}{S})\right]\varepsilon_{m\,ult}^T \tag{7.16}$$

By substituting Equation (7.16) to the (7.8) the longitudinal compressive strength is obtained as follows.

$$X_c = \frac{E_1}{v_{12}}\left[\frac{d}{S}\frac{E_m}{E_f} + (1 - \frac{d}{S})\right]\frac{Y_m}{E_m} \tag{7.17}$$

7.2.2.2 Micro-buckling of fibres in shear or extensional mode

The failure is due to the fibre micro-buckling when individual fibres buckle inside the matrix. The buckling of fibres that causes the failure under the compressive load also identifies the mode of failure as either extensional mode or shear mode. The extensional mode occurs when the fibres buckle in opposite directions to the adjacent fibres. This mode causes an extension to the matrix in a direction perpendicular to fibre. The shear mode occurs when all fibre buckle in the same wavelength. Therefore, the deformation of the matrix between the fibres is a shear deformation. That buckling is affected by fibres misalignment, shear modulus, and shear strength of composite (Kaw, 2005).

The compressive strength of extensional mode as follows.

$$X_1^c = 2\left[V_f + (1 - V_f)\frac{E_m}{E_f}\right]\sqrt{\frac{V_f E_m E_f}{3(1-V_f)}} \tag{7.18}$$

with the compressive strength of shear mode being.

$$X_2^c = \frac{G_m}{1-V_f} \tag{7.19}$$

Then, the final expression of the compressive strength of composites is given by:

$$X_c = \min[X_1^c, X_2^c] \tag{7.20}$$

7.2.2.3 Shear failure of fibres

This mode of failure could occur when unidirectional laminates are under compressive load, as a result of direct shear failure of fibres. In this case, the rule of mixtures could be used to calculate the shear strength of the unidirectional composite as follows (Kaw, 2005).

$$\tau_{12\,ult} = \tau_{f\,ult} V_f + \tau_{m\,ult} V_m \tag{7.21}$$

where $\tau_{f\,ult}$ and $\tau_{m\,ult}$ are the ultimate shear strength of the fibre and ultimate shear strength of the matrix, respectively.

Since the maximum shear stress in the lamina is half of the longitudinal compressive load, the compressive strength can be defined as follows.

$$X_c = 2[\tau_{f\,ult} V_f + \tau_{m\,ult} V_m] \tag{7.22}$$

The minimum value of the compressive strength that obtained by the micro-buckling of fibres should be compared with that obtained by shear failure of fibres, whereas the minimum value will be used as the compressive strength.

7.2.3 Transverse tensile strength (Y_t)

The transverse tensile strength is obtained according to a mechanics of materials approach, by assuming a complete fibre matrix bonding, the uniform distance between the fibres as shown in Figure 7.3 and the absence of residual stresses (Kaw, 2005).

The transverse strain of composites under transverse tensile load can be given as follows.

$$\varepsilon_c^T = \left[\frac{d}{S}\frac{E_m}{E_f} + (1 - \frac{d}{S})\right]\varepsilon_m^T \tag{7.23}$$

Hence, the ultimate transverse tensile strength will become as follows.

$$Y_t = E_2\left[\frac{d}{S}\frac{E_m}{E_f} + (1 - \frac{d}{S})\right]\frac{Y_{m\_ult}^t}{E_m} \tag{7.24}$$

where E_2 and $Y_{m\_ult}^t$ are the transverse Young's modulus of the composite and ultimate tensile strain of matrix, respectively.

7.2.4 Transverse compressive strength (Y_c)

Equation (7.24) for the transverse tensile strength can be employed to calculate the transverse compressive strength of the lamina (Kaw, 2005). The imperfect fibre/matrix bond and longitudinal fibre splitting reduce the actual compressive strength of composites. The transverse compressive strength is obtained as follows:

$$Y_c = E_2 \varepsilon_c^C \tag{7.25}$$

where E_2 and ε_c^C are the transverse Young's modulus of composite and the compressive strain of composite, respectively.

$$Y_c = E_2 \left[\frac{d}{S}\frac{E_m}{E_f} + (1 - \frac{d}{S})\right] \frac{Y_{m\_ult}^C}{E_m} \tag{7.26}$$

where $Y_{m\_ult}^c$ is the ultimate compressive strain of the matrix.

7.2.5 In-plane shear strength (τ_c)

To determine the in-plane shear strain of unidirectional lamina by using a mechanics of materials approach, one can assume that shear stress of τ_{12} is applied to composite and the shear deformation of the representative volume element is equal to the sum of the deformation of fibre and matrix (Kaw, 2005).

The total shear deformation of the composite is given as:

$$\Delta_c = \Delta_f + \Delta_m \tag{7.27}$$

where Δ_f and Δ_m are the shear deformation of fibre and matrix, respectively.

The shear strains of composite, fibre and matrix material could be defined, respectively, as follows:

$$\gamma_{12_c} = \frac{\Delta_c}{S} \tag{7.28}$$

$$\gamma_{12_f} = \frac{\Delta_f}{d} \tag{7.29}$$

$$\gamma_{12_m} = \frac{\Delta_m}{(S-d)} \tag{7.30}$$

Hence, the in-plane shear strain of composite is rewritten as follows:

$$\gamma_{12_c} = \frac{d}{s}\gamma_{12_f} + \left[1 - \frac{d}{s}\right]\gamma_{12_m} \tag{7.31}$$

Assuming the shear stress of fibre is equal to the shear stress of the matrix under the shear load yields

$$\gamma_{12_m} G_m = \gamma_{12_f} G_f \tag{7.32}$$

Then the expression of the shear strain of composite is obtained as follows:

$$\gamma_{12_c} = \left[\frac{d}{s}\frac{G_m}{G_f} + \left(1 - \frac{d}{s}\right)\right]\gamma_{12_m} \tag{7.33}$$

If the shear failure of the lamina occurred due to the failure of the matrix, the ultimate shear strain of composite would be as follows.

$$\gamma_{12_{c\,ult}} = \left[\frac{d}{s}\frac{G_m}{G_f} + \left(1 - \frac{d}{s}\right)\right]\gamma_{12_{m\,ult}} \tag{7.34}$$

Finally, the in-plane shear strength of composites is defined as follows:

$$\tau_c = G_{12}\left[\frac{d}{s}\frac{G_m}{G_f} + \left(1 - \frac{d}{s}\right)\right]\frac{\tau_m}{G_m} \tag{7.35}$$

7.3 Linearisation of Tsai-Wu failure criterion

The Tsai-Wu failure criterion is considered to provide a classical representation of global strength. It is described as a simple interpolation polynomial constructed from strength values of the unidirectional lamina and does not consider the effect of the dominated value of strength.

The polynomial of the Tsai-Wu Tsai and Wu, 1971 can be written as follows (Puck et al., 2002).

$$F(\{\sigma\}) = \sum L + \sum Q \tag{7.36}$$

where $\sum L$ and $\sum Q$ are the summation of linear and quadratic terms, namely

$$\sum L = (F_1\sigma_1 + F_2\sigma_2) \tag{7.37}$$

$$\sum Q = \left(F_{11}\sigma_1^2 - \sqrt{F_{11}F_{22}}\sigma_1\sigma_2 + F_{22}\sigma_2^2 + F_{66}\sigma_{12}^2\right) \tag{7.38}$$

In order to simplify the Equations (7.37) and (7.38), a common factor, which will be referred to as load factor, can be extracted from the stress state vector as follows:

$$\begin{Bmatrix} \sigma_1 \\ \sigma_2 \\ \sigma_3 \\ \tau_{23} \\ \tau_{13} \\ \tau_{12} \end{Bmatrix} = \lambda \begin{Bmatrix} \bar{\sigma}_1 \\ \bar{\sigma}_2 \\ \bar{\sigma}_3 \\ \bar{\tau}_{23} \\ \bar{\tau}_{13} \\ \bar{\tau}_{12} \end{Bmatrix} \tag{7.39}$$

Hence, the Tsai-Wu criterion will become a function of the load factor λ, as the concept of Puck et al. (2002), and the second-order equation is rewritten as follows:

$$F(\{\sigma\}) = F(\lambda, \{\overline{\sigma}\}) = \lambda \sum \bar{L} + \lambda^2 \sum \bar{Q} \tag{7.40}$$

where $\sum \bar{L}$ and $\sum \bar{Q}$ are the summation of linear and quadratic terms, respectively, after extraction of the common factor.

In order to linearise Tsai-Wu criterion such that it would capture the value of unity of the failure index, one can assume the linear form of failure index as follows:

$$F_l(\{\sigma\}) = \frac{1}{2}\left(\sum L + \sqrt{(\sum L)^2 + 4\sum Q}\right) \tag{7.41}$$

Rearranging Equation (7.41), one has

$$2F_l - \sum L = \sqrt{(\sum L)^2 + 4\sum Q} \tag{7.42}$$

and

$$4F_l^2 - 4F_l \sum L + (\sum L)^2 = (\sum L)^2 + 4\sum Q \tag{7.43}$$

Equation (7.43) is simplified to

$$F_l^2 = F_l \sum L + \sum Q \tag{7.44}$$

When $F_l = 1$ then the Equation (7.44) becomes

$$\sum L + \sum Q = 1 \tag{7.45}$$

As shown in Figure 7.4, the line corresponding to the linearised form of Tsai-Wu criterion given by (7.45) intersects curve obtained using conventional Tsai-Wu criterion at unity, i.e.

$$F_l = F = 1 \tag{7.46}$$

Finally, by taking the common factor λ from the stress vector, the linear form can be written as follows:

$$F_l = \frac{\lambda}{2}\left(F_1\bar{\sigma}_1 + F_2\bar{\sigma}_2 + \sqrt{(F_1\bar{\sigma}_1 + F_2\bar{\sigma}_2)^2 + 4\left(F_{11}\bar{\sigma}_1^2 - \sqrt{F_{11}F_{22}}\bar{\sigma}_1\bar{\sigma}_2 + F_{22}\bar{\sigma}_2^2 + F_{66}\bar{\sigma}_{12}^2\right)}\right) \tag{7.47}$$

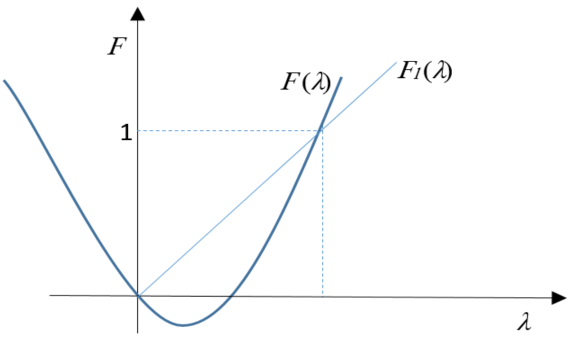

Figure 7.4: Schematic illustrates the quadratic form and the linear form of Tsai-Wu failure index

In order to understand the relationship between the quadratic and linear forms of Tsai-Wu failure index and to ensure that the former works well, it was implemented as UMAT subroutine. Simple calculations of failure index for a different range of unidirectional laminates were carried out. Figure 7.5 shows the linear form and quadratic form intersecting at unity for each orientation of the unidirectional laminates with the material properties given Table 7.1. It can be seen the failure load could be predicted for both cases of uniaxial loading, tensile or compressive. Linearisation the Tsai-Wu criterion is beneficial in terms of reducing computational costs. It does not require as many increments to capture the failure load as the quadratic polynomial form of Tsai-Wu criterion. In addition, it could be used to determine the failure envelope of in-plane stress state according to the state of the interactive strength property F_{12}, as mentioned in the study of Li et al. (2017).

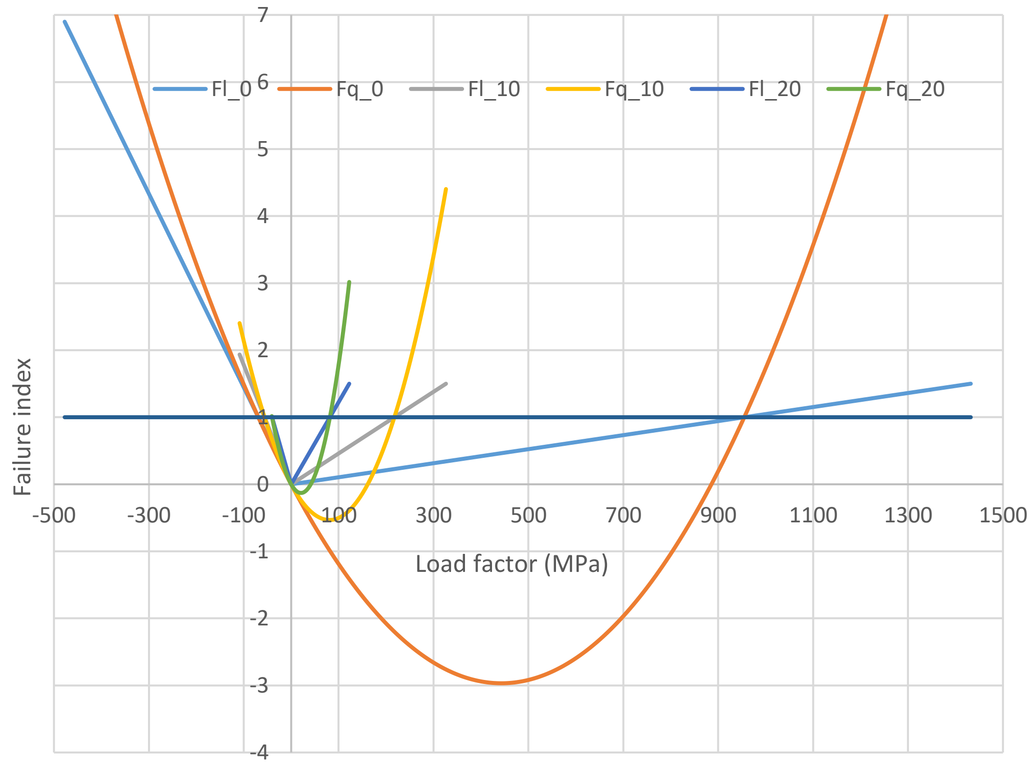

Figure 7.5: The linear and quadratic form of a failure index of Tsai-Wu for different orientations of the unidirectional lamina

Table 7.1: Material properties according to Kaw (2005).

Material property	Glass fibre	Epoxy
Axial modules (GPa)	85	3.4
Transverses modules (GPa)	85	3.4
Shear modules (GPa)	35.42	27
Major Poisson's ratio	0.2	0.3
Axial tensile strength (MPa)	1550	72
Axial compressive strength (MPa)	1550	102
Transverses tensile strength (MPa)	1550	72
Transverses compressive strength (MPa)	1550	102
Shear strength (MPa)	35	34
Fibre volume fraction of tow	60%	

7.4 The finite element model

In order to predict the failure load of laminates having curved tows and compare it with that in conventional laminates, the finite element analysis has been implemented by using the Abaqus/Standard (2017). Each element of the FE model of VS laminates is associated with a certain local angle, unlike in straight fibre laminates, where the same orientation applies to the whole element domain. The particular orientation of each element is defined at each integration point by user-defined subroutine ORIENT. The composite laminate of 12 layers is generally assumed symmetric and balanced with $[\pm<T_0|T_1>]3_s$. This definition of lay-up refers to a variable-stiffness laminate with curved tows has a local angle of T_0 at the centre of the laminate and T_1 at the edges. The local angle between T_0 and T_1 varies linearly.

The maximum stress and Tsai-Wu failure criteria have been implemented as UMAT subroutine. The analysis was conducted over two increments, which were sufficient to capture the load level corresponding to the unity value of failure index in the linearised Tsai-Wu criterion. As was explained in the previous section, a small number of increments required is one of the advantages of using this form of the criterion. According to the first ply failure, once the failure index of any element of any lamina reached the unity, this lamina and the entire laminate is considered to have failed.

The FE models have been meshed with S4 and shell elements where each shell element is considered as a small unidirectional lamina with a local variation of material properties due to variation of gap width and a specific local angle. The element size was defined according to mesh convergence study for the case of rapid change of local angles, where the panel has the largest difference between the values of T_0 and T_1. The results of the convergence study are shown in Figure 7.6, based on which the element size of 0.4mm was chosen for all models. The laminates were loaded by applying the uniform displacements in an axial direction on the left and right edges of the panel. In addition, the boundary conditions have been applied to constrain rigid body movement of the panel. The material properties and strengths of fibre and matrix are specified in Table 7.1.

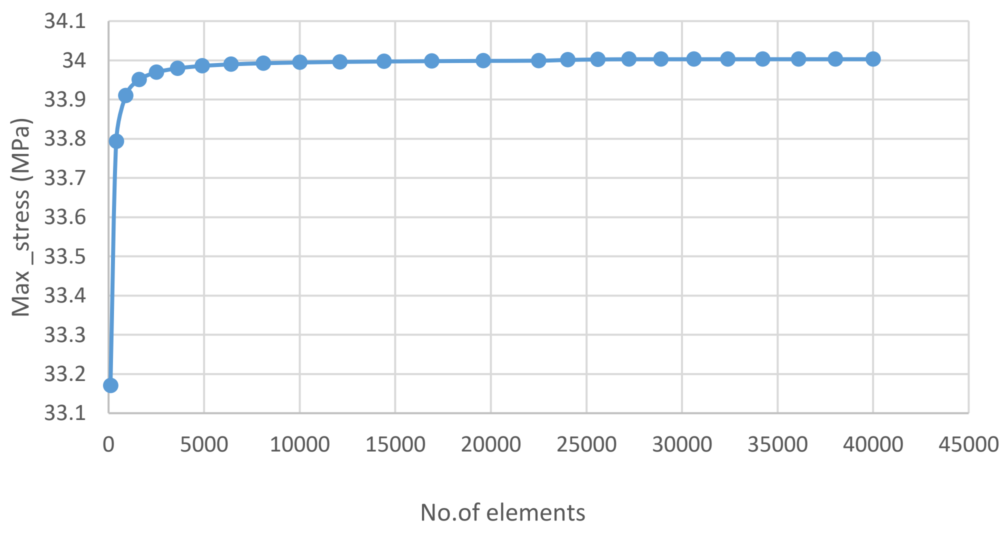

Figure 7.6: Mesh convergence for a curvilinear fibres having raped change of local angles between T_0=0° and T_1=90°

7.5 Results and discussion

7.5.1 Calculations of the minimum value of fibre volume fraction

The minimum value of fibre volume fraction can be calculated based on the strength material properties and the variable gap width as mentioned in Section 7.2.1, to specify which scenario is applicable to calculate the longitudinal strength of the composite. Figure 7.7 shows the distribution of the minimum of local fibre volume fraction defined by Equation (7.6) over the entire domain of local angles T_0 and T_1. As can be seen, the largest value of this minimum is obtained when T_0=T_1, that is, when the tows in a lamina are straight. The lowest value of the minimum volume fraction is obtained in lamina with a large difference between T_0 and T_1.

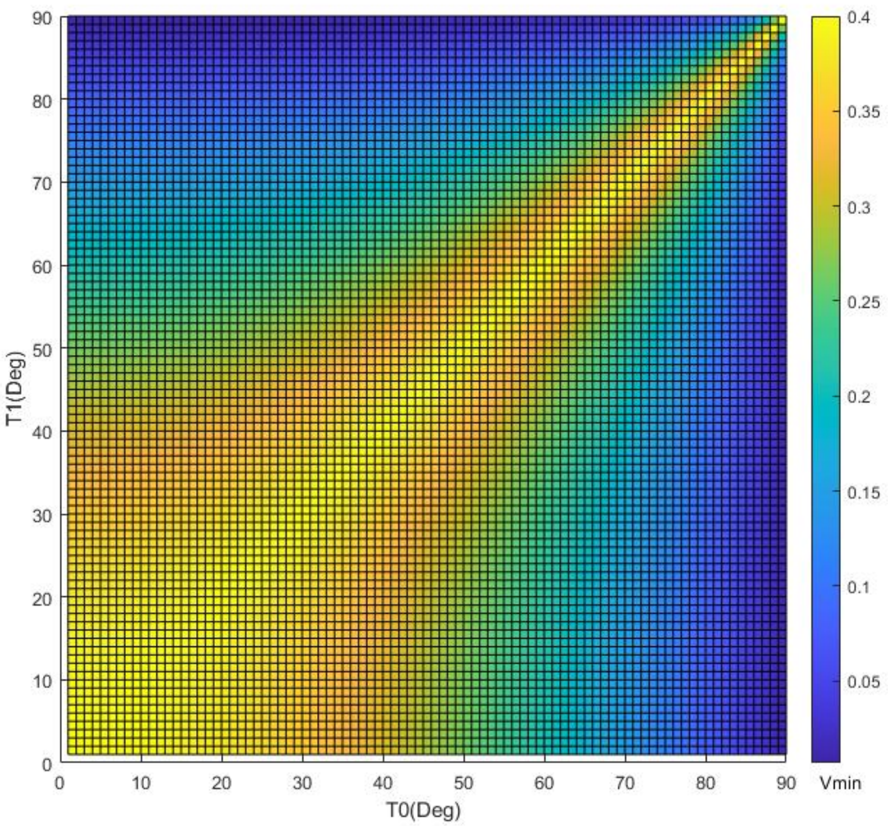

Figure 7.7: The minimum value of fibre volume fraction due to a different configuration of curvilinear fibre lamina

Figure 7.8 state the minimum value of fibre volume fraction calculated based on the strength parameters and the variation of local angles according to the Equation (7.2) and (7.6), respectively. The minimum value based on the strength parameters is 0.0064 (threshold). It was represented by a horizontal plane. Below this value, the fibres inside the lamina will behave reversely and reduce the strength of the composite. In addition, it can be seen there is no intersection between the horizontal plane and the curved surface of the minimum value of fibre volume fraction based on the variable gap width. Therefore, the varying of the local angles of T_0 and T_1 does not reduce the value of minimum fibre volume fraction below 0.0064.

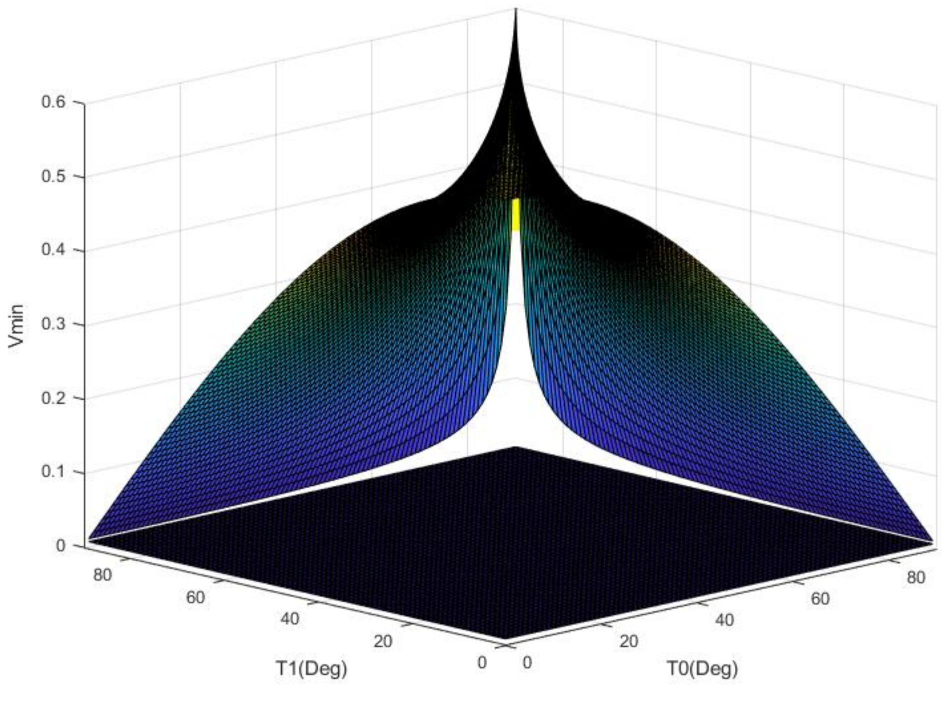

Figure 7.8: The fibre volume fraction due to constituent materials of composite and due to pattern of curvilinear fibre.

7.5.2 Failure load of lamina has curvilinear tows.

The failure criteria were defined earlier for a single lamina based on curvilinear tows, with their local angles changing linearly from T_0 at a centre to T_1 at the edge of lamina. Locally, at each point in a lamina can be considered to be a UD lamina. The variation of local gap width has been accounted for by employing it in definition and calculation of the non-uniform fibre volume fraction.

Figure 7.9 and 7.10 show the failure load according to the maximum stress criterion of a lamina having curvilinear tows with a variation of local angle in *x*- and *y*-direction, respectively. Each figure shows a family of curves, each representing a set of laminae having various values of T_0 (from 0° to 90° with increments of 10°). In both cases of local angle variation, the curves with T_0= T_1 and T_0=0° have three parts, each corresponding to a different mode of failure, namely, the fibre failure, the shear failure and transverse matrix failure. The curves T_0=10°, T_0=20°, T_0=30° and T_0=40° have two parts, corresponding to shear and transverse matrix failure modes. For the remaining curves, all the laminae failed in the same mode, namely, the transverse matrix failure. It can be seen there is some difference between the respective curves in Figure 7.9 and 7.10. This is due to the direction of variation of local angle, since in case of a variation in the *x*-direction the local angles at the edges of the panel where the load is applied are the same, while for variation in *y*-direction the local angles on the edges where load is applied are different. For two different directions of local angle variation, the local stiffness distributions can be considered to be in parallel and in series forms as discussed of Section 5.7.3 of Chapter 5.

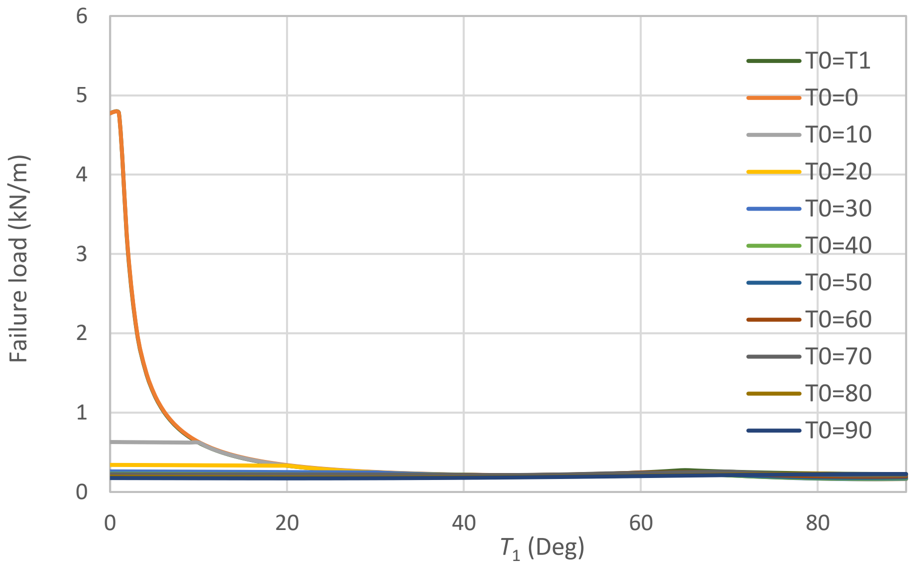

Figure 7.9: Failure load for different configurations of curved fibre lamina according to MAXSTRS criterion for laminae having $\theta = \theta(x)$

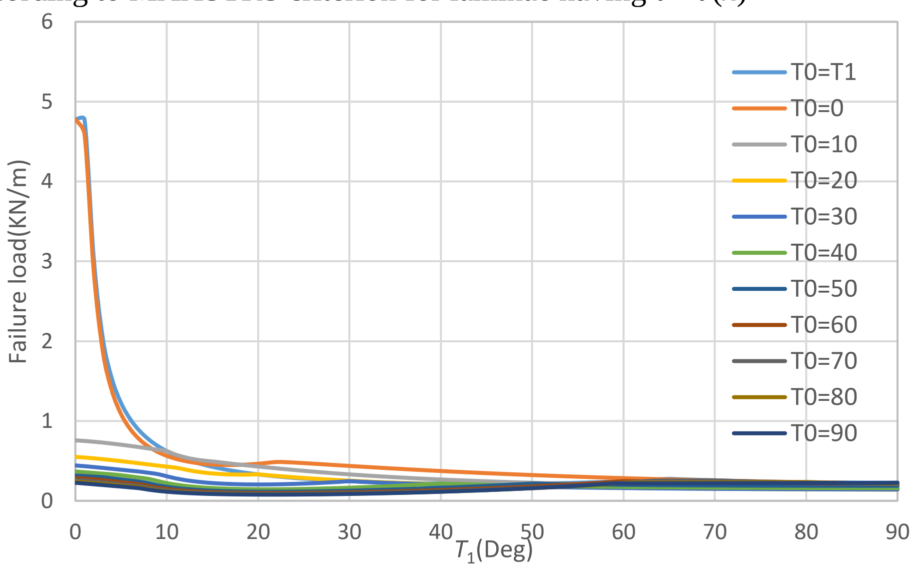

Figure 7.10: Failure load of different configurations of curved fibre lamina according to MAXSTRS criterion for laminae having $\theta = \theta(y)$

Figure 7.11(a) and (b) show a comparison of failure load according to the maximum stress criterion under uniaxial load for laminae with uniform and non-uniform fibre volume fraction distributions having a variation of local angle in *x*- and *y*-direction, respectively. Angle T_0 in all cases was kept constant at 20°. They reveal that the difference between the failure loads gradually increases with increasing value of the local angle T_1, during which the gap width also increases. It can be seen in Figure 7.11(a) that the failure of the lamina is first predicted in the point within the lamina corresponding to the largest value of the local angle. As was elaborated in Section 5.7.3 of Chapter 5, in panels having variation of local angles in the x-direction the in-plane stress resultant $N_x(y)$ was constant along the edges where the load was applied, while for panels having the variation of local angle in the y-direction $N_x(y)$ varied as a function of y-coordinate. This explains differences in appearances of the curves in Figure 7.11(b) when compared to those in Figure 7.11(a), in particular, absence of horizontal straight part in curves in Figure 7.11(b).

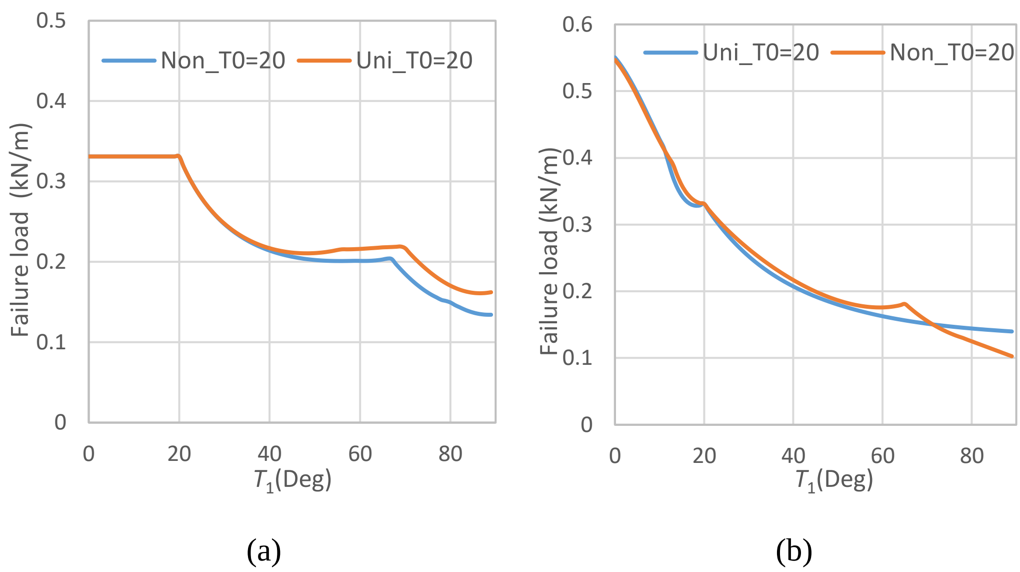

Figure 7.11: A comparison of failure load based on MAXSTRS between uniform and non-uniform fibre volume fraction distributions; (a) laminae having $\theta = \theta(x)$ and T_0=20°, and (b) laminae having $\theta = \theta(y)$ and T_0=20°

Figure 7.12 and 7.13 show the failure load curves which were constructed in the same way as those in Figure 7.9 and 7.10, but Tsai-Wu criterion was used this time. These curves do not have any indication in which modes the lamina has failed, unlike in case of the maximum stress criterion. It can be seen in Figure 7.12 and

7.13 that the curves with T_0=T_1, and T_0=0° are smooth because the Tsai-Wu criterion is quadratic and allows the stress interactions. The remaining curves have straight and curved parts which state the dominated failure load at the largest value of local angles. The boundary between the two parts is at the intersection point with a curve defining failure load in straight tows laminae.

Figure 7.14(a) and (b) show a comparison of failure load according to the Tsai-Wu criterion under uniaxial load in laminae with the uniform and non-uniform distributions of fibre volume fraction having a variation of local angle in *x*- and *y*-direction, respectively. As can be seen, when the difference between the local angles T_0 and T_1 increases, the difference between failure loads in laminates with uniform and non-uniform fibre volume fraction also increases.

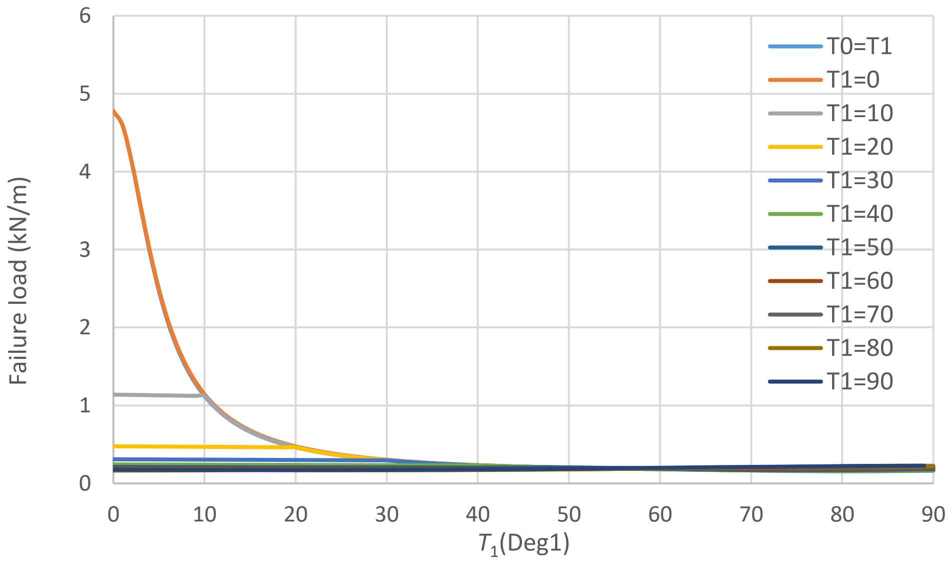

Figure 7.12: Failure load in curved fibre laminae of different configurations with θ= $\theta(x)$ according to Tsai-Wu criterion

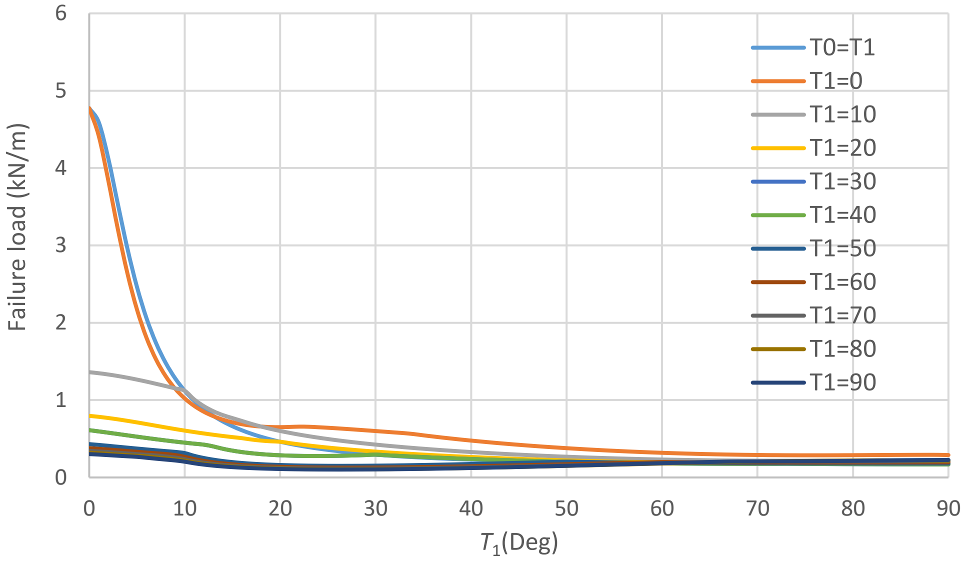

Figure 7.13: Failure load in curved fibre laminae of different configurations θ= with $\theta(y)$ according to Tsai-Wu criterion

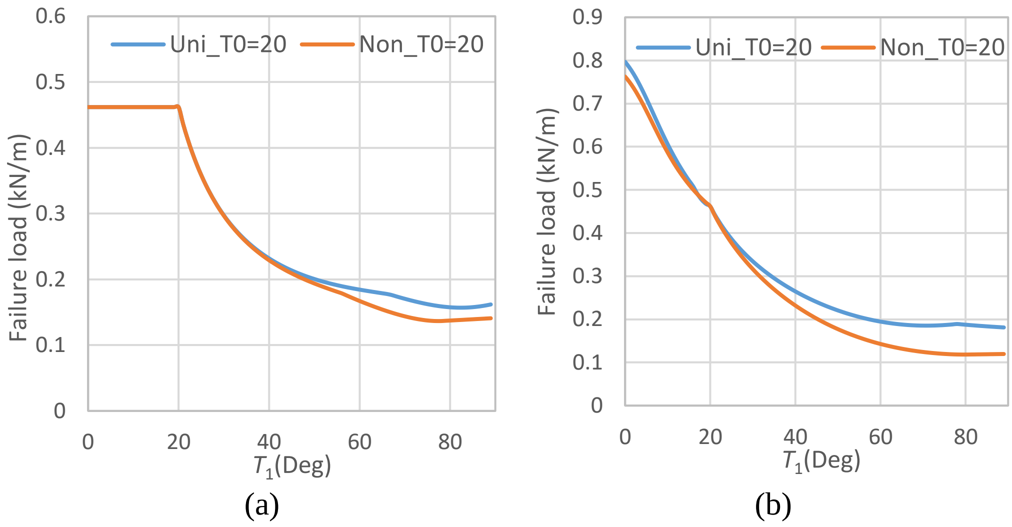

Figure 7.14: A comparison of failure load based on Tsai-Wu criterion in laminae with uniform and non-uniform fibre volume fraction distributions; (a) laminae having θ= $\theta(x)$ and T_0=20°, and (b) laminae having θ= $\theta(y)$ and T_0=20°

7.5.3 Failure load of laminates having curvilinear tows.

In Figure 7.15 and 7.16 failure load curves were produced for laminates with local angle variation in the *x*-direction for a uniform and non-uniform distributions of fibre volume fraction, respectively. The failure load in laminate has been calculated according to the maximum stress criterion by using the first ply failure analysis. As can be seen in Figure 7.15 the failure load for the curves with T_0=T_1 and T_0=0° have three part corresponding to three modes of failure, fibre failure, shear and transverse matrix failure. The curves with T_0=10°, T_0=20°, T_0=30° and T_0=40° suggest that the failure can be in either of two failure modes, i.e. shear or transverse matrix failure. For the remaining curves, the failure was in just one failure mode, the transverse matrix failure. The failure load curves in Figure 7.16 which were calculated accounting for non-uniform fibre volume fraction are generally similar to those in Figure 7.15 with a little difference for the cases having a significant difference between T_0 and T_1.

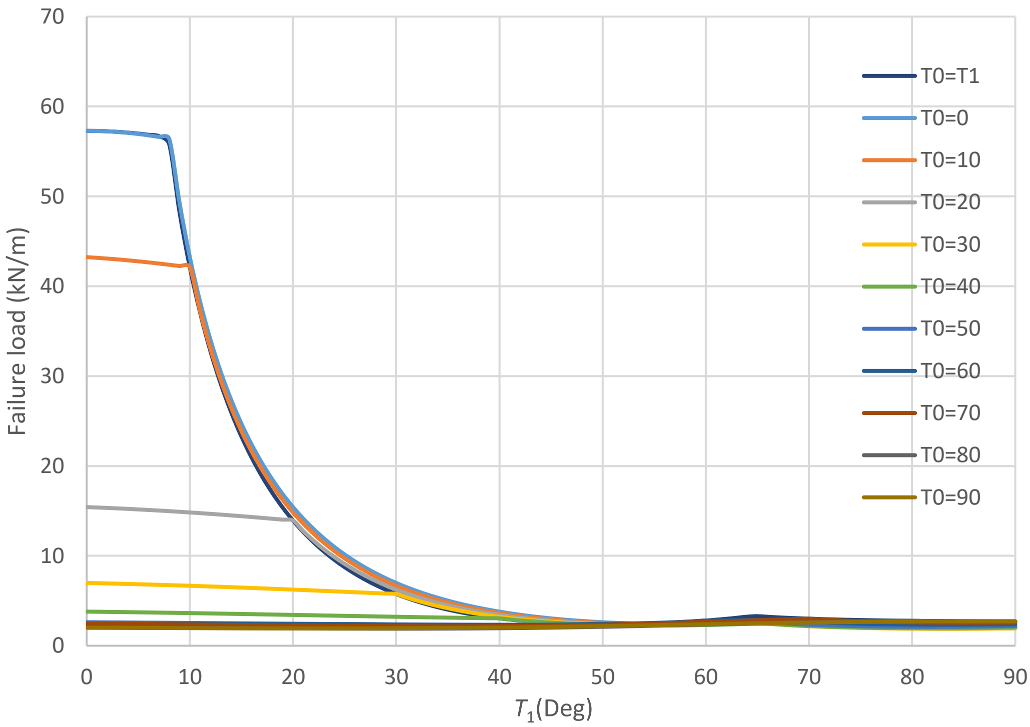

Figure 7.15: Failure load according to maximum stress criterion of curved fibre laminates [±<T_0 | T_1>]3s having a uniform fibre volume fraction and θ= $\theta(x)$

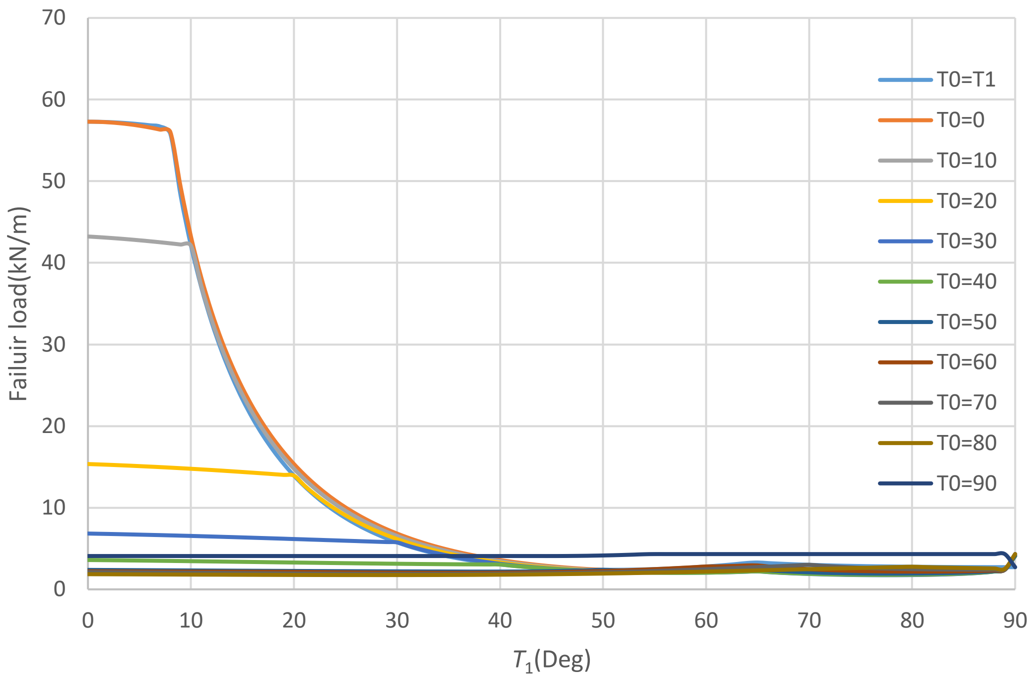

Figure 7.16: Failure load according to maximum stress criterion of curved fibre laminates [±<T_0 | T_1>]3s having a non-uniform fibre volume fraction and $\theta = \theta(x)$

The effect of a gap can be assessed by considering curves in Figure 7.17(a) that shows a difference in failure loads obtained using the maximum stress criterion for both uniform and non-uniform fibre volume fraction distributions in laminates with T_0=0°. As can be seen, there is a slight difference in the failure load as T_1 approaches 90°. In Figure 7.17(b), where the same types of curves are plotted at T_0=30° the difference is more apparent since the gap width, in this case, is larger than in the previous one.

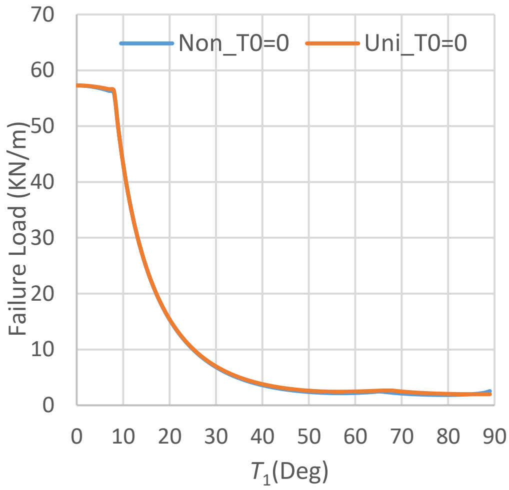

(a)

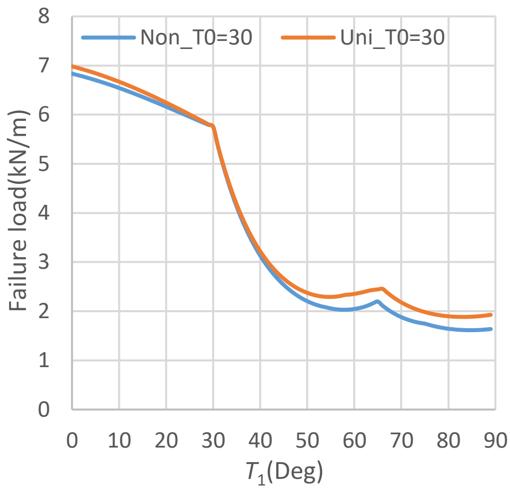

(b)

Figure 7.17: A comparison of failure load based on maximum stress criterion between uniform and non-uniform fibre volume fraction distributions: (a) laminates having $\theta = \theta(x)$ and T_0=0°, and (b) laminates having $\theta = \theta(x)$ and T_0=30°

Failure load curves calculated using maximum stress criterion and assuming local angle variation in the *y*-direction are shown in Figure 7.18 and 7.19 for curvilinear laminates with a uniform and non-uniform fibre volume fraction distributions, respectively. Same as before, there are three modes of failure in the curves obtained for laminates with T_0=T_1 and T_0=0, the curves of T_0=10°, T_0=20°, T_0=30° and T_0=40° indicate two failure modes, while for the remaining curves the failure was in transverse mode. Overall, in laminates with local angle variation in the *y*-direction, the failure loads were a little larger than their counterparts in laminates with a variation of local angles in the *x*-direction.

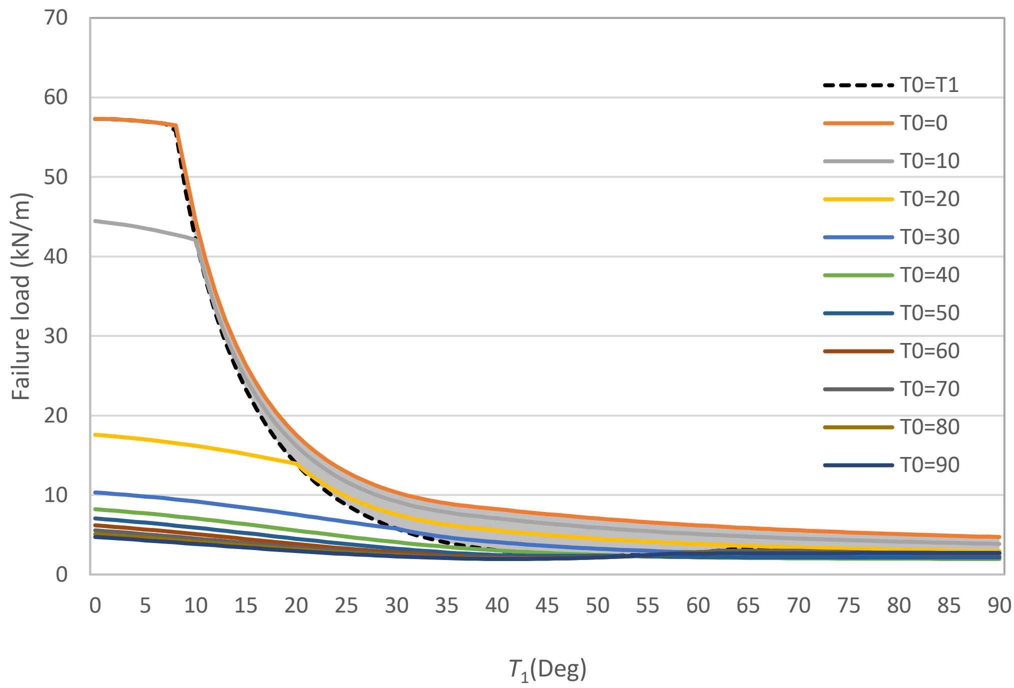

Figure 7.18: Failure load according to maximum stress criterion in curved fibre laminates [±<T_0 | T_1>]3s having a uniform fibre volume fraction and $\theta = \theta(y)$

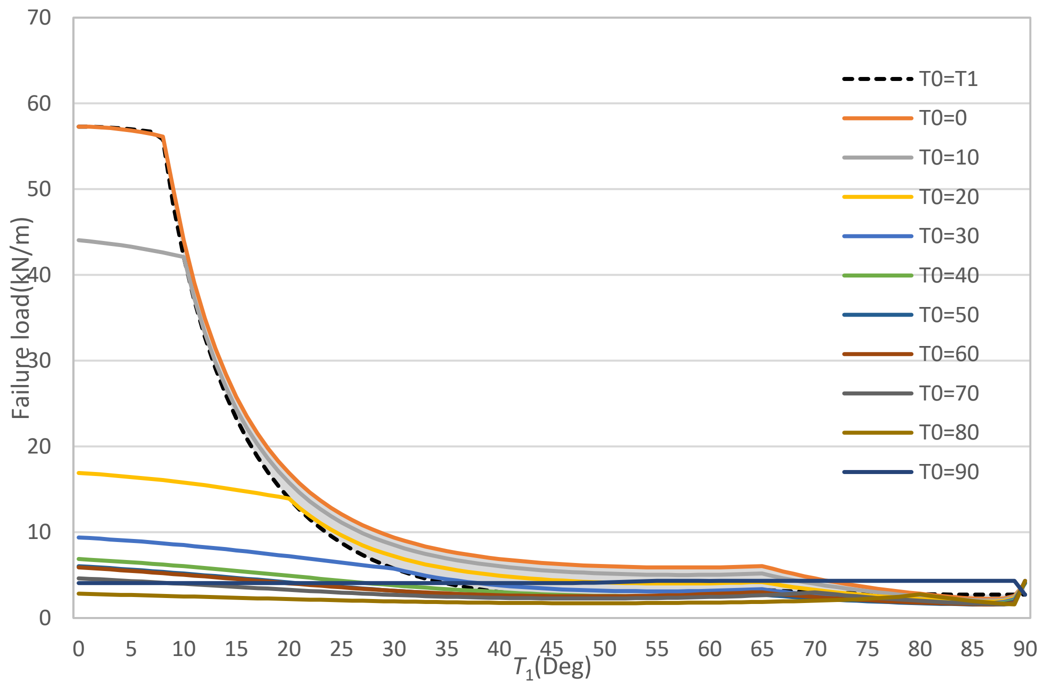

Figure 7.19: Failure load according to maximum stress criterion in curved fibre laminates [±<T_0 | T_1>]3s having a non-uniform fibre volume fraction and $\theta = \theta(y)$

Figure 7.20(a) shows the difference between the failure load curves calculated based on the maximum stress criterion in laminates with the uniform and non-uniform of fibre volume fraction distributions at T_0=0° with a variation of local angles in the *y*-direction. The curves of failure tend to diverge when the gap size increases as the difference between T_0 and T_1 increases. Figure 7.20(a) shows the effect of the direction of the variation of local angles on the failure load based on the maximum stress criterion for laminates having T_0=0 and uniform fibre volume fraction distributions. It can be seen, there is no difference in the failure load at smaller values of T_1, as fibres in such laminates are relatively straight. Then, that difference becomes clear since the failure load of the laminates having variation in the *y*-direction is higher than that in the *x*-direction.

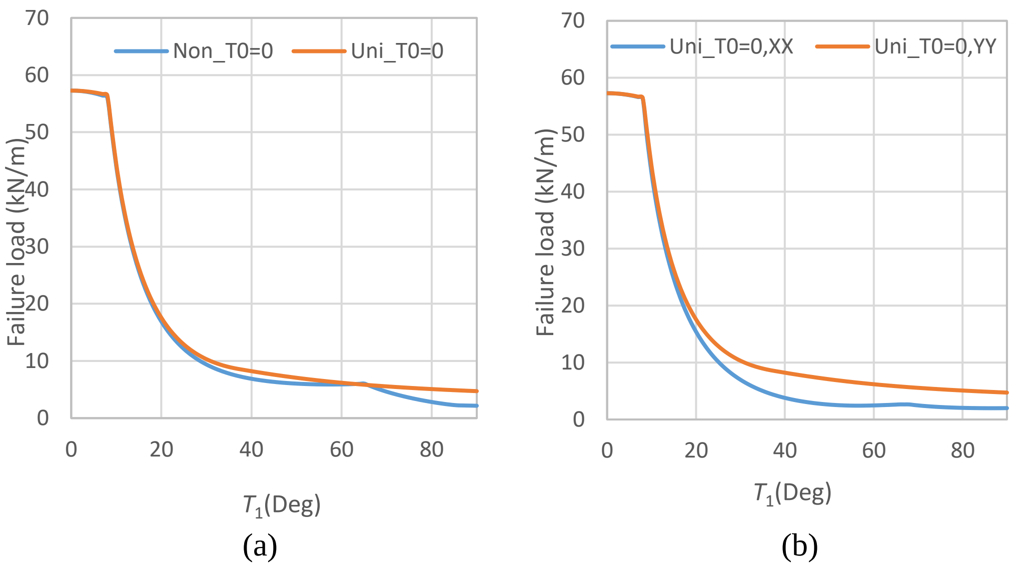

Figure 7.20: Failure loads calculated based on maximum stress criterion in laminates with; (a) uniform and non-uniform fibre volume fraction distributions when $\theta = \theta(y)$ and T_0=0°, and (b) uniform fibre volume fraction distribution when local angles are varied in *x*- and *y*-directions

The failure load curves calculated based on Tsai-Wu criterion are shown Figure 7.21 and 7.22 for the laminates having the local angles varying in the *x*-direction with a uniform and non-uniform distributions of fibre volume fraction, respectively. They have the same trends of failure load. However, the failure load latter case is smaller than in the former case. The failure load curve corresponding to laminates with T_0=0° has the highest value compared to all other curves.

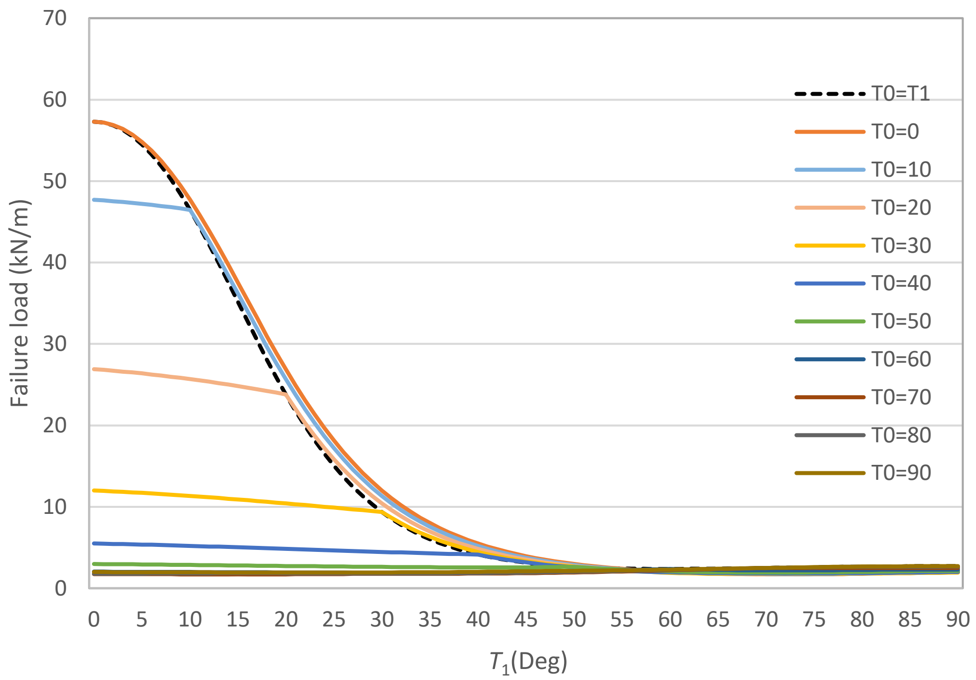

Figure 7.21: Failure load calculated based on the Tsai-Wu criterion for curved fibre laminates [±<T_0 | T_1>]3s having uniform fibre volume fraction and $\theta = \theta(x)$

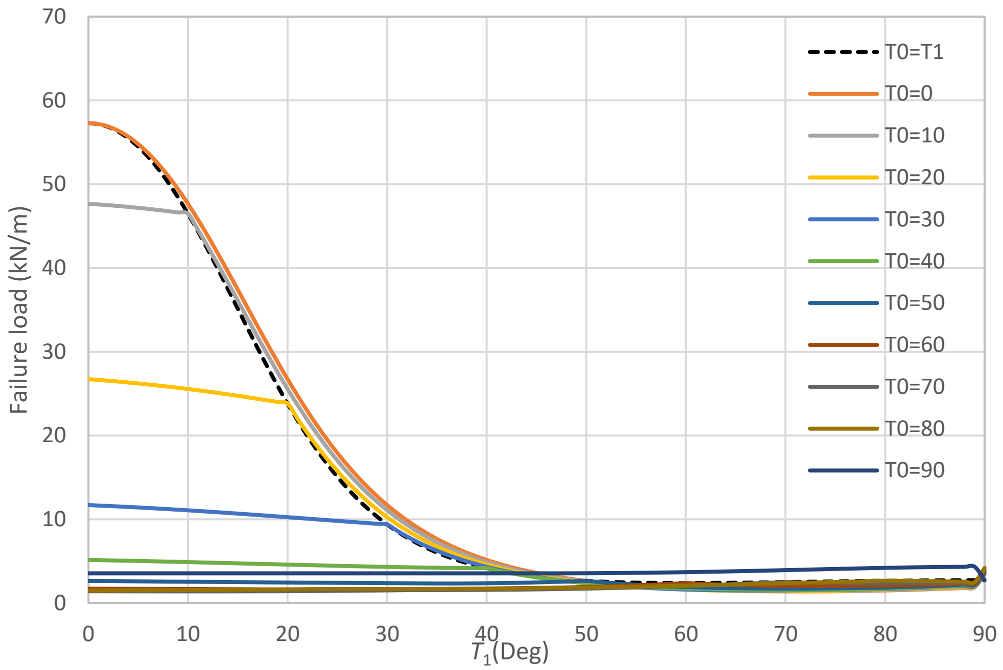

Figure 7.22: Failure load calculated based on the Tsai-Wu criterion for curved fibre laminates [±<T_0| T_1>]3s having a non-uniform fibre volume fraction and $\theta = \theta(x)$

Figure 7.23 and 7.24 show the failure load of the laminates having the local angles varying in the *y*-direction with a uniform and non-uniform distributions of fibre volume fraction, respectively. Qualitatively, the curves calculated for laminates with uniform fibre volume fraction distribution are similar to their counterparts obtained assuming non-uniform distribution. However, in the latter case, the values of failure load are smaller than in the former case.

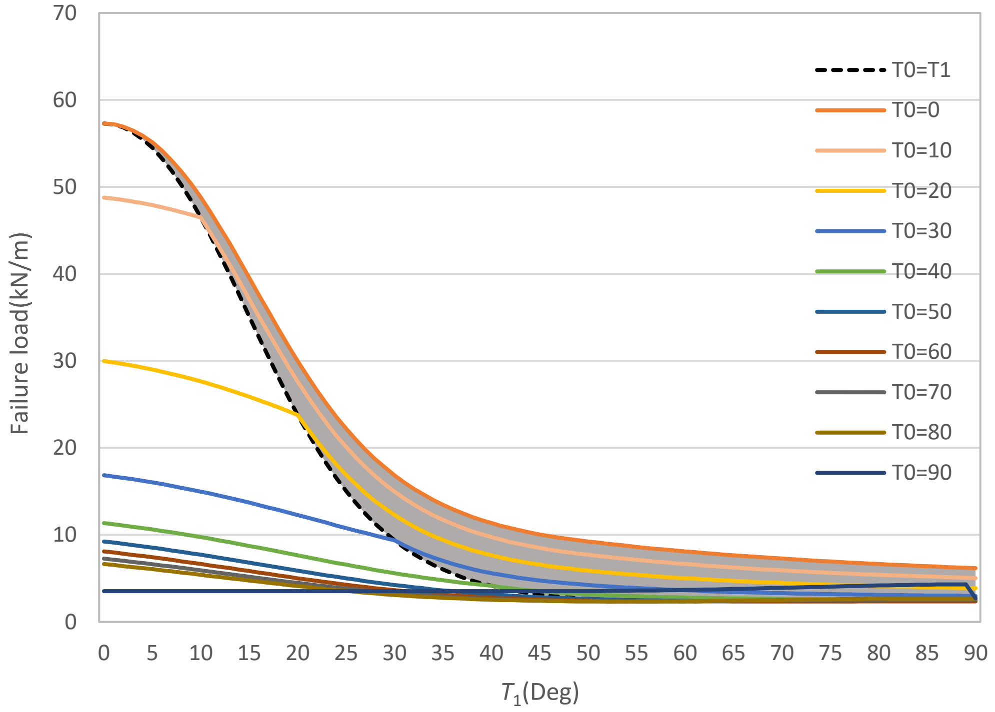

Figure 7.23: Failure load according to the Tsai-Wu criterion for curved fibre laminates [±<T_0 | T_1>]3s having a uniform fibre volume fraction and $\theta = \theta(y)$

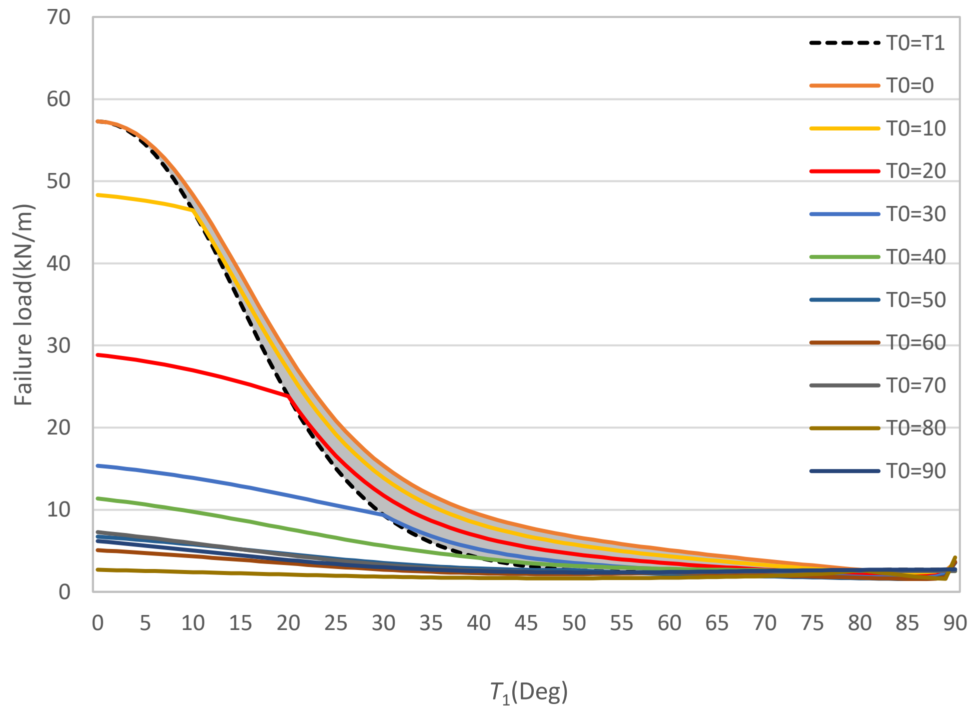

Figure 7.24: Failure load according to Tsai-Wu criterion for curved fibre laminates [±<T_0 | T_1>]3s having a non-uniform fibre volume fraction and $\theta = \theta(y)$

A comparison of failure load curves calculated based on the Tsai-Wu criterion for laminates having T_0=0° with a uniform and non-uniform distributions of fibre volume fraction is shown in Figure 7.25(a). They reveal a slight difference since local volume fraction of fibres of non-uniform distribution is approximately same of the uniform distribution of fibre volume fraction at a single point where failure takes place. For this configuration of laminates, the largest value of the failure index is achieved at the edge of laminate as can be seen in failure index contours in Figure 7.26. Also, there is little variation in the local fibre volume fraction in this case since the placement the tows, in this case, produces a very small gap between them. Therefore, the failure load in panels with non-uniform fibre volume fraction is slightly smaller or the same as in panels with the uniform volume fraction. A comparison between failure loads calculated based on Tsai-Wu criterion for laminates having the variation of local angles in *x*- and *y*-direction with T_0=0° Figure 7.25(b). The curves show the failure loads for the panels with variation in the *y*-direction are higher than those with variation in the *x*-direction.

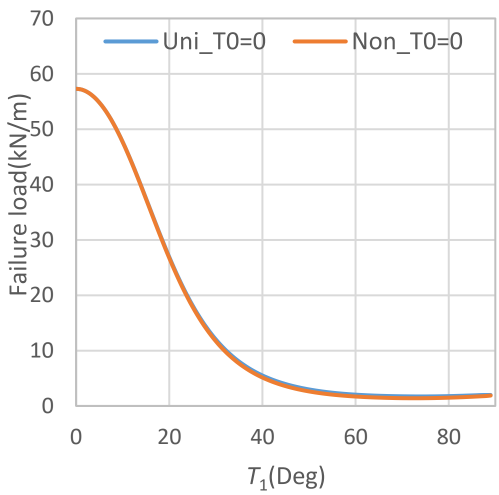

(a)

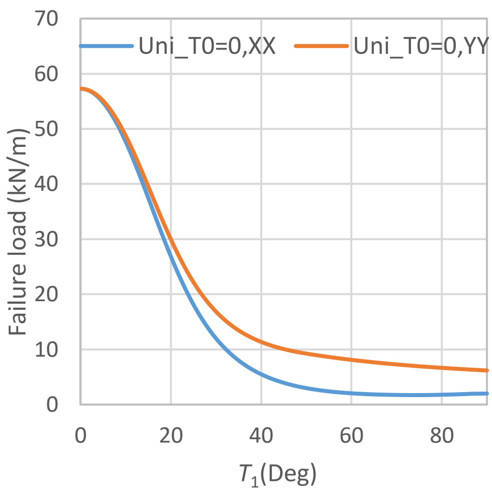

(b)

Figure 7.25: Failure loads calculated based on Tsai-Wu criterion in laminates having; (a) uniform and non-uniform fibre volume fraction distribution, with $\theta=\theta(x)$ and T_0=0°, and (b) a variation of local angle in *x*- and *y*-directions for uniform volume fraction distribution

The contour plots of failure index are shown in Figure 7.26(a)-(d) for the laminates having the uniform and non-uniform of fibre volume fraction distributions. They were obtained for different sets of local angles varying in the *x*-direction. As can be seen, the maximum failure index of Tsai-Wu criterion based on the uniaxial load is at the edges of the laminate when $T_0 < T_1$, while at $T_0 > T_1$, the failure index was equal one at the centre of laminate. In addition, the effect of the gap on predictions of failure index can clearly be seen. Specifically, the area where the failure index is the smallest (dark blue contour) is larger in laminates having a non-uniform fibre volume fraction distribution than in laminates with a uniform fibre volume fraction distribution.

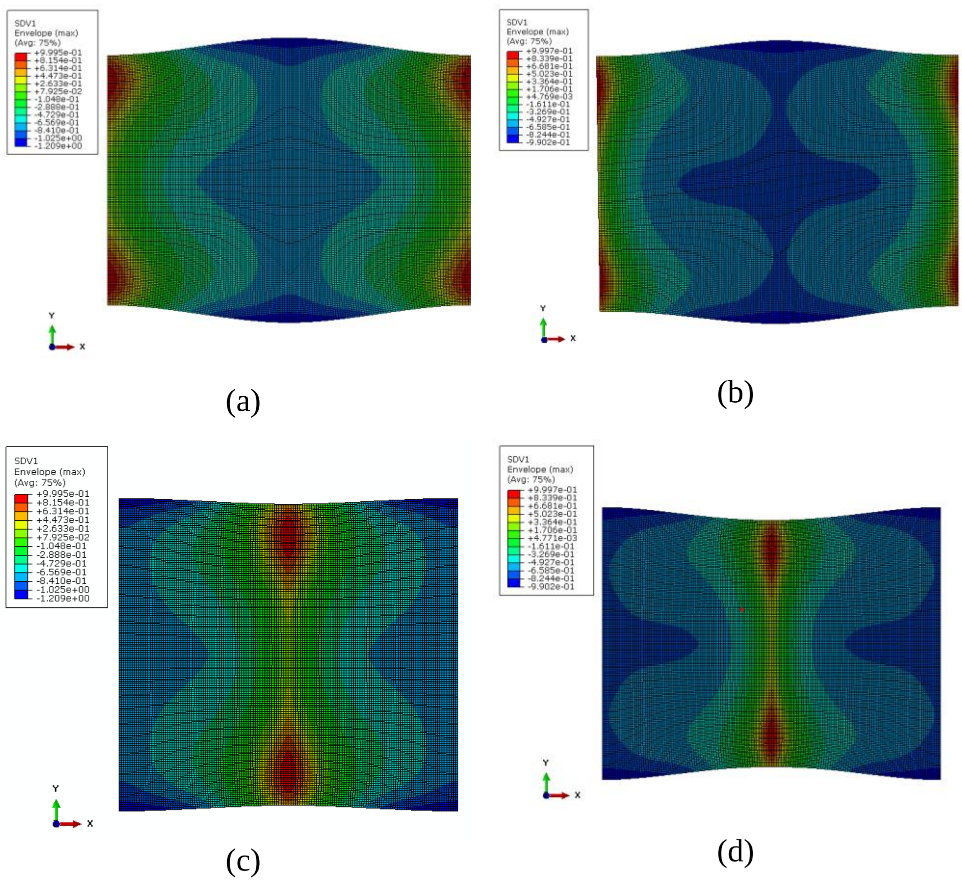

Figure 7.26: Comparison of contour plots of failure index for laminates having uniform and non-uniform distributions and $\theta = \theta(x)$: (a) $T_0 = 0°$, $T_1 = 45°$ uniform distribution, (b) $T0 = 0°$, $T_1 = 45°$ non-uniform distribution, (c) $T_0 = 45°$, $T_1 = 0°$ uniform distribution and (d) $T_0 = 45°$, $T_1 = 0°$ non-uniform distribution

Typical examples of the contour plots of Tsai-Wu criterion failure index for laminates having a variation of local angles in *y*-direction and perpendicular to the applied load are presented in Figure 7.27(a)-(d). Contours in Figure 7.27(a) and (c) were obtained for laminates with uniform fibre volume fraction distribution, whilst those in Figure 7.27(b) and (d) for laminates with non-uniform of fibre volume fraction distribution. As can be seen, the failure index varies according to the variation of the local angles in the *y*-direction.

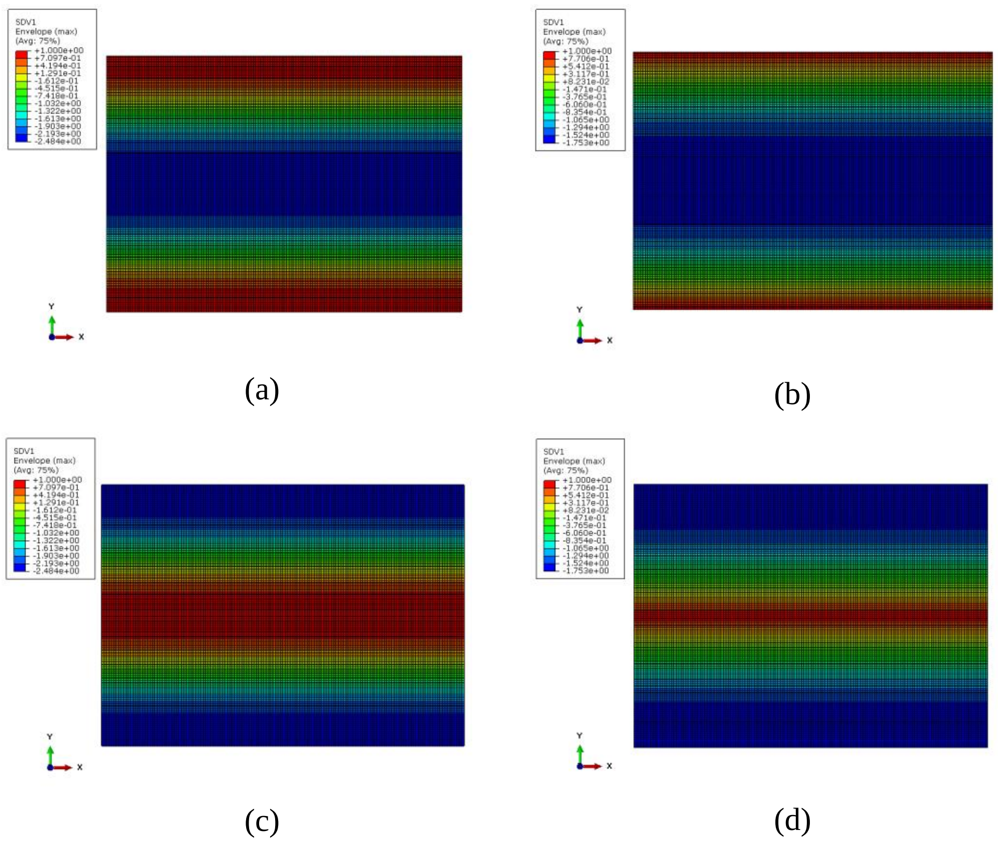

Figure 7.27: Comparison of contour plots of failure index for laminates having uniform and non-uniform distribution and $\theta = \theta(y)$: (a) $T_0 = 0°$, $T_1 = 45°$ uniform distribution, (b) $T_0 = 0°$, $T_1 = 45°$ non-uniform distribution, (c) $T_0 = 45°$, $T_1 = 0°$ uniform distributions and (d) $T_0 = 45°$, $T_1 = 0°$ non-uniform distribution

7.5.4 Optimum fibre path of uniform and non-uniform fibre volume fraction distributions laminates having a cut-out.

To demonstrate the improvement of failure load that could be gained by using the curvilinear tows with laminates having a cut-out, the case study was carried out where a simply supported laminate with a circular cut-out with a ratio of diameter to the length equal to 0.5 was analysed. The uniaxial tensile load was applied in *x*-direction on the laminate edges. The optimum combinations of T_0 and T_1 that should give maximum failure load based on the Tsai-Wu criterion for laminates with uniform and non-uniform fibre volume fractions have been obtained using optimisation framework that was elaborated in Chapter 4. The results are summarised in Table 7.2, along with those obtained for equivalent quasi-isotropic laminate which was used as a benchmark case. The optimum patterns of curvilinear tows are shown Figure 7.28(a) and (b) for laminates with the uniform and non-uniform distributions of fibre volume fraction, respectively.

Table 7.2: Optimum design of the laminates with circular cut-out

Composite laminates with circular cut-out	Optimum design	Failure load (kN/m)
Quasi isotropic	[+45°, -45°, 0°, 90°]s	0.71985
Uniform distribution of fibre volume fraction	$[\pm\langle 23^\circ \vert 5^\circ \rangle]_{2s}$	3.10539
Non-uniform distribution of fibre volume fraction	$[\pm\langle 16^\circ \vert 29^\circ \rangle]_{2s}$	3.1251

It can be seen the failure load in optimised laminates with both the uniform and the non-uniform fibre volume fraction distributions around four times greater than that for the quasi-isotropic laminate. In addition, the maximum failure load for the laminate with the non-uniform volume fraction was approximately same of the laminate with uniform volume fraction.

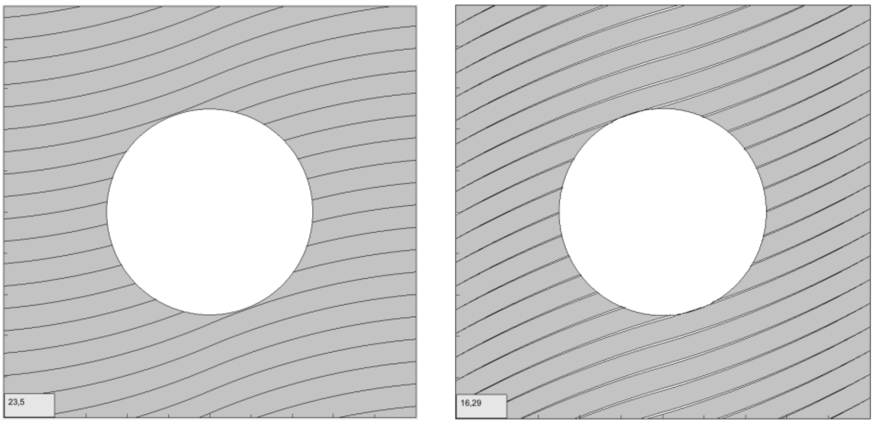

(a) (b)

Figure 7.28: Optimum pattern of a laminate with cut-out; (a) uniform distribution, and (b) non-uniform distributions

7.6 Summary

Failure in the lamina with a curvilinear path of tows under a uniaxial tensile load has been analysed numerically. Lamina was assumed to have failed when failure was predicted in single point of the lamina. Three failure modes were accounted for, namely, the fibre failure, shear and transverse matrix failure. To predict the failure modes a maximum stress criterion has been employed, and failure load curves were generated, which could comprise up to three parts corresponding to different failure modes. When using Tsai-Wu criterion, the failure load curves were predicted to be smooth since the criterion is defined by polynomial equation and does not allow for distinction between different failures modes.

In order to apply failure criteria, such as maximum stress or Tsai-Wu criteria, local material strengths should be obtained first, since the fibre volume fraction changes locally as a result of changing the gap width along the lamina. They were calculated based on the properties of fibre and matrix properties. A number of assumptions were employed to determine local strengths from the micromechanics considerations. In order to determine the strengths, minimum (threshold) value of fibre volume fraction has been calculated and compared with that calculated for cases where a change in gap width along the lamina was accounted for. The minimum (threshold) value of fibre volume fraction calculated based on the strength parameters is smaller than that in laminae with a variable gap.

The linearisation of the Tsai-Wu failure criterion has been conducted. Use of this form of criterion helps to reduce the computational costs when applying it in FE modelling, as it requires only two load increment to predict the load corresponds to a unity failure index in the conventional Tsai-Wu criterion. This approach does not calculate the failure index below and above the unity, just gives a point that corresponds to the unity of the failure index.

The failure indices were calculated based on the maximum stress and Tsai-Wu criterion for laminae as well as the laminates with different configurations on curvilinear tows having a variation of local angle in *x*- and *y*-directions. The failure load in laminates has been obtained by first ply failure. The calculations were carried out for laminates with both the uniform and non-uniform fibre volume fractions. Since the failure load was defined as the load when the failure criteria are first satisfied in single point of a lamina, the failure load for some patterns of curvilinear fibre panels with non-uniform fibre volume fraction show only a marginal or no difference with that in panels with a uniform fibre volume fraction even if the gap size in the lamina is large. The failure in lamina initiated at a location of the large value of the local angles and this is stated clearly in the contour plot of the failure index. For the variation of local angles in the *y*-direction, the in-plane resultant $N_x(y)$ varies as function of *y*-coordinate, and this could increase the predicted failure load than that for the case of variation in the *x*-direction.

The local angles in curved fibre laminates can generate a variable gap width which would lead to a redistribution of the stresses. Therefore, the failure index at every single point in a laminate can be locally dependent on the local angle and local gap width. The laminate was considered to have failed when a single point in any lamina failed. This approach to failure definition was employed in the optimisation study aiming to maximise the failure load of laminate with cut-out. The numerical results of curved fibre laminates showed around four times improvement in the failure load as compared with quasi-isotropic laminates.

8 Unit cell model for curved tows with gaps

8.1 Introduction

One of the most important advantages of fibre-reinforced laminated composites is that change the stiffness and strength properties of the laminate can be changed by changing the orientation of fibres and/or changing the stacking sequence. In addition, the ability of steering fibre tows along a curved path offers more flexibility in the design of laminates of the required stiffness and strength properties. The study of Gurdal and Olmedo (1993) introduced a linear variation of local orientation for the fibre path. The local angles vary along the *x*-axis or *y*-axis in the model. Gürdal et al. (2008) generalised the procedure of varying the local angles relative to an auxiliary axis at a given angle φ to the *x*-axis, instead of limiting varying the angle only to the *x*- or *y*-direction.

A constant thickness of ply without overlaps is ensured by placing the curved tows that having a linear variation of local angles, side by side. Therefore, a gap with a variable width between the neighbouring tows is present, as shown in Figure 8.1. This results in the local fibre volume fraction, which changes from point to point and causes the mechanical properties to change locally. In order to define these local material properties via a single value of the effective material properties, many assumptions have been made and numerous techniques adopted such as rule of mixtures (Voigt, 1889), the inverse rule of mixtures (Reuss, 1929), modified rule of mixtures and Halpin–Tsai model (Halpin and Kardos, 1976). However, the existence of the periodicity in the geometry of the composite structure and the multiscale nature allow to use a finite element-based numerical approach using a unit cell (UC) model (Li, 2001, Li and Wongsto, 2004, Li, 2008 and Li et al., 2011a) which can homogenise the composite and evaluate the effective elastic stiffness properties.

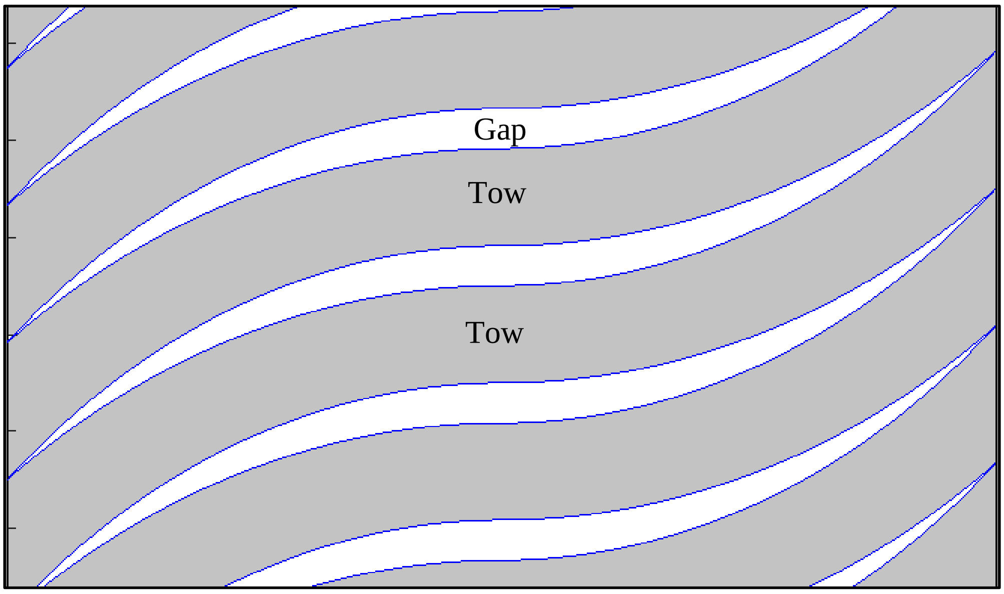

Figure 8.1: The curved fibre of linear variation of orientation with gaps

8.2 Relative displacement field under uniform microscopic strains

In order to implement the unit cell procedure, the stress and strain states at the macroscopic scale are assumed to be uniform. In addition, periodicity is assumed in the architecture of the material. These assumptions allow the use of a unit cell to predict the effective properties. The relative displacements will be given in a state corresponding to uniform strains at the macroscopic scale. UCs in Figure 8.2 will be referred to in order to illustrate the relative displacement for the periodic geometry as follows.

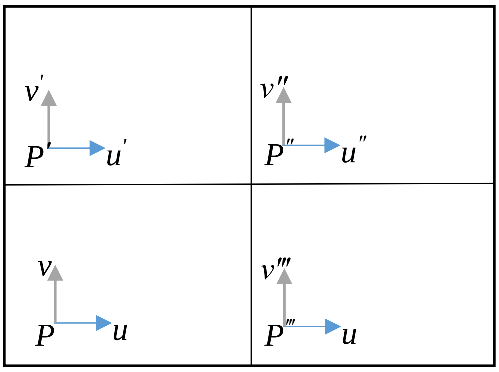

Figure 8.2: A periodic geometry and the relative displacements

In Figure 8.2, point *P* is an arbitrary point that acts as a reference on a certain unit cell that could reproduce itself to cover all areas of geometry; *P′, P″, P‴* are the images of *P* in other cells, *u* and *v* the in-plane displacements in the *x*- and *y*-directions, respectively, at point *P*, and (*u′*,*v′*), (*u″*,*v″*) and (*u‴*,*v‴*) are those at *P′*, *P″*, *P‴*, respectively. The relationship between displacements of point *P* and any point of *P′* can be described as in the study of Li and Wongsto (2004), and the similar relationships can also be obtained for *P″* and *P‴* as well.

$$u' - u = (x' - x)\varepsilon_x^0 + (y' - y)\gamma_{xy}^0 + (z' - z)\gamma_{xz}^0$$

$$v' - v = (y' - y)\varepsilon_y^0 + (z' - z)\gamma_{yz}^0 \tag{8.1}$$

$$w' - w = (z' - z)\varepsilon_z^0$$

where x, y and z are the coordinates of point *P*, x', y' and z' are the coordinates of point *P*', and $\varepsilon_x^0, \varepsilon_y^0, \varepsilon_z^0, \gamma_{xy}^0, \gamma_{xz}^0$ and γ_{yz}^0 are the macroscopic strains.

When expressing the relative displacement in terms of macroscopic strains, the rigid body rotational degrees of the *x*-axis about the *y*- and *z*-axes and the *y*-axis about the x-axis have been eliminated by assuming the following as elaborated in the study of Li and Wongsto (2004).

$$\frac{\partial w}{\partial x} = \frac{\partial v}{\partial x} = \frac{\partial w}{\partial y} = 0 \tag{8.2}$$

In addition, to prevent rigid body movement in the model, the three rigid body translations are eliminated by constraining the displacements at an arbitrary point by assuming

$$u=v=w=0. \tag{8.3}$$

Different ways of constraining the rigid body rotations lead to different coefficients of Equation (8.1) and may result in different presentations for periodic boundary conditions. The difference between them is by a rigid body rotation and hence does not affect the strain field.

8.3 The geometry of the unit cell model

The unit cell model consists of a curved tow with its gap. The curved tow has its local orientation that varies linearly along the x-axis according to the Gürdal et al. (2008) from T_0 at the centre of model and T_1 at the end of positive x, as follows:

$$\theta(x) = T_0 + (T_1 - T_0)\frac{2x}{a} \tag{8.4}$$

The actual path $y(x)$ of the centre line of the tow, as shown in Figure 8.3 in blue dash-dot can be found by integrating the Equation (8.4) as follows:

$$y = \int_0^{L/2} \tan\big(\theta(x)\big)\, dx \tag{8.5}$$

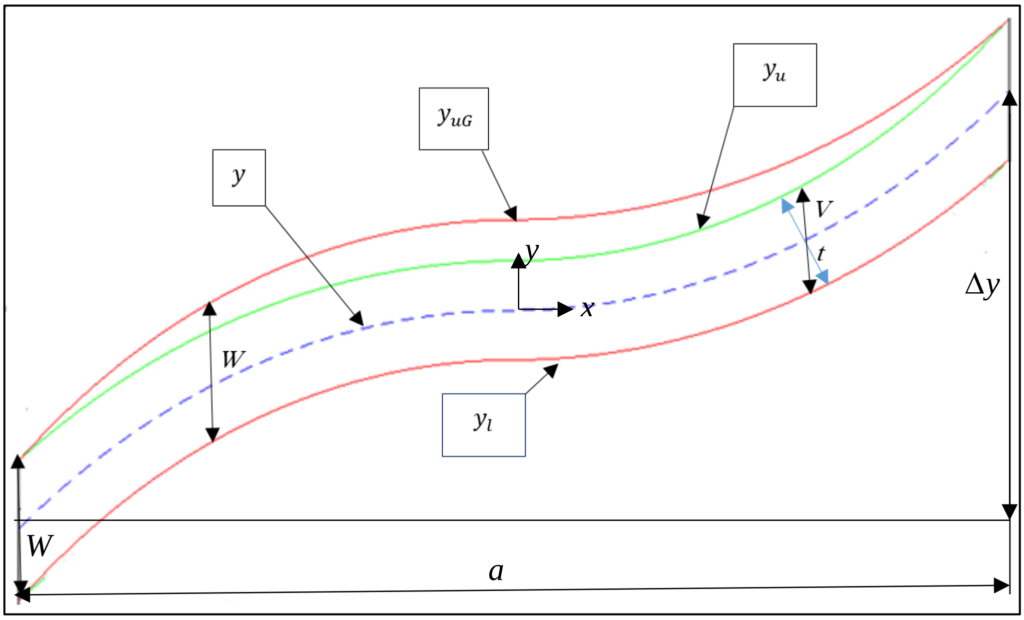

Figure 8.3: A sketch showing the dimensions of the UC model (tow plus gap)

The centre line of the tow will be as follows:

$$y = -\frac{\ln\left|\cos\left(\frac{2x\,(T1-T0)}{a}+T_0\right)\right|}{\left(T_1-T_0\right)\frac{2}{a}} + \frac{\ln|\cos T_0|}{\left(T_1-T_0\right)\frac{2}{a}} \tag{8.6}$$

where a is the length of UC in the x-direction.

The upper edge of the tow y_u is calculated by adding half of the vertical distance of the tow and can be given as follows:

$$y_u = y + v/2 \tag{8.7}$$

where v is the vertical distance of tow and defined as follows:

$$v = \frac{t}{\cos\left(\frac{2x\,(T1-T0)}{a}+T_0\right)} \tag{8.8}$$

where t is the tow width in the direction perpendicular to the centre line.

The lower edge of tow y_l is as follows:

$$y_l = y - v/2 \tag{8.9}$$

It will be taken as the lower boundary of the UC. Since the gap is formed by placing tows next to each other while following the identical path but shifted above, each UC will have to include a gap, and the upper boundary of the UC model is therefore defined by y_{uG} as follows

$$y_{uG} = y - v/2 + W \tag{8.10}$$

where W is the vertical distance of the UC model

$$W = t/\cos T_1 \tag{8.11}$$

One can define the difference between the *y*-coordinates Δy of both ends of the centre line of the model (tow and gap) as follows:

$$\Delta y = WN/2 \tag{8.12}$$

where *N* is the number of models that cross one model to cover the area.

8.4 Geometric periodicity and periodic boundary conditions

Given the complicated geometry, FE modelling is necessary to analyse the UC while incorporating geometrical characteristics of the structure. With the linear variation of the orientation of curved tow in the *x*- or *y*-direction as defined in (Gurdal and Olmedo, 1993), the way of placing the tows next to each other, avoiding overlapping between the neighbouring tows, would leave a gap between the tows. The geometry of the gap varies along the path of tow. A regular pattern forms as gaps and tows repeat themselves and are joined together to cover all area of the layer. Alternatively, one may consider that the complete layer has been tessellated into an array of unit cells as shown in Figure 8.4. Several studies (Meijer et al., 2000 and Li and Wongsto, 2004) have used different idealised particle-matrix packing systems and differently shaped UCs have been obtained. The tessellation of gap and tow can be incorporated into a pattern, as shown in Figure 8.4 representing a ply in an angle-ply laminate with two layers. With one of the blocks from each ply, a unit cell as shown in Figure 8.5 can be introduced. Translating it up, down, left and right will cover the complete volume of the laminate.

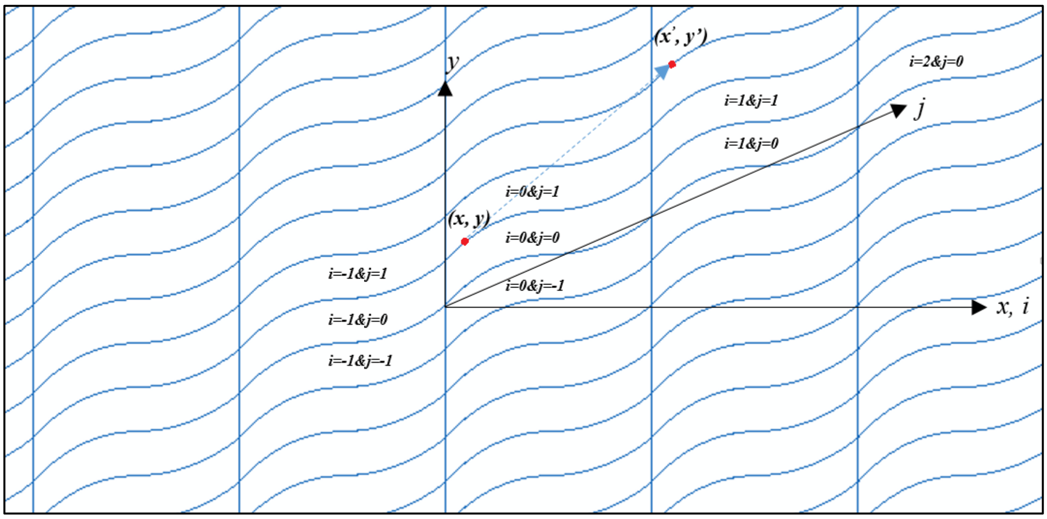

Figure 8.4: Front view of the cells for periodic pattern

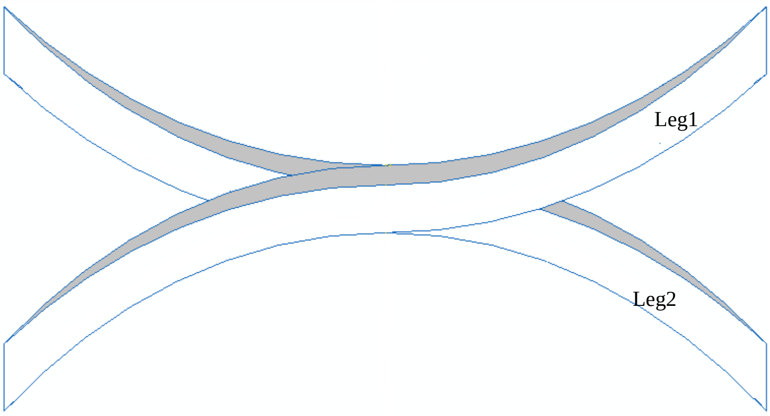

Figure 8.5: A single unit cell with curved tows with and companion gaps

The periodic boundary conditions (PBCs) are a set of boundary conditions of any representative volume element (RVE) that satisfy the geometric periodicity of the microstructure. They are necessary requirements as a part of the formulation of the physical problem. In a mechanical problem of deformation, for example, PBCs of displacement field are required by the deformation kinematics as the displacement continuity condition to avoid non-physical deformations in the deformable body. The PBCs could be obtained according to the state of symmetry.

8.4.1 PBCs of translation symmetries

This type of PBCs is based on the translational symmetry, where the location of UC can be in any of the directions of the translational symmetries by any distance as the multiplicity of the corresponding distances of translation. The UC reproduces itself by the vector of distances $\Delta x, \Delta y, \Delta z$. The existence of translational symmetry for the geometry and the physical properties is a necessary condition for the symmetry of physical fields (Li, 2001).

The relationship between a point in the original cell and its image in another cell could be identified for leg 1 and leg 2, respectively, in a cell as shown in Figure 8.5. In order to describe the periodicity of in the ply represented by leg 1, the two translations along axes i and j (i.e. *y*), respectively, are employed, as shown in Figure 8.4. Thus, the mapping of any point to its image can be described by integers *i* and *j* and the relationship between their coordinates becomes as follows:

$$x' - x = i\, a \tag{8.13}$$

$$y' - y = i\, \Delta y + W\, j \tag{8.14}$$

where the (x, y) is the coordinate of a point on the origin cell in leg1, and (x', y') is the coordinate of the image point on the cell (i, j) in leg1. Δy is defined by Equation (8.12).

Leg 2 can be obtained by a 180° rotational symmetry of leg 1 about the *y*-axis as shown in Figure 8.6. The relationship of *x*-coordinate of a point in origin cell in leg 2 and its image in leg 2, should be similar to that of leg 1 but with a negative sign to the *x*-coordinate, while the relationship of *y*-coordinate stays to the same as that of leg 1, given as follows:

$$x' - x = -i\, a \tag{8.15}$$

$$y' - y = i\, \Delta y + W\, j \tag{8.16}$$

In order to avoid redundant constraints of PBCs, the edges in UC model should be excluded from the faces, and the vertices should be excluded from the edges, with the constraint equations for the edges and vertices defined separately. Figure 8.6 describes the names and position of faces of the UC model, and their constraint equations are summarised in Appendices

Appendix A. Figure 8.7 specifies 24 edges of UC model and each leg has 12 edges, the constraint equations of these edges are given in Appendix B. The vertices positions and their constraint equations are given in Figure 8.8 and Appendix C, respectively. According to the rules for equation constraints in Abaqus/Standard (2017) the first degree of freedom on the left side of the equation is eliminated. Therefore, all equations of constraints have been prepared in a manner that prevents a single degree of freedom appearing in the first term of two different constraint equations.

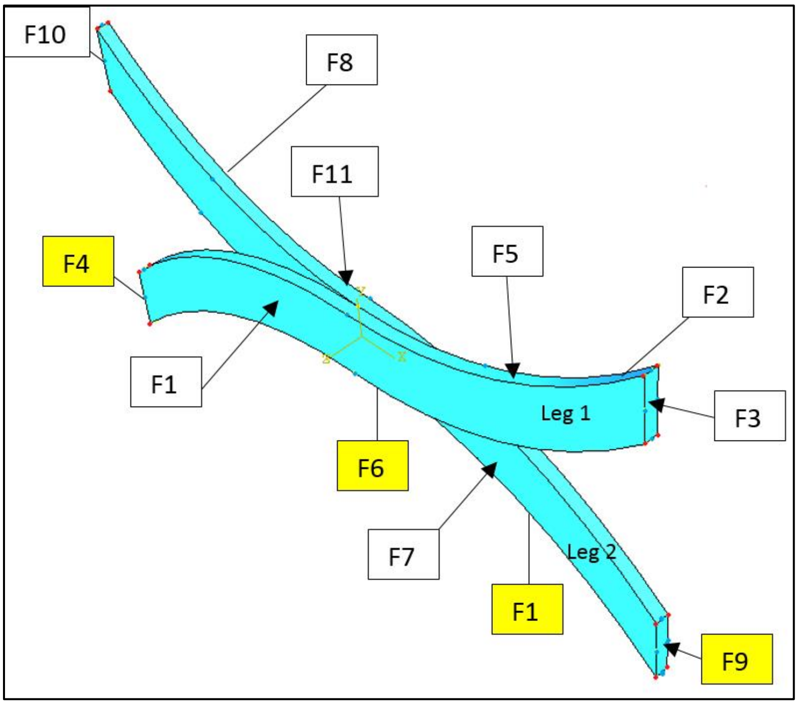

Figure 8.6: Faces of a unit cell

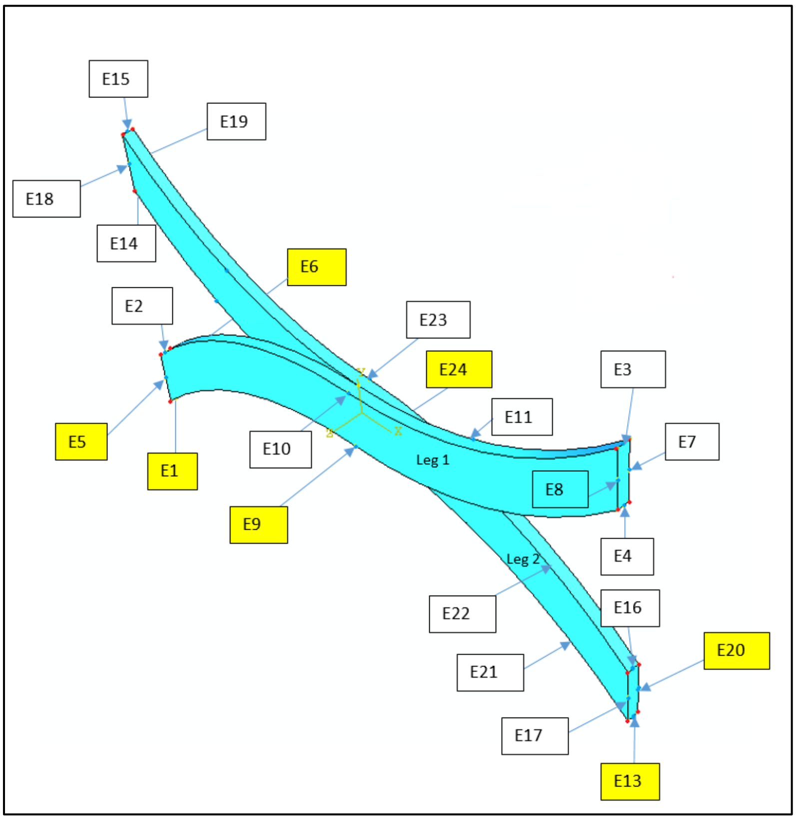

Figure 8.7: Edges of a unit cell

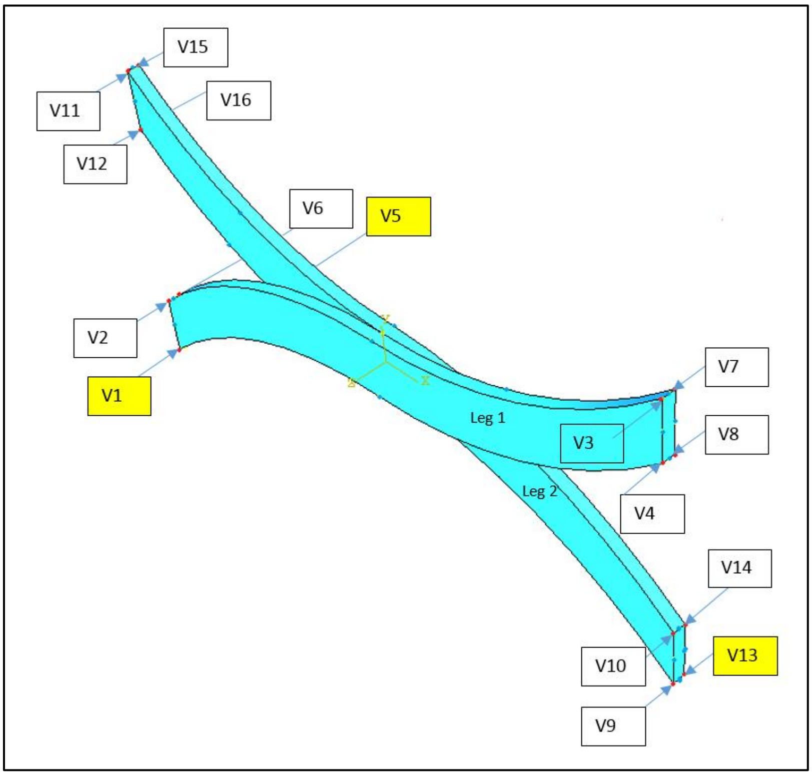

Figure 8.8: Vertices of a unit cell

8.4.2 PBCs of Translation symmetries in the interface area.

The interface area refers to the surface area that is formed between two adjacent laminae in a continuous fibre composite. In order to model the laminate (two laminae) and fulfil load transfer between the adjacent laminae over the interface area, the perfect bonding is assumed. This assumption could be implemented by using periodic boundary conditions in this area, requiring the displacements on the right and left side of the interface area to be equal. The proposed unit cell consists of two legs (tow and its gap) as shown in Figure 8.5, and the laminate is produced by arranging cells in a periodic manner. The effect of perfect bonding between cells over the interfaces implies that stacked legs from different cells are involved. Therefore, the legs of the unit cell have to be divided into many segments as shown in Figure 8.9, and the number of segments on the left or right side of a leg could be defined as the number of legs that cross another leg in one cell $N = \frac{2*\Delta y}{w}$. Furthermore, each segment within the interface area of leg 1 should be related to the corresponding segment on leg 2 by the equation of periodic boundary conditions as illustrated in Appendix D, to satisfy the continuity, i.e. perfect bonding achieved.

The equations of PBCs in the interface area are obtained from the distances of translations in the vertical direction between the segments of the lower and upper legs.

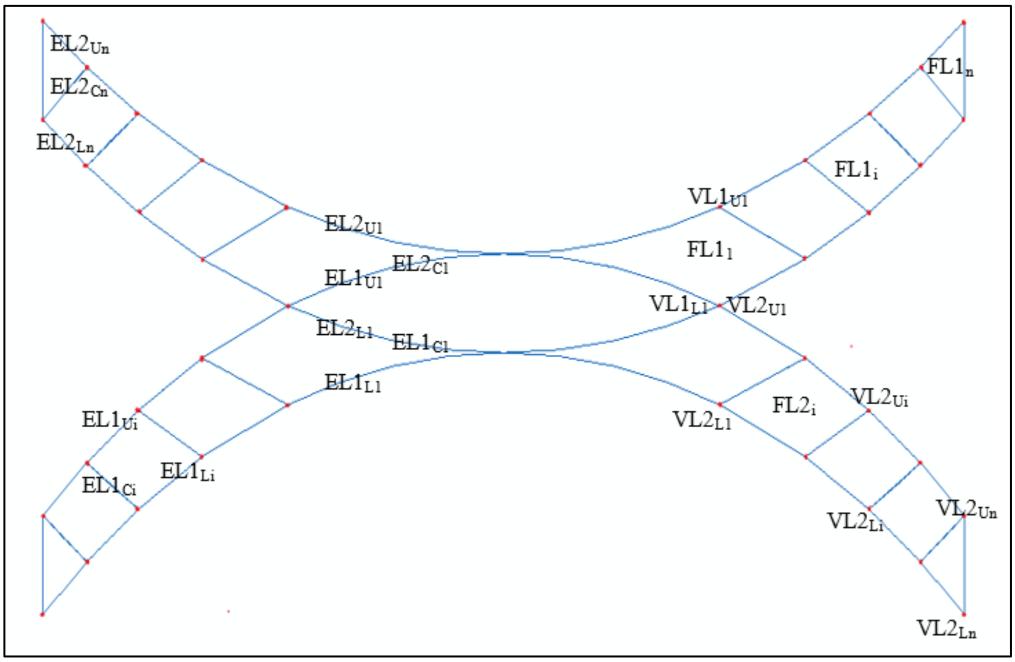

Figure 8.9: Interface area with a divided area

where $FL1_i$ and $FL2_i$ are faces at segment *i* of leg 1 and leg 2, respectively. $EL1_{Ui}$, $EL1_{Li}$ and $EL1_{Ci}$ are the upper, lower and crossing edges, respectively, at segment *i* of the leg 1. $EL2_{Ui}$, $EL2_{Li}$, $EL2_{Ci}$ are the upper, lower and crossing edges, respectively at segment *i* of the leg 2. $VL1_{Ui}$ and $VL1_{Li}$ are upper and lower vertices, respectively, at segment *i* of the leg 1 and finally, the $VL2_{Ui}$ and $VL2_{Li}$ are upper and lower vertices, respectively, at segment *i* of the leg 2 as shown in Figure 8.9.

8.5 Effective material properties.

According to the micromechanical analyses that are used in a unit cell, the response of the unit cell under the applied load offers microscopic stress, strains and displacement distributions, whilst in order to obtain the effective material properties of the unit cell, the macroscopic or average responses are required, since the effective material properties are defined from the relationships between the macroscopic stresses and strains. With the formulation of the UCs employed here, either macroscopic stresses or strains can be applied as the load and others will be the response. For instance, if the macroscopic strain is applied to the unit cell, the macroscopic stresses need to be calculated. As the finite element analysis used for unit cell analyses, the reaction forces at the key degrees of freedom are obtained directly and are related to the macroscopic stresses as follows (Li and Sitnikova, 2018b):

$$F_x = \sigma_x^0 V \tag{8.17}$$

$$F_y = \sigma_y^0 V \tag{8.18}$$

$$F_{xy} = \tau_{xy}^0 V \tag{8.19}$$

where *V* is the volume of the unit cell and *F* is the reaction force with a dimension of force time length.

The in-plane effective material properties can be described as follows:

$$E_x^0 = \frac{\sigma_x^0}{\varepsilon_x^0} = F_x/V\varepsilon_x^0 \tag{8.20}$$

$$E_y^0 = \frac{\sigma_y^0}{\varepsilon_y^0} = F_y/V\varepsilon_y^0 \tag{8.21}$$

$$G_{xy}^0 = \frac{\tau_{xy}^0}{\gamma_{xy}^0} = F_{xy}/V\gamma_{xy}^0 \tag{8.22}$$

8.6 Mesh

In finite element analysis, a reasonable mesh is required for numerical convergence, especially in applications that have non-uniform stress distribution and stress concentrations. On the other hand, additional requirements must be involved in the mesh to implement the UCs. To implement the periodic boundary conditions that satisfy the continuity, the opposite corresponding faces must share the same mesh pattern. The identical mesh pattern could be achieved by using the copy function and seed the edges in Abaqus/Standard (2017) to duplicate a mesh pattern from one face to another. One may also use the Python script to automate the process. The appropriate mesh density that satisfies the convergence of the effective material properties could be achieved relatively easier than other aspects, such as stress distribution.

For more complex geometries of composites like in textile composites, UC models can be meshed with voxel mesh in TexGen developed by the University of Nottingham (TexGen, 2014). A model of the unit cell with voxel mesh would be acceptable to calculate the effective elastic material properties. However, it becomes unsuitable for implementing the curved tow and its variable gap because the stress distribution at the interface (matrix/tow) would be unrealistic. Thus, the predicted effective strengths would become irrelevant. In addition, the voxel mesh cannot describe the right variability of the gap in the model because the interface between the two faces would not be smooth as shown in Figure 8.10 in the case of plain weave textile preform. Such artificial discontinuity will also be imposed on the material properties which are assigned to the elements and will not reflect the real geometric characteristics.

The mesh quality also depends on the type of elements used in the unit cell model. For instance, the hexahedral elements are economic in terms of the number of elements because at the same number of degrees of freedom for one hexahedral element it corresponds to six tetrahedral ones. Therefore, the CPU time required to calculate the stiffness matrix and mass matrix is less than that used in the case of tetrahedral elements (Cifuentes and Kalbag, 1992 and Tadepalli et al., 2011). In addition, the hexahedral elements could be considered a good choice to avoid the mesh distortion problem in textile composites. The tetrahedral elements have been used a lot because they fit very well arbitrarily shaped geometries with their simple topology and their surface patterns can be easily copied from one face to another to accomplish the requirements of PBCs.

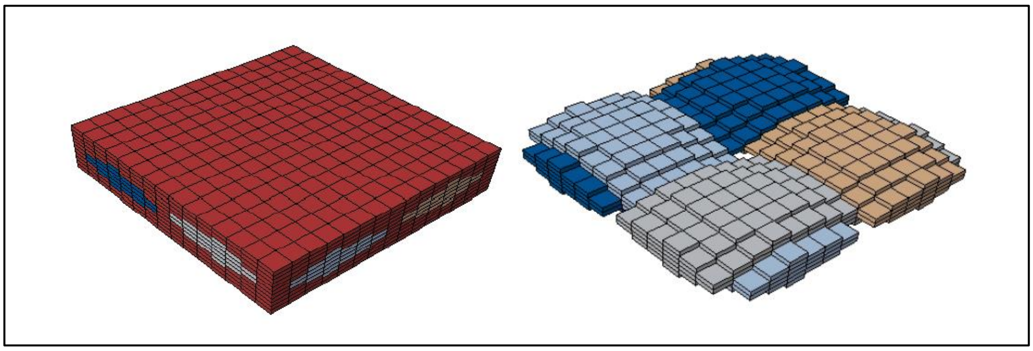

Figure 8.10: Voxel mesh for textile wave model in TexGen

8.7 Verification

Verification for the unit cell model has been performed to ensure FE model is working perfectly and is defined as follow.

8.7.1 Sanity check verification

When any new FE model is produced, its verification is essential. ‘Sanity checks’ are some simple checks to quickly evaluate whether boundary conditions have been imposed correctly, or if the calculated results make sense. These checks have been conducted for the model developed here to ensure that the opposite faces have been tessellated identically, the boundary conditions have been imposed appropriately, and the macroscopic strain states have been defined correctly for the unit cell. A correct procedure should give uniform stress and strain distribution if the material properties of two phases are the same and isotropic. The results of such analyses employing the same material properties should not be affected by the mesh density because of the uniform stress distribution and uniform deformation. Most errors that appear during the production of the analysing unit cell from formulation and implementation can be eliminated at this step. Passing the ‘sanity checks’ is a necessary step, and usually the most demanding step, for the establishment of any unit cell model.

8.7.2 Checking by modelling with straight tow

Since a straight tow can be considered as a special case of the curved tow, where the variation of orientation is equal to zero, and there is no gap between the adjacent tows. The outcome of this case should reproduce the available theoretical results of UD laminates having the same orthotropic material properties and angle orientation.

This verification used the same procedure as was followed in the study of Xia et al. (2003). It used the FEM micromechanical analysis for unidirectional and angle ply laminates subject to multiaxial loading conditions. This study showed a good agreement between the micromechanical results obtained based on the properties of two constitute (fibre and matrix) and the experimental results.

Verification of the UC model with the straight tows is based on comparison with the results obtained based on the classical laminate theory (CLT), using which one can find strains, displacements and curvatures that are produced in the laminates as a result of the thermal and mechanical loading as described in Chapter 3. The calculated stresses and strains are used to determine the stress resultant force in order to calculate the equivalent in-plane stiffness and compare it with that of the UC model.

Table 8.1: Material properties of constituents (Kaddour et al., 2013)

Property	Glass fibre	Matrix (8552 epoxy)
Elastic modulus *E* (GPa)	74	4.08
Major Poisons's ratio v_{12}	0.2	0.38
Elastic shear modulus *G* (GPa)	30.8	1.478
Fibre volume fraction of tow	60%	

8.8 Results and discussion

In order to determine the effective elastic properties accounting for variable gap and variation in local fibre orientation, three different cases of unit cell models are considered to be presented sequentially. The constituent material properties of fibre and matrix used in these cases are extracted from Kaddour et al. (2013) as shown in Table 8.1

To determine the in-plane effective elastic constants, three kinds of the load should be applied, namely, the uniaxial loads in both vertical and horizontal direction and pure shear. These loading cases are applied on faces, edges and vertices according to the constraint equations.

The first case considered a UC with a single straight tow without a gap. It is dealt with as a UD composite with a uniform fibre volume fraction at 60%. The purpose of this case is to check how well results obtained with a straight tow UC model and compare with results obtained from the CLT.

The second case was conducted for a UC with a single curved tow according to the linear variation of local angles.

The third case deals with the two layers of curved tows with their corresponding gaps in configuration $\pm\theta$. This UC model, in this case, is more complicated because of the existence of the connection area between the two curved tows. It illustrates the difference between the responses of the laminate and the lamina.

8.8.1 Case one

The first case involves a single straight tow inclined at T_0=T_1 =15° with respect to the *x*-axis, under three kinds of applied load to obtain in-plane stiffnesses, is shown in Figure 8.11. When a homogeneous isotropic material is employed for the tow, a uniform stress field has been obtained as shown in Figure 8.11(a). It is equal to the applied macroscopic stresses. This result confirms that the periodic boundary conditions were imposed correctly. If there were any mistakes, it would be clear during that stage as non-uniform stresses or abnormal shapes of deformation would be predicted. In order to reproduce the in-plane effective material properties, three loading conditions have been considered, where common boundary conditions were shared. Figure 8.11(b), (c) and (d) present the local stresses σ_{11}, σ_{22} and σ_{12}, respectively, for the respective loading conditions. These stresses over the UC represent the effective stresses from which one can calculate the effective properties of the material represented by the UC. The effective properties can be obtained from the reactional forces at the key degrees of freedom after dividing them by the volume of the UC (Li et al., 2011a).

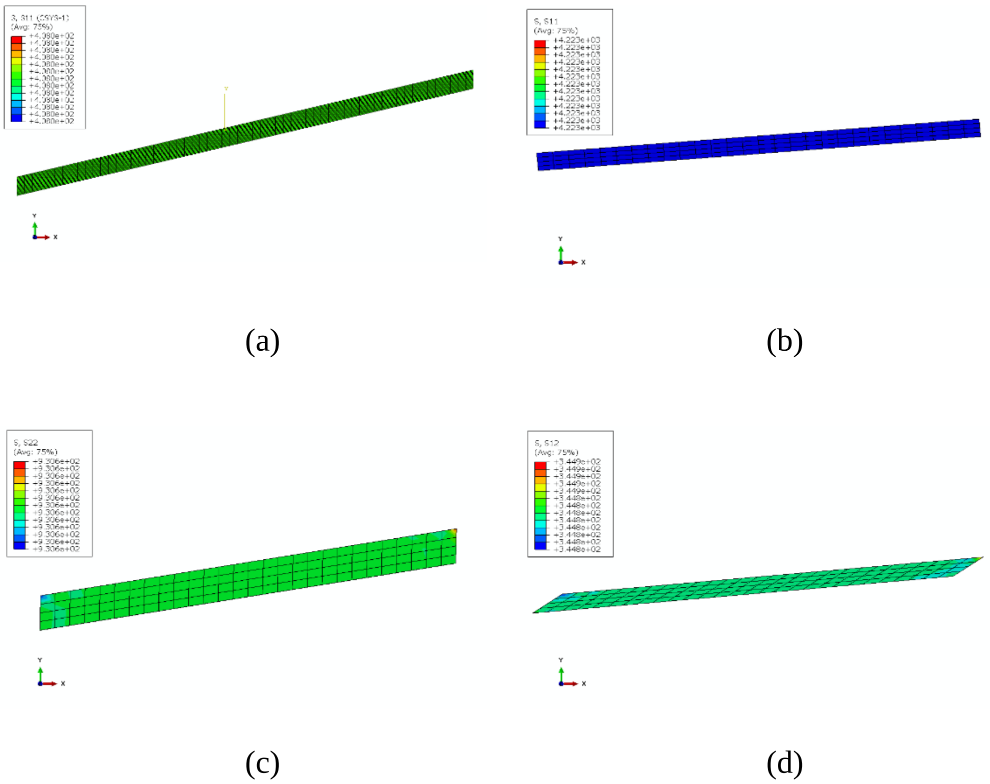

Figure 8.11: UC model of straight tow with T_0=T_1=15°; (a) σ_{11} of isotropic material under loading in *x*-direction, (b) σ_{11} of UD material under loading in *x*-direction, (c) σ_{22} of UD material under loading *y*-direction, and (d) σ_{12} of UD material under shear loading

Figure 8.12 and 8.13 present a comparison between the effective material properties E_x and G_{xy}, respectively, from the UC model and their counterparts obtained based on the CLT. They show good agreement.

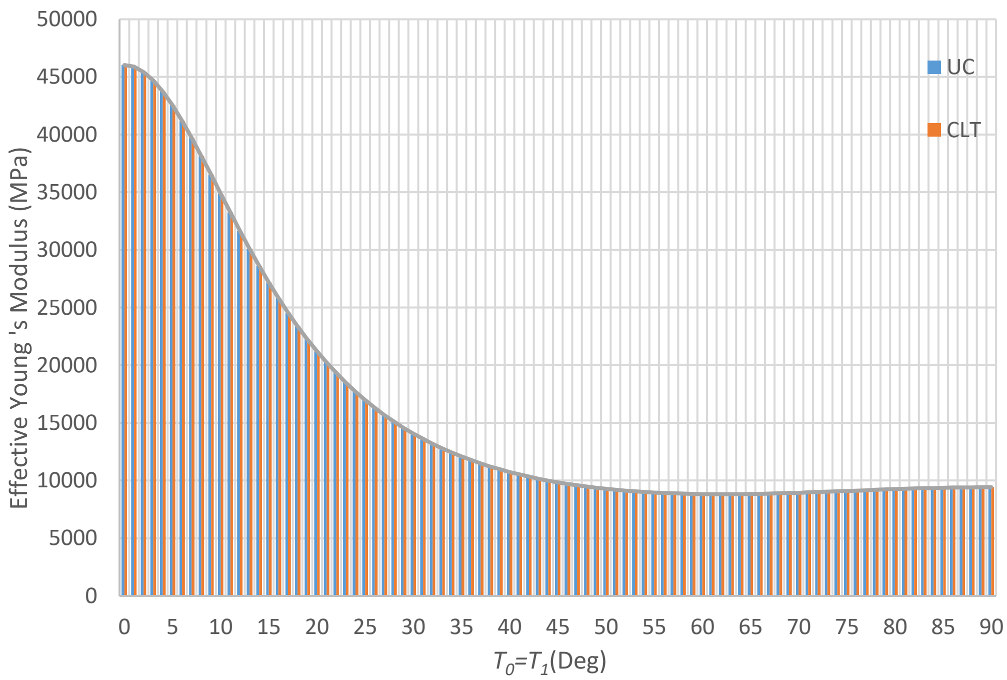

Figure 8.12: A comparison of effective elastic modules E_x for straight fibre UC obtained with CLT and UC FE modelling

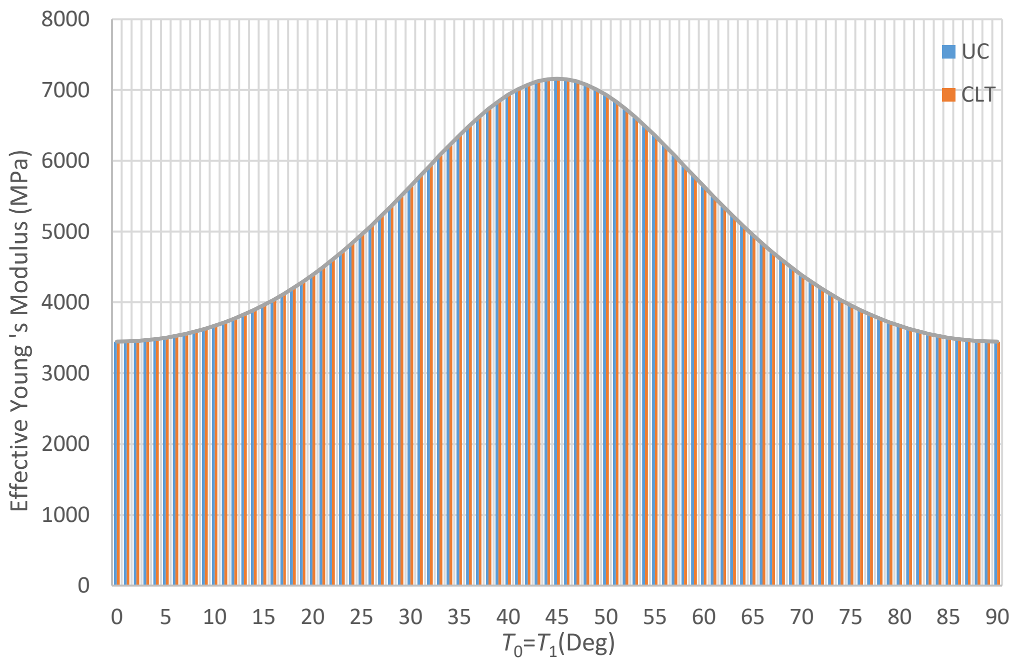

Figure 8.13: A comparison of effective shear modules G_{xy} for straight fibre UC obtained with CLT and UC FE modelling

8.8.2 Case two

The results of the second case were obtained for a UC model having a single tow of a linear variation of local angles with T_0=0° and T_1=45° and a gap of variable width. Figure 8.14(a) presents the obtained stress in the UC model of homogenous isotropic material with the gap filled with the same materials under an applied macroscopic strain of 10% in the *x*-direction. Uniform stress field was obtained, verifying that the model passed the 'sanity check'.

A more realistic UC has been analysed where the gap and the tow were prescribed with appropriate material properties. The stress in the fibre direction when the UC is under tension in the *x*-direction is shown in Figure 8.14(b). The maximum stress is predicted in the middle of fibre tow where the tow orientation is the most closely aligned with the direction of applied load, while the minimum stresses are observed at both ends when T_1=45°.

The applied load for the case as shown in Figure 8.14(c) is tensile in the *y*-direction. It can be seen that stress in fibre direction σ_{11} reached its maximum at both ends of the fibre tow and it takes its minimum at the centre. The trend is opposite to that of Figure 8.14(b).

Under applied pure shear loading, Figure 8.14(d) shows that the σ_{11} along the fibre, direction tend to maximise when the local orientation approaches 45° and minimise when angles approach 0°. This is because pure shear is equivalent to the equal bi-axial tensile and compressive stress state and the maximum tension is expected at 45°.

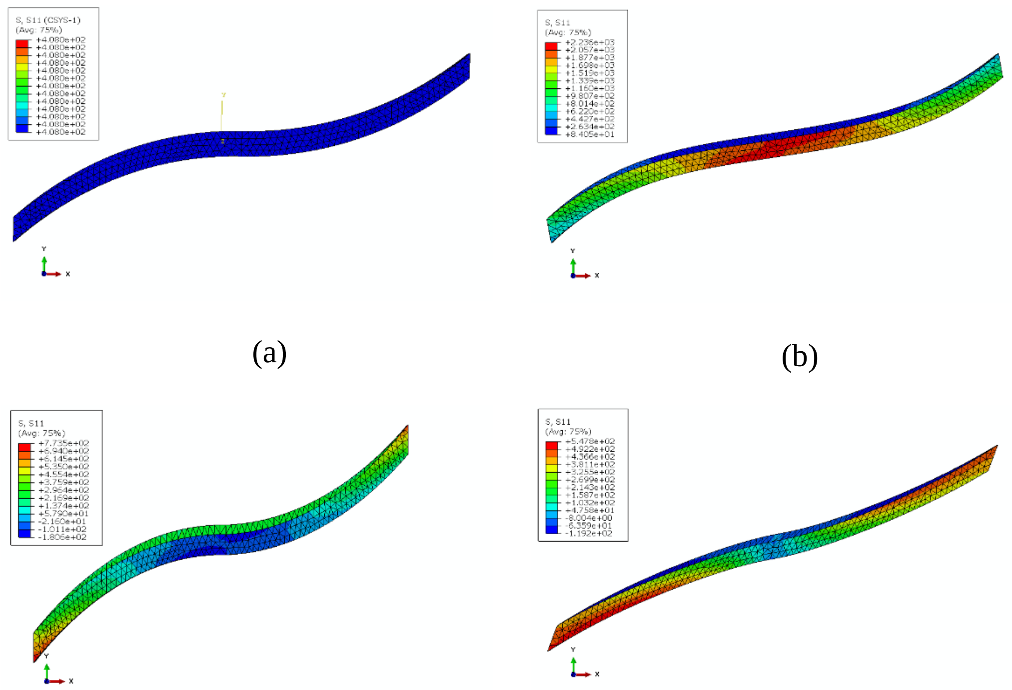

(a) (b)

(c) (d)

Figure 8.14: UC model of curved tow with T_0=0° andT_1=45°; (a) σ_{11} of isotropic material under loading in x-direction, (b) σ_{11} of UD material under loading in x-direction, (c) σ_{11} of UD material under loading in y-direction, and (d) σ_{11} of UD material under shear loading

The local orientation varies linearly from T_0 at the centre to T_1 at the end. Therefore, different sets of values of T_0 and T_1 lead to different UC models. Figure 8.15(a) presents the effective material properties of E_x. The highest value of the effective material property E_x is associated with the curve of T_0=0 when the effect of the gap on the effective material property E_x, becomes least pronounced. Increase in either T_0 or T_1 tends to rotate the orientation of the gap away from the x-axis. As a result, the effective elastic modulus decreases. Figure 8.15(b) presents the effective Young's modulus in E_y as a family of curves corresponding to various values of T_0 as indicated with T_1 varying from 35° to 55° with an increment of 5°. It can be seen the effective material property E_y decreases with increasing the value of T_1. Furthermore, this figure shows the curve for T_0=20° has the largest value among the range of values chosen for T_0 as this is to closest to the case of a straight tow. The effective shear modulus G_{xy} is predicted as shown in Figure 8.15(c). It seems to be predominantly determined by T_0 while T_1 has little effect on the predicted shear modulus from the UC model. Within the range of T_0 as shown in Figure 8.15(c), G_{xy} increases with T_0 as fibres deviate from *x*-axis towards 45° direction which is most effective in resisting shear stress.

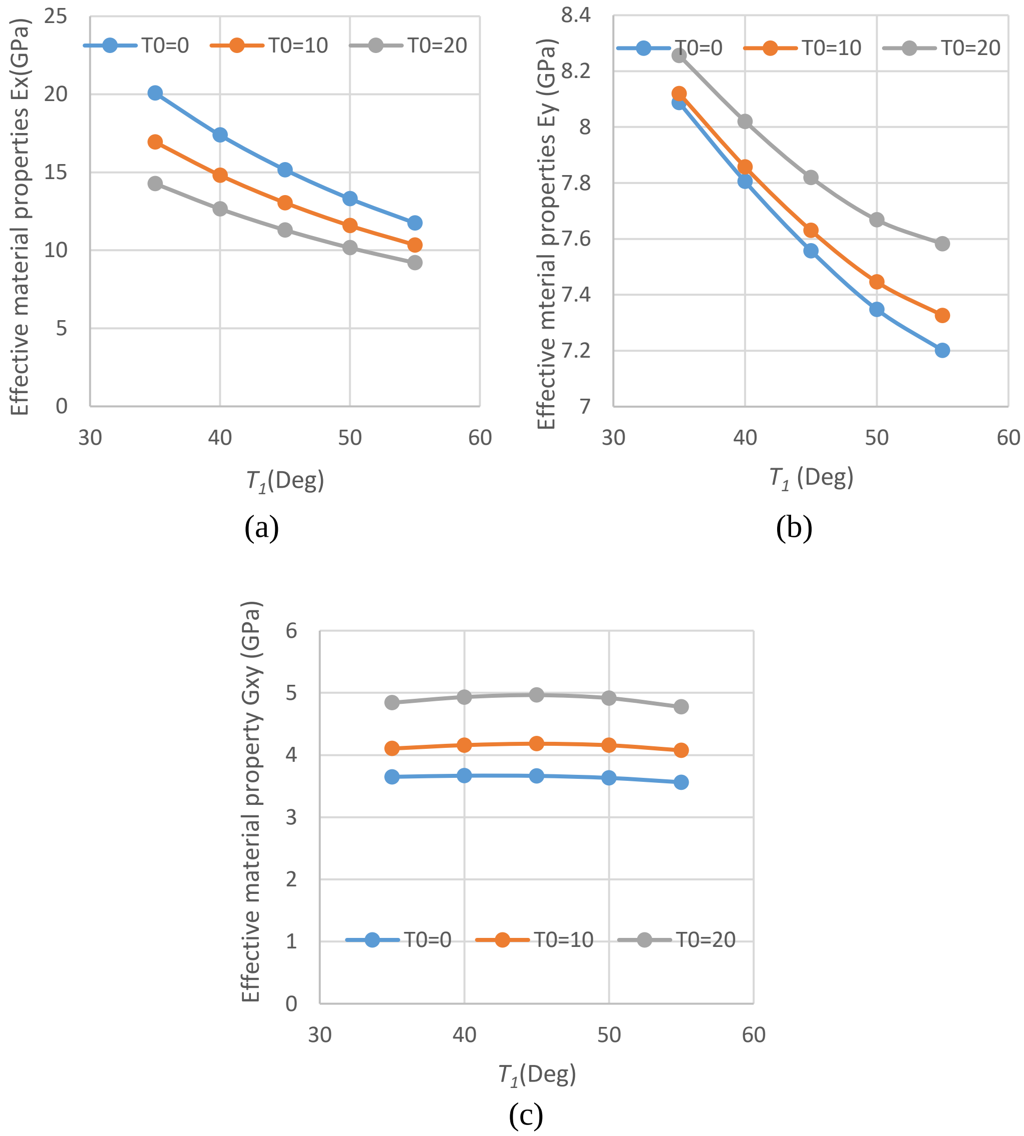

(a) (b)

(c)

Figure 8.15: Effective elastic property of single layer of curved tows (a) E_x moduli, (b) E_y moduli, and (c) G_{xy} moduli

The performance of the material represented by the UC is apparently affected by the presence of the gap. The size of the gap can be employed as a measure of its presence. In Figure 8.16, the gap size is plotted against T_1 at T_0 =0. Apparently, it increases with T_1. This is accompanied by the reduction in the Effective elastic properties of E_x, E_y and G_{xy}.

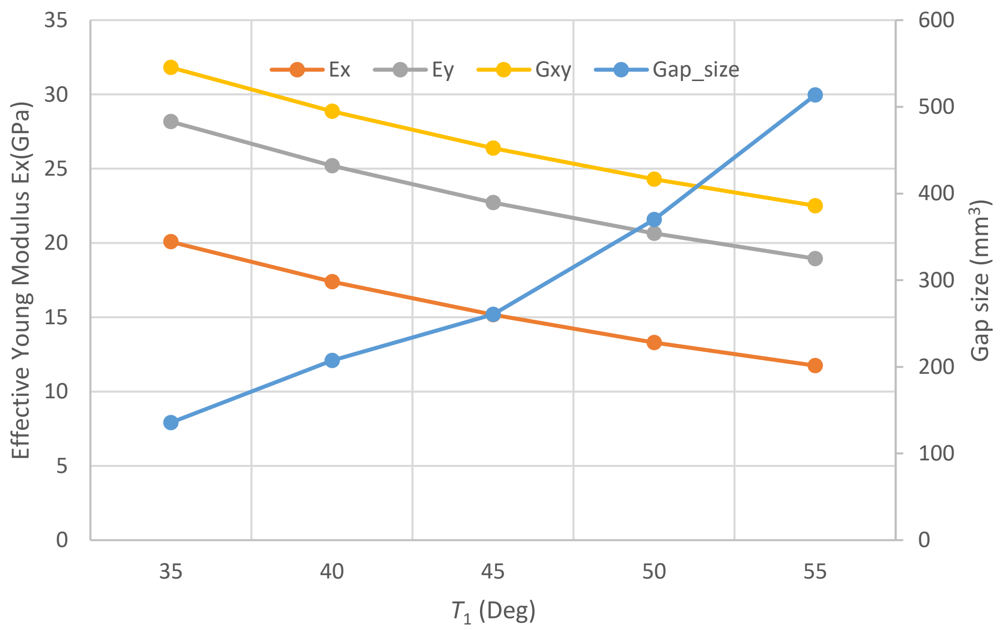

Figure 8.16: A comparison of o effective material properties with gap size of UC models having T_0=0°

In Figure 8.17 the percent ratio of the gap size to the total size of the UC model has been plotted over a range of different values of T_0. It is clear that, while it increases with T_1 as has been shown previously, it reduces with T_0 over the range as indicated. This is because the fibre tow tends to straighten up as T_0 increases at fixed T_1. The presence of the gap is due to the variation of the curvature along the tow path. The less the variation, the lower the volume percentage of the gap.

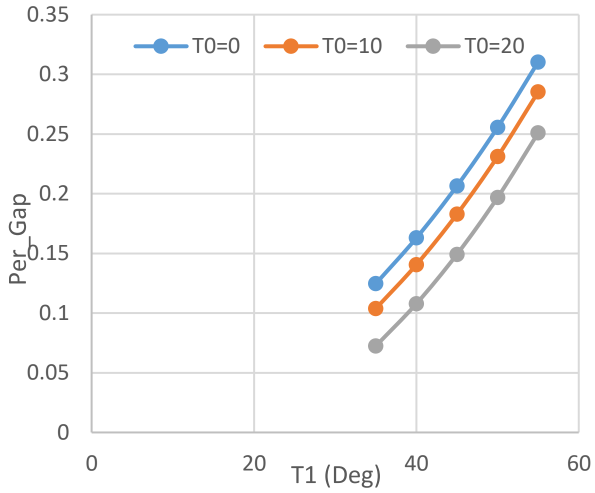

Figure 8.17: Gap size percent against local angles

A comparison has been made between the predictions from the rule of the mixtures and the unit cell model on the obtained effective material elastic moduli in the *x*- and *y*-directions respectively. The predictions of the in-plane stiffness based on the role of mixtures is done as a procedure used in Chapter 5. However, the used material properties and characteristic dimensions are the same as the UC model to keep the comparison sensible. In Figure 8.18(a) the effective elastic modulus E_x is plotted against T_1 at T_0=0°. Both approaches result in very similar predictions. This is because, with the range of fibre orientation as involved, E_x is approximately dictated by local effective elastic modulus in the fibre direction for which the rule of mixtures is meant to be very accurate. The disparity can be observed in E_y as shown in Figure 8.18(b) because of the limited accuracy the rule of mixtures for effective properties in directions other than along fibres. E_y of the material represented by the UC here is no longer dictated by the local effective elastic modulus over the range of fibre orientation involved. Even so, it can be seen that if one can put up with the amount of errors as presented, the rule of mixtures results can offer a rough approximation. However, it is deemed to be rather inaccurate if one expects more reasonable approximations.

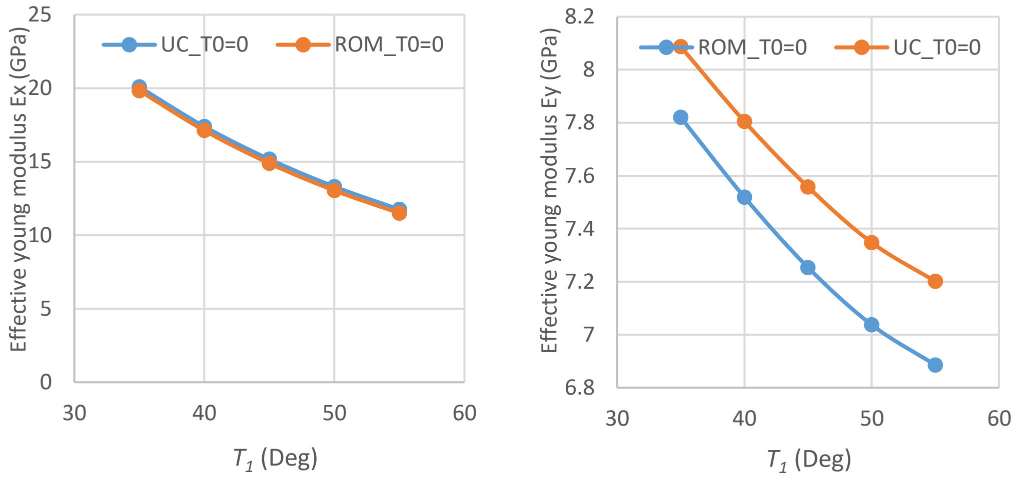

(a) (b)

Figure 8.18: A comparison of effective material properties obtained by the ROM and UC model; (a) E_x moduli, and (b) E_y moduli

8.8.3 Case three

The two cases in the two previous sections have been examined as a measure of verifications at different levels of sophistication. The third case is meant to be more relevant to applications. A two-layered laminate of curved tows with their companion gaps in the $\pm\theta$ configuration is modelled as the UC with two legs. The UC is first loaded in the x-direction with its materials for the fibre tows and the gaps assumed to be the same, homogenous and isotropic. A uniform stress field is obtained, as shown in Figure 8.19, as a 'sanity check' to verify the model.

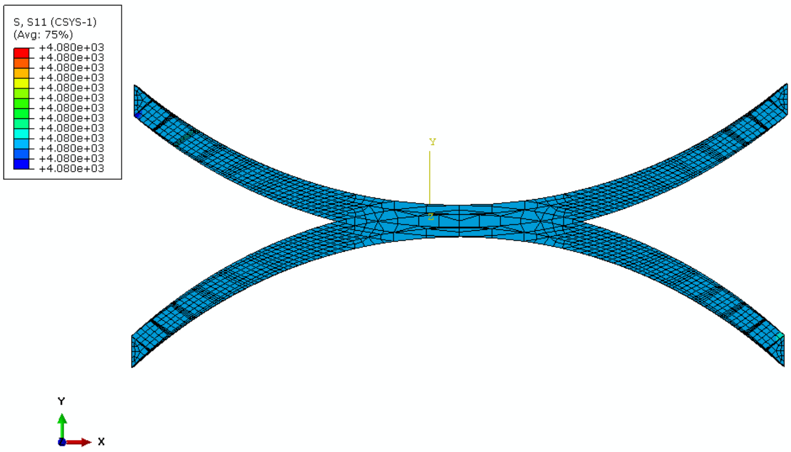

Figure 8.19: Stress in *x*-direction for isotropic material of two layers model of UC due to the tensile load in *x*-direction

The UC model has been analysed where the fibre tows are considered transversely isotropic with their material properties as given in Table 8.1, while the gaps are genuinely voids of a matrix. The local stresses in the fibre tows under tensile loading in the *x*- and *y*-directions and in-plane shear loading are shown in Figure 8.20-8.23, respectively, for local angles T_0=0° and T_1=45°.

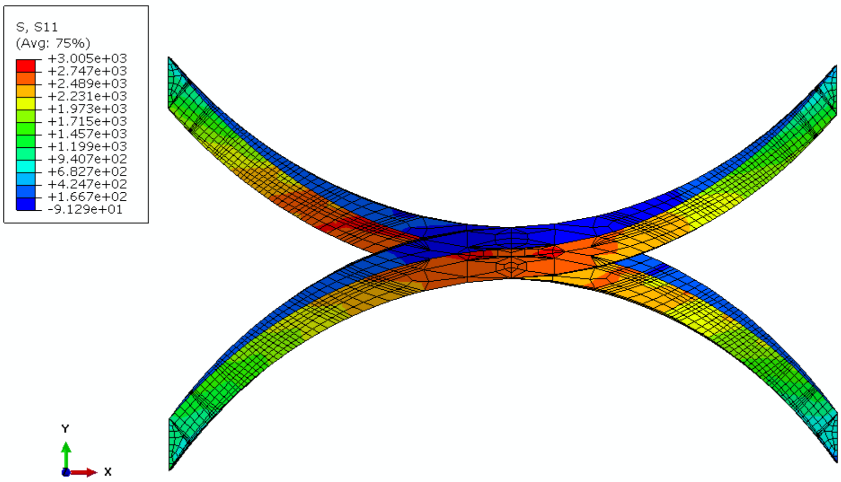

Figure 8.20: Stress in fibre direction for orthotropic material of two layers model of UC due to the tensile load in *x*-direction

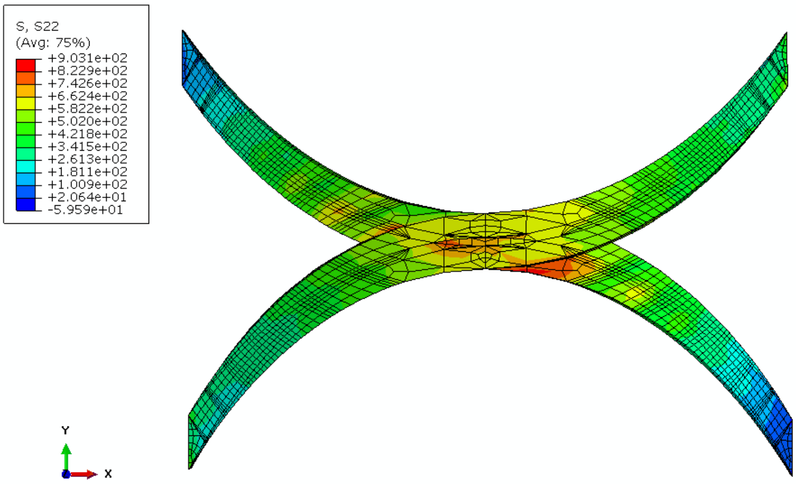

Figure 8.21: Stress in a direction perpendicular to the fibre for orthotropic material of two layers model of UC due to the tensile load in *y*-direction

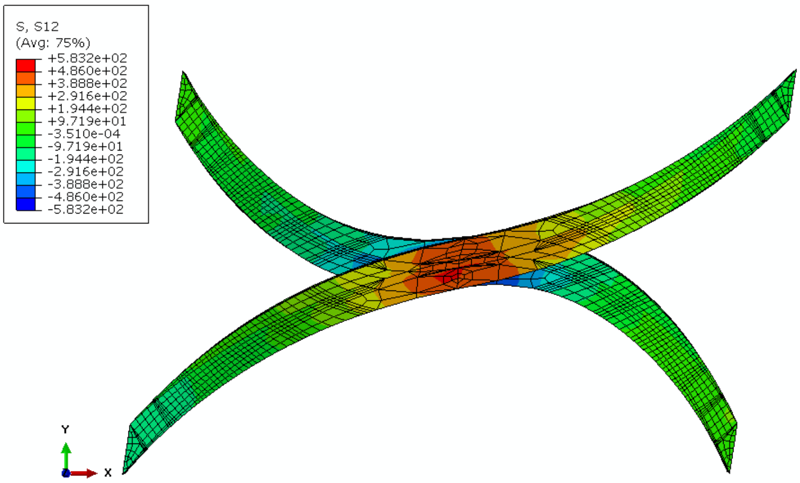

Figure 8.22: Shear stress in local coordinate for orthotropic material of two layers model of UC due to shear loading

The effective material properties E_x, E_y and G_{xy} were also extracted from these loading cases. Figure 8.23(a) states the effective material property E_x for the different sets of T_0 and T_1 of two layer UC model. The largest value of E_x is for the family of points having T_0 = 0° and the lowest value for the set of point having T_0=20°. It could be because the variable gap does not have a vital effect on the E_x. In addition, the local angles of UC models are converted from a zero angle with increasing T_0. Figure 8.23(b) presents the effective material E_y for a different range of local angles. It shows the E_y increases with the shrinking of the gap due to the decreasing the difference between the T_0 and T_1. The effective shear modules G_{xy} for certain range of T_0 and T_1 has been presented in Figure 8.23(c). It can be seen that the value of G_{xy} is still approximately the same for each family of T_0. The reason behind that is the presenting range of T_1 is small, between 35° and 45°, and increasing the size of the gap.

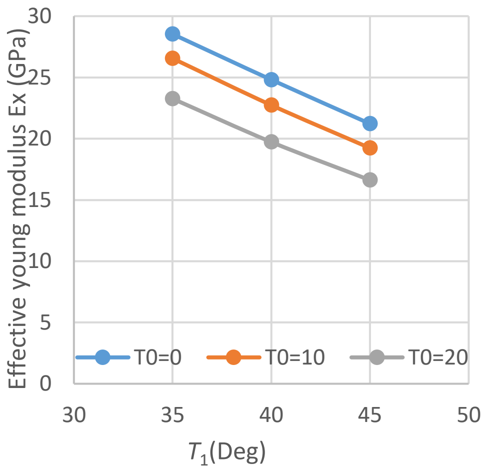

(a)

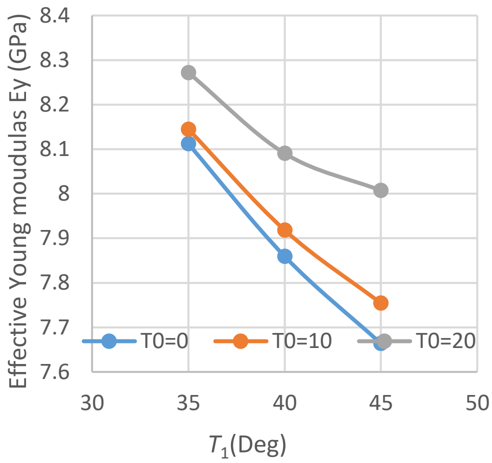

(b)

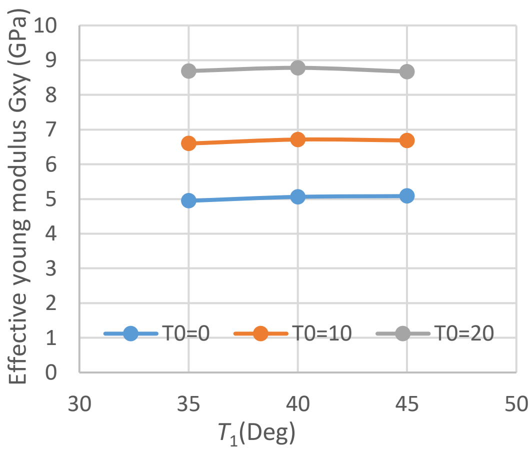

(c)

Figure 8.23: Effective elastic property of two layers of curved tow: (a) E_x moduli, (b) E_y moduli, and (c) G_{xy} moduli

In Figure 8.24 the gap size is inversely proportional to the effective material properties of E_x, E_y and G_{xy}. as a result of the linear variation of the local angle of the tow with T_0=0°. Figure 8.25(a) and (b) illustrate the comparison between the effective material properties E_x and E_y obtained using the rule of mixtures and out of UC FE analysis, respectively. It can be seen that effective material property in the *x*-direction compare well, while there is a clear difference for the effective material property in the *y*-direction. However, that difference does not suggest that the UC model is not valid for getting the transverse effective material properties, because of the rule of mixtures offers upper bound for longitudinal stiffness and lower bound for transverse stiffness.

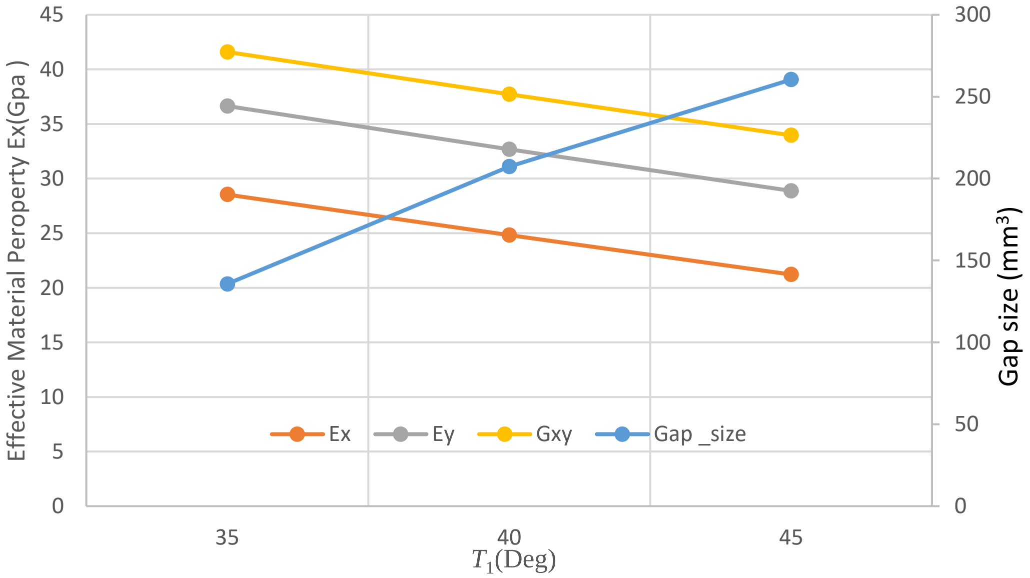

Figure 8.24: A comparison of o effective material properties with gap size of UC models having T_0=0°

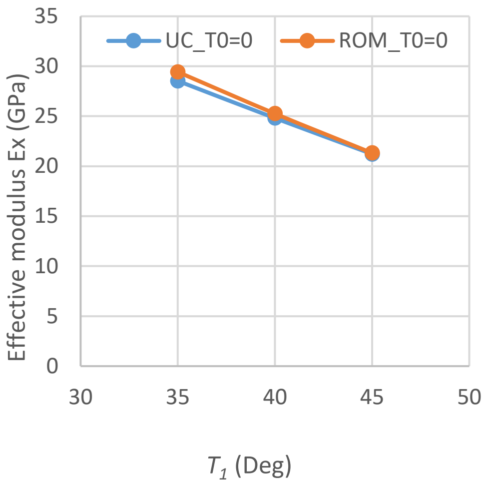

(a)

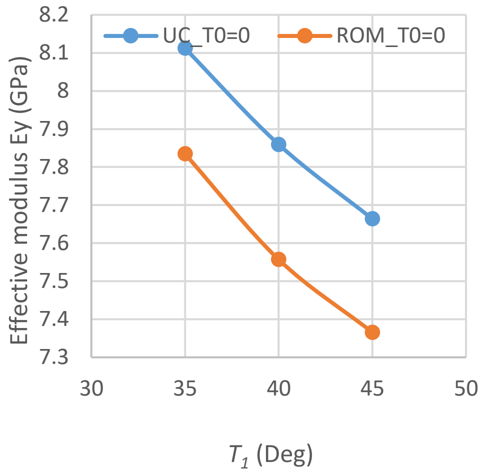

(b)

Figure 8.25: A comparison of properties obtained by the ROM and out of UC FE modelling; (a) E_x moduli (b) E_y moduli

8.9 Summary

Estimating the effective material properties of composite material can be extremely challenging. In particular, the numerical results may not be in a good agreement with test data, for example when employing ROM for calculating a transverse property of such as E_{22} and G_{12}. A homogenization approach based on the use of the representative volume element or UC is more accurate and effective in its FE implementation.

The correct definition and application of periodic boundary conditions can guarantee the displacement and the traction continuity at the boundaries of the UC model. Periodic boundary conditions have been derived for the UC model with translational symmetries along two axes as a template that could be used for different UC models having different local angles in a direct way. The translational symmetry transformations are employed to satisfy the condition of continuous tow.

Also, the boundary conditions based on translation symmetry transformation have been used to employ perfect bonding the interface area of the adjacent legs of the UC.

UC models have been implemented in Abaqus/Standard, and the process of generating the models was fully automated using a Python script as a secondary development of Abaqus/CAE. Specifically, it creates the UC geometry with different local angles, generates a periodic mesh to suit the PBCs, creates and imposes the equations of PBCs, runs the FE analysis and extracts the effective material properties.

Extensive verification has been carried out, such as comparing the prediction of a straight tow model with the results obtained using CLT and ‘sanity checks’ for all cases of UC models analysed. The results from UC FE modelling and those obtained ROM were found to be in a good agreement in terms of the effective material property in the *x*-direction. The transverse effective material property predictions from FE analysis and ROM calculations have the same tendency yet quantitatively, and there is some difference between them.

The size of the gap between tows causes a drop in the effective material properties. The linear variation of local angles has an important effect on the size of the gap, whereas the gap size increases with increasing the difference between T_0 and T_1.

9 Conclusions and Future Work

9.1 Conclusions

It is the interest of this thesis to investigate the effects of controlled fibre placement on the performances of the composite structure produced and to make use of such effects in order to optimise the performances of structures. The main outcomes of the research are summarised as follows.

1. An optimisation framework has been devised to carry out the optimisation using Abaqus/Standard as an FE solve for stress analysis and Matlab as the optimiser. The technique of the client and server has been established as the key for in the framework which facilitates the communications between these two independent commercial packages so that the optimisation can be performed in an automated manner with less time.
2. Based on the optimisation of different orders of variations of local fibre angles, the effect of higher-order variations (second and third-order), is considered as not effective in improving the buckling load as compared with that obtained with a linear variation, given the substantial increased computational efforts and time consumed. Therefore, the improvement in the buckling load from the first-order variation is considered as sufficiently representative.
3. The first-order variation of local angles in the direction transverse to the loading direction offered a significant improvement in buckling load around 40%, while for the variation in the loading direction the improvement was negligible.

4. The overall stiffness of the steered fibre laminates having linear variation in the direction transverse to loading was higher than that of variation in the loading direction.
5. Steering the fibre with a linear variation of local angle improved the structural performance as a result of the re-distribution of the applied loads. Also, provided more flexibility in the design process to achieve the optimum performances.
6. A gap of variable width between adjacent tows, which produces a non-uniform of fibre volume fraction distribution, offered a negative impact on the buckling load and the overall stiffness of laminates. The negative effect was proportional directly with the size of the gap, which increases with increasing the difference between the local fibre angle variations.
7. The structural performance of cylindrical shells improved by steering the fibre path, which enables the structures to sustain higher buckling load as a result of the improved local stiffness. Since steering, the fibre in the circumferential direction increased the surface area of a cylindrical shell, which is exposed to axial compression by redistributing the load.
8. The improvement of the buckling load of the cylindrical shell depended on the direction of the applied bending moment, where the gain in the buckling load could turn into a loss if the load is applied in other directions.
9. The time and the computational effort to predict the failure load of the steered fibre laminates was reduced by using linearisation technique for the Tsai-Wu criterion.
10. In general, the variable gap width in the laminates reduced the strength of the laminates. However, the variable gap width that changes with variation of local

angle does not significantly affect the strength of some patterns of the curvilinear laminates.

11. The effective material properties of the steered fibre with gaps of variable width were achieved by using a unit cell (UC) model in conjunction with the finite element method.
12. The equations of PBCs, which were derived based on the translational symmetry transformations satisfied the continuity conditions by the verification through ‘sanity checks’. In addition, the results of the UC models having straight fibre paths with results of the classical laminate theory and showed a good agreement.

9.2 Future Work

After achieved what has been presented in the thesis, a number of areas have been identified where more efforts could be made in order to extend the understanding but have not been attended due to the limited resources and time allowed. There have therefore been provided here as future work.

1) Performing a multi-objective design optimisation to include multiple loading cases instead of single load case since in real life the structures, e.g. in fuselage of airplane, are subjected to multi-loading cases.
2) A post-buckling analysis could be as a recommendation in future work for variable stiffness laminates.
3) The variable stiffness laminates could be used to tailor the coefficient of thermal expansion in the aerospace structure. Therefore, performing the thermal expansion analysis to minimise thermally produced stresses could be considered as future work.

4) The unit cell model employed in the prediction of the effective material properties could be used to model the effects of damage so that analysis could be more reliable.
5) The analysis of the unit cell model of the curved tow with its variable gap could be developed into a toolbox as a plug-in of ABAQUS to allow more automated simulations in future

References

ABAQUS/ 2017. SIMULIA, Alalysis User's Manual. 2017.

ABOSBAIA, A., MAHDI, E., HAMOUDA, A. & SAHARI, B. 2003. Quasi-static axial crushing of segmented and non-segmented composite tubes. *Composite structures*, 60**,** 327-343.

ABOUHAMZE, M. & SHAKERI, M. 2007. Multi-objective stacking sequence optimization of laminated cylindrical panels using a genetic algorithm and neural networks. *Composite Structures,* 81**,** 253-263.

ADALI, S., SUMMERS, E. & VERIJENKO, V. 1993. Optimisation of laminated cylindrical pressure vessels under strength criterion. *Composite structures,* 25**,** 305-312.

AKBULUT, M. & SONMEZ, F. O. 2008. Optimum design of composite laminates for minimum thickness. *Computers & Structures,* 86**,** 1974-1982.

ANTONIOU, A. & LU, W.-S. 2007. *Practical Optimization Algorithms and Engineering Applications*, Springer.

ARORA, R. K. 2015. *Optimization: algorithms and applications*, Chapman and Hall/CRC.

AZARAFZA, R., KHALILI, S., JAFARI, A. & DAVAR, A. 2009. Analysis and optimization of laminated composite circular cylindrical shell subjected to compressive axial and transverse transient dynamic loads. *Thin-Walled Structures,* 47**,** 970-983.

BLOM, A. W. 2010a. Structural performance of fiber-placed, variable-stiffness composite conical and cylindrical shells. *Delft University of Technology,* 9.

BLOM, A. W. 2010b. *Structural performance of fiber-placed, variable-stiffness composite conical and cylindrical shells*, TU Delft, Delft University of Technology.

BLOM, A. W., LOPES, C. S., KROMWIJK, P. J., GURDAL, Z. & CAMANHO, P. P. 2009a. A Theoretical Model to Study the Influence of Tow-drop Areas on the Stiffness and Strength of Variable-stiffness Laminates. *Journal of Composite Materials,* 43**,** 403-425.

BLOM, A. W., RASSAIAN, M., STICKLER, P. B. & GÜRDAL, Z. Modal testing of a composite cylinder with circumferentially varying stiffness. Proceedings of the 50th AIAA/ASME/ASCE/AHS/ASC Structures, Structural Dynamics and Materials Conference. Palm Springs, California, 2009b.

BLOM, A. W., RASSAIAN, M., STICKLER, P. B. & GÜRDAL, Z. 2010a. *Bending Test of a Variable-Stiffness Fiber-Reinforced Composite Cylinder*, American Institute of Aeronautics and Astronautics (AIAA).

BLOM, A. W., STICKLER, P. B. & GURDAL, Z. Design and manufacture of a variable-stiffness cylindrical shell. Proceedings of the SAMPE Europe 30th International Conference, 1-8.(2009), 2009c. SAMPE Europe.

BLOM, A. W., STICKLER, P. B. & GÜRDAL, Z. 2010b. Optimization of a composite cylinder under bending by tailoring stiffness properties in circumferential direction. *Composites Part B: Engineering,* 41**,** 157-165.

CAMPBELL, F. C. 2004. *Manufacturing Processes for Advanced Composites*, Elsevier Science

CIFUENTES, A. & KALBAG, A. 1992. A performance study of tetrahedral and hexahedral elements in 3-D finite element structural analysis. *Finite Elements in Analysis and Design,* 12**,** 313-318.

COMPTON, B. G. & LEWIS, J. A. 2014. 3D-printing of lightweight cellular composites. *Adv Mater,* 26**,** 5930-5.

CURRY, J. M., OHNSON, E. R. & TARNES, J. H. 1992. Effect of dropped plies on the strength of graphite-epoxy laminates. *AIAA journal,* 30**,** 449-456.

DANIELS, R. W. 1978. *Introduction to numerical methods and optimization techniques,* Elsevier North-Holland.

DIACONU, C. G., SATO, M. & SEKINE, H. 2002. Buckling characteristics and layup optimization of long laminated composite cylindrical shells subjected to combined loads using lamination parameters. *Composite Structures,* 58**,** 423-433.

FALCÓ, O., MAYUGO, J. A., LOPES, C. S., GASCONS, N., TURON, A. & COSTA, J. 2014. Variable-stiffness composite panels: As-manufactured modeling and its influence on the failure behavior. *Composites Part B: Engineering,* 56**,** 660-669.

FUCHS, H., STARNES, J. J., HYER, M.1997. Collapse of composite cylinders in bending. *AIAA Journal,* 37**,** 2414-2424.

FUKUNAGA, H. & SEKINE, H. 1993. Optimum design of composite structures for shape, layer angle and layer thickness distributions. *Journal of composite materials,* 27**,** 1479-1492.

GHAYOOR, H., ROUHI, M., HOA, S. V. & HOJJATI, M. 2017. Use of curvilinear fibers for improved bending-induced buckling capacity of elliptical composite cylinders. *International Journal of Solids and Structures,* 109**,** 112-122.

GUO-DONG, F., JUN, L., YU, W. & BAO-LAI, W. 2009. The effect of yarn distortion on the mechanical properties of 3D four-directional braided composites. *Composites Part A: Applied Science and Manufacturing,* 40**,** 343-350.

GÜRDAL, Z., HAFTKA, R. T. & HAJELA, P. 1999a. *Design and Optimization of Laminated Composite Materials,* John Wiley& Sons.

GÜRDAL, Z., HAFTKA, R. T. & HAJELA, P. 1999b. *Design and optimization of laminated composite materials,* John Wiley & Sons.

GURDAL, Z. & OLMEDO, R. 1993. In-plane response of laminates with spatially varying fiber orientations-variable stiffness concept. *AIAA journal,* 31**,** 751-758.

GÜRDAL, Z., TATTING, B. F. & WU, C. 2008. Variable stiffness composite panels: effects of stiffness variation on the in-plane and buckling response. *Composites Part A: Applied Science and Manufacturing,* 39**,** 911-922.

GÜRDAL, Z., TATTING, B. F. & WU, K. C. Tow-placement technology and fabrication issues for laminated composite structures. Proceedings of the AIAA/ASME/ASCE/AHS/ASC structures, 46th structural dynamics & materials conference, 2005.

HALPIN, J. & KARDOS, J. 1976. The Halpin-Tsai equations: a review. *Polymer Engineering & Science,* 16**,** 344-352.

HALPIN, J. & TSAI, S. W. 1969. Effects of Environmental Factors on Composite Materials. *AFML-TR, 1969.*

HART-SMITH, L. J. 1992. The ten-percent rule for preliminary sizing of fibrous composite structures. *Weight Engineering,* 52, 29-45.

HASHIN, Z. & ROSEN, B. W. 1964. The elastic moduli of fiber-reinforced materials. *Journal of Applied Mechanics*, 31**,** 223-232.

HASHIN., Z. 1980. Failure criteria for unidirectional fibre composites. *Journal of Applied Mechanics,* 47(2)**,** 329-334.

HONDA, S., IGARASHI, T. & NARITA, Y. 2013. Multi-objective optimization of curvilinear fiber shapes for laminated composite plates by using NSGA-II. *Composites Part B: Engineering,* 45**,** 1071-1078.

HUANG, J. & HAFTKA, R. 2005. Optimization of fiber orientations near a hole for increased load-carrying capacity of composite laminates. *Structural and Multidisciplinary Optimization,* 30**,** 335-341.

HYER, M. & CHARETTE, R. 1991. Use of curvilinear fiber format in composite structure design. *AIAA journal,* 29**,** 1011-1015.

HYER, M. & RIDDICK, J. 1999. Internal pressure loading of segmented-stiffness composite cylinders. *Composite structures,* 45**,** 311-320.

IJSSELMUIDEN, S. T. 2011a. *Optimal Design of Variable Stiffness Composite Structures using Lamination Parameters.* PhD doctoral thesis, TU Delft.

IJSSELMUIDEN, S. T. 2011b. *Optimal design of variable stiffness composite structures using lamination parameters,* TU Delft, Delft University of Technology.

JONES, R. M. 2014. *Mechanics of Composite Materials,* Taylor & Francis.

KADDOUR, A., HINTON, M. J., SMITH, P. A. & LI, S. 2013. Mechanical properties and details of composite laminates for the test cases used in the third world-wide failure exercise. *Journal of Composite Materials,* 47**,** 2427-2442.

KAW, A. K. 2005. *Mechanics of Composite Materials,* CRC Press, 6000 Broken Sound Parkway NW

KHANI, A., IJSSELMUIDEN, S. T., ABDALLA, M. M. & GÜRDAL, Z. 2011. Design of variable stiffness panels for maximum strength using lamination parameters. *Composites Part B: Engineering,* 42**,** 546-552.

KNOPS, M. 2008. *Analysis of Failure in Fiber Polymer Laminates-The Theory of Alfred Puck-Springer*, Springer-Verlag Berlin Heidelberg.

KOIDE, R. M. & LUERSEN, M. A. 2013. Maximization of fundamental frequency of laminated composite cylindrical shells by ant colony algorithm. *Journal of Aerospace Technology and Management,* 5**,** 75-82.

KRAMER, O. 2017. *Genetic algorithm essentials,* Springer, .

LI, S. 2000. General unit cells for micromechanical analyses of unidirectional composites. *Composites Part A: applied science and manufacturing,* 32(6)**,** 815-826.

LI, S. 2001. General unit cells for micromechanical analyses of unidirectional composites. *Composites Part A: applied science and manufacturing,* 32**,** 815-826.

LI, S. 2008. Boundary conditions for unit cells from periodic microstructures and their implications. *Composites Science and Technology,* 68**,** 1962-1974.

LI, S., JEANMEURE, L. & PAN, Q. 2015. A composite material characterisation tool: UnitCells. *Journal of Engineering Mathematics,* 95**,** 279-293.

LI, S. & SITNIKOVA, E. 2018a. A critical review on the rationality of popular failure criteria for composites. *Composites Communications,* 8**,** 7-13.

LI, S. & SITNIKOVA, E. 2018b. An Excursion into Representative Volume Elements and Unit Cells. *In:* ZWEBEN, C. H. & BEAUMONT, P. (eds.) *Comprehensive Composite Materials II.* 2nd ed. Oxford: Academic Press.

LI, S., SITNIKOVA, E., LIANG, Y. & KADDOUR, A.-S. 2017. The Tsai-Wu failure criterion rationalised in the context of UD composites. *Composites Part A: Applied Science and Manufacturing,* 102**,** 207-217.

LI, S., WARRIOR, N., ZOU, Z. & ALMASKARI, F. 2011a. A unit cell for FE analysis of materials with the microstructure of a staggered pattern. *Composites Part A: Applied Science and Manufacturing,* 42**,** 801-811.

LI, S. & WONGSTO, A. 2004. Unit cells for micromechanical analyses of particle-reinforced composites. *Mechanics of materials,* 36**,** 543-572.

LI, S., ZHOU, C., YU, H. & LI, L. 2011b. Formulation of a unit cell of a reduced size for plain weave textile composites. *Computational materials science,* 50**,** 1770-1780.

LIU, G., WEI, G. & GAO, H. 2019. A novel structure of woven composite pressure pipes and its multi-scale analysis. *The Journal of The Textile Institute***,** 1-10.

LOPES, C., GÜRDAL, Z. & CAMANHO, P. 2008a. Variable-stiffness composite panels: Buckling and first-ply failure improvements over straight-fibre laminates. *Computers & Structures,* 86**,** 897-907.

LOPES, C. S., GÜRDAL, Z. & CAMANHO, P. P. 2008b. Variable-stiffness composite panels: Buckling and first-ply failure improvements over straight-fibre laminates. *Computers & Structures,* 86**,** 897-907.

LOZANO, G. G., TIWARI, A., TURNER, C. & ASTWOOD, S. 2015. A review on design for manufacture of variable stiffness composite laminates. *Proceedings of the Institution of Mechanical Engineers, Part B: Journal of Engineering Manufacture***,** 0954405415600012.

LUCIANO, R. & BARBERO, E. J. 1994. Formulas for the Stiffness of Composites with Periodic Microstructure. *Int. J. Solids Structures* 31**,** 2933-2944.

MATLAB2017A, *The MathWorks, Inc., Natick, Massachusetts, United States.*

MATSUZAKI, R., UEDA, M., NAMIKI, M., JEONG, T. K., ASAHARA, H., HORIGUCHI, K., NAKAMURA, T., TODOROKI, A. & HIRANO, Y. 2016. Three-dimensional printing of continuous-fiber composites by in-nozzle impregnation. *Sci Rep,* 6**,** 23058.

MCLAUGHLAN, P. B., FORTH, S. C., GRIMES-LEDESMA, L. & CENTER, L. B. J. S. 2011. *Composite overwrapped pressure vessels: a primer*, National Aeronautics and Space Administration, Johnson Space Center.

MEGSON, T. H. G. 2007. Aircraft Structures for Engineering Students-Butterworth-Heinemann (2007).pdf>. Great Britain: Elsevier aerospace engineering series.

MEIJER, G., ELLYIN, F. & XIA, Z. 2000. Aspects of residual thermal stress/strain in particle reinforced metal matrix composites. *Composites Part B: Engineering,* 31**,** 29-37.

MIAN, H. H., WANG, G., DAR, U. A. & ZHANG, W. 2013. Optimization of composite material system and lay-up to achieve minimum weight pressure vessel. *Applied Composite Materials,* 20**,** 873-889.

MICHALEWICZ, Z. 2013. *Genetic algorithms +data structures= evolution programs,* Springer Science & Business Media.

MUKHOPADHYAY, T. & ADHIKARI, S. 2016. Equivalent in-plane elastic properties of irregular honeycombs: An analytical approach. *International Journal of Solids and Structures,* 91**,** 169-184.

OLMEDO, R. & GURDAL, Z. Buckling response of laminates with spatially varying fiber orientations. AIAA/ASME/ASCE/AHS/ASC 34th Structures, Structural Dynamics, and Materials Conference, 1993. 2261-2269.

PARANDOUSH, P. & LIN, D. 2017. A review on additive manufacturing of polymer-fiber composites. *Composite Structures*, 182**,** 36-53.

PASCHERO, M. & HYER, M. W. 2009. Improvement of Axial Load Capacity of Elliptical Cylindrical Shells. *AIAA Journal,* 47**,** 142-156.

PETERS, S. T. 2011. *Composite filament winding*, ASM International.

PUCK, A., KOPP, J. & KNOPS, M. 2002. Guidelines for the determination of the parameters inPuck's action plane strength criterion. *Composites Science and Technology* 62**,** 371-378.

REDDY, J. N. 2004. *Mechanics of laminated composite plates and shells theory and analysis*, CRC press.

REDDY, J. N. & LIU., C. F. 1985. A higher-order shear deformation theory of laminated elastic shells *International Journal of Engineering Science* 23(23)**,** 319-330.

REISSNER, E. 1945. The effect of transverse shear deformation on the bending of elastic plates. 12:10.

REUSS, A. 1929. Berechnung der fließgrenze von mischkristallen auf grund der plastizitätsbedingung für einkristalle. *ZAMM-Journal of Applied Mathematics and Mechanics/Zeitschrift für Angewandte Mathematik und Mechanik*, 9**,** 49-58.

RIDDICK, J. C. & HYER, M. W. 1997. Response of segmented-stiffness composite cylinders to axial end shortening. *Composite structures,* 40**,** 103-114.

ROUHI, M., GHAYOOR, H., HOA, S. V. & HOJJATI, M. 2014. Effect of structural parameters on design of variable-stiffness composite cylinders made by fiber steering. *Composite Structures*, 118**,** 472-481.

ROUHI, M., GHAYOOR, H., HOA, S. V. & HOJJATI, M. 2015. Multi-objective design optimization of variable stiffness composite cylinders. *Composites Part B: Engineering,* 69**,** 249-255.

SAPOZHNIKOV, S. B. & CHEREMNYKH, S. I. 2013. The strength of fibre reinforced polymer under a complex loading. *Journal of Composite Materials*, 47**,** 2525-2552.

SHOKRIEH, M. M. & MAZLOOMI, M. S. 2012. A new analytical model for calculation of stiffness of three-dimensional four-directional braided composites. *Composite Structures,* 94**,** 1005-1015.

SILVA, R. F., ROCHA, I. B., PARENTE JÚNIOR, E., MELO, A. & HOLANDA, Á. S. D. 2010. Optimization of laminated tubes using finite element analysis. *SILVA*.

SUN, M. & HYER, M. W. 2008. Use of Material Tailoring to Improve Buckling Capacity of Elliptical Composite Cylinders. *AIAA Journal,* 46**,** 770-782.

TADEPALLI, S. C., ERDEMIR, A. & CAVANAGH, P. R. 2011. Comparison of hexahedral and tetrahedral elements in finite element analysis of the foot and footwear. *Journal of biomechanics,* 44**,** 2337-2343.

TAM, A. S. & GUTOWSKI, T. G. 1990. The kinematics for forming ideal aligned fibre composites into complex shapes *Composites Manufacturing* Vol 1**,** 219-228.

TATTING, B. & GÜRDAL, Z. Analysis and design of tow-steered variable stiffness composite laminates. American Helicopter Society Hampton Roads Chapter, Structure Specialists' Meeting, Williamsburg, VA, 2001.

TATTING, B. F. 1998. Analysis and design of variable stiffness composite cylinders.

TEXGEN 2014. University of Nottingham (2014) TexGen, version 3.6.1.

THOMPSON, E. D. 2012. *Incorporation of computational fluid dynamics into flight vehicle preliminary design.* University of Dayton.

TODOROKI, A. & ISHIKAWA, T. 2004. Design of experiments for stacking sequence optimizations with genetic algorithm using response surface approximation. *Composite Structures,* 64**,** 349-357.

TOPAL, U. 2009. Multiobjective optimization of laminated composite cylindrical shells for maximum frequency and buckling load. *Materials & Design,* 30**,** 2584-2594.

TORRES, J. P., VANDI, L. J., VEIDT, M. & HEITZMANN, M. T. 2017. The mechanical properties of natural fibre composite laminates: A statistical study. *Composites Part A: Applied Science and Manufacturing,* 98**,** 99-104.

TSAI, S. W. 1984. A Survey of Macroscopic Failure Criteria for Composite Materials. *Journal of REINFORCED PLASTICS AND COMPOSITES,* 3(1)**,** 40-62.

TSAI, S. W. & WU, E. M. 1971. A general theory of strength for anisotropic materials. *Journal of composite materials,* 5**,** 58-80.

UNGWATTANAPANIT, T. & BAIER, H. Strength-stability optimization of hybrid-stiffness laminated plates with cut-outs subjected to multiple loads. RAeS-3rd Aircraft Structural Design Conference, 2012.

VLACHOUTSIS, S. 1992. Shear correction factors for plates and shells. *International Journal for Numerical Methods in Engineering,* 33**,** 1537-1552.

VOIGT, W. 1889. Ueber die Beziehung zwischen den beiden Elasticitätsconstanten isotroper Körper. *Annalen der physik,* 274**,** 573-587.

WALDHART, C. 1996. *Analysis of tow-placed, variable-stiffness laminates.* Virginia Polytechnic Institute and State University.

WALDHART, C., GURDAL, Z. & RIBBENS, C. Analysis of tow placed, parallel fiber, variable stiffness laminates. AIAA/ASME/ASCE/AHS/ASC Structures, Structural Dynamics and Materials Conference and Exhibit, 37 th, Salt Lake City, UT, 1996. 2210-2220.

WU, K. C. 2008. Design and analysis of tow-steered composite shells using fiber placement.

WU, K. C., TATTING, B. F., SMITH, B. H. & THORNBURGH, R. P. 2009. Design and Manufacturing of Tow steered composite using fiber placement. *Structures, Structural Dynamics, and Materials Conference 17th AIAA/ASME/AHS Adaptive Structures Conference 11th AIAA*.

WU, Z., WEAVER, P. M., RAJU, G. & CHUL KIM, B. 2012. Buckling analysis and optimisation of variable angle tow composite plates. *Thin-Walled Structures,* 60**,** 163-172.

XIA, Z., ZHANG, Y. & ELLYIN, F. 2003. A unified periodical boundary conditions for representative volume elements of composites and applications. *International Journal of Solids and Structures,* 40**,** 1907-1921.

ZHUO, P., LI, S., ASHCROFT, I., JONES, A. & PU, J. 2017. 3DPrinting of Continuous Fibre Reinforced Thermoplastic Composites *21st International Conference on Composite Materials*.

Appendices

Appendix A
Constraint equations for faces of unit cell model

Faces (excluding edges)	Constraint equations
F1, F8 at *z*=*b*, at *z*=-*b*	Free
F2 & F7 at *z*=0, at *z*=0	Interface area followed
F3 & F4 at *x*=*a*/2, at *x*=-*a*/2 on leg 1	$\begin{Bmatrix}\Delta u\\ \Delta v\end{Bmatrix}_{(F3-F4)} = [\varepsilon^0]\begin{Bmatrix}a\\ \Delta y\end{Bmatrix} = \begin{Bmatrix}a\varepsilon_x + \Delta y\gamma_{xy}\\ \Delta y\varepsilon_y\end{Bmatrix}$
F9 & F10 at *x*=*a*/2, at *x*=-*a*/2 on leg 2	$\begin{Bmatrix}\Delta u\\ \Delta v\end{Bmatrix}_{(F10-F9)} = [\varepsilon^0]\begin{Bmatrix}-a\\ \Delta y\end{Bmatrix} = \begin{Bmatrix}-a\varepsilon_x + \Delta y\gamma_{xy}\\ \Delta y\varepsilon_y\end{Bmatrix}$
F5 & F6 on leg 1	$\begin{Bmatrix}\Delta u\\ \Delta v\end{Bmatrix}_{(F5-F6)} = [\varepsilon^0]\begin{Bmatrix}0\\ W\end{Bmatrix} = \begin{Bmatrix}W\gamma_{xy}\\ W\varepsilon_y\end{Bmatrix}$
F11 & F12 on leg 2	$\begin{Bmatrix}\Delta u\\ \Delta v\end{Bmatrix}_{(F11-F12)} = [\varepsilon^0]\begin{Bmatrix}0\\ W\end{Bmatrix} = \begin{Bmatrix}W\gamma_{xy}\\ W\varepsilon_y\end{Bmatrix}$

Appendix B
Constraint equations for edges of unit cell model

Edges (excluding vertices)	Constraint equations
Edges// *z*-axis on the leg 1 [E1,E2,E3, E4]	$\begin{Bmatrix}\Delta u\\ \Delta \mathrm{v}\end{Bmatrix}_{(E2-E1)} = [\varepsilon^0]\begin{Bmatrix}0\\ W\end{Bmatrix} = \begin{Bmatrix}W\gamma_{xy}\\ W\varepsilon_y\end{Bmatrix}$ $\begin{Bmatrix}\Delta u\\ \Delta \mathrm{v}\end{Bmatrix}_{(E3-E1)} = [\varepsilon^0]\begin{Bmatrix}a\\ \Delta y + W\end{Bmatrix} = \begin{Bmatrix}a\varepsilon_x + \Delta y\gamma_{xy} + W\gamma_{xy}\\ \Delta y\varepsilon_y + W\varepsilon_y\end{Bmatrix}$ $\begin{Bmatrix}\Delta u\\ \Delta \mathrm{v}\end{Bmatrix}_{(E4-E1)} = [\varepsilon^0]\begin{Bmatrix}a\\ \Delta y\end{Bmatrix} = \begin{Bmatrix}a\varepsilon_x + \Delta y\gamma_{xy}\\ \Delta y\varepsilon_y\end{Bmatrix}$
Edges //*z*-axis on the leg 2	$\begin{Bmatrix}\Delta u\\ \Delta \mathrm{v}\end{Bmatrix}_{(E16-E13)} = [\varepsilon^0]\begin{Bmatrix}0\\ W\end{Bmatrix} = \begin{Bmatrix}W\gamma_{xy}\\ W\varepsilon_y\end{Bmatrix}$ $\begin{Bmatrix}\Delta u\\ \Delta \mathrm{v}\end{Bmatrix}_{(E15-E13)} = [\varepsilon^0]\begin{Bmatrix}-a\\ \Delta y + W\end{Bmatrix} = \begin{Bmatrix}-a\varepsilon_x + \Delta \mathrm{y}\gamma_{xy} + W\gamma_{xy}\\ \Delta \mathrm{y}\varepsilon_y + W\varepsilon_y\end{Bmatrix}$

[E13,E14,E15,E16]	$\begin{Bmatrix}\Delta u\\ \Delta v\end{Bmatrix}_{(E14-E13)} = [\varepsilon^0]\begin{Bmatrix}-a\\ \Delta y\end{Bmatrix} = \begin{Bmatrix}-a\varepsilon_x + \Delta y\gamma_{xy}\\ \Delta y\varepsilon_y\end{Bmatrix}$
Edges// y-axis on the leg 1 [E5,E8]	$\begin{Bmatrix}\Delta u\\ \Delta v\end{Bmatrix}_{(E8-E5)} = [\varepsilon^0]\begin{Bmatrix}a\\ \Delta y\end{Bmatrix} = \begin{Bmatrix}a\varepsilon_x + \Delta y\gamma_{xy}\\ \Delta y\varepsilon_y\end{Bmatrix}$
Edges// y-axis on the leg 2 [E19,E20]	$\begin{Bmatrix}\Delta u\\ \Delta v\end{Bmatrix}_{(E19-E20)} = [\varepsilon^0]\begin{Bmatrix}-a\\ \Delta y\end{Bmatrix} = \begin{Bmatrix}-a\varepsilon_x + \Delta y\gamma_{xy}\\ \Delta y\varepsilon_y\end{Bmatrix}$
Edges// y-axis on the leg 1&2 [E6,E7, E18,E17]	$\begin{Bmatrix}\Delta u\\ \Delta v\end{Bmatrix}_{(E7-E6)} = [\varepsilon^0]\begin{Bmatrix}a\\ \Delta y\end{Bmatrix} = \begin{Bmatrix}a\varepsilon_x + \Delta y\gamma_{xy}\\ \Delta y\varepsilon_y\end{Bmatrix}$ $\begin{Bmatrix}\Delta u\\ \Delta v\end{Bmatrix}_{(E17-E6)} = [\varepsilon^0]\begin{Bmatrix}a\\ 0\end{Bmatrix} = \begin{Bmatrix}a\varepsilon_x\\ 0\end{Bmatrix}$ $\begin{Bmatrix}\Delta u\\ \Delta v\end{Bmatrix}_{(E18-E6)} = [\varepsilon^0]\begin{Bmatrix}0\\ \Delta y\end{Bmatrix} = \begin{Bmatrix}\Delta y\gamma_{xy}\\ \Delta y\varepsilon_y\end{Bmatrix}$
Curved edges on the leg1 [E9, E10]	$\begin{Bmatrix}\Delta u\\ \Delta v\end{Bmatrix}_{(E10-E9)} = [\varepsilon^0]\begin{Bmatrix}0\\ W\end{Bmatrix} = \begin{Bmatrix}W\gamma_{xy}\\ W\varepsilon_y\end{Bmatrix}$
Curved edges on the leg2 [E23, E24]	$\begin{Bmatrix}\Delta u\\ \Delta v\end{Bmatrix}_{(E23-E24)} = [\varepsilon^0]\begin{Bmatrix}0\\ W\end{Bmatrix} = \begin{Bmatrix}W\gamma_{xy}\\ W\varepsilon_y\end{Bmatrix}$
Curved Edges on the leg 1 & leg 2 [E11,E12, E21,E22]	Interface area followed

Appendix C
Constraint equations for vertices of unit cell model

Vertices	Constraint equations
[V1,V2, V3, V4] on leg 1	$\begin{Bmatrix}\Delta u\\ \Delta \mathrm{v}\end{Bmatrix}_{(V2-V1)} = [\varepsilon^0]\begin{Bmatrix}0\\ W\end{Bmatrix} = \begin{Bmatrix}W\gamma_{xy}\\ W\varepsilon_y\end{Bmatrix}$ $\begin{Bmatrix}\Delta u\\ \Delta \mathrm{v}\end{Bmatrix}_{(V3-V1)} = [\varepsilon^0]\begin{Bmatrix}a\\ \Delta \mathrm{y}+W\end{Bmatrix} = \begin{Bmatrix}a\varepsilon_x+\Delta \mathrm{y}\gamma_{xy}+W\gamma_{xy}\\ \Delta \mathrm{y}\varepsilon_y+W\varepsilon_y\end{Bmatrix}$ $\begin{Bmatrix}\Delta u\\ \Delta \mathrm{v}\end{Bmatrix}_{(V4-V1)} = [\varepsilon^0]\begin{Bmatrix}a\\ \Delta \mathrm{y}\end{Bmatrix} = \begin{Bmatrix}a\varepsilon_x+\Delta \mathrm{y}\gamma_{xy}\\ \Delta \mathrm{y}\varepsilon_y\end{Bmatrix}$
[V5,V6, V7,V8, V9,V10, V11, V12] on leg 1 &2	$\begin{Bmatrix}\Delta u\\ \Delta \mathrm{v}\end{Bmatrix}_{(V6-V5)} = [\varepsilon^0]\begin{Bmatrix}0\\ W\end{Bmatrix} = \begin{Bmatrix}W\gamma_{xy}\\ W\varepsilon_y\end{Bmatrix}$ $\begin{Bmatrix}\Delta u\\ \Delta \mathrm{v}\end{Bmatrix}_{(V7-V5)} = [\varepsilon^0]\begin{Bmatrix}a\\ \Delta \mathrm{y}+W\end{Bmatrix} = \begin{Bmatrix}a\varepsilon_x+\Delta \mathrm{y}\gamma_{xy}+W\gamma_{xy}\\ \Delta \mathrm{y}\varepsilon_y+W\varepsilon_y\end{Bmatrix}$ $\begin{Bmatrix}\Delta u\\ \Delta \mathrm{v}\end{Bmatrix}_{(V8-V5)} = [\varepsilon^0]\begin{Bmatrix}a\\ \Delta \mathrm{y}\end{Bmatrix} = \begin{Bmatrix}a\varepsilon_x+\Delta \mathrm{y}\gamma_{xy}\\ \Delta \mathrm{y}\varepsilon_y\end{Bmatrix}$ $\begin{Bmatrix}\Delta u\\ \Delta \mathrm{v}\end{Bmatrix}_{(V12-V5)} = [\varepsilon^0]\begin{Bmatrix}0\\ \Delta \mathrm{y}\end{Bmatrix} = \begin{Bmatrix}\Delta \mathrm{y}\gamma_{xy}\\ \Delta \mathrm{y}\varepsilon_y\end{Bmatrix}$ $\begin{Bmatrix}\Delta u\\ \Delta \mathrm{v}\end{Bmatrix}_{(V11-V5)} = [\varepsilon^0]\begin{Bmatrix}0\\ \Delta \mathrm{y}+W\end{Bmatrix} = \begin{Bmatrix}\Delta \mathrm{y}\gamma_{xy}+W\gamma_{xy}\\ \Delta \mathrm{y}\varepsilon_y+W\varepsilon_y\end{Bmatrix}$ $\begin{Bmatrix}\Delta u\\ \Delta \mathrm{v}\end{Bmatrix}_{(V10-V5)} = [\varepsilon^0]\begin{Bmatrix}a\\ W\end{Bmatrix} = \begin{Bmatrix}a\varepsilon_x+W\gamma_{xy}\\ W\varepsilon_y\end{Bmatrix}$ $\begin{Bmatrix}\Delta u\\ \Delta \mathrm{v}\end{Bmatrix}_{(V9-V5)} = [\varepsilon^0]\begin{Bmatrix}a\\ 0\end{Bmatrix} = \begin{Bmatrix}a\varepsilon_x\\ 0\end{Bmatrix}$
[V13, V14, V15, V16]	$\begin{Bmatrix}\Delta u\\ \Delta \mathrm{v}\end{Bmatrix}_{(V14-V13)} = [\varepsilon^0]\begin{Bmatrix}0\\ W\end{Bmatrix} = \begin{Bmatrix}W\gamma_{xy}\\ W\varepsilon_y\end{Bmatrix}$ $\begin{Bmatrix}\Delta u\\ \Delta \mathrm{v}\end{Bmatrix}_{(V15-V13)} = [\varepsilon^0]\begin{Bmatrix}-a\\ \Delta \mathrm{y}+W\end{Bmatrix} = \begin{Bmatrix}-a\varepsilon_x+\Delta \mathrm{y}\gamma_{xy}+W\gamma_{xy}\\ \Delta \mathrm{y}\varepsilon_y+W\varepsilon_y\end{Bmatrix}$ $\begin{Bmatrix}\Delta u\\ \Delta \mathrm{v}\end{Bmatrix}_{(V16-V13)} = [\varepsilon^0]\begin{Bmatrix}-a\\ \Delta y\end{Bmatrix} = \begin{Bmatrix}-a\varepsilon_x+\Delta y\gamma_{xy}\\ \Delta y\varepsilon_y\end{Bmatrix}$

Appendix D
Constraint equations for interface area of the unit cell model

Faces (excluding edges)	Constraint equations
$FL1_i$, $FL2_i$ on interface area of leg 1 & leg 2 on the right part of unit cell	$\begin{Bmatrix}\Delta u\\ \Delta v\end{Bmatrix}_{(FL1_i-FL2_i)} = [\varepsilon^0]\begin{Bmatrix}0\\ i*W\end{Bmatrix} = \begin{Bmatrix}i\,W\gamma_{xy}\\ i\,W\varepsilon_y\end{Bmatrix}$
$FL2_i$, $FL1_i$ on interface area of leg1 & leg2 on the left part of unit cell	$\begin{Bmatrix}\Delta u\\ \Delta v\end{Bmatrix}_{(FL2_i-FL1_i)} = [\varepsilon^0]\begin{Bmatrix}0\\ i*W\end{Bmatrix} = \begin{Bmatrix}i\,W\gamma_{xy}\\ i\,W\varepsilon_y\end{Bmatrix}$
Edges (excluding vertices)	Constraint equations
$EL1_{Ui}$, $EL1_{Li}$, $EL1_{Ci}$ $EL2_{Ui}$, $EL2_{Li}$, $EL2_{Ci}$ on interface area of leg1 & leg2 on the right part of a unit cell	$\begin{Bmatrix}\Delta u\\ \Delta v\end{Bmatrix}_{(EL1_{Li}-EL2_{Ci})} = [\varepsilon^0]\begin{Bmatrix}0\\ (i-1)W\end{Bmatrix} = \begin{Bmatrix}(i-1)W\gamma_{xy}\\ (i-1)W\varepsilon_y\end{Bmatrix}$ $\begin{Bmatrix}\Delta u\\ \Delta v\end{Bmatrix}_{(EL1_{Ui}-EL2_{Ci})} = [\varepsilon^0]\begin{Bmatrix}0\\ i\,W\end{Bmatrix} = \begin{Bmatrix}i\;W\gamma_{xy}\\ i\;W\varepsilon_y\end{Bmatrix}$ $\begin{Bmatrix}\Delta u\\ \Delta v\end{Bmatrix}_{(EL2_{Ui}-EL2_{Li})} = [\varepsilon^0]\begin{Bmatrix}0\\ W\end{Bmatrix} = \begin{Bmatrix}W\gamma_{xy}\\ W\varepsilon_y\end{Bmatrix}$ $\begin{Bmatrix}\Delta u\\ \Delta v\end{Bmatrix}_{(EL1_{Ci}-EL2_{Li})} = [\varepsilon^0]\begin{Bmatrix}0\\ (i-1)W\end{Bmatrix} = \begin{Bmatrix}(i-1)W\gamma_{xy}\\ (i-1)W\varepsilon_y\end{Bmatrix}$
$EL2_{Ui}$, $EL2_{Li}$, $EL2_{Ci}$ $EL1_{Ui}$, $EL1_{Li}$, $EL1_{Ci}$ on interface area of leg1 & leg2 on the left part of unit cell	$\begin{Bmatrix}\Delta u\\ \Delta v\end{Bmatrix}_{(EL1_{Ui}-EL1_{Li})} = [\varepsilon^0]\begin{Bmatrix}0\\ W\end{Bmatrix} = \begin{Bmatrix}W\gamma_{xy}\\ W\varepsilon_y\end{Bmatrix}$ $\begin{Bmatrix}\Delta u\\ \Delta v\end{Bmatrix}_{(EL2_{Ci}-EL1_{Li})} = [\varepsilon^0]\begin{Bmatrix}0\\ (i-1)W\end{Bmatrix} = \begin{Bmatrix}(i-1)W\gamma_{xy}\\ (i-1)W\varepsilon_y\end{Bmatrix}$ $\begin{Bmatrix}\Delta u\\ \Delta v\end{Bmatrix}_{(EL2_{Li}-EL1_{Ci})} = [\varepsilon^0]\begin{Bmatrix}0\\ (i-1)W\end{Bmatrix} = \begin{Bmatrix}(i-1)W\gamma_{xy}\\ (i-1)W\varepsilon_y\end{Bmatrix}$ $\begin{Bmatrix}\Delta u\\ \Delta v\end{Bmatrix}_{(EL2_{Ui}-EL1_{Ci})} = [\varepsilon^0]\begin{Bmatrix}0\\ i*W\end{Bmatrix} = \begin{Bmatrix}i*W\gamma_{xy}\\ i*W\varepsilon_y\end{Bmatrix}$
Vertices	Constraint equations
$VL1_{Ui}$, $VL1_{Li}$ $VL2_{Ui}$, $VL2_{Li}$ on interface area of leg1 & leg2 on the right part of unit cell	$\begin{Bmatrix}\Delta u\\ \Delta v\end{Bmatrix}_{(VL2_{Ui}-VL2_{Li})} = [\varepsilon^0]\begin{Bmatrix}0\\ W\end{Bmatrix} = \begin{Bmatrix}W\gamma_{xy}\\ W\varepsilon_y\end{Bmatrix}$ $\begin{Bmatrix}\Delta u\\ \Delta v\end{Bmatrix}_{(VL1_{Li}-VL2_{Li})} = [\varepsilon^0]\begin{Bmatrix}0\\ i\,W\end{Bmatrix} = \begin{Bmatrix}i\,W\gamma_{xy}\\ i\,W\varepsilon_y\end{Bmatrix}$ $\begin{Bmatrix}\Delta u\\ \Delta v\end{Bmatrix}_{(VL1_{Ui}-VL2_{Li})} = [\varepsilon^0]\begin{Bmatrix}0\\ (i+1)W\end{Bmatrix} = \begin{Bmatrix}(i+1)W\gamma_{xy}\\ (i+1)W\varepsilon_y\end{Bmatrix}$

VL2$_{Ui}$, VL2$_{Li}$ VL1$_{Ui}$, VL1$_{Li}$ on interface area of leg1 & leg2 on the left part of unit cell	$\begin{Bmatrix}\Delta u\\ \Delta v\end{Bmatrix}_{(VL1_{Ui}-VL1_{Li})} = [\varepsilon^0]\begin{Bmatrix}0\\ W\end{Bmatrix} = \begin{Bmatrix}W\gamma_{xy}\\ W\varepsilon_y\end{Bmatrix}$ $\begin{Bmatrix}\Delta u\\ \Delta v\end{Bmatrix}_{(VL2_{Li}-VL1_{Li})} = [\varepsilon^0]\begin{Bmatrix}0\\ i\,W\end{Bmatrix} = \begin{Bmatrix}iW\gamma_{xy}\\ i\,W\varepsilon_y\end{Bmatrix}$ $\begin{Bmatrix}\Delta u\\ \Delta v\end{Bmatrix}_{(VL2_{Ui}-VL1_{Li})} = [\varepsilon^0]\begin{Bmatrix}0\\ (i+1)W\end{Bmatrix} = \begin{Bmatrix}(i+1)W\gamma_{xy}\\ (i+1)W\varepsilon_y\end{Bmatrix}$